

**MULTI-SCALE INVESTIGATIONS OF
CARBOXYMETHYL CELLULOSE-COATED
NANOSCALE ZERO VALENT IRON PARTICLE
TRANSPORT IN POROUS MEDIA**

by

Jing Li



**MCGILL UNIVERSITY
DEPARTMENT OF CIVIL ENGINEERING AND APPLIED MECHANICS**

Dec. 13, 2013

A THESIS SUBMITTED TO MCGILL UNIVERSITY
IN PARTIAL FULFILLMENT OF THE REQUIREMENTS FOR THE DEGREE
OF DOCTOR OF PHILOSOPHY

Abstract

Subsurface injection of nano scale zero valent iron (NZVI) particles is an emerging technology for in situ remediation of the sites contaminated by toxic contaminants such as chlorinated organic dense non aqueous phase liquids (DNAPLs) and heavy metals. One of the key challenges in applying NZVI particles for remediation at the field scale is that NZVI particles are not readily transported in subsurface porous media.

The overall objective of this research is to address this challenge by conducting a number of column experiments and 2-D pilot scale tank experiments as well as by exploring the deposition mechanics of metal nanoparticles theoretically. Although numerous studies have focused the stability and transport of polymer/polyelectrolyte coated NZVI particles, the comparison of the effect of the same type of polyelectrolyte stabilizer with different molecular weight on the stability and transport of the corresponding coated NZVI particles has not been systematically conducted to date. Varying molecular weights of homologous polyelectrolytes can cause changes in viscosity and rheology in free solution, and alter the extent of colloidal stability when coated on the nanoparticles. Furthermore, most of the studies on NZVI particle transport have been conducted in the vertically placed columns, which are not representative with the actual flow orientation in field, leading to a potential difference of transport performance of NZVI particles between the commonly used vertical flow orientation and the horizontal flow model. In addition, the scale-up effects (from laboratory-scale column to pilot-scale or field-scale demonstrations) on NZVI transport are reported. In this study, a thorough investigation on NZVI transport is conducted in a 2-D pilot-scale tank to shed some light on the transport performance of NZVI particles under conditions that are more close to actual circumstances. Finally, to calculate the deposition rate coefficient of metal nanoparticles during transport, a considerable number of studies on NZVI particles transport employed equations for predicting the single collector contact efficiency that are developed on the basis of the numerical calculations for common colloidal particles such as latex particles, which have smaller densities than those of metal particles. Taking the horizontal flow mode and the density effects for metal nanoparticles into consideration, a new methodology is developed in three dimensions (3-D) to more precisely predict the single collector efficiency of NZVI particles.

In the first study, the influence of the molecular weight of the polyelectrolyte grafted on NZVI particle on its stability and transport was investigated. Three carboxymethyl celluloses (CMC) with different molecular weights (90,000 Da, 250,000 Da and 700,000 Da) were used to stabilize NZVI particles. The comparison of the results revealed that the stability and transport of NZVI particles were improved significantly by CMC with high molecular weight, due to its high viscosity property. In the second study, the effects of gravity on NZVI particle during its transport were extensively assessed in vertical and horizontal placed columns under different conditions (mean sand diameters and NZVI concentrations). The results indicated that the gravity forces significantly reduced NZVI particles transport in coarse sand and at high NZVI concentration in horizontally placed columns. To thoroughly study the impact of horizontal orientation flow on the transport of NZVI particles at a larger scale, a series of transport experiments were conducted in a pilot-scale 2-D tank. Furthermore, to address the challenges met in predicting the single collector efficiency in horizontal orientation flow mode, a methodology based on trajectory analysis of particles around a Happel sphere-in-cell model for porous media in 3-D was developed.

Résumé

L'injection souterraine des nanoparticules de fer à zéro valence (NZVI) est une technologie émergente pour l'assainissement *in situ* des sites contaminés par des polluants toxiques comme les solvants chlorés et les métaux lourds. L'un des principaux défis dans l'application des particules de NZVI à des fins de rémédiation est que les particules de NZVI ne sont pas facilement transportées dans des milieux poreux souterrains. L'objectif général de cette recherche est de relever ce défi en réalisant un certain nombre d'expériences en colonnes et en 2-D sur des bassins à l'échelle pilote ainsi que par l'analyse de la mécanique de dépôt de nanoparticules métalliques en théorie. Bien que de nombreuses études ont porté sur la stabilité et le transport de nanoparticules de fer (NZVI) revêtues de polymère / poly-électrolyte, la comparaison de l'effet du même type de stabilisant en polyélectrolyte ayant des poids moléculaires différents, sur la stabilité et le transport des particules de NZVI enrobées n'ont pas été effectués systématiquement à ce jour. Des poids moléculaires variables des polyélectrolytes homologues peuvent provoquer des variations de viscosité en solution libre et dans l'étendue de la stabilisation colloïdale électrostatique de NZVI en s'attachant sur la surface des nanoparticules. Des études antérieures sur le transport des particules NZVI ont été menées dans les colonnes placées verticalement, qui souvent ne sont pas représentatifs de l'orientation de l'écoulement réel sur le champ, ce qui conduit à une différence de potentiel de performance du transport de particules NZVI entre l'orientation de l'écoulement vertical couramment utilisé et le modèle à flux horizontal. Outre, les effets à l'échelle grandissante (de la colonne à l'échelle de laboratoire, pilote ou des manifestations à l'échelle du champ) sur le transport de NZVI sont rapportés. Dans cette étude, une enquête approfondie sur le transport de NZVI est effectuée dans un réservoir en 2-D à l'échelle pilote afin de faire la lumière sur la performance du transport des particules de NZVI dans des conditions qui sont plus près de la situation réelle. Enfin, pour calculer le coefficient de vitesse de dépôt des nanoparticules de métal en cours de transport, un nombre considérable d'études sur les particules de NZVI ont été effectuées en employant des équations de transport à fin de prédire le contact de rendement du capteur unique qui sont mis au point sur la base des calculs numériques pour les particules colloïdales communes moins denses tels que des particules de latex, qui ont des densités plus inférieures que celles des particules de métal. Prenant le mode d'écoulement horizontal et les effets de la densité de nanoparticules métalliques en considération,

une nouvelle méthode est développée en trois dimensions (3-D) afin de prédire plus précisément l'efficacité du collecteur unique de particules NZVI .

Dedication

To my parents

Acknowledgements

I will forever be grateful for my supervisor, Prof. Subhasis Ghoshal, who provided me the opportunity and gave me so many assistances I needed for my Ph.D study. I appreciated him for his patience in training me in many aspects.

I would like to thank NZVI program members in Mcgill, Prof. Nathalie Tufenkji for the DLS and zeta potential measurements conducted in her laboratory. Many thanks to Sai R. C. Rajajayavel for his assistance in the tank experiments.

I want to thank my friend Xiaohu Xie in the department of Computer Science in Mcgill University for his help in the 3-D model creation.

Within the Environmental Engineering laboratory, I would like to thank John Bartczak for his so much help in constructing our tank system and to Daina Brumelis for her help in trainings. I would like to thank many of my colleagues, Arti Bhakta (she trained me on how to do a lot of bacterial experiments and how to order chemicals as well as helped me to be familiar with our laboratory once I came to Mcgill), Ali Akbari and Siavash Isazadeh, Sharmin Sultana. I would also give my thanks to many of Chinese friends: Xiaoyong Liu, Hechuan Jiang, Bing Guo, Min Feng, Guowei Zhong, Yan Zhao, Ping Wang, Yongzheng Zhang and Fang Shang for their helps in my research discussion and in personal life. Thanks to CGSA (Chinese Graduate & Scholar Associate) for letting me to serve it for almost one and half years (from Feb. 2011 to July 2012) as a president. Thanks all officials in Education Office, Embassy of the People's Republic of China in Canada.

I would give my special thanks to my family: my parents, elder brother and younger sister. My parents deserve much more appreciation than I can give. My father always encouraged me to pursue my dream in his particular ways. Even after he passed away, his spirit still bestirred me to surmount the difficulties in my study.

Finally, I would like to acknowledge Mcgill Engineering Doctoral Award (MEDA) and the Natural Sciences and Engineering Research Council of Canada (NSERC) for the financial support.

Table of Contents

Abstract	i
Dedication	v
Acknowledgements	vi
Table of Contents	vii
LIST OF TABLES	x
LIST OF FIGURES	x
LIST OF ABBREVIATION	xvi
LIST OF SYMBOLS	xvii
Chapter 1 Introduction	1
1.1 Background—significance of DNAPL contamination in subsurface	1
1.2 The DNAPLs remediation technologies and challenges	1
1.3 Motivation of the study	2
1.3.1 Rationale for applying NZVI particles to remediate DNAPLs contaminated sites	2
1.3.2 Limitations to transport of NZVI in the subsurface	3
1.3.3 Research Scope	4
1.4 The specific objectives	5
1.5 Scope and structure of the thesis	6
1.6 Contribution of Authors	7
Literature cited	9
Chapter 2 Literature Reveiw	11
2.1 Introduction	11
2.1.1 Chlorinated solvent toxicity	12
2.1.2 Chlorinated solvent remediation technologies	13
2.2 Nanoscale zero valent iron (NZVI) particle	17
2.2.1 Discoveries	17
2.2.2 Properties and applications	18
2.2.3 Aggregation of NZVI particles	20
2.3 Transport of NZVI particles	20
2.4 Prediction of the transport of NZVI particles by the colloid filtration theory	23
Literature cited	25

Chapter 3 Colloidal stability and transport of NZVI particles coated with Carboxymethyl cellulose of various molecular weights.....	32
3.1 Introduction.....	33
3.2 Materials and Methods.....	37
3.3 Results.....	41
3.3.1. Nanoparticle characterization.....	41
3.3.2 The effects the molecular weight of CMC on NZVI particle stability.....	45
3.3.3 The effects of the molecular weight of CMC on the transport of NZVI particles.....	50
3.4 Conclusions.....	60
Acknowledgments.....	61
Supporting information.....	62
References.....	73
Chapter 4 Comparison of transport of nanoscale zero valent iron nanoparticles under vertical and horizontal flow.....	78
4.1 Introduction.....	79
4.2 Materials and methods.....	81
4.3 Results.....	85
4.3.1 NZVI aggregate size characterization.....	85
4.3.2 Tracer tests.....	86
4.3.3 Breakthrough curves of CMC-NZVI from horizontal and vertical columns.....	88
4.3.4 Retention of CMC-NZVI in vertical and horizontal columns.....	92
4.4 Analyses of deposition mechanisms in vertical and horizontal columns.....	95
4.5 Conclusions.....	107
Acknowledgments.....	107
Supporting information.....	108
References.....	119
Chapter 5 Transport of polyelectrolyte-coated zero valent iron particles in a sand tank: effects of nanoparticle concentration and injection velocity.....	123
5.1 Introduction.....	124
5.2 Materials and Methods.....	128
5.3 Results and Discussion.....	132
5.3.1 Particle Characterization.....	132
5.3.2 Flow test by Dye Tracer.....	133
5.3.3 The Effect of Sand Size on NZVI Transport.....	133
5.3.4 The Effect of CMC concentration on NZVI Particle Transport.....	136

5.3.5	The Effect of Injection Velocity on NZVI Transport	138
5.3.6	Deposition of NZVI Particles	140
5.3.7	The Aggregation of NZVI Particles during Transport.....	141
5.3.8	The Conductivity and Pressure Drop Measurements.....	142
5.4	Implications for Assessment of NZVI Injections	143
	Supporting information	145
	References	162
Chapter 6 Correlation equation for predicting single-collector efficiency using trajectory analysis method in three dimensions		165
6.1	Introduction	166
6.2	Numerical simulation for η_0	170
6.3	Results.....	179
6.3.1	Comparison of the Numerical Results with the RT Equation and TE Equation	179
6.3.2	New Correlation Equation for Colloid Transport.....	184
6.4	Conclusions	189
	Acknowledgements	190
	Nomenclature	190
	Supporting information	193
	References	205
Chapter 7 Intellectual contributions.....		209
7.1	Determining the role of stabilizing polymer molecular weights on enhancing colloidal stabilization and transport of NZVI.	210
7.2	Demonstrating the role of horizontal and vertical flow direction on CMC-NZVI transport behavior.....	210
7.3	The changes in temporal and spatial distribution of NZVI particles during NZVI injection and transport in a scaled-up 2-D tank was demonstrated for a range of porous media size and particle suspension characteristics.	211
7.4	This study is the first to mathematically simulate the trajectory of colloidal particles around a collector under horizontal flow mode by using Lagrangian trajectory analysis combined with Brownian motion. A new correlation equation for horizontal flow of colloids around a collector was presented. The study demonstrates that the density of engineered nanoparticles result in different trajectories in horizontal flow mode from those in vertical flow mode.	212

LIST OF TABLES

Table 3.1. Size and Physicochemical Characteristics of CMC-NZVI results.	42
Table 3.S1. CMC mass content of different CMC-NZVI particles.	69
Table 3.S2. Layer thickness of different CMC-NZVI particles determined by TEM measurement.	69
Table 4.1. The diameter of NZVI aggregates as measured by conventional optical microscopy under different conditions.	85
Table 4.2. Deposition parameters for CMC NZVI transport in vertical and horizontal columns.	96
Table 4.3. The calculations of the single collector contact efficiency (η_0) of the current modified trajectory analysis as well as the profiles of particles' trajectories under different conditions. ...	99
Table 4.4. The comparisons of the mean of minimum distances between NZVI and latex particles' trajectories and the upper/lower half collector surface under different conditions.	104
Table 5.S1. Review of the studies on the synthesis, stability and transport of CMC-NZVI particles.	146
Table 5.S2. The parameters for the tank experiments and the CFT calculation results.	154
Table 5.S3. Mean diameters of iron NPs measured by microscopy.	160
Table 5.S4. Conductivity changes of different tank experiments.	161
Table 5.S5. The pressure drop of 1 g/L CMC in 0.5 mM NaHCO ₃ in the tank.	161
Table 5.S6. The pressure drop of 2 g/L CMC in the tank.	162
Table 6.1. Summary of the dimensionless parameters.	172
Table 6.2. Forces and torques acting on the suspended particles through 2-D and 3-D collectors.	173
Table 6.3. Summary of Parameter Values Used in Numerical Calculations.	178
Table 6.S1. Summary of the studies on the simulation and modeling of single collector contact contact efficiency ^a	193

LIST OF FIGURES

Figure 3.1. Extended DLVO calculations (a) the electrosteric interaction energies of different CMC-NZVI particles (between particle and particle); (b) total interaction energies of different CMC-NZVI particles (between particle and particle); (c) the secondary minima of different CMC-NZVI particles (between particle and particle); (d) the changes of the total interaction energies of 700K CMC-NZVI particles with NaHCO₃ concentrations (between particle and particle); (e) the total interaction energies of different CMC-NZVI particles (between particle

and collector); (f) the changes of the total interaction energy of 700K CMC-NZVI with NaHCO ₃ concentration (between particle and collector).....	48
Figure 3.2. The transport of different CMC-NZVI particles at 1 g/L (in 3 mM Na ⁺ solution) in column experiments.....	51
Figure 3.3. Changes of the single collector contact efficiency with varying viscosity of dispersant.....	53
Figure 3.4. The effects of IS and washing on transport of 700K CMC- and 250K CMC-NZVI particles.....	54
Figure 3.5. The transport of different CMC-NZVI particles at 3 g/L (in 3 mM Na ⁺ solution). ...	57
Figure 3.6. Retention profiles along with the column length of 250K CMC- and 700K CMC-NZVI particles.	59
Figure 3.S1. The changes of particle size distribution of different CMC-NZVI particles with time.....	67
Figure 3.S2. Representatives of size distributions of different NZVI particles determined by optical microscopy, (a) 1 g/L NZVI in 1 g/L 700K CMC (3 mM Na ⁺); (b) 1 g/L NZVI in 1 g/L 250K CMC (3 mM Na ⁺); (c) 1 g/L NZVI in 1 g/L 90K CMC (3 mM Na ⁺).....	68
Figure 3.S3. Electrophoretic mobility of different CMC grafted NZVI particles as a function of NaHCO ₃ concentration. The surface charge densities (N/m ³) and the softness (λ) of different CMC-NZVI particles were 2.923 and 9.0 (90K CMC-NZVI), 6.538 and 6.0 (250K CMC-NZVI) and 7.769 and 5.8 (700K CMC-NZVI) obtained from the fittings.....	70
Figure 3.S4. The electrostatic interaction energy of different CMC-NZVI particles in NaHCO ₃ solutions (with varied concentrations) calculated from equation (3.S7) and N values obtained in Figure 3.S3. (a) 90K CMC-NZVI; (b) 250K CMC-NZVI; (c) 700K CMC-NZVI.....	71
Figure 3.S5. Sedimentation results (a) the effects of different CMC and washing on the sedimentation rate of NZVI particles (all samples were prepared with 3 mM NaHCO ₃); (b) the effect of NaHCO ₃ concentration on sedimentation rate of 700K CMC-NZVI.	71
Figure 4.1. Breakthrough curves of nitrate through vertical and horizontal columns packed with coarse sand (average diameter 1140 μ m).....	87
Figure 4.2. Breakthrough curves of latex particles (average diameter 1 μ m) through vertical and horizontal columns packed with intermediate sand (average diameter 340 μ m).	87
Figure 4.3. Comparison of transport in vertical and horizontal columns at 0.3 g/ L CMC-NZVI.....	89
Figure 4.4. Comparison of transport in vertical and horizontal columns at 1 g/ L CMC-NZVI. .	90
Figure 4.5. Comparison of transport in vertical and horizontal columns at 3 g/ L CMC-NZVI. .	92
Figure 4.6. The picture of the peculiar column with six sample ports in the both top and bottom sides.....	93
Figure 4.7. The retention of NZVI particles in the vertical and horizontal columns packed with intermediate sand at the end of the NZVI injection and electrolyte flushing periods: (a) 0.3 g/L NZVI; (b) 1 g/L NZVI; (c) 3 g/L NZVI.	93
Figure 4.S1. The gravity decomposition on the collector: a) 2-D collector; b) 3-D collector....	108

Figure 4.S2. The uniform partition of the cross-section area into 20 regions (equal area method).	114
Figure 4.S3. Sedimentation experimental results of CMC-NZVI at different concentrations. ..	115
Figure 4.S4. Iron retention in the coarse sand: a) 0.3 g/L 700K CMC-NZVI; b) 1 g/L 700K CMC-NZVI; c) 3 g/L 700K CMC-NZVI.	116
Figure4. S5. Iron retention in the fine sand: a) 0.3 g/L 700K CMC-NZVI; b) 1 g/L 700K CMC-NZVI; c) 3 g/L 700K CMC-NZVI.....	117
Figure 5.1. (a) The image of the tank; (b) Schematic of 2-D tank system.....	132
Figure 5.2. The iron concentration distribution in the aqueous phase (1 g/L NZVI in 1 g/L CMC solution), packed with coarse sand ($d_{50}=1140 \mu\text{m}$), at injection velocity of 0.96 cm/min.	134
Figure 5.3. The iron concentration distribution in the aqueous phase (1 g/L NZVI in 1 g/L CMC solution); packed with intermediate sand ($d_{50}=340 \mu\text{m}$), at injection velocity of 0.96 cm/min.	135
Figure 5.4. The iron concentration distribution in the aqueous phase (1 g/L NZVI in 1 g/L CMC solution), packed with fine sand ($d_{50}=180 \mu\text{m}$), at injection velocity of 0.96 cm/min.	136
Figure 5.5. The iron concentration distribution in the aqueous phase (3 g/L NZVI suspension in 2 g/L CMC solution), packed with intermediate sand ($d_{50}=340 \mu\text{m}$), at injection velocity of 0.96 cm/min.	137
Figure 5.6. The iron concentration distribution in the aqueous phase (3 g/L NZVI suspension in 1 g/L CMC solution), packed with intermediate sand ($d_{50}=340 \mu\text{m}$), at injection velocity of 0.96 cm/min.	138
Figure 5.7. The iron concentration distribution in the aqueous phase (1 g/L NZVI suspension in 1 g/L CMC solution), packed with intermediate sand ($d_{50}=340 \mu\text{m}$), at injection velocity of 0.40 cm/min.	139
Figure 5.S1. The pressure drop at different places in the tank (electrolyte flow).....	150
Figure 5.S2. Representative images illustrating the transport of the red tracer.	152
Figure 5.S3. Representative images illustrating the transport of NZVI particles.	153
Figure 5.S4. The comparison of the experimental retention of iron NPs (with flow distance) and the calculated retention of iron NPs (with flow distance) in the coarse sand tank (under the conditions: 1 g/L NZVI in 1 g/L 700K CMC with 0.5 mM NaHCO_3 at 0.96 cm/minute).....	155
Figure 5.S5. The comparison of the experimental retention of iron NPs (with flow distance) and the calculated retention of iron NPs (with flow distance) in the intermediate sand tank (under the conditions: 1 g/L NZVI in 1 g/L 700K CMC with 0.5 mM NaHCO_3 at 0.96 cm/minute).....	155
Figure 5.S6. The comparison of the experimental retention of iron NPs (with flow distance) and the calculated retention of iron NPs (with flow distance) in the fine sand tank (under the conditions: 1 g/L NZVI in 1 g/L 700K CMC with 0.5 mM NaHCO_3 at 0.96 cm/minute).....	156
Figure 5.S7. The comparison of the experimental retention of iron NPs (with flow distance) and the calculated retention of iron NPs (with flow distance) in the intermediate sand tank (under the conditions: 3 g/L NZVI in 2 g/L 700K CMC at 0.96 cm/min.	156

Figure 5.S8. The retention of iron NPs on sand (coarse sand packed tank) under the conditions: 1 g/L NZVI in 1 g/L 700K CMC (with 0.5 mM NaHCO ₃) and 0.96 cm/minute of injection velocity.....	157
Figure 5.S9. The retention of iron NPs on sand (intermediate sand packed tank) under the conditions: 1 g/L NZVI in 1 g/L 700K CMC (with 0.5 mM NaHCO ₃) and 0.96 cm/minute of injection velocity.....	157
Figure 5.S10. The retention of iron NPs on sand (fine sand packed tank) under the conditions: 1 g/L NZVI in 1 g/L 700K CMC (with 0.5 mM NaHCO ₃) and 0.96 cm/minute of injection velocity.....	158
Figure 5.S11. The retention of iron NPs on sand (intermediate sand packed tank) under the conditions: 3 g/L NZVI in 2 g/L 700K CMC (with 0.5 mM NaHCO ₃) and 0.96 cm/minute of injection velocity.....	158
Figure 5.S12. The retention of iron NPs on sand (intermediate sand packed tank) under the conditions: 1 g/L NZVI in 1 g/L 700K CMC (with 0.5 mM NaHCO ₃) and 0.40 cm/minute of injection velocity.....	159
Figure 5.S13. The retention of iron NPs on sand (intermediate sand packed tank) under the conditions: 3 g/L NZVI in 1 g/L 700K CMC (with 0.5 mM NaHCO ₃) and 0.96 cm/minute of injection velocity.....	159
Figure 6.1. The gravity decomposition on the collector: a) 2-D collector; b) 3-D collector.	169
Figure 6.2. Happel's sphere-in-cell porous media model in horizontal flow origination. (a) The symmetrical deposition of colloids on top and bottom of the collector under small gravity forces (small particle size and/or particle density); (b) The unsymmetrical trajectory of colloids around the collector under significant gravity forces.....	171
Figure 6.3. The comparison of predictions of single collector contact efficiency (η_0) based on rigorous numerical simulations of trajectories of particles (closed circle) , the new correlation (red line), the predictions from TE equation (blue line) and the predictions from the RT equation under the conditions: $\rho_p=1.05$ g/cm ³ , $\nu=1$ cP, U=0.508 cm/min, $d_s=340$ μ m.....	185
Figure 6.4. The comparison of predictions of single collector contact efficiency (η_0) based on rigorous numerical simulations of trajectories of particles (closed circyle) , the new correlation (red line), the predictions from TE equation (blue line) and the predictions from the RT equation under the conditions: $\rho_p=6.58$ g/cm ³ , $\nu=1$ cP, U=0.508 cm/min, $d_s=340$ μ m.....	186
Figure 6.5. The comparison of predictions of single collector contact efficiency (η_0) based on rigorous numerical simulations of trajectories of particles (closed circyle) , the new correlation (red line), the predictions from TE equation (blue line) and the predictions from the RT equation under the conditions: $d_p=4000$ nm, $\nu=1$ cP, U=0.508 cm/min, $d_s=340$ μ m.....	187
Figure 6.6. The comparison of predictions of single collector contact efficiency (η_0) based on rigorous numerical simulations of trajectories of particles (closed circyle) , the new correlation (red line), the predictions from TE equation (blue line) and the predictions from the RT equation under the conditions: $d_p=4000$ nm, $\nu=1$ cP, $\rho_p=6.58$ g/cm ³ , $d_s=340$ μ m.	188

Figure 6.7. The comparison of predictions of single collector contact efficiency based on rigorous numerical simulations of trajectories of particles (closed circle) , the new correlation (red line), the predictions from TE equation (blue line) and the predictions from the RT equation under the conditions: $d_p=4000$ nm, $\nu=1$ cP, $U=0.508$ cm/min, $\rho_p=6.58$ g/cm³. 189

Figure 6.S1. The predictions of η_0 from the TE and RT equations as well as the 3-D numerical simulated η_0 with particle diameter under the conditions: $\rho_p=1.05$ g/cm³, $d_s=340$ μ m, $f=0.37$, $U=0.508$ cm/min, $\mu=1$ cP. 195

Figure 6.S2. The predictions of η_0 from the TE and RT equations as well as the 3-D numerical simulated η_0 with particle diameter under the conditions: $\rho_p=6.58$ g/cm³, $d_s=340$ μ m, $f=0.37$, $U=0.508$ cm/min, $\mu=1$ cP. 196

Figure 6.S3. The demonstrations of the deposition locations of particles. a) the particles with the density of 1.05 g/cm³ and 4000 nm diameter; b) the particles with the density of 6.58 g/cm³ and 4000 nm, (other conditions: $U=0.508$ cm/min, $d_s=340$ μ m, $\mu=1$ cP). 196

Figure 6.S4. The predictions of η_0 from the TE and RT equations as well as the 3-D numerical simulated η_0 with particle density under the conditions: $d_p=200$ nm, $d_s=340$ μ m, $f=0.37$, $U=0.508$ cm/min, $\mu=26.3$ cP. 197

Figure 6.S5. The predictions of η_0 from the TE and RT equations as well as the 3-D numerical simulated η_0 with particle density under the conditions: $d_p=2000$ nm, $d_s=340$ μ m, $f=0.37$, $U=0.508$ cm/min, $\mu=1$ cP. 198

Figure 6.S6. The predictions of η_0 from the TE and RT equations as well as the 3-D numerical simulated η_0 with particle density under the conditions: $d_p=4000$ nm, $d_s=340$ μ m, $f=0.37$, $U=0.508$ cm/min, $\mu=1$ cP. 199

Figure 6.S7. The predictions of η_0 from the TE and RT equations as well as the 3-D numerical simulated η_0 with the viscosity of the suspension under the conditions: $d_p=2000$ nm, $d_s=340$ μ m, $f=0.37$, $U=0.508$ cm/min, $\rho_p=6.58$ g/cm³. 199

Figure 6.S8. The predictions of η_0 from the TE and RT equations as well as the 3-D numerical simulated η_0 with the viscosity of the suspension under the conditions: $d_p=2000$ nm, $d_s=340$ μ m, $f=0.37$, $U=0.508$ cm/min, $\rho_p=1.05$ g/cm³. 200

Figure 6.S9. The predictions of η_0 from the TE and RT equations as well as the 3-D numerical simulated η_0 with the viscosity of the suspension under the conditions: $d_p=400$ nm, $d_s=340$ μ m, $f=0.37$, $U=0.508$ cm/min, $\rho_p=1.05$ g/cm³. 200

Figure 6.S10. The predictions of η_0 from the TE and RT equations as well as the 3-D numerical simulated η_0 with the viscosity of the suspension under the conditions: $d_p=400$ nm, $d_s=340$ μm , $f=0.37$, $U=0.508$ cm/min, $\rho_p=6.58$ g/cm³..... 201

Figure 6.S11. The predictions of η_0 from the TE and RT equations as well as the 3-D numerical simulated η_0 with approach velocity under the conditions: $d_p=400$ nm, $d_s=340$ μm , $f=0.37$, $\mu=1$ cP, $\rho_p=6.58$ g/cm³. 201

Figure 6.S12. The predictions of η_0 from the TE and RT equations as well as the 3-D numerical simulated η_0 with approach velocity under the conditions: $d_p=4000$ nm, $d_s=340$ μm , $f=0.37$, $\mu=1$ cP, $\rho_p=6.58$ g/cm³. 202

Figure 6.S13. The predictions of η_0 from the TE and RT equations as well as the 3-D numerical simulated η_0 with approach velocity under the conditions: $d_p=4000$ nm, $d_s=340$ μm , $f=0.37$, $\mu=1$ cP, $\rho_p=1.05$ g/cm³. 202

Figure 6.S14. The predictions of η_0 from the TE and RT equations as well as the 3-D numerical simulated η_0 with the diameter of collector under the conditions: $d_p=200$ nm, $U=0.508$ cm/min, $f=0.37$, $\mu=1$ cP, $\rho_p=6.58$ g/cm³. 203

Figure 6.S15. The predictions of η_0 from the TE and RT equations as well as the 3-D numerical simulated η_0 with the diameter of collector under the conditions: $d_p=2000$ nm, $U=0.508$ cm/min, $f=0.37$, $\mu=1$ cP, $\rho_p=6.58$ g/cm³. 203

Figure 6.S16. The predictions of η_0 from the TE and RT equations as well as the 3-D numerical simulated η_0 with the diameter of collector under the conditions: $d_p=2000$ nm, $U=0.508$ cm/min, $f=0.37$, $\mu=1$ cP, $\rho_p=1.05$ g/cm³. 204

Figure 6.S17. The predictions of η_0 from the TE and RT equations as well as the 3-D numerical simulated η_0 with the diameter of collector under the conditions: $d_p=4000$ nm, $U=0.508$ cm/min, $f=0.37$, $\mu=1$ cP, $\rho_p=6.58$ g/cm³. 204

Figure 6.S18. The predictions of η_0 from the TE and RT equations as well as the 3-D numerical simulated η_0 with the diameter of collector under the conditions: $d_p=4000$ nm, $U=0.508$ cm/min, $f=0.37$, $\mu=1$ cP, $\rho_p=1.05$ g/cm³. 205

LIST OF ABBREVIATION

AAS	Atomic Absorption Spectroscopy
BTC	Break Through Curves
CFT	Colloid Filtration Theory
CHN	Carbon Hydrogen Nitrogen analysis
CMC	Carboxymethyl Cellulose
DLS	Dynamic Light Scattering
DLVO	Darjaguin-Landue-Varwey-Overbeek
DNAPL	Dense Non-Aqueous Phase Liquids
EMP	Electrophoretic Mobility
IS	Ionic Strength
MW	Molecular Weight
NAPL	Non-Aqueous Phase Liquids
NTA	Nanoparticle Tracking Analyzer
NZVI	Nano-scale Zero-Valent Iron
PAA	Polyacrylic Acid
PAP	Polyaspartate
PRB	Permeable Reactive Barrier
PSS	Polystyrenesulfonate
PV	Pore Volume

RT	Rajagopalan and Tien
TEM	Transmission Electron Microscopy
TE	Tufenkji and Elimelech

LIST OF SYMBOLS

A	Hamaker constant
A_C	the coefficient in equation 6.S4
A_C^+	the dimensionless A_C defined by $A_C a_p^2 / U$
A_s	porosity-dependent parameter of Happel's model; $A_s = 2(1 - p^5) / (2 - 3p + 3p^5 - 2p^6)$
α	the attachment efficiency
a_1, a_2	radius of two particles for interaction energy calculations
a_p	radius of particle
a_s	radius of the spherical collector
$a(\delta, a_p, \lambda_e)$	the retardation correction factor
b	radius of the Happel cell
B_C	the coefficient in equation 6.S4
B_C^+	the dimensionless B_C defined by $B_C a_p / U$
C_0	the number concentration of particles in the suspension
C	effluent particle mass concentration
D_C	the coefficient in equation 6.S4
D_C^+	the dimensionless D_C defined by $D_C a_p^2 / U$
D_∞	diffusion coefficient in an infinite medium, $D_\infty = k_B T / (6\pi\eta a_p)$
d_s	diameter of spherical collector, $d_s = 2a_s$

d_p	diameter of particle, $d_p = 2a_p$
e	the elementary electron charge
e_r, e_θ, e_φ	unit vectors in r, θ and φ directions
$f_r^t, f_\theta^t, f_r^m, f_\theta^m, f_{1\theta}^m, f_{2\theta}^m$ and f_θ^r	Drag correction factors in Table 6.2, functions of δ
f_i^j	force vector on the particle, superscript specifies the source of the force
f	the porosity of the porous media
g	magnitude of the gravity vector, $g=9.81 \text{ g/s}^2$
$g_\varphi^r, g_\varphi^t, g_{1\varphi}^m$ and $g_{2\varphi}^m$	torque correction factors in Table 6.2, functions of δ
h	the separation distance between two particles
I	ionic strength of the electrolyte
κ	Debye-Hückel parameter of the solution
κ_m	the effective Debye-Hückel parameter of the solution
k	particle deposition rate constant
k_B	Boltzmann constant, $1.3805 \times 10^{-23} \text{ J/K}$
K_1, K_2, K_3 and K_4	coefficients that appear in equations 6.S1
l	the film thickness on particle surface
m	the mass of particle
M	the ionic species in the electrolyte
M_S	the measured saturation magnetization for the iron nanoparticle
n	electrolyte bulk concentration
N	the density of ionized group
N_G	gravity group, $N_G = 2a_p^2(\rho_p - \rho_f)g/9\nu U$
N_{Lo}	London group, $N_{Lo} = A/9\pi\alpha_p^2 U$
N_{PE}	Peclet number, $N_{PE} = Ud_s / D_\infty$
N_R	relative size group, $N_R = a_p / a_s$
p	Defined in equation 6.S2, $p = a_s / b$
r	radial coordinate

r^*	dimensionless radial coordinate, $r^* = r/a_s$
s	the distance between polymer chains
s_1	$s_1 = (f_\theta^t g_\varphi^r - f_\theta^r g_\varphi^t) / g_\varphi^r$
s_2	$s_2 = (f_\theta^r g_{1\varphi}^m - y^+ f_{1\theta}^m g_\varphi^r) / g_\varphi^r$
s_3	$s_3 = (f_\theta^r g_{2\varphi}^m - y^+ f_{2\theta}^m g_\varphi^r) / g_\varphi^r$
t	time variable
T	absolute temperature
U	approach velocity
u	Darcy velocity
u_r, u_θ, u_ϕ	the velocity vectors in different directions
μ_0	electrophoretic mobility
u_0	the permeability of free space
V	liquid flow field
y	$y = (r - a_s)$
z	the valence of a symmetrical electrolyte
Z	the valence of the ionized groups on the polyelectrolyte
λ	the softness of particle
ε	dielectric constant of the media
ε_0	the permittivity of free space
ε_r	the relative permittivity of the solvent
ϕ_0	the potential at the boundary between polymer layer and electrolyte
ϕ_{DON}	Donnan potential inside polymer layer
δ	surface-to-surface separation between the collector and the particle
δ^+	dimensionless parameter, $\delta^+ = \delta/a_p$
η	the effective single collector contact efficiency
η_0	the single collector contact efficiency
η_D, η_I and η_G	collection efficiencies due to diffusion, sedimentation and interception, respectively

θ	angular coordinate
φ	angular coordinate
λ_e	wavelength of electron oscillation, $\lambda_e = 100nm$
ν	viscosity of suspension
π	circular constant, $\pi = 3.14$
ρ_f	the density of the liquid
ρ_p	the density of the particle
ψ	stream function
π	circular constant, $\pi = 3.14$

Chapter 1

Introduction

1.1 Background—significance of DNAPL contamination in subsurface

The contamination of groundwater and aquifers by toxic organic chemicals is one of the major environmental and public health concerns because of health risks associated with the exposure to various organic chemicals found in groundwater [1, 2]. Among high health risk organic chemicals, chlorinated solvents such as trichloroethylene (TCE) and tetrachloroethylene (PCE) are one of the most prevalent organic pollutants found in groundwater. It has been received considerable attention to groundwater contamination by these compounds due to their toxicity properties (carcinogenicity, teratogenesis and mutagenesis) and the resultant health hazards to human [3, 4]. Furthermore, once these chlorinated solvents are released from industrial sites (usually in metal parts manufacturing plants), they can remain in subsurface for as long time in the form of dense non-aqueous phase liquids (DNAPLs). Due to their low solubility in water, slow mass transfer from the DNAPL to the groundwater, and density greater than that of water, DNAPLs can serve as a long-term source of dissolved contaminant plumes in the subsurface [5-7]. Chlorinated solvents have been found in a large number of contaminated sites, and have already caused water supply from various aquifers to be unavailable for potable water use [8]. Therefore, it is urgent to develop clean-up strategies for these contaminated aquifers.

1.2 The DNAPLs remediation technologies and challenges

Substantial investigation of various technologies, such as aquifer flushing with surfactant (or bio surfactant), in situ oxidation, permeable reactive barriers (PRB), bioremediation, phytoremediation and thermal remediation technologies for restoring DNAPL-contaminated sites to meet drinking-water quality standards has been conducted [9]. However, to date, no large site contaminated by chlorinated organic DNAPLs have been successfully restored to meet drinking-water quality guidelines using the above technologies, due to the limitations of different remediation technologies in restoring DNAPLs contaminated sites as summarized in a recent review paper [9]. Because DNAPLs can penetrate deep into the aquifer to the bedrock layers, technologies such as permeable reactive barriers (PRBs), which can only address shallow contamination, are ineffective. Bioremediation is often ineffective for chlorinated DNAPL remediation, as very few microorganisms can degrade chlorinated solvents to innocuous end products. Surfactant flushing carries risks of mobilizing the DNAPL beyond the contaminated zone if the groundwater hydraulics of the site is not perfectly controlled.

1.3 Motivation of the study

1.3.1 Rationale for applying NZVI particles to remediate DNAPLs contaminated sites

Zero valent iron can reduce TCE and PCE to non-toxic products, such as ethane, ethene and chloride ions [10]. Nanoscale zero valent iron (NZVI) has several properties, such as very high surface area and high redox potential that result in high reactivity to these compounds and its direct injection into chlorinated solvent-contaminated subsurface zones make it a promising technology to restore aquifers contaminated with chlorinated organics [11]. NZVI is relatively inexpensive to produce industrially in large quantities, and they may be introduced in to the

subsurface by injection of its suspensions in DNAPL-contaminated zones or packed in the barrier walls to intercept dissolved plumes [12-14].

Polymer-coated NZVI generally has low toxicity potential [15-18]. However, more in depth and extensive studies are needed to test the potential toxicity of NZVI particles under a variety of environmental conditions to ensure that NZVI-based remediation does not pose any health risks [19].

1.3.2 Limitations to transport of NZVI in the subsurface

The effectiveness of NZVI-based site remediation applications will depend on several factors, the three most important of which are colloidal stability, feasible transport performance, and high reactivity [20]. However, numerous studies have pointed out that bare NZVI has poor colloidal stability and mobility in porous media. This is due to severe aggregation and binding caused by magnetic attraction between NZVI particles and a considerably weak repulsion interaction forces between particles [21-23]. The aggregation process leads to large-sized particles which may be easily deposited on collector grain surfaces or filtered out in the porous media during transport and subsequently lead to failure of NZVI in reaching the target contaminated zones [24]. Coating NZVI with polymers or polyelectrolytes has been considered as an effective method to overcome colloidal instability and aggregation [25, 26].

Despite good transport results obtained in a number of laboratory-scale studies, several field scale demonstrations indicated that the transport of NZVI particles was very limited [27, 28], unlike predicted from the column results. This is attributed to the lower velocity, heterogeneous media size, higher NZVI concentrations used in the actual field situation than those used in the column experiments and etc.

1.3.3 Research Scope

To address the difficulties in stabilizing NZVI particles and to solve the issue of the limited transport of NZVI particles, this study focuses on the transport of CMC-NZVI particles in model porous media to identify the influence of various factors on NZVI transport. The transport experiments were conducted in laboratory-scale 1-D column (10 cm length) in vertical and horizontal orientation columns as well as in a pilot-scale 2-D tank (Plexiglas, length=70 cm, height=35 cm, width=2 cm) to investigate the factors, which are expected to influence the transport of NZVI particles, such as the physico-chemical properties of the polyelectrolyte stabilizer (carboxymethyl cellulose, referred to as CMC in this study), the ionic strength of the background electrolyte medium, the concentration of NZVI particles, the size of the porous media, the flow orientation, system scale-up, the injection velocity and the viscosity of the suspension etc. Further, the modification of the classical model for predicting the single collector efficiency developed by Rajagopalan and Tien [29] (RT model) was conducted to investigate the effect of altering the flow direction from vertical to orientation on NZVI deposition on sand.

First, three types of CMC with different mean molecular weights (90,000 Da, 250,000 Da and 700,000 Da, referred as 90K CMC, 250K CMC and 700K CMC, respectively) were selected to investigate the effect of molecular weights of the same type of polyelectrolyte on stabilizing NZVI and improving its transport. The viscosities of three different CMC solutions and the three CMC-NZVI suspensions were measured. The adsorbed mass of CMC on NZVI particles was analyzed, based on which the interactions between particles as well as between the particles and the collector were calculated by DLVO theory. The stability and transport of the three CMC-NZVI particles under varied ionic strength and free CMC concentrations as well as particle concentrations were studied.

Second, the transport experiments with 700K CMC stabilized NZVI particles were conducted in the both vertically-placed and horizontally-placed columns to investigate the effect of the two flow modes on the transport of NZVI particles.

Third, tank experiments with 700K CMC stabilized NZVI particles were conducted to study the scale-up effect on the transport. The effects of CMC concentration, NZVI concentration, porous media size and the injection velocity on the transport in the 2-D tanks were investigated.

Finally, the trajectory analysis of particles in 2-D developed in the RT model (corresponding to the vertical flow model) was modified and extended to 3-D to simulate the trajectory of particles around collector surfaces in 3-D. The scenario to include Brownian motion in the calculation was developed. Much wider ranges of several parameters (particle density, collector size, viscosity and flow velocity) were included in the simulation calculations to reveal the distinct properties of NZVI particle (dispersed in viscous polymer or polyelectrolyte solution) from common colloids on its trajectory around the collector.

1.4 The specific objectives

This study focuses on the transport of CMC coated NZVI particles under different conditions and in different scale reactors. The overall goal of this study was to evaluate the transport of polyelectrolyte-coated, industrially produced NZVI in clean homogeneous packed in laboratory scale 1-D column and 2-D pilot scale tanks.

The specific objectives of this study are:

- To evaluate the effect of different molecular weight CMC (polyelectrolyte) coatings on NZVI colloidal stability and transport in laboratory-scale columns under various particle concentrations and sand sizes;
- To investigate the effects of the viscosity of CMC-NZVI suspension on the stability and the transport of NZVI particles;
- To compare the effects of vertical and horizontal flow on the transport of NZVI particles in porous media in a model aquifer system represented by a sand-packed column;
- To investigate the effects of viscosity of the suspension, the flow injection velocity and the NZVI particles concentration as well as the collector size on the transport of NZVI particles and on the change of hydraulic conductivity in a model aquifer system represented by a 2-D tank;
- To develop a mathematical model to predict the single collector efficiency of NZVI particles in horizontal flow.

1.5 Scope and structure of the thesis

This thesis is a manuscript-based thesis. The submitted and/or accepted manuscripts are presented in the thesis. The co-authorships and connection texts are presented on the first page of each chapter. Chapter 2 presents a critical review of previous studies related to the relevant research topics. Chapter 3 presents the stability and transport of three different types of CMC-NZVI particles (CMC with different mean molecular weights). Chapter 4 presents the transport of 700K CMC-NZVI particles in vertically and horizontally placed columns. Chapter 5 presents the transport of 700K CMC-NZVI particles in a bench-scale 2-D tank. Chapter 6 presents the

development of a new correlation equation for single collector efficiency prediction based on the trajectory analysis of particles in 3-D. Intellectual contributions are summarized in Chapter 7.

1.6 Contribution of Authors

The Methods, Results, Discussion and Conclusion sections of the thesis are presented in Chapters 3-6 as four journal manuscripts. Authorships of four articles are stated as below:

Chapter 3

Colloidal stability and transport of NZVI particles coated with carboxymethyl cellulose of various molecular weights, to be submitted to Water Research, December 2013, **J. Li, S.**

Ghoshal

Experimental design and execution, including the particle characterizations (TEM, DLS, NTA, zeta potential, conventional optical microscope and elements analysis), sedimentation settling experiments, column transport experiments, data analysis, DLVO theory calculations as well as the manuscript writing were conducted by J. Li. S. Ghoshal provided the supervision of the research and the experimental design as well as the editing of the manuscript.

Chapter 4

Comparison of Transport of Nanoscale Zero Valent Iron Nanoparticles under Vertical and Horizontal Flow, to be submitted to Water Research, December 2013, **J. Li, S. Ghoshal**

Experimental design and execution, including the particle and sand characterizations, sedimentation settling experiments, column transport experiments, data analysis, primary theory

calculations as well as the manuscript writing were conducted by J. Li. S. Ghoshal provided the supervision of the research and the experimental design as well as the editing of the manuscript.

Chapter 5

Transport of polyelectrolyte-coated zero valent iron nanoparticles in a sand tank: Effects of nanoparticle concentration and injection velocity, to be submitted to Environmental Science and Technology, December 2013, **J. Li, S. R. C. Rajajayavel, S. Ghoshal**

The design and the tank system and the experiments were conducted by J. Li. S. R. C. Rajajayavel gave assistance in execution of the tank experiments. The samples measurements, data analysis and the manuscript writing were also conducted by J. Li. S. Ghoshal provided the supervision of the research and tank design as well as the editing of the manuscript.

Chapter 6

Correlation equation for predicting single-collector efficiency using trajectory analysis method in three dimensions, to be submitted to Environmental Science and Technology, December 2013, **J. Li, X. H. Xie, S. Ghoshal**

The model design was conducted by J. Li. X. H. Xie provided assistance in Matlab codes and forth order Runge-Kutta calculations. The simulation calculations and data analysis as well as the manuscript writing were conducted by J. Li. X. H. Xie conducted the regression calculations. S. Ghoshal provided the supervision of the research and the editing of the manuscript.

Literature cited

- [1] P.E. Stackelberg, E.T. Furlong, M.T. Meyer, S.D. Zaugg, A.K. Henderson, D.B. Reissman, Persistence of pharmaceutical compounds and other organic wastewater contaminants in a conventional drinking-water-treatment plant, *Science of The Total Environment*, 329 (2004) 99-113.
- [2] H.A.G. Kenny S. Crump, DRINKING WATER AND CANCER: Review of Recent Epidemiological Findings and Assessment of Risks *Ann. Rev. Public Health*, 3 (1982) 19.
- [3] L.J.-H. Lee, C.-W. Chung, Y.-C. Ma, G.-S. Wang, P.-C. Chen, Y.-H. Hwang, J.-D. Wang, Increased mortality odds ratio of male liver cancer in a community contaminated by chlorinated hydrocarbons in groundwater, *Occupational and Environmental Medicine*, 60 (2003) 364-369.
- [4] R.P. Schwarzenbach, B.I. Escher, K. Fenner, T.B. Hofstetter, C.A. Johnson, U. von Gunten, B. Wehrli, The Challenge of Micropollutants in Aquatic Systems, *Science*, 313 (2006) 1072-1077.
- [5] C.A.R. John A. Christ, 2 Linda M. Abriola, 2 Kurt D. Pennell, 3 and Frank E. Löffler 3, Coupling Aggressive Mass Removal with Microbial Reductive Dechlorination for Remediation of DNAPL Source Zones: A Review and Assessment, *Environmental Health Perspectives*, 113 (2005) 13.
- [6] I.D.J.P.G. Steyl, Effect of fracture zone on DNAPL transport and dispersion: a numerical approach, *Environ Earth Sci*, 61 (2010) 10.
- [7] D.J. Wright, P.S. Birak, J.A. Pedit, C.T. Miller, Effectiveness of Source-Zone Remediation of DNAPL-Contaminated Subsurface Systems, *Journal of Environmental Engineering*, 136 (2010) 452-465.
- [8] D.D. Reible, Katerina Innovative Approaches to the On-Site Assessment and Remediation of Contaminated Sites., in: *NATO Science Series: IV: Earth and Environmental Sciences*, Vol. 15 2003.
- [9] H.F. Stroo, A. Leeson, J.A. Marqusee, P.C. Johnson, C.H. Ward, M.C. Kavanaugh, T.C. Sale, C.J. Newell, K.D. Pennell, C.A. Lebrón, M. Unger, Chlorinated Ethene Source Remediation: Lessons Learned, *Environmental Science & Technology*, 46 (2012) 6438-6447.
- [10] Y. Liu, T. Phenrat, G.V. Lowry, Effect of TCE Concentration and Dissolved Groundwater Solutes on NZVI-Promoted TCE Dechlorination and H₂ Evolution, *Environmental Science & Technology*, 41 (2007) 7881-7887.
- [11] X.-q. Li, J. Cao, W.-x. Zhang, Stoichiometry of Cr(VI) Immobilization Using Nanoscale Zerovalent Iron (nZVI): A Study with High-Resolution X-Ray Photoelectron Spectroscopy (HR-XPS), *Industrial & Engineering Chemistry Research*, 47 (2008) 2131-2139.
- [12] S.M. Hosseini, B. Ataie-Ashtiani, M. Kholghi, Bench-Scaled Nano-Fe⁰ Permeable Reactive Barrier for Nitrate Removal, *Ground Water Monitoring & Remediation*, (2011) no-no.
- [13] Y.-T. Wei, S.-C. Wu, C.-M. Chou, C.-H. Che, S.-M. Tsai, H.-L. Lien, Influence of nanoscale zero-valent iron on geochemical properties of groundwater and vinyl chloride degradation: A field case study, *Water Research*, 44 (2010) 131-140.
- [14] D.W. Elliott, W.-x. Zhang, Field Assessment of Nanoscale Bimetallic Particles for Groundwater Treatment, *Environmental Science & Technology*, 35 (2001) 4922-4926.
- [15] T. Phenrat, T.C. Long, G.V. Lowry, B. Veronesi, Partial Oxidation (“Aging”) and Surface Modification Decrease the Toxicity of Nanosized Zerovalent Iron, *Environmental Science & Technology*, 43 (2008) 195-200.
- [16] Z. Li, K. Greden, P.J.J. Alvarez, K.B. Gregory, G.V. Lowry, Adsorbed Polymer and NOM Limits Adhesion and Toxicity of Nano Scale Zerovalent Iron to *E. coli*, *Environmental Science & Technology*, 44 (2010) 3462-3467.

- [17] J. Chen, Z. Xiu, G.V. Lowry, P.J. Alvarez, Effect of natural organic matter on toxicity and reactivity of nano-scale zero-valent iron, *Water Research*, 45 (2011) 1995-2001.
- [18] Z.-m. Xiu, K.B. Gregory, G.V. Lowry, P.J. Alvarez, Effect of Bare and Coated Nanoscale Zerovalent Iron on *tceA* and *vcrA* Gene Expression in *Dehalococcoides* spp, *Environmental Science & Technology*, 44 (2010) 7647-7651.
- [19] B. Karn, T. Kuiken, M. Otto, Nanotechnology and *in Situ* Remediation: A Review of the Benefits and Potential Risks, *Environ Health Perspect*, 117 (2009).
- [20] S.M. Cook, Assessing the Use and Application of Zero-Valent Iron Nanoparticle Technology for Remediation at Contaminated Sites, in, Washington, DC, 2009, pp. 39.
- [21] T. Phenrat, H.-J. Kim, F. Fagerlund, T. Illangasekare, R.D. Tilton, G.V. Lowry, Particle Size Distribution, Concentration, and Magnetic Attraction Affect Transport of Polymer-Modified Fe₀ Nanoparticles in Sand Columns, *Environmental Science & Technology*, 43 (2009) 5079-5085.
- [22] K.M. Sirk, N.B. Saleh, T. Phenrat, H.-J. Kim, B. Dufour, J. Ok, P.L. Golas, K. Matyjaszewski, G.V. Lowry, R.D. Tilton, Effect of Adsorbed Polyelectrolytes on Nanoscale Zero Valent Iron Particle Attachment to Soil Surface Models, *Environmental Science & Technology*, 43 (2009) 3803-3808.
- [23] T. Phenrat, N. Saleh, K. Sirk, R.D. Tilton, G.V. Lowry, Aggregation and Sedimentation of Aqueous Nanoscale Zerovalent Iron Dispersions, *Environmental Science & Technology*, 41 (2006) 284-290.
- [24] P. Jiemvarangkul, W.-x. Zhang, H.-L. Lien, Enhanced transport of polyelectrolyte stabilized nanoscale zero-valent iron (nZVI) in porous media, *Chemical Engineering Journal*, 170 (2011) 482-491.
- [25] B.W. Hydutsky, E.J. Mack, B.B. Beckerman, J.M. Skluzacek, T.E. Mallouk, Optimization of Nano- and Microiron Transport through Sand Columns Using Polyelectrolyte Mixtures, *Environmental Science & Technology*, 41 (2007) 6418-6424.
- [26] K.S. Navid Saleh, Yueqiang Liu, Tanapon Phenrat, Surface Modifications Enhance Nanoiron Transport and NAPL Targeting in Saturated Porous Media, *ENVIRONMENTAL ENGINEERING SCIENCE*, 24 (2007) 15.
- [27] R.L. Johnson, J. Nurmi, R. Johnson, Z. Shi, P. Tratnyek, T. Phenrat, G. Lowry, Injection of nano zero-valent iron for subsurface remediation: A controlled field-scale test of transport, in: *Proceedings of the 7th International Conference on Remediation of Chlorinated and Recalcitrant Compounds*. Battelle, Monterey, CA, 2010.
- [28] R.L. Johnson, J.T. Nurmi, G.S. O'Brien Johnson, D. Fan, R.L. O'Brien Johnson, Z. Shi, A.J. Salter-Blanc, P.G. Tratnyek, G.V. Lowry, Field-Scale Transport and Transformation of Carboxymethylcellulose-Stabilized Nano Zero-Valent Iron, *Environmental science & technology*, (2013).
- [29] R. Rajagopalan, C. Tien, Trajectory analysis of deep - bed filtration with the sphere - in - cell porous media model, *AIChE Journal*, 22 (1976) 523-533.

Chapter 2

Literature review

2.1 Introduction

Site contamination is often caused by past disposal practices for toxic chemicals in land. Among these contaminated sites, the sites, where the contaminants spread to the aquifer and cause groundwater contamination, are often more challenging to restore than those with surface soil contamination only. The contamination of groundwater with toxic chemicals can put human and ecological health at risk. Among priority pollutants, chlorinated solvents such as trichloroethylene (TCE) and tetrachloroethylene (PCE) are the among the most prevalent organics in groundwater [1]. These compounds have received considerable attention due to their carcinogenicity, teratogenesis and mutagenesis properties as well as other health hazards to human [2, 3]. Furthermore, once these chlorinated solvents are released from industrial sites, where most of the chlorinated solvents are used, they can remain in subsurface for as long time in the form of dense non-aqueous phase liquids (DNAPLs). Due to their low solubility in water, slow mass transfer from the DNAPL to the groundwater, and density greater than that of water, DNAPLs can serve as a long-term source of dissolved contaminant plumes in the subsurface [4-6]. Chlorinated solvents have been found in a large number of contaminated sites, and have already caused water supply from various aquifers to be unavailable for potable water use [7]. Therefore, it is urgent to develop clean-up strategies for these contaminated aquifers. Substantial investigation of various technologies, such as aquifer flushing, in situ oxidation, permeable reactive barriers (PRB), bioremediation and phytoremediation for restoring DNAPL-contaminated sites to meet drinking-water quality standards has been conducted [8]. However, to

date, none of large sites contaminated by chlorinated organic DNAPLs have been successfully restored to meet drinking-water quality guidelines using the above technologies [9, 10]. According to an inventory [11], during 1998-2001 total on- and off-site releases of methylene chloride, PCE, TCA, and TCE averaged about 33 million pounds, 4 million pounds, 0.5 million pounds, and 11 million pounds in U.S., respectively. Environment Canada reported that a huge amount of chlorinated solvents was consumed in Canada as degreasers and dry cleansers as well as chemical intermediates [12, 13]. These data imply that there a a large number of chlorinated organic DNAPLs contaminated sites in US and Canada.

2.1.1 Chlorinated solvent toxicity

Chlorinated solvents in general are harmful to human and ecological health because they can cause or are suspected of causing cancer. Chlorinated solvents have been associated with both acute and chronic human-health problems including liver damage and possible kidney effects, spontaneous abortions, reduced fertility, cancer, and childhood leukemia [14, 15]. Based on a series of studies about the toxicity of chlorinated solvents, USEPA has set very low concentrations of the maximum contaminants levels for chlorinated solvents [16].

As the industrial introduction of chlorinated solvents in the beginning of the last century, symptoms relating to cranial and peripheral nerves have been identified. During the last few decades of the last century, toxic effects on the liver and kidneys, cardiac effects and mutagenic outcomes have also been recognised.

Spills and leaks of chlorinated solvents have caused widespread subsurface contamination in the environment. Considerable efforts have been focused on the risk assessment of the groundwater containing with chlorinated solvents contaminants [17, 18].

2.1.2 Chlorinated solvent remediation technologies

Extensive remediation efforts have been made in testing of the commonly available approaches such as pump-and-treat and in investigating new approaches to restore the sites contaminated by chlorinated solvents. The advantages and disadvantages of the possible treatment technologies for chlorinated solvent contamination of soil and groundwater are briefly described here.

2.1.4.1 Conventional Pump-and-Treat

Pump-and-treat remediation involves extracting contaminated water from aquifers, which would be directly adsorbed by granular activated carbon or would be extracted by air stripping, followed by the adsorption of granular activated carbon in the gas phase. The conventional pump-and-treat method represented 73% of cleanup agreements between 1982 and 1992 [19]. Pump-and-treat method was proposed to meet different objectives in plume management, plume migration control or complete plume remediation. However, an NRC panel review pointed out that most of the chlorinated contaminated sites remediated with pump-and-treat method did not meet the cleanup goals [20, 21], due to the complexity of geological settings and slow rates of chlorinated solvents desorption from the aquifer solid matrix.

2.1.4.2 Air-Injection Systems

Chlorinated solvents contaminants can also be readily removed from site by injecting air into subsurface. Alternative air-injection approaches include vacuum extraction, bioventing and air sparging [22].

Vapor extraction is one type of air injection method with the purpose to enhance the movement of the injected air through soil and vadose zone by applying a vacuum at a sealed wellhead or with the aid of blowers. Vapor extraction method may be used to rapidly remove the chlorinated solvents contaminants

in vadose zone and soil. However, due to the slow desorption rate of chlorinated solvents from the porous media in subsurface, the removal usually cannot be complete. Additionally, the subsequent ex-situ treatment system to remove contaminants from the contaminated air is needed, which renders the cost to be high.

Air sparging is by injecting pressurized air to remove chlorinated solvents from groundwater. The contaminants are anticipated to be brought to vadose zone, where they can be removed by the above soil vapor extraction approach. Air sparging approach is operated with very complicated wells design. Further, as very expensive subsequent treatment work is needed to remove chlorinated solvents from the soil gas [23].

2.1.4.3 Biodegradation

Considerable research involving aerobic and anaerobic biological transformations of chlorinated solvents began from the 1980s. However, to date, the knowledge gained indicates that the transformation products are generally hazardous, with possibility of generation of some vinyl chloride, which can be even more hazardous than the original contaminants [24]. Thus bioremediation is not always be feasible for chlorinated solvents. By mixing methane, oxygen and TCE and cultures naturally present on aquifer solids, TCE could be destroyed to smaller molecules rather than simply transforming into other hazardous compounds [25]. Two field demonstrations were conducted to evaluate the feasibility of using cometabolism for groundwater bioremediation of TCE [26, 27], one of which was successful in removing 97% of TCE [26]. Initially, anaerobic transformation of vinyl chloride ethane to non-hazardous ethane was found by Freedman and Gossett [28]. Based on this finding, the natural attenuation was developed and has been considered as an alternative remediation approach. Chlorinated solvents can be anaerobically destructed at very high concentration (even higher than 100 mg/L) [29, 30]. However, anaerobic bioremediation approach of chlorinated solvents can only be used for plume rather than source zone, due to the toxicity of concentrated chlorinated solvents to

microorganism [31-33]. Another disadvantage of bioremediation is long term needed (usually, several years is needed).

2.1.4.4 Cosolvent and surfactant flushing

Adding chemicals or surfactant to chlorinated solvent contaminant source zone to improve the solubility of DNAPLs (or residual chlorinated solvents) is referred as cosolvent or surfactant flushing. Cosolvent and surfactant flushing approach has been applied in many field sites [34-36].

Cosolvent flushing usually uses the mixture of ethanol and water with or without other common chemical solvents such as n-pentanol [37]. Several sites results have shown that a significant amount of contaminants was removed [37-39]. Apart from the very high efficiency of contaminants removal, the remained ethanol in the subsurface after finishing the flushing process could be favorable for the subsequent bioremediation [40]. However, the issue that the flow of the dissolved chlorinated solvents could be uncontrolled is of concern. The flushing produced mixture (cosolvent, water and dissolved chlorinated solvents) would be difficult to treat. Additionally, cosolvents are usually costly.

Using surfactant to replace the above cosolvent is proposed to promote the solubility of DNAPLs or residual chlorinated solvents much more effective, due to the stronger capability of surfactant to enhance the solubility of hydrophobic molecules. Several types of the surfactants such as Tween 80 and sodium dihexyl sulfosuccinate, have been tested to flush the chlorinated solvent contaminants zone. Very high removal rates were obtained in these field demonstrations [41, 42]. However, the concern that the surfactant can lower the interfacial tension of DNAPLs, causing them to migrate away from the contaminated site more readily, has been discussed [34]. Additionally, the issues for cosolvent flushing approach also exist in surfactant flushing approach.

2.1.4.5 In situ thermal technologies

As it is difficult to remove the adsorbed chlorinated solvent contaminants in the soil matrix via the in situ air stripping processes, adding heat to an aquifer was considered to be

effective to remove adsorbed solvents [43]. Thermal techniques include stream injection, electrical resistive heating and thermal conductive heating. Several remediation cases have been applied the in situ thermal technologies and very attractive results have been gained [44-46]. The thermal remediation technologies, however, rely on substantial energy generation capacity and are costly.

2.1.4.6 In situ chemical transformation

Adding chemicals (oxidants or reducers) to destruct the chlorinated solvents in the contaminated sites are referred as in situ chemical transformation. Two common scenarios are oxidative and reductive chemical processes.

1) Oxidative chemical transformation processes

Adding oxidants such as Fenton's reagent and permanganate to effectively oxidize chlorinated solvents to form the carbon dioxide and chloride has been demonstrated by several field cases [41, 47, 48]. Most of chlorinated solvents were oxidized and removed in these cases studies [41]. Oxidative chemical process, however, would not be widely applied, due to the possible subsequent consequence after using these strong oxidants: they can destroy not only chlorinated solvents but also microorganism and organic compounds which are favourable for ecosystem.

2) Reductive chemical processes

Adding chemicals to replace chlorides with hydrogen in the chlorinated solvents molecules and to reach the reduction purpose is stated as reductive chemical process. The most popular chemical agent used in the reductive chemical process is zero valent iron (ZVI), which was initiated by Gillham and O'hannesin [49]. Fourteen different chlorinated solvents, including chlorinated methanes, ethenes and ethanes, have been reduced by ZVI in the literature. Based on

this finding, a new remediation technology, called permeable reactive wall (PRB) was developed, which has been widely employed worldwide [50, 51]. However, PRB approach is a passive approach, which can only be used to treat the contaminants in relatively passive groundwater plumes. This indicates that it needs a very long time to remove all contaminants to meet the remediation objectives or to meet the guideline of drinking water quality, and can only be applied for shallow contamination [52].

2.2 Nanoscale zero valent iron (NZVI) particle

2.2.1 Discoveries

In 1972, zerovalent metals were first reported to be effective in breaking down pesticides and other chlorinated organic compounds in aqueous solution by Sweeny and Fisher [53]. And until the end of 1980s, Gillham's group at University of Waterloo conducted investigations to evaluate the dechlorination reaction mechanisms of TCE and PCE by granular ZVI [54]. Based on these research findings, several field scale ZVI-PRB were built up in the sites contaminated by chlorinated solvents. From 1996, in which year Weixian Zhang reported that nanoscale ZVI (NZVI) particle showed a much better reactivity with chlorinated solvents than that of ZVI, due to its small size and the resulting large surface area [55], substantial studies investigated the effects of NZVI particles on dechlorinating chlorine(s) from chlorinated solvents or stabilizing heavy metals as well as on reducing nitrates [50, 56-61]. Since the past decade, the application of NZVI in site remediation has been thoroughly studied in several aspects—the improvement the reactivity of NZVI by combining NZVI with a noble metal (such as, Pd, Pt, Ag) salt solution to yield a bimetal nanoparticle [62], the stabilization of NZVI particles, the transport of NZVI particles and the combination of NZVI particle technology with other site remediation

technology (such as bioremediation) as well as the potential toxicity of NZVI particles to ecosystem [63, 64]. Due to the small size of NZVI particles, they can potentially transport through the porous media in the subsurface. Thus, it has been proposed to directly inject NZVI particles into the subsurface as a new remediation technology.

2.2.2 Properties and applications

Zero valent iron can reduce TCE and PCE to non-toxic products, such as ethane and ethene and chloride ions [65]. Nanoscale zero valent iron (NZVI) has several properties such as very small size (usually ranging from tens nm to several hundred nm), very high surface area and resulting high reactivity to these compounds and its direct injection into chlorinated solvent-contaminated subsurface zones make it a promising technology to restore aquifers contaminated with chlorinated organic compounds [66]. Moreover, NZVI has other distinct advantages of implementation in remediation: it is relatively inexpensive to produce industrially in large quantities, and they may be introduced into the subsurface by injection of its suspensions in DNAPL-contaminated zones or packed in the barrier walls to intercept dissolved plumes [67-69].

NZVI particles are prone to aggregation in aqueous suspensions to form big particles, resulting from the strong magnetic attraction between particles and relatively weak repulsion interaction forces between particles [70-72]. This aggregation process leads to large-sized particles which may be easily deposited on collector grain surfaces or filtered out in the porous media during transport and subsequently lead to failure of NZVI in reaching the target contaminated zones [73]. Thus, stabilization of NZVI particles in the suspension is a key challenge. Coating NZVI with polymers or polyelectrolytes has been considered as an effective method to overcome colloidal instability and aggregation [74, 75]. Several other methods have been developed to stabilize NZVI particles—emulsifying NZVI particles with oil and surfactant

[76, 77], supporting NZVI particles on microscale activated carbon or silicon gel [78-81]. Emulsified NZVI (ENZVI) particles have been tested in several field demonstrations [69, 82], but the limitation of ENZVI—the very high viscosity of the suspension—makes the injection difficult and the failure of delivery of NZVI particles to the contaminated zones. Thus, when using ENZVI to reduce the contaminants in site, the contaminant source zones are required to be close to the injection point. Supporting NZVI particles on microscale activated carbon or silicon gel have been reported in literature, but no case study has been reported yet [83]. One concern with this approach is that it is difficult to impregnate a large amount of NZVI particles into the support, which would result in the deficient of the overall reactivity [80]. Further, the capability of the adsorption of support (activated carbon or silicon gel) would be significantly decreased by the impregnated NZVI particles. In turn, the proposed scenario that the adsorption performance of activated carbon can concentrate the contaminants to rapid access to the supported NZVI to expedite the reduction reaction of contaminants is likely to be impracticable [78].

Polymer-coated NZVI have been found to show lower toxicity potential [84]. However, more in depth and extensive studies are needed to test the potential toxicity of NZVI particles under a variety of environmental conditions to ensure that NZVI-based remediation does not pose any health risks [85].

The effectiveness of NZVI-based site remediation applications will depend on several factors, the three most important of which are colloidal stability, feasible transport performance, and high reactivity [86]. However, numerous studies have pointed out that bare NZVI has poor colloidal stability and mobility in porous media.

2.2.3 Aggregation of NZVI particles

For NZVI particles, in addition to the Van der Waals force and electrostatic force, the magnetic force (as well as the steric force for polymer stabilized NZVI) was also taken into the account in the calculation of the extended DLVO theory to predict the extent of aggregation between particles [87]. The extended DLVO theory calculations results reveal that pristine NZVI particles always show a very deep secondary minimum in the range of IS from 10 mM to 100 mM with the nearly neutral pH, indicating a very strong trend of aggregation [87]. However, after coating with polyelectrolytes, steric repulsion needs to be accounted for in the extended DLVO calculations. As a result of the polyelectrolyte coating, the secondary minimum between NZVI particle and particle is usually reduced significantly or even negligible [87, 88], leading to very less attractions between particle and particle and in turn causing very little aggregation. The effects of aggregation on NZVI particle transport have also been extensively studied.

2.3 Transport of NZVI particles

The transport performance of NZVI particles is usually assessed in laboratory by conducting transport experiment in packed bed columns. From the breakthrough curve, the transport performance can be assessed. Various parameters such as flow velocity, ionic strength, pH, collector size, collector material, NZVI particle concentration and NZVI particle size as well as polymer (polyelectrolyte) type, which can affect the transport of NZVI particles, are extensively studied by several research groups. Lowry's group in Carnegie Mellon University has published on the transport of NZVI particles in laboratory column [70, 89, 90]. Their work includes the investigations of the effects of different types of polyelectrolyte on the transport of NZVI particles, the effects of the concentration of NZVI particle on its transport, the magnetic

property of nanoscaled iron particles and its effects on transport, the effects of ionic strength and aging of NZVI particle on its transport. Zhao's group in Auburn University has also published several papers on NZVI particle transport in packed bed column [91, 92], including one study on investigating the effects of flow velocity and collector material on CMC stabilized NZVI particle and one study on the effect of NZVI particle size on its transport. Sethi's group has focused on the effects of polymer such as guar gum and xanthan gum on the stabilization and transport of NZVI particles [93]. Additionally, O'Carroll's group in the University of Western Ontario has investigated the transport of CMC stabilized NZVI and Pd-Fe nanoparticle transport [94]. Raychoudhury et al studied the effect of the increase of particle size during transport on the single collector efficiency and the resultant deposition rate of NZVI particles [95]. Taken together, the transport results obtained in these studies indicated that polymer or polyelectrolyte stabilized particles show a significantly improved transport.

A large number of pilot-scale tests and field scale demonstrations of NZVI particle have been conducted to assess the long-term transport performance of NZVI particles in field [96]. Zhang's group in Lehigh University have conducted two field demonstrations on NZVI transport [62, 69]. The results from their demonstrations show that NZVI particles can effectively transport in the subsurface and degrade the chlorinated solvents there effectively. Quinn and her colleagues also conducted several pilot- and field-scale demonstrations on the transport of emulsified NZVI particles [96, 97] and their results indicate that ENZVI can effectively transport with groundwater flow and reduce the mass and concentrations of chlorinated solvents. Zhao's group in Auburn University also conducted one small pilot-scale tank experiment to attempt to use SEAWAT software to simulate the transport performance of NZVI particles in porous media [98] and two field demonstration of CMC stabilized NZVI particles [99, 100]. The small tank

experimental results showed that NZVI particle can not only move forward with the flow but also settle with gravity, due to its high density [98]. One of their field demonstrations results show that CMC stabilized NZVI particles are very mobile once they are injected into the subsurface while the mobility reduces with time and after 13 hs, the particles are immobile [99]. The other demonstration showed that CMC stabilized Fe-Pd nanoparticles are more mobile in the soil under the injection with high pressure [100]. Phenret et al conducted a laboratory-scale 2-D tank experiment to compare the effects of NZVI particle concentration, Fe⁰ content in the particle and the polyelectrolyte types on the transport of particles [101]. Transport of NZVI particles at low concentration (0.3 g/L) was more efficient than those at high concentrations (3 g/L and 6 g/L) and that the particle with high Fe⁰ content exhibited less transport [101]. Only one pore volume of NZVI particles was injection in the study, which implies the results may not be true for the long-term field application. Further, the estimated thicknesses values of different polyelectrolyte coatings in NZVI particles reported in the study are prone to be too thick (from 30 nm to 70 nm) [101] and may be not correct, because only around 2.5% of the total coated particle mass was the polyelectrolyte and the particle diameter was less than 50 nm, unlikely generating a such thick coating. Recently, Wei et al also conducted a field demonstration on the transport and reactivity of Fe-Pd particle from Lehigh Nanotech and self-prepared NZVI coated by a nonionic surfactant in Taiwan [68]. Their results indicate that NZVI particles can transport efficiently in the soil and around 50-99% of VC was reduced, might due to the fact that the authors used a type of containing a non-ionic surfactant to on-site synthesize their NZVI particles. Johnson et al published a field demonstration work on CMC stabilized NZVI particles [102]. A very limited transport of NZVI particles is reported in the study [102], which would be due to the fact that 4 g/L CMC solution was used to stabilize NZVI particles and a large volume of free

CMC solution was injected into the site, whose viscosity is likely to be too high and to cause a very high resistance for flow to move forward. Taken together, the results obtained in these field demonstrations reveal that the transport of NZVI particles is not as efficient as those obtained in the laboratory-scale column, due to many factors such as the heterogeneous geophysical and geochemical properties and the less flow rate in the field.

2.4 Prediction of the transport of NZVI particles by the colloid filtration theory

Colloid transport equations that account for dispersion, advection and deposition on collector surfaces, is often used to calculate NZVI transport in porous media in such 1-dimensional columns [88, 91].

$$\frac{\partial C}{\partial t} = D \frac{\partial^2 C}{\partial x^2} - u \frac{\partial C}{\partial x} - kC \quad (2.1)$$

where C is particle concentration, D is hydrodynamic dispersion coefficient, u is average linear velocity and k (T^{-1}) is the first order deposition rate coefficient, described in [103].

Nanoparticle deposition in porous media has been described by the colloid filtration theory in several studies [104, 105]. According to this theory, the particle deposition rate coefficient is represented as function of the single collector contact efficiency (η_0) and the attachment efficiency (α) as shown in equation 2.2.

$$k = \left[\frac{3(1-f)u}{2d_c f} \alpha \right] \eta_0 \quad (2.2)$$

In the above equation ε is porosity of media and d_c is the average diameter of collector and u is Darcy velocity. The parameter η_0 is the probability of collision of a particle flowing

through the porous media and can be theoretically determined by Tufenkji and Elimelech equation (T&E model) [106]. The parameter α represents the probability of sticking of a particle on the collector after collision, or in other words the probability of a collision that leads to deposition. The attachment efficiency is usually determined from experimental data of C versus t (or breakthrough curves) by solving for equation 2.1 and 2.2 with the assumption of steady state transport (or $\partial C/\partial t=0$) and negligible dispersion [91, 107].

In addition to the general deposition mechanisms mentioned above, the other deposition mechanisms such as detachment, straining and wedging, blocking as well as ripening are usually taken into account to explain the transport performance of NZVI particles under various conditions [70, 95, 108, 109].

The density scale of NZVI particles ranges from 6.3 g/cm³ to 7.8 g/cm³, and is beyond the density scale covered in T&E model (which is from 1.0 g/cm³ to 1.8 g/cm³). Yet, many studies on NZVI particle transport in 1-D column used T&E model to predict the single collector efficiency and subsequently to calculate the attachment efficiency as well as the deposition rate of NZVI particles [89, 91, 95, 110, 111]. Further, the transport of NZVI particles in field injection cases would subject to be horizontal orientation, which is different from the flow orientation in the 1-D downward or upward flow columns. The T&E model was formulated based on downward flow column and two dimensional (2-D) analysis of collector frame was used in the model. More precisely predicting the single collector efficiency of NZVI particles transport in field or in any cases with horizontal flow orientation, three dimensions (3-D) of collector frame should be taken into account.

Literature cited

- [1] P.L. McCarty, Groundwater contamination by chlorinated solvents: History, remediation technologies and strategies, in: *In Situ Remediation of Chlorinated Solvent Plumes*, Springer, 2010, pp. 1-28.
- [2] L.J.-H. Lee, C.-W. Chung, Y.-C. Ma, G.-S. Wang, P.-C. Chen, Y.-H. Hwang, J.-D. Wang, Increased mortality odds ratio of male liver cancer in a community contaminated by chlorinated hydrocarbons in groundwater, *Occupational and Environmental Medicine*, 60 (2003) 364-369.
- [3] R.P. Schwarzenbach, B.I. Escher, K. Fenner, T.B. Hofstetter, C.A. Johnson, U. von Gunten, B. Wehrli, The Challenge of Micropollutants in Aquatic Systems, *Science*, 313 (2006) 1072-1077.
- [4] C.A.R. John A. Christ, 2 Linda M. Abriola, 2 Kurt D. Pennell, 3 and Frank E. Löffler 3, Coupling Aggressive Mass Removal with Microbial Reductive Dechlorination for Remediation of DNAPL Source Zones: A Review and Assessment, *Environmental Health Perspectives*, 113 (2005) 13.
- [5] I.D.J.P.G. Steyl, Effect of fracture zone on DNAPL transport and dispersion: a numerical approach, *Environ Earth Sci*, 61 (2010) 10.
- [6] D.J. Wright, P.S. Birak, J.A. Pedit, C.T. Miller, Effectiveness of Source-Zone Remediation of DNAPL-Contaminated Subsurface Systems, *Journal of Environmental Engineering*, 136 (2010) 452-465.
- [7] D.D. Reible, Katerina Innovative Approaches to the On-Site Assessment and Remediation of Contaminated Sites., in: *NATO Science Series: IV: Earth and Environmental Sciences*, Vol. 15 2003.
- [8] H.F. Stroo, M. Unger, C.H. Ward, M.C. Kavanaugh, C. Vogel, A. Leeson, J.A. Marqusee, B.P. Smith, Peer Reviewed: Remediating Chlorinated Solvent Source Zones, *Environmental Science & Technology*, 37 (2003) 224A-230A.
- [9] K. Soga, J.W.E. Page, T.H. Illangasekare, A review of NAPL source zone remediation efficiency and the mass flux approach, *Journal of Hazardous Materials*, 110 (2004) 13-27.
- [10] A. Taghavy, J. Costanza, K.D. Pennell, L.M. Abriola, Effectiveness of nanoscale zero-valent iron for treatment of a PCE-DNAPL source zone, *Journal of Contaminant Hydrology*, 118 (2010) 128-142.
- [11] U.S.E.P. Agency, 2001 Toxics Release Inventory Public Data Release Report, in: Office of Environmental Information, Washington, DC, 2003.
- [12] E. Canada, Trichloroethylene and Tetrachloroethylene in Solvent Degreasing, in: E. Canada (Ed.), 2010, pp. 30.
- [13] E. Canada, Screening Assessment for the Challenge, in, 2009.
- [14] C.D. Klaassen, G.L. Plaa, Relative effects of various chlorinated hydrocarbons on liver and kidney function in dogs, *Toxicology and Applied Pharmacology*, 10 (1967) 119-131.
- [15] A.M. Fan, Trichloroethylene: water contamination and health risk assessment, in: *Reviews of environmental contamination and toxicology*, Springer, 1988, pp. 55-92.
- [16] U.S.E.P. Agency, 2004 Edition of the Drinking Water Standards and Health Advisories, in, Office of Water, Washington, DC, 2004.
- [17] M.J. Moran, J.S. Zogorski, P.J. Squillace, Chlorinated Solvents in Groundwater of the United States, *Environmental Science & Technology*, 41 (2006) 74-81.
- [18] M. Stuart, D. Lapworth, E. Crane, A. Hart, Review of risk from potential emerging contaminants in UK groundwater, *Science of the Total Environment*, 416 (2012) 1-21.
- [19] NRC, Alternatives for Ground Water Cleanup, in, National Academies Press, Washington, DC, USA., 1994.

- [20] M.O. Rivett, S.W. Chapman, R.M. Allen-King, S. Feenstra, J.A. Cherry, Pump-and-treat remediation of chlorinated solvent contamination at a controlled field-experiment site, *Environmental science & technology*, 40 (2006) 6770-6781.
- [21] N.R.C. Committee on Source Removal of Contaminants in the Subsurface, *Contaminants in the subsurface: Source zone Assessment and remediation*, in, Washington, D.C., 2005.
- [22] B.C. Alleman, H.F. Stroo, C.C.H. Ward, *In situ remediation of chlorinated solvent plumes*, Springer, 2010.
- [23] K.R. REDDY, S. KOSGI, J. Zhou, A review of in-situ air sparging for the remediation of VOC-contaminated saturated soils and groundwater, *Hazardous waste and hazardous materials*, 12 (1995) 97-118.
- [24] N. Singhal, P. Jaffé, W. Maier, E.H. Jho, The opposing effects of bacterial activity and gas production on anaerobic TCE degradation in soil columns, *Chemosphere*, 69 (2007) 1790-1797.
- [25] J.T. Wilson, B.H. Wilson, Biotransformation of trichloroethylene in soil, *Applied and Environmental Microbiology*, 49 (1985) 242.
- [26] G.D. Hopkins, P.L. McCarty, Field Evaluation of in Situ Aerobic Cometabolism of Trichloroethylene and Three Dichloroethylene Isomers Using Phenol and Toluene as the Primary Substrates, *Environmental Science & Technology*, 29 (1995) 1628-1637.
- [27] L. Semprini, G.D. Hopkins, P.V. Roberts, D. Grbic-Galic, P.L. McCarty, A Field Evaluation of In-Situ Biodegradation of Chlorinated Ethenes: Part 3, Studies of Competitive Inhibition, *Ground Water*, 29 (1991) 239-250.
- [28] D.L. Freedman, J.M. Gossett, Biological reductive dechlorination of tetrachloroethylene and trichloroethylene to ethylene under methanogenic conditions, *Applied and Environmental Microbiology*, 55 (1989) 2144-2151.
- [29] M. Lee, J. Odom, R. Buchanan Jr, New perspectives on microbial dehalogenation of chlorinated solvents: insights from the field, *Annual Reviews in Microbiology*, 52 (1998) 423-452.
- [30] M. Häggblom, D. Fennell, Y.-B. Ahn, B. Ravit, L. Kerkhof, ANAEROBIC DEHALOGENATION OF HALOGENATED ORGANIC COMPOUNDS: NOVEL STRATEGIES FOR BIOREMEDIATION OF CONTAMINATED SEDIMENTS OF CONTAMINATED SEDIMENTS OF CONTAMINATED SEDIMENTS, in: I. Twardowska, H. Allen, M. Häggblom, S. Stefaniak (Eds.) *Soil and Water Pollution Monitoring, Protection and Remediation*, Springer Netherlands, 2006, pp. 505-521.
- [31] H.F. Stroo, B.C. Alleman, *In situ remediation of chlorinated solvent plumes*, Springer, 2010.
- [32] R.C. Prince, Rapporteur Comments on the Bioremediation Session, in: *Opportunities for Environmental Applications of Marine Biotechnology: Proceedings of the October 5-6, 1999, Workshop*, National Academies Press, 2000, pp. 161.
- [33] W.A. Sack, K.D. Jones, J.E. Cuddeback, A.K. Shiemke, *In-situ bioremediation of chlorinated solvents-A review*, (1993).
- [34] C. Mulligan, R. Yong, B. Gibbs, Surfactant-enhanced remediation of contaminated soil: a review, *Engineering Geology*, 60 (2001) 371-380.
- [35] J. Childs, E. Acosta, M.D. Annable, M.C. Brooks, C.G. Enfield, J.H. Harwell, M. Hasegawa, R.C. Knox, P.S.C. Rao, D.A. Sabatini, Field demonstration of surfactant-enhanced solubilization of DNAPL at Dover Air Force Base, Delaware, *Journal of contaminant hydrology*, 82 (2006) 1-22.
- [36] L. Strbak, *In situ flushing with surfactants and cosolvents*, USEPA, July, (2000).

- [37] P.S.C. Rao, M.D. Annable, R.K. Sillan, D. Dai, K. Hatfield, W.D. Graham, A.L. Wood, C.G. Enfield, Field-scale evaluation of in situ cosolvent flushing for enhanced aquifer remediation, *Water Resources Research*, 33 (1997) 2673-2686.
- [38] M.C. Brooks, M.D. Annable, P.S.C. Rao, K. Hatfield, J.W. Jawitz, W.R. Wise, A.L. Wood, C.G. Enfield, Controlled release, blind test of DNAPL remediation by ethanol flushing, *Journal of contaminant hydrology*, 69 (2004) 281-297.
- [39] G.R. Tick, F. Lourenso, A.L. Wood, M.L. Brusseau, Pilot-scale demonstration of cyclodextrin as a solubility-enhancement agent for remediation of a tetrachloroethene-contaminated aquifer, *Environmental science & technology*, 37 (2003) 5829-5834.
- [40] S.C. Mravik, R.K. Sillan, A.L. Wood, G.W. Sewell, Field evaluation of the solvent extraction residual biotreatment technology, *Environmental science & technology*, 37 (2003) 5040-5049.
- [41] T.M. McGuire, J.M. McDade, C.J. Newell, Performance of DNAPL source depletion technologies at 59 chlorinated solvent - impacted sites, *Ground Water Monitoring & Remediation*, 26 (2006) 73-84.
- [42] J.W. Jawitz, M.D. Annable, P. Rao, R.D. Rhue, Field implementation of a Winsor type I surfactant/alcohol mixture for in situ solubilization of a complex LNAPL as a single-phase microemulsion, *Environmental Science & Technology*, 32 (1998) 523-530.
- [43] G. Heron, M. Van Zutphen, T.H. Christensen, C. Enfield, Soil heating for enhanced remediation of chlorinated solvents: A laboratory study on resistive heating and vapor extraction in a silty, low-permeable soil contaminated with trichloroethylene, *Environmental science & technology*, 32 (1998) 1474-1481.
- [44] G. Beyke, D. Fleming, In situ thermal remediation of DNAPL and LNAPL using electrical resistance heating, *Remediation journal*, 15 (2005) 5-22.
- [45] G. Heron, S. Carroll, S.G. Nielsen, Full - Scale Removal of DNAPL Constituents Using Steam - Enhanced Extraction and Electrical Resistance Heating, *Ground Water Monitoring & Remediation*, 25 (2005) 92-107.
- [46] G. Heron, R. Baker, J. Bierschenk, J. LaChance, Heat it All the Way-Mechanisms and Results Achieved using In-Situ Thermal Remediation, in: Paper F-13, in: Bruce M. Sass (Conference Chair), *Remediation of Chlorinated and Recalcitrant Compounds—2006. Proceedings of the Fifth International Conference on Remediation of Chlorinated and Recalcitrant Compounds (Monterey, CA, 2006)*.
- [47] Y. Seol, H. Zhang, F.W. Schwartz, A review of in situ chemical oxidation and heterogeneity, *Environmental & Engineering Geoscience*, 9 (2003) 37-49.
- [48] T. Tsai, C. Kao, T. Yeh, M. Lee, Chemical oxidation of chlorinated solvents in contaminated groundwater: review, *Practice Periodical of Hazardous, Toxic, and Radioactive Waste Management*, 12 (2008) 116-126.
- [49] R.W. Gillham, S.F. O'Hannesin, Enhanced degradation of halogenated aliphatics by zero - valent iron, *Ground water*, 32 (1994) 958-967.
- [50] A.B. Cundy, L. Hopkinson, R.L. Whitby, Use of iron-based technologies in contaminated land and groundwater remediation: A review, *Science of the total environment*, 400 (2008) 42-51.
- [51] N.E. Korte, Zero-valent iron permeable reactive barriers: A review of performance, in, ORNL Oak Ridge National Laboratory (US), 2001.
- [52] A.D. Henderson, A.H. Demond, Long-term performance of zero-valent iron permeable reactive barriers: a critical review, *Environmental Engineering Science*, 24 (2007) 401-423.
- [53] K.H. Sweeny, Reductive degradation of halogenated pesticide, in, Google Patents, 1972.

- [54] W.S. Orth, R.W. Gillham, Dechlorination of trichloroethene in aqueous solution using Fe₀, *Environmental Science & Technology*, 30 (1995) 66-71.
- [55] C.-B. Wang, W.-X. Zhang, Synthesizing nanoscale iron particles for rapid and complete dechlorination of TCE and PCBs, *Environmental Science & Technology*, 31 (1997) 2154-2156.
- [56] A. Taghavy, J. Costanza, K.D. Pennell, L.M. Abriola, Effectiveness of nanoscale zero-valent iron for treatment of a PCE–DNAPL source zone, *Journal of contaminant hydrology*, 118 (2010) 128-142.
- [57] Y. Liu, G.V. Lowry, Effect of particle age (Fe₀ content) and solution pH on NZVI reactivity: H₂ evolution and TCE dechlorination, *Environmental Science & Technology*, 40 (2006) 6085-6090.
- [58] Y. Cho, S.-I. Choi, Degradation of PCE, TCE and 1, 1, 1-TCA by nanosized FePd bimetallic particles under various experimental conditions, *Chemosphere*, 81 (2010) 940-945.
- [59] S.-S. Chen, H.-D. Hsu, C.-W. Li, A new method to produce nanoscale iron for nitrate removal, *Journal of Nanoparticle Research*, 6 (2004) 639-647.
- [60] K.-H. Shin, D.K. Cha, Microbial reduction of nitrate in the presence of nanoscale zero-valent iron, *Chemosphere*, 72 (2008) 257-262.
- [61] Z. Jiang, L. Lv, W. Zhang, Q. Du, B. Pan, L. Yang, Q. Zhang, Nitrate reduction using nanosized zero-valent iron supported by polystyrene resins: role of surface functional groups, *water research*, 45 (2011) 2191-2198.
- [62] W.-x. Zhang, Nanoscale Iron Particles for Environmental Remediation: An Overview, *Journal of Nanoparticle Research*, 5 (2003) 323-332.
- [63] Y.S. El-Temseh, E.J. Joner, Ecotoxicological effects on earthworms of fresh and aged nano-sized zero-valent iron (nZVI) in soil, *Chemosphere*, 89 (2012) 76-82.
- [64] X. Wang, M.Y. Dong, L. Liu, Y. Liu, Z.H. Jin, T.L. Li, Study on Cytotoxicity of Nanoscale Zero Valent Iron Particles, in: *Materials Science Forum*, Trans Tech Publ, 2011, pp. 224-228.
- [65] Y. Liu, T. Phenrat, G.V. Lowry, Effect of TCE Concentration and Dissolved Groundwater Solutes on NZVI-Promoted TCE Dechlorination and H₂ Evolution, *Environmental Science & Technology*, 41 (2007) 7881-7887.
- [66] X.-q. Li, J. Cao, W.-x. Zhang, Stoichiometry of Cr(VI) Immobilization Using Nanoscale Zerovalent Iron (nZVI): A Study with High-Resolution X-Ray Photoelectron Spectroscopy (HR-XPS), *Industrial & Engineering Chemistry Research*, 47 (2008) 2131-2139.
- [67] S.M. Hosseini, B. Ataie-Ashtiani, M. Kholghi, Bench-Scaled Nano-Fe₀ Permeable Reactive Barrier for Nitrate Removal, *Ground Water Monitoring & Remediation*, (2011) no-no.
- [68] Y.-T. Wei, S.-C. Wu, C.-M. Chou, C.-H. Che, S.-M. Tsai, H.-L. Lien, Influence of nanoscale zero-valent iron on geochemical properties of groundwater and vinyl chloride degradation: A field case study, *Water Research*, 44 (2010) 131-140.
- [69] D.W. Elliott, W.-x. Zhang, Field Assessment of Nanoscale Bimetallic Particles for Groundwater Treatment, *Environmental Science & Technology*, 35 (2001) 4922-4926.
- [70] T. Phenrat, H.-J. Kim, F. Fagerlund, T. Illangasekare, R.D. Tilton, G.V. Lowry, Particle size distribution, concentration, and magnetic attraction affect transport of polymer-modified Fe₀ nanoparticles in sand columns, *Environmental Science & Technology*, 43 (2009) 5079-5085.
- [71] K.M. Sirk, N.B. Saleh, T. Phenrat, H.-J. Kim, B. Dufour, J. Ok, P.L. Golas, K. Matyjaszewski, G.V. Lowry, R.D. Tilton, Effect of Adsorbed Polyelectrolytes on Nanoscale Zero Valent Iron Particle Attachment to Soil Surface Models, *Environmental Science & Technology*, 43 (2009) 3803-3808.
- [72] T. Phenrat, N. Saleh, K. Sirk, R.D. Tilton, G.V. Lowry, Aggregation and Sedimentation of Aqueous Nanoscale Zerovalent Iron Dispersions, *Environmental Science & Technology*, 41 (2006) 284-290.

- [73] P. Jiemvarangkul, W.-x. Zhang, H.-L. Lien, Enhanced transport of polyelectrolyte stabilized nanoscale zero-valent iron (nZVI) in porous media, *Chemical Engineering Journal*, 170 (2011) 482-491.
- [74] B.W. Hydutsky, E.J. Mack, B.B. Beckerman, J.M. Skluzacek, T.E. Mallouk, Optimization of Nano- and Microiron Transport through Sand Columns Using Polyelectrolyte Mixtures, *Environmental Science & Technology*, 41 (2007) 6418-6424.
- [75] K.S. Navid Saleh, Yueqiang Liu, Tanapon Phenrat, Surface Modifications Enhance Nanoiron Transport and NAPL Targeting in Saturated Porous Media, *ENVIRONMENTAL ENGINEERING SCIENCE*, 24 (2007) 15.
- [76] T. Krug, S. O'Hara, M. Watling, Emulsified Zero-Valent Nano-Scale Iron Treatment of Chlorinated Solvent DNAPL Source Areas, in, DTIC Document, 2010.
- [77] T. Krug, S. O'Hara, Final Laboratory Treatability Report for: Emulsified Zero Valent Iron Treatment of Chlorinated Solvent DNAPL Source Areas. Revision 1.0, in, DTIC Document, 2006.
- [78] H. Zhu, Y. Jia, X. Wu, H. Wang, Removal of arsenic from water by supported nano zero-valent iron on activated carbon, *Journal of Hazardous Materials*, 172 (2009) 1591-1596.
- [79] L.B. Hoch, E.J. Mack, B.W. Hydutsky, J.M. Hershman, J.M. Skluzacek, T.E. Mallouk, Carbothermal synthesis of carbon-supported nanoscale zero-valent iron particles for the remediation of hexavalent chromium, *Environmental Science & Technology*, 42 (2008) 2600-2605.
- [80] B. Sunkara, J. Zhan, J. He, G.L. McPherson, G. Piringer, V.T. John, Nanoscale zerovalent iron supported on uniform carbon microspheres for the in situ remediation of chlorinated hydrocarbons, *ACS Applied Materials & Interfaces*, 2 (2010) 2854-2862.
- [81] J. Zhan, B. Sunkara, L. Le, V.T. John, J. He, G.L. McPherson, G. Piringer, Y. Lu, Multifunctional colloidal particles for in situ remediation of chlorinated hydrocarbons, *Environmental Science & Technology*, 43 (2009) 8616-8621.
- [82] R.L. Johnson, J.T. Nurmi, G.S. O'Brien Johnson, D. Fan, R.L. O'Brien Johnson, Z. Shi, A.J. Salter-Blanc, P.G. Tratnyek, G.V. Lowry, Field-Scale Transport and Transformation of Carboxymethylcellulose-Stabilized Nano Zero-Valent Iron, *Environmental science & technology*, (2013).
- [83] N.C. Mueller, J. Braun, J. Bruns, M. Černík, P. Rissing, D. Rickerby, B. Nowack, Application of nanoscale zero valent iron (NZVI) for groundwater remediation in Europe, *Environmental Science and Pollution Research*, 19 (2012) 550-558.
- [84] T. Phenrat, T.C. Long, G.V. Lowry, B. Veronesi, Partial Oxidation ("Aging") and Surface Modification Decrease the Toxicity of Nanosized Zerovalent Iron, *Environmental Science & Technology*, 43 (2008) 195-200.
- [85] B. Karn, T. Kuiken, M. Otto, Nanotechnology and *in Situ* Remediation: A Review of the Benefits and Potential Risks, *Environ Health Perspect*, 117 (2009).
- [86] S.M. Cook, Assessing the Use and Application of Zero-Valent Iron Nanoparticle Technology for Remediation at Contaminated Sites, in, Washington, DC, 2009, pp. 39.
- [87] J. Fatisson, S. Ghoshal, N. Tufenkji, Deposition of Carboxymethylcellulose-Coated Zero-Valent Iron Nanoparticles onto Silica: Roles of Solution Chemistry and Organic Molecules, *Langmuir*, 26 (2010) 12832-12840.
- [88] T. Raychoudhury, G. Naja, S. Ghoshal, Assessment of transport of two polyelectrolyte-stabilized zero-valent iron nanoparticles in porous media, *Journal of contaminant hydrology*, 118 (2010) 143-151.
- [89] N. Saleh, H.-J. Kim, T. Phenrat, K. Matyjaszewski, R.D. Tilton, G.V. Lowry, Ionic strength and composition affect the mobility of surface-modified Fe⁰ nanoparticles in water-saturated sand columns, *Environmental Science & Technology*, 42 (2008) 3349-3355.

- [90] H.-J. Kim, T. Phenrat, R.D. Tilton, G.V. Lowry, Fe⁰ nanoparticles remain mobile in porous media after aging due to slow desorption of polymeric surface modifiers, *Environmental science & technology*, 43 (2009) 3824-3830.
- [91] F. He, M. Zhang, T. Qian, D. Zhao, Transport of carboxymethyl cellulose stabilized iron nanoparticles in porous media: Column experiments and modeling, *Journal of Colloid and Interface Science*, 334 (2009) 96-102.
- [92] F. He, D. Zhao, J. Liu, C.B. Roberts, Stabilization of Fe-Pd nanoparticles with sodium carboxymethyl cellulose for enhanced transport and dechlorination of trichloroethylene in soil and groundwater, *Industrial & Engineering Chemistry Research*, 46 (2007) 29-34.
- [93] E.D. Vecchia, M. Luna, R. Sethi, Transport in porous media of highly concentrated iron micro- and nanoparticles in the presence of xanthan gum, *Environmental science & technology*, 43 (2009) 8942-8947.
- [94] N. Sakulchaicharoen, D.M. O'Carroll, J.E. Herrera, Enhanced stability and dechlorination activity of pre-synthesis stabilized nanoscale FePd particles, *Journal of contaminant hydrology*, 118 (2010) 117-127.
- [95] T. Raychoudhury, N. Tufenkji, S. Ghoshal, Aggregation and deposition kinetics of carboxymethyl cellulose-modified zero-valent iron nanoparticles in porous media, *Water research*, 46 (2012) 1735-1744.
- [96] Q. Jacqueline, E. Daniel, O.H. Suzanne, B. Alexa, Use of Nanoscale Iron and Bimetallic Particles for Environmental Remediation: A Review of Field-scale Applications, in: *Environmental Applications of Nanoscale and Microscale Reactive Metal Particles*, American Chemical Society, 2009, pp. 263-283.
- [97] J. Quinn, C. Geiger, C. Clausen, K. Brooks, C. Coon, S. O'Hara, T. Krug, D. Major, W.-S. Yoon, A. Gavaskar, T. Holdsworth, Field Demonstration of DNAPL Dehalogenation Using Emulsified Zero-Valent Iron, *Environmental Science & Technology*, 39 (2005) 1309-1318.
- [98] S. Kanel, R. Goswami, T. Clement, M. Barnett, D. Zhao, Two dimensional transport characteristics of surface stabilized zero-valent iron nanoparticles in porous media, *Environmental science & technology*, 42 (2007) 896-900.
- [99] P. Bennett, F. He, D. Zhao, B. Aiken, L. Feldman, In situ testing of metallic iron nanoparticle mobility and reactivity in a shallow granular aquifer, *Journal of contaminant hydrology*, 116 (2010) 35-46.
- [100] T. Phenrat, H.-J. Kim, F. Fagerlund, T. Illangasekare, G.V. Lowry, Empirical correlations to estimate agglomerate size and deposition during injection of a polyelectrolyte-modified Fe⁰ nanoparticle at high particle concentration in saturated sand, *Journal of Contaminant Hydrology*, 118 (2010) 152-164.
- [101] T. Phenrat, A. Cihan, H.-J. Kim, M. Mital, T. Illangasekare, G.V. Lowry, Transport and Deposition of Polymer-Modified Fe⁰ Nanoparticles in 2-D Heterogeneous Porous Media: Effects of Particle Concentration, Fe⁰ Content, and Coatings, *Environmental Science & Technology*, 44 (2010) 9086-9093.
- [102] R.L. Johnson, J.T. Nurmi, G.S. O'Brien Johnson, D. Fan, R.L. O'Brien Johnson, Z. Shi, A.J. Salter-Blanc, P.G. Tratnyek, G.V. Lowry, Field-Scale Transport and Transformation of Carboxymethylcellulose-Stabilized Nano Zero-Valent Iron, *Environmental Science & Technology*, 47 (2013) 1573-1580.
- [103] N. Tufenkji, J.A. Redman, M. Elimelech, Interpreting Deposition Patterns of Microbial Particles in Laboratory-Scale Column Experiments, *Environmental Science & Technology*, 37 (2003) 616-623.
- [104] B. Schrick, B.W. Hydutsky, J.L. Blough, T.E. Mallouk, Delivery Vehicles for Zerovalent Metal Nanoparticles in Soil and Groundwater, *Chemistry of Materials*, 16 (2004) 2187-2193.
- [105] H.F. Lecoanet, J.-Y. Bottero, M.R. Wiesner, Laboratory Assessment of the Mobility of Nanomaterials in Porous Media, *Environmental Science & Technology*, 38 (2004) 5164-5169.

- [106] N. Tufenkji, M. Elimelech, Correlation Equation for Predicting Single-Collector Efficiency in Physicochemical Filtration in Saturated Porous Media, *Environmental Science & Technology*, 38 (2003) 529-536.
- [107] A. Tiraferri, R. Sethi, Enhanced transport of zerovalent iron nanoparticles in saturated porous media by guar gum, *Journal of Nanoparticle Research*, 11 (2009) 635-645.
- [108] T. Tosco, R. Sethi, Transport of non-Newtonian suspensions of highly concentrated micro-and nanoscale iron particles in porous media: a modeling approach, *Environmental Science & Technology*, 44 (2010) 9062-9068.
- [109] R.L. Johnson, J. Nurmi, R.B. Johnson, Z. Shi, P. Tratnyek, T. Phenrat, G. Lowry, Injection of nano zero-valent iron for subsurface remediation: A controlled field-scale test of transport, in: *Proceedings of the 7th International Conference on Remediation of Chlorinated and Recalcitrant Compounds*. Battelle, Monterey, CA, 2010.
- [110] R.L. Johnson, G.O.B. Johnson, J.T. Nurmi, P.G. Tratnyek, Natural organic matter enhanced mobility of nano zerovalent iron, *Environmental Science & Technology*, 43 (2009) 5455-5460.
- [111] R.N. Lerner, Q. Lu, H. Zeng, Y. Liu, The effects of biofilm on the transport of stabilized zerovalent iron nanoparticles in saturated porous media, *water research*, 46 (2012) 975-985.

Chapter 3

Colloidal stability and transport of NZVI particles coated with carboxymethyl cellulose of various molecular weights

by

Jing Li, Subhasis Ghoshal*

Department of Civil Engineering,

McGill University, Montreal, Canada H3A 2K6

Keywords: NZVI particles, colloid transport, viscosity, carboxymethyl cellulose, DLVO theory calculations, single collector efficiency prediction, ionic strength

*Corresponding author, Department of Civil Engineering, McGill University, 817 Sherbrooke Street West, Montreal, QC, Canada H3A 2K6, e-mail: subhasis.ghoshal@mcgill.ca,

Tel: (514) 398-6867, Fax: (514) 398-7361

To be published on Water research

3.1 Introduction

The direct injection of nanoscale zero valent iron particles (NZVI) into the subsurface for remediation of sites and aquifers contaminated with organic and inorganic pollutants including chlorinated solvents or heavy metals has generated considerable interest [1-5]. The high redox activity of zero valent iron which can readily yield at least two electrons from each iron atom, combined with the high specific surface area of nanoscale particles makes NZVI a potential agent for chemical reduction of a variety of pollutants, e.g. chlorinated solvents [6-8], chlorinated biphenyls [9, 10], flame retardant compounds [11, 12], hexavalent chromium and arsenic [4, 13, 14].

A major hindrance to field-scale implementation of NZVI-based groundwater remediation is the aggregation of NZVI due to the magnetic forces [7, 10-13]. Furthermore, remediation of typical sites contaminated by chlorinated solvents via *in situ* injection of NZVI is expected to require injecting g/L concentrations of NZVI, and at such elevated concentrations there will be extensive aggregation due to the increased likelihood of particle-particle collisions [15]. Aggregates of several microns in size may be formed from NZVI, and these aggregates are likely to get filtered out during subsurface transport, and remain close to the point of injection [16].

To improve the efficacy of NZVI-based *in situ* remediation, reducing aggregation and promoting its colloidal stability is essential [17, 18]. Several approaches have been suggested to alleviate aggregation and to stabilize NZVI particles: suspending NZVI in emulsified oil [19, 20], embedding NZVI onto supports of carbon or silica particles [21, 22], and coating NZVI particles with polymer or polyelectrolyte molecules [23-30]. Among these approaches, colloidal

stabilization by coating with polymers or polyelectrolytes is more commonly reported [16, 29, 31-33]. Polyelectrolyte layers on the corresponding coated NZVI particle surface can provide considerable interparticle repulsion by steric and electrostatic forces against attractive by van der Waals and magnetic forces [28, 31, 34, 35].

A wide variety of polyelectrolytes and polymers such as poly (styrene sulfonate) (PSS), polyacrylic acid (PAA), polyaspartate (PAP), carboxymethyl cellulose (CMC) and guar gum, has been tested to stabilize NZVI particles [28, 36-38]. Our prior studies have shown that CMC is an effective agent in stabilizing NZVI due to its carboxylate and hydroxyl groups, which can bind with NZVI surface and thus stabilize NZVI particles efficiently [39-41]. Different CMCs with varied molecular weights such as 90 000 Da, 250 000 Da and 700 000 Da (referred to as 90K, 250K and 700K CMC respectively) have been used to coat NZVI particles. He et al reported that 90K CMC can effectively amend the size of NZVI particles [38] and the particles obtained by pre-coating 90K CMC can transport effectively in the lab scale columns [25] and in real field [42]. The significant mobility of 90K CMC coated NZVI particles was also reported by Raychoudhury et al. [28] and Kim et al. [43]. A newly published field study [44], however reported that 90K CMC modified NZVI particles were not very mobile (1 g/L NZVI dispersed in 4 g/L CMC solution). Recently, Kocur et al extensively studied the effects of 250K CMC dose and flow velocity on the stability and transport of NZVI particles [45]. They found that the stability and transport of NZVI particles increased with increasing of CMC concentration. The stability and transport of both 90K CMC and 700K CMC modified NZVI particles were reported in the studies conducted by Phenrat et al [46] and Kim et al [43].

Comparisons of the effectiveness of various polymers in reducing aggregation do not indicate a clear dependence on molecular weight, as factors such as charge on the

polyelectrolytes, the binding of the polyelectrolyte to the particle surface and the chemical properties of the polymer can influence the extent of stabilization. The extent of aggregation however is reduced by increasing molecular weights of homologous polymers and polyelectrolytes [31, 47]. Varying molecular weights of the same polyelectrolyte can cause changes in viscosity and rheology, which may also alter the colloidal stability of NZVI [48]. Varied physical and structural properties of the same type of polyelectrolyte could affect their colloidal stabilization efficiency on NZVI particles [31, 38, 49].

Admixtures of NZVI particles with shear-thinning fluids, which show less viscosity at higher flow rate, have been proposed as a promising method for enhancing NZVI transport [50-53]. Shear fluids are viscous when static and can stabilize NZVI particles, while the viscosity of fluids would reduce with increasing flow rate. As the hydraulic conductivity of the saturated porous media is negatively related with the viscosity of the flow, the resistance for NZVI particles, which is stabilized by the shear-thinning fluid, to transport through would be reduced with the increase of the flow rate. It is important to study the effects of shear-thinning on the stability and mobility of NZVI particles. Several studies have compared the effects of homologous polyelectrolytes with different molecular weights on the stability and transport of NZVI particles, such as PSS, PAP and CMC [30, 43]. However, these studies have only investigated the effects of molecular weight of homologous polyelectrolytes on the changes of electrostatic and steric stabilization of NZVI and its impact on aggregation and transport [46] [43], and have not considered the role of polyelectrolyte viscosity and rheology on the stability and transport of NZVI.

The objective of the study was to assess the role of viscosity of homologous CMC polyelectrolytes on the transport of NZVI. . The effects of 90K, 250K and 700K CMC on

NZVI particle size, surface charge, charge density and polymer coating thickness were assessed. The impacts of these particles as well as that the CMC solution viscosity on the colloid filtration theory-derived transport parameters were analyzed based on transport patterns observed in column experiments using the three CMC polyelectrolytes. The particle sizes of the different CMC-NZVI particles and their aggregates were characterized by transmission electron microscope (TEM), dynamic light scattering (DLS), nanoparticle tracking analysis (NTA) and optical microscopy at different NZVI concentration levels. The transport performance of 90K, 250K and 700K CMC-NZVI particles were investigated in packed column with different NZVI concentrations (1 g/L and 3 g/L) and ionic strength (3 mM Na⁺ and 10 mM Na⁺). The viscosities of these three CMC solutions (at 1 g/L) in different ionic strengths were measured and the effects of viscosity of free CMC in NZVI suspension on particles transport were analyzed by comparing the transport of washed and unwashed CMC-NZVI particles under identical conditions. The mass fraction of CMC absorbed on NZVI particles were determined by elemental analysis. The new Ohshima soft particle model [54] and the extended DLVO theory were employed to estimate the surface charge density and the particle-particle and particle-collector interaction potential to explain how the different CMCs can affect the stability and mobility of the grafted NZVI particles. It is expected that this detailed understanding of the effects of various molecular weights of the same type of polyelectrolyte on the stability and transport performance of the grafted NZVI particles can enable practitioners to choose an appropriate molecular weight of a polyelectrolyte to modify NZVI particles, offering optimal transport performance for specific delivery objective.

3.2 Materials and Methods

Chemicals. 90K CMC (Mw 90000 Da, D.S. =0.9), 250K CMC (Mw 250000 Da, D.S. =0.9) and 700K CMC (Mw 700000 Da, D.S. =0.9) as their sodium salt was obtained from Sigma Aldrich. Sodium bicarbonate (99.9%), Fisher Scientific, was used as electrolyte.

Porous media. Silica sand (Unimin corp., WI, USA) with an average diameter of 340 μm was used as a model porous media. The sand grains were 11.6% by weight in the size range of 285 μm -300 μm , 78.9% in the size range of 300-395 μm and the rest 9.5% of the sand ranged from 395 μm to 450 μm . Prior to being used, the sand was washed by concentrated hydrochloric acid to remove all unwanted components, followed by rinsing with distilled water until the pH value of the final rinsing solution was approximately 6.5. The sand was then dried in a furnace at 550 $^{\circ}\text{C}$ for overnight.

Preparation of CMC-NZVI. NZVI samples with a Fe^0 core and iron oxides outer shell was provided by Golder Associates, Canada. Bare NZVI particles were anaerobically stored as concentrated aqueous slurry (240 g/L) in a sealed container at pH 9.3. A NZVI stock solution (with concentration of 30 g/L) was prepared in degassed 3 mM NaHCO_3 solution and sonicated using a Cole-Parmer 8892 sonicator for 20 min to break-up aggregates which had been formed during storage. NZVI suspensions (1 g/L and 3 g/L) were each prepared in 1 g/L CMC solutions with different NaHCO_3 concentrations. It should be noted here that 1 g/L CMC solution can contribute 2.5 mM Na^+ determined by AAS, due to dissociation of NaCMC. Therefore, to obtain the desired solution with specific Na^+ concentration, the dose of NaHCO_3 concentration was adjusted accordingly. The mixtures then were shaken at 250 rpm for 1 hour to promote

interactions between CMC and NZVI particles. Finally, the grafted NZVI particles were sonicated for another 20 min.

Washing NZVI particles. 30 mL 700K CMC grafted NZVI suspension was taken into a centrifuge tube with N₂ headspace and centrifuged for 100 min at 10,000 rpm. Then the supernatant was taken out and replaced by the same volume of degassed 3 mM NaHCO₃ solution. The above mixture was resuspended and centrifuged again. This washing process was repeated three times.

Physical characterizations. The viscosities of different CMC solutions were measured by a viscometer (Brookfield, LVDV-I+ with LV1 spindle). The speed rate of the spindle was set at 30 rpm. After the spindle ran for 4 min, the viscosity was measured. In addition, the shear rate was calculated by accounting for the speed rate of the spindle and was determined to be 0.15/s.

Transmission electron microscopy (TEM) was used to obtain high-resolution images of the CMC-NZVI particles under selected conditions. Samples were prepared by placing a drop of the nanoparticle suspension on a Formvar grid, which was remained to air dry overnight prior to being examined under TEM. Accurate measurement of the average particle size was given by a TECNAI microscope equipped with an AMTCCD camera operating at 120 kV with a LaB6 filament.

Dynamic light scattering (DLS) (Malvern ZetaSizer Nano) and electrophoretic mobility (EPM) measurement were conducted as reported elsewhere [27, 28]. The NTA, DLS, and EPM measurement techniques as well as that for the elemental analysis of CMC grafted on NZVI particles are described in the SI.

Both DLS and NTA measurement of NZVI particles were conducted at low concentrations due to instrument limitations [55, 56]. TEM measurement of NZVI particles was

conducted at even lower concentration, because at high concentrations, too many particles would be accumulated on the grid, leading to the impossibility to discriminate the individual particle. Optimal microscopy was thus used to measure CMC-NZVI aggregates sizes at concentrations relevant to the transport experiments reported in this study. Optical microscopy has been employed in this study to measure NZVI aggregates sizes to avoid artefacts related to the effects of disaggregation cause by large dilutions on particle size. Optical microscopy measurements were conducted as follows: A latex particle sample with mean diameter of 200 nm (the diameter of 96% of particles ranged from 190 nm to 210 nm) was used as standard particles for method validation. The standard particles were imaged in a microscope (Olympus BX51) with bright field filter under the 100x objective as well as by phase contrast technique. Images were analyzed by ImageJ (totally around 2000 particles were analyzed) to provide the Fetet's diameter of 200 nm particle. Following the same process, NZVI suspensions with original concentrations (1 g/L and 3 g/L, in this study) were directly imaged in the microscope to obtain the actual aggregates sizes at these concentrations.

The measurements of the mean diameters of different CMC-NZVI aggregates were conducted after the samples prepared for 24 min. Unlike the size measurement protocols used in previous studies [15, 25, 27, 28, 31, 43, 49, 57], no sonication process was conducted for all size measurements. Additionally, the suspension was stored on an end-over-end rotator, which rotated very slowly to ensure the suspension uniform. The particles diameters measured by this protocol could reflect the actual size distribution in aqueous phase. It should be noted that the average diameters measured by the conventional microscope at 24 min after different CMC-NZVI particles prepared were used as their average aggregates diameters in column transport, because the duration of injection process was around 48 min. Elemental analysis was conducted

on an EAS1108 (Fisons instruments S.p.A., Italy) to examine how much CMC was coated on NZVI particles (the detailed analysis processes were explained in section S1 in SI).

Sedimentation. The colloidal stability of the newly modified NZVI particles was assessed by using UV-vis (508 nm) spectrophotometry to monitor the sedimentation processes of different CMC-NZVI suspensions at 1 g/L for 70 min at 25 °C [28].

Transport experiment. Transport studies were conducted in water-saturated silica sand ($d_p=340 \mu\text{m}$) in glass columns (Chromaflex, Fisher, 1.0 cm i.d., and 10 cm length). Columns were wet-packed and flushed with 3 mM NaHCO_3 solution for 15 pore volumes (PV) to obtain a uniform distribution of charges on sand surface. The porosity of the sand used here was 0.341, and water velocity was maintained at 0.508 cm/min with a peristaltic pump (Masterflex L/S, model 77200-12). The flow rate was controlled at constant by the pump. 8 PVs of NZVI suspension at different concentrations (1 g/L or 3 g/L) was each injected into the column during which the suspension was mixed evenly by a shaker at 380 rpm to minimize aggregation and sedimentation. Once the injection was complete, the column was flushed with 10 PV of NaHCO_3 . The effluent was collected with 2 min interval by an automatic fraction collector (Spectrum Chromatography Inc). An aliquot of the effluent was digested in acidic mixture ($\text{H}_2\text{O}:\text{HCl}:\text{HNO}_3=65:30:5$ (vol ratio) for 24 hours so that the amount of oxidized iron could be measured by flame atomic absorption spectrometry (Perkin Elmer, Flame-AAS Analyst 100 AAS system). The influent particle concentration was measured in the same manner.

Ohshima and extended DLVO theories. Ohshima theory for soft particle calculation was introduced here to acquire surface charge density of the grafted NZVI particles and in turn to assess the particle-particle electrostatic potential (calculation methods are presented in the SI). Extended DLVO theory was also introduced in this study to assess the interactions between

different CMC-NZVI particles and the interaction between different CMC-NZVI particles and the collector (see section S2 in the supporting information for details) [28, 31, 58, 59].

3.3 Results

3.3.1. Nanoparticle characterization

3.3.1.1. Particle size characterization

Table 3.1 shows the mean diameter of NZVI aggregates under different conditions by using DLS and microscopy. DLS measurement showed that the mean diameters of 90K CMC-, 250K CMC- and 700K CMC-NZVI particles in 3 mM Na⁺ solution were 1115 nm, 811 nm and 540 nm, respectively. Similar to previous studies [33, 49] our results confirm that with increasing CMC molecular weight, the colloidal stability of NZVI particles is improved, resulting in a lower extent of aggregation as characterized by the mean aggregate size. The mean diameter of 700K CMC-NZVI aggregates measured by DLS increased from 540 nm to 738 nm when Na⁺ concentration in the solution rose from 3 mM to 10 mM. This result can be explained by the effect of charge screening at higher electrolyte ionic strengths as well as changes in conformations of the CMC polymeric structure on the surface of the NZVI.

Table 3.1. Size and Physicochemical Characteristics of CMC-NZVI results.

Sample	IS (mM)	Viscosity (cP)	EPM ($ums^{-1}V^{-1}cm$)	C/C ₀	K _d (s ⁻¹)	NTA			DLS			Microscopy		
						Diameter (nm)	η	α	Diameter (nm)	η	α	Diameter (nm)	η	α
Bare NZVI (1 g/L)	3	1.0	-2.78	0	Na	Na	Na	Na	Na	Na	Na	15940±2458	Na	1
1 g/L NZVI in 1 g/L 90K CMC	3	3.2±0.3	-4.26	0.08	2.16*10 ⁻⁵	284±32.2	8.69*10 ⁻³	1.36	1115±95	8.67*10 ⁻³	0.90	6340±589	8.80*10 ⁻³	0.034
1 g/L NZVI in 1 g/L 250K CMC	3	7.3±0.5	-5.61	0.38	8.27*10 ⁻⁶	260 ±29.4	3.33*10 ⁻³	0.81	811±88.6	3.33*10 ⁻³	0.88	5250±477	3.37*10 ⁻³	0.045
1 g/L NZVI in 1 g/L 700K CMC	3	26.3 ±1.2	-7.20	0.77	2.34*10 ⁻⁶	206±35.8	8.98*10 ⁻⁴	0.47	540±118	8.98*10 ⁻⁴	0.69	2220±384	9.54*10 ⁻⁴	0.19
1 g/L NZVI in 1 g/L 90K CMC	10	1.4±0.2	-2.31	0	Na	Na	Na	Na	1866	0.0667	1.00	9968±1022	1.5469	1.00
1 g/L NZVI in 1 g/L 250K CMC	10	3.1±0.5	-4.20	0.12	5.20*10 ⁻³	265±40.5	7.29*10 ⁻³	0.97	1128	0.0073	0.42	7668±924	0.3917	0.0186
1 g/L NZVI in 1 g/L 700K CMC	10	11.3±1.0	-5.23	0.55	5.03*10 ⁻⁶	257±37.8	2.06*10 ⁻³	0.69	738±101	2.06*10 ⁻³	0.79	3440±452	2.05*10 ⁻³	0.092
1 g/L NZVI in 1 g/L 250K CMC (washed)	3	1.0	-3.88	0	Na	Na	Na	Na	1671	0.0793	1.00	10082±1049	2.2869	1.00
1 g/L NZVI in 1 g/L 700K CMC (washed)	3	1.0	-4.46	0.41	7.41*10 ⁻⁶	Na	Na	Na	1077	3.06*10 ⁻³	0.066	4450±749	3.02*10 ⁻³	0.0066
3 g/L NZVI in 1 g/L 90K CMC	3	3.2±0.3	-4.26	0	Na	Na	Na	Na	Na	Na	Na	11350±1562	Na	Na
3 g/L NZVI in 1 g/L 250K CMC	3	7.3±0.5	-5.61	0.23	1.25*10 ⁻⁵	Na	Na	Na	1551	5.05*10 ⁻³	0.464	8490±1031	5.20*10 ⁻³	0.027
3 g/L NZVI in 1 g/L 700K CMC	3	26.3 ±1.2	-7.20	0.93	6.11*10 ⁻⁷	Na	Na	Na	1181	2.49*10 ⁻⁴	0.073	3130±611	2.49*10 ⁻⁴	0.028

Optical microscopy derived measurements of the same NZVI particle and aggregate diameters were significantly larger but showed the same trends as the DLS measurements. The mean diameters of 90K CMC-, 250K CMC- and 700K CMC-NZVI aggregates measured by microscopy at 1 g/L were 6340 nm, 5250 nm and 2220 nm, respectively. The discrepancy in the DLS and microscopy can be attributable to the fact that samples for DLS measurements were diluted down to 150 g/L. At lower concentrations, the extent of aggregation is reduced as the probability of collision between particles decreases with decreasing concentrations. The NTA measurements require dilution to even lower concentration of 40 mg/L, which in part contributes to the lower mean particle sizes in the range of 200 to 300 nm (shown in SI Table 3.S1). Particle size distribution data shown in Figure 3.S1, even the mean diameter of 1 g/L NZVI particles in 1 g/L 700K CMC solution was around 2.22 μm , smaller particles (around 500 and 600 nm) constitute a significant fraction. Furthermore, with optical microscopy the minimum diameter which could be observed was 200 nm, and smaller particles were ignored.

In general, measuring the *in situ* aggregate sizes of NZVI in aqueous solutions is challenging. Different techniques pose different challenges. For instance, direct-observation measurement methods such as TEM and AFM would take the size of aggregates as that of individual particles [60]. The diffusion coefficient measurement methods such as NTA, DLS, FCS and FIFFF can produce a very big deviation from the actual diameter for polydisperse samples due to the sensitivity of light intensity to the particle sizes [60].

Micron-sized aggregates in high concentration suspensions of NZVI with post-grafted polymers have been observed in several other studies. Phenrat et al also observed that polyelectrolyte stabilized NZVI particles in high concentration suspensions could be in the range of several microns [46, 61], for example, the mean diameters of 700K CMC-NZVI (6 g/L)

ranged from 4.39 to 8.72 μm [61]. Our attempts at measuring particle sizes by DLS at these high concentrations did not yield reproducible results. However, optical microscopy provided reproducible results and particle size trends are consistent with typical of colloid stabilization behavior with the addition of polyelectrolytes as increasing CMC molecular weight decreased the mean particle size. The aggregation extents of different CMC-NZVI particles determined by DLS and the particle size distributions of different CMC-NZVI determined by microscopy were shown in Figure 3.S1 and 3.S2, respectively.

Washing the CMC-NZVI suspensions resulted in larger particle sizes, because of reduced electrosteric stabilization at lower CMC concentrations caused by washing. Mean particle sizes at 3 g/L NZVI concentration were larger than with 1 g/L. Washed 700K CMC-NZVI aggregates showed a bigger mean diameter (4450 nm) than that of unwashed particles (2220 nm) under identical conditions. The presence of the free CMC in the suspension would be favorable to the prevention of NZVI particle aggregation. The free CMC in the suspension caused the suspension to be very viscous, leading to the Brownian motion of particles to slow down. Finally, the collision between particles would be significantly reduced, reducing the aggregation rate. Furthermore, the unwashed particles had a higher CMC layer thickness (8.0 nm) than that of washed (5.4 nm) as observed from TEM images (the results shown in Table 3.S2). The higher layer thickness provided more electrostatic and steric repulsions between particle and particle, resulting in less aggregation rate.

3.3.1.2 Zeta potential measurement

Electrophoretic mobilities of 700K CMC-, 250K CMC- and 90K CMC-NZVI particles in 3 mM Na^+ solution are $-4.46 \text{ } \mu\text{m s}^{-1} \text{ V}^{-1} \text{ cm}$, $-3.88 \text{ } \mu\text{m s}^{-1} \text{ V}^{-1} \text{ cm}$ and $-3.16 \text{ } \mu\text{m s}^{-1} \text{ V}^{-1} \text{ cm}$ and the

corresponding zeta potential, calculated using Henry equation are -60.39 mV, -52.48 mV and -42.81 mV, shown in Figure 3.S4 for IS ranging from 3 to 150 mM, at a pH range of 7.28-8.92. Sakulchaicharoen et al also reported higher electrophoretic mobility of 700K CMC-NZVI than with 250K and 90K CMC-NZVI particles [49]. CMC with higher molecular weight are possess more carboxylate and hydroxyl groups and thus, the EPM values of these three CMC-NZVI particles increased with increasing CMC molecular weight.

3.3.2 The effects the molecular weight of CMC on NZVI particle stability

3.3.2.1 Viscosity measurements

The viscosities of different CMC-NZVI solutions were measured and shown in Table 3.1. The viscosity of the CMC solutions were assumed to be identical to that of CMC-NZVI suspension based on the findings of Comba et al [62], who found that at high shear rates (1/s to 10^5 /s), addition of NZVI particles (5 g/L, 17.5 g/L and 30 g/L) into 3 g/L xanthan gum solution does not change the viscosity of the solution. As described in the experimental and materials section, the shear rate used for the measurement of our samples was about 0.15/s. Thus, the viscosities of different CMC-NZVI suspensions were considered to be as the same value of the corresponding pure CMC solution. This was additionally verified by a viscosity measurement results that the viscosities of the 700K CMC solution (3 mM Na⁺) with and without NZVI were found to be identical and 26.3 cP.

CMCs with different molecular weights yielded significantly different viscosities: 700K CMC-NZVI in 3 mM Na⁺ had the highest viscosity of 26.3 cP, while 250K CMC-NZVI and 90K CMC-NZVI suspensions showed relatively lower viscosities of 7.3 cP and 3.2 cP under the identical IS. The increase trend of CMC solution's viscosity with increasing CMC molecular

weight has been reported elsewhere [50]. Furthermore, the viscosities of 700K CMC- and 250K CMC-NZVI suspensions significantly decreased with the increase of NaHCO_3 concentration. This can be accounted for by the restraint of the expansion of CMC molecules with higher IS [63].

Additionally, Comba et al [62], found that the viscosities of both xanthan solution and NZVI-xanthan suspension measured in the bulk were the same as those measured in the porous media under the same shear rate condition. Thus, the viscosities of different CMC-NZVI suspensions listed in Table 3.1 could be directly used to for particle-collector interaction energies and to conduct the single collector efficiency prediction.

3.3.2.2 CHN analysis and measurement of the layer thickness of CMC layer by TEM

The elemental analysis for determination of the amounts of bound and free CMC in solution is shown in Table 3.S1. It can be observed that the CMC mass contents of all these different CMC-NZVI particles were less than 1.8%. Previous studies also reported that CMC mass contents on the CMC post-grafted NZVI particles were very low, from 3% to 4.5% [31, 43]. Additionally, CMC mass contents of these different types of CMC-NZVI particles did not significantly differ from each other. This is in contrast to another study which reported that the higher molecular weight of polyelectrolytes, such as PSS, PAP and CMC, had much more adsorption on NZVI particle [43]. CMC contents of 700K CMC-NZVI decreased from 1.78% in 3 mM Na^+ solution to 1.56% in 10 mM Na^+ solution. Additionally, CMC mass content of 700K CMC-NZVI particles reduced after washing (from 1.78% to 1.27%). These results indicated that CMC mass content would decrease with the increase of salt concentration in NZVI suspension and adsorbed CMC molecules on the grafted NZVI particle can be washed off to some extent.

3.3.2.3 New Ohshima theory and the extended DLVO theory calculations

The new Ohshima theory was employed in this study to analyze the surface charge density of different CMC-NZVI particles [54]. The calculated charge number densities on 90K CMC-, 250K CMC- and 700K CMC-NZVI particles surfaces are 2.923 N/m^3 , 6.538 N/m^3 and 7.769 N/m^3 , which are higher than those reported in Phenrat et al's paper (0.33 N/m^3 and 0.35 N/m^3 for 700K CMC- and 90K CMC-NZVI particles, respectively) [31]. This charge density result indicates that CMC with higher molecular weight can bring more surface charge on the corresponding coated NZVI particle. Further, among these three CMC-NZVI samples, the surface layer of 700K CMC-NZVI particles displayed much more resistance (least softness, 5.8), while the surface layer of 90K CMC-NZVI particle exhibited the lowest resistance (highest softness, 9.0) for surrounding solution to transport through them.

Using the above simulated surface charge density values and the methodology to calculate the electrostatic interaction between particle and particle, described by Ohshima [54], the electrostatic particle-particle interactions of different CMC-NZVI particles were obtained and shown in Figure 4.S4. It is obvious that the electrostatic repulsion interaction between 700K CMC-NZVI particles is much stronger than those between 250K CMC-NZVI particles and between 90K CMC-NZVI particles. Moreover, it can be observed that for all these three types of CMC-NZVI particles, the electrostatic repulsion rapidly decreased with the increase of NaHCO_3 concentration, potentially causing quite high aggregation at high IS. Additionally, the barrier of the electrostatic particle-particle interaction of 90K CMC-NZVI particle in 3 mM Na^+ solution showed in Figure 3.S4a is around 60 KT , which is higher than that reported in Phenrat et al's

paper (around 20 KT) [31]. This could be attributable to the surface charge density results discussed in the above paragraph.

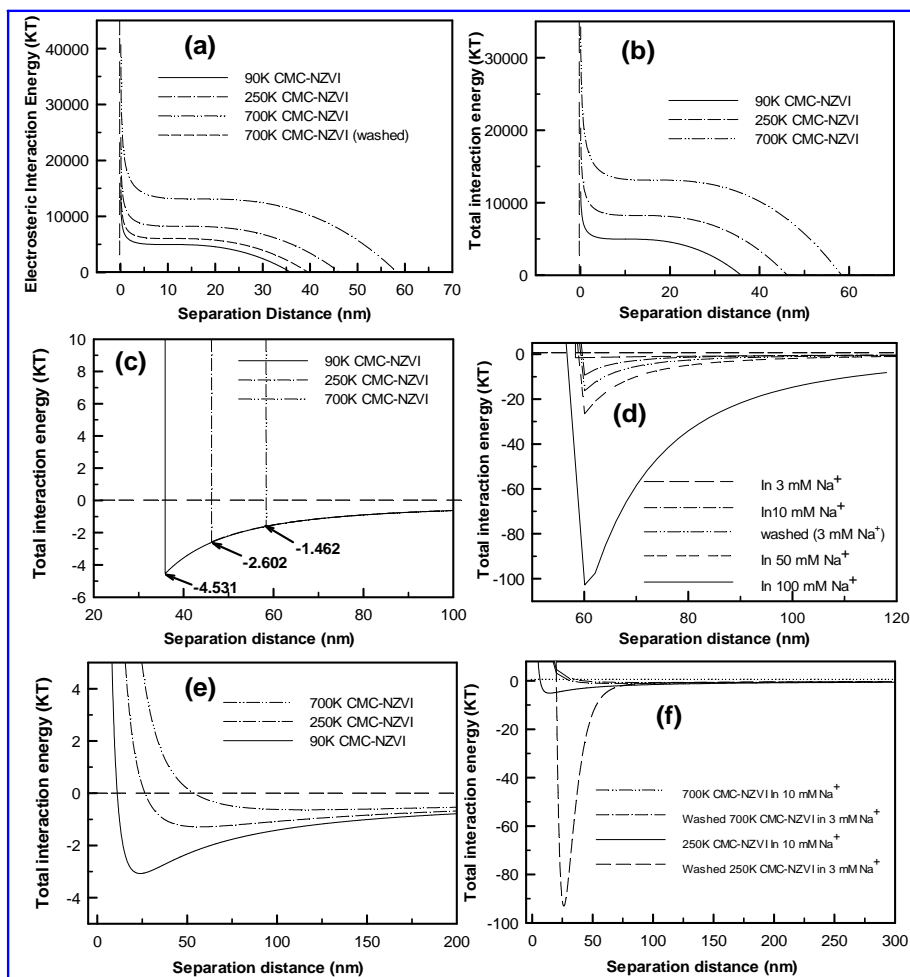


Figure 3.1. Extended DLVO calculations (a) the electrosteric interaction energies of different CMC-NZVI particles (between particle and particle); (b) total interaction energies of different CMC-NZVI particles (between particle and particle); (c) the secondary minima of different CMC-NZVI particles (between particle and particle); (d) the changes of the total interaction energies of 700K CMC-NZVI particles with NaHCO₃ concentrations (between particle and particle); (e) the total interaction energies of different CMC-NZVI particles (between particle and collector); (f) the changes of the total interaction energy of 700K CMC-NZVI with NaHCO₃ concentration (between particle and collector).

The electrosteric repulsions between particle and particle were calculated using Byrd et al's equation [64] (see Section equation (3.S10) in SI). And the results are shown in Figure 3.1a.

The electrosteric interaction of 700K CMC-NZVI particle was about 1.6 times and 3 times of 250 K CMC- and 90K CMC-NZVI, respectively. The electrosteric interaction energy of washed 700K CMC-NZVI particles was even higher than that of unwashed 90K CMC-NZVI particles. The much stronger electrosteric interaction energy of 700K CMC-NZVI particle can be accounted by the much longer polymer segment in 700K CMC polymer, which can generate a stronger electrosteric repulsion.

Figure 3.1b presents the total interaction energy profiles of different CMC-NZVI particles. It can be observed that 700K CMC-NZVI particles had the highest barrier, which can be attributed to both the highest electrostatic potential in Figure 3.S4 and the highest electrosteric interaction in Figure 3.1a. Nevertheless, 90K CMC-NZVI particles possessed the lowest barrier. The secondary minima of the total interaction energy between particle and particle of different types of CMC-NZVI suspensions was amplified and shown in Figure 3.1c. The deeper minima occurred to 90K CMC-NZVI particles than those occurred to 250K CMC-, and 700K CMC-NZVI particles, indicating that there was a stronger attraction between particle and particle. Both these secondary minima results the barrier results shown in Figure 3.1b demonstrate 700K CMC-NZVI particle would be much more stable than 250K CMC- and 90K CMC-NZVI particles, verifying the size characterization results in 3.1.1 section and the sedimentation results shown in Figure 3.S5.

Several studies had investigated the effects of IS on the aggregation rate and transport of NZVI particles [27, 34]. The effects of IS on the secondary minima between particle and particle of 700K CMC-NZVI suspension are shown in Figure 3.1d. The interparticle attraction increased with the increase in IS, due to the increased charge screening effects on particle's electrical double layer. The data shown in Figure 3.1d also revealed that the attractive forces between

washed 700K CMC-NZVI particles was higher than that of the unwashed sample under the identical solution chemistry because less electrosteric energy existed between the washed particles than that existed between unwashed particles (shown in Figure 3.1a). This can be used to explain that the aggregate size of washed particles is bigger than that of the unwashed particles stated in microscope results and the washed 700K CMC-NZVI particle shows less stability than that of unwashed (shown in Figure 3.S3a).

Figure 3.1e shows the interaction between the different CMC-NZVI particles and the collector in 3 mM SI. It is obvious that the depth of the secondary minimums between these three CMC-NZVI particles and the collector increases with the decrease of the molecular weight of CMC, indicating that the attraction between these three CMC-NZVI particles and the collector increases with the decrease of CMC molecular weight. A positive relationship between the particle-collector maximum attractions of 700K CMC-NZVI particles and NaHCO_3 concentration can be found from Figure 3.1f. Moreover, the secondary minima between washed particle in 3 mM Na^+ solution and collector was shallower than that between unwashed particle in 10 mM Na^+ solution and collector. This indicates that the attraction exerted on washed particle by collector was stronger than that exerted on unwashed particle.

3.3.3 The effects of the molecular weight of CMC on the transport of NZVI particles

3.3.3.1 Transport of different CMC-NZVI particles at 1 g/L

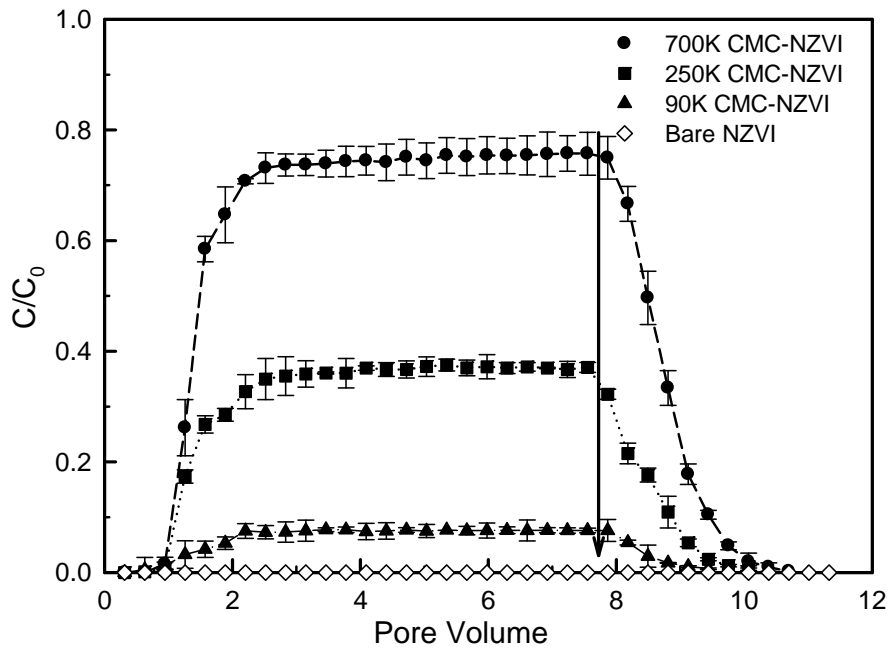


Figure 3.2. The transport of different CMC-NZVI particles at 1 g/L (in 3 mM Na⁺ solution) in column experiments.

The breakthrough curves of different CMC-NZVI particles at 1 g/L in 3 mM IS are shown in Figure 3.2. It can be observed that 700K CMC-NZVI has the highest steady state effluent concentration ($C/C_0 \approx 0.77$), followed by 250K CMC-NZVI ($C/C_0 \approx 0.38$), while 90K CMC-NZVI showed negligible effluent concentrations ($C/C_0 \approx 0.08$). These results indicate that 700K CMC is the most effective polyelectrolyte to improve the transport of NZVI particles among three samples.

These results are in agreement with the above CMC-NZVI particle characterization results: the 700K CMC can extensively stabilize NZVI particles, resulting in the final aggregate sizes (mean diameter was 2.22 μm) are easily transported through sand of the 340 μm average diameter used. However, the mean diameters of 250K CMC- and 90K CMC-NZVI particles were 5.25 μm and 6.34 μm which result in limited mobility. It should be noted that after

switching the NZVI suspension to electrolyte to flush the column, only a very small amount of NZVI particles was flushed out. Very similar observations were also found in earlier studies [65-67]. This can be attributed to the different viscosity property of the suspension and the flushing electrolyte: the suspensions used here and in these early studies were polymer solutions, which were very viscous (resulting in a very small single collector contact efficiency), while, the viscosities of electrolytes were not very high (close to 1 cP), which caused that NZVI particles easily contacted with sand granules, leading to more deposition during flushing process.

Nanoparticle deposition in porous media has been described by the colloid filtration theory in several studies [68, 69]. According to this theory, the particle deposition rate coefficient is represented as function of the single collector contact efficiency (η_0) and the attachment efficiency (α), with the assumption of steady state transport (or $\partial C/\partial t=0$) and negligible dispersion.

$$k = \left[\frac{3(1-f)u}{2d_s f} \alpha \right] \eta_0 \quad (3.1)$$

In the above equation f is porosity of media and d_s is the average diameter of collector. The parameter η_0 is the probability of collision of a particle flowing through the porous media and can be predicted by the Tufenkji and Elimelech equation [70].

The parameter α represents the probability of sticking of a particle on the collector after collision, or in other words the probability of a collision that leads to deposition. The attachment efficiency is usually determined from experimental data of C versus t (or breakthrough curves) by solving for equations 3.1 [24, 25].

$$\alpha = -\frac{2d_s * \ln(C/C_0)}{3(1-f) * L * \eta_0} \quad (3.2)$$

In equation 3.2 the dimensionless parameters of N_G and N_A are negatively related with the viscosity of the suspension. Thus, scrutinizing equation 3.2, one can find that the single collector contact efficiency is negatively determined by the viscosity. Figure 3.3 shows the effect of viscosity on the single collector contact efficiency.

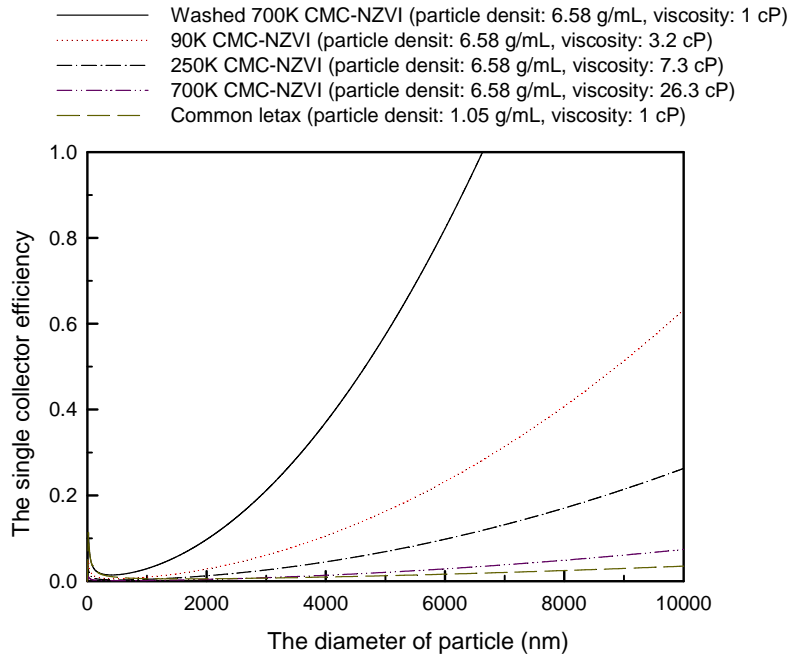


Figure 3.3. Changes of the single collector contact efficiency with varying viscosity of dispersant.

As listed in Table 3.1, CMC with higher molecular weight shows higher viscosity value. And the single collector contact efficiency values for the three CMC-NZVI particles are listed in Table 3.1. The η_0 values of 700K CMC-, 250K CMC- and 90K CMC-NZVI aggregates at 1 g/L were calculated to be 5.02×10^{-3} , 7.57×10^{-2} and 0.26. As a result the effluent concentrations of 250K- and 90K-CMC NZVI compared to the 700K CMC-NZVI. Several studies have showed that 90K CMC-NZVI can transport through porous media [25, 28, 43, 49], whereas, the transport of 90K CMC-NZVI particles in this study is not significant, might due to the very concentrated NZVI particles used in this study and more aggregation extent as a result of the nature of the

product. This is due to the fact that the NZVI particles used in this study were more magnetic. Further, NZVI particles concentrations used in the early studies were very low (in tens of mg/L level) [25, 28], while it is 1 g/L here which tends to form very big aggregates. Additionally, the bare NZVI particle was not mobile at all due to its very rapid aggregation rate, as previously reported in other studies [28, 34, 68].

3.3.3.2 Impacts of IS and washing on transport of 700K CMC- and 250K CMC-NZVI particles

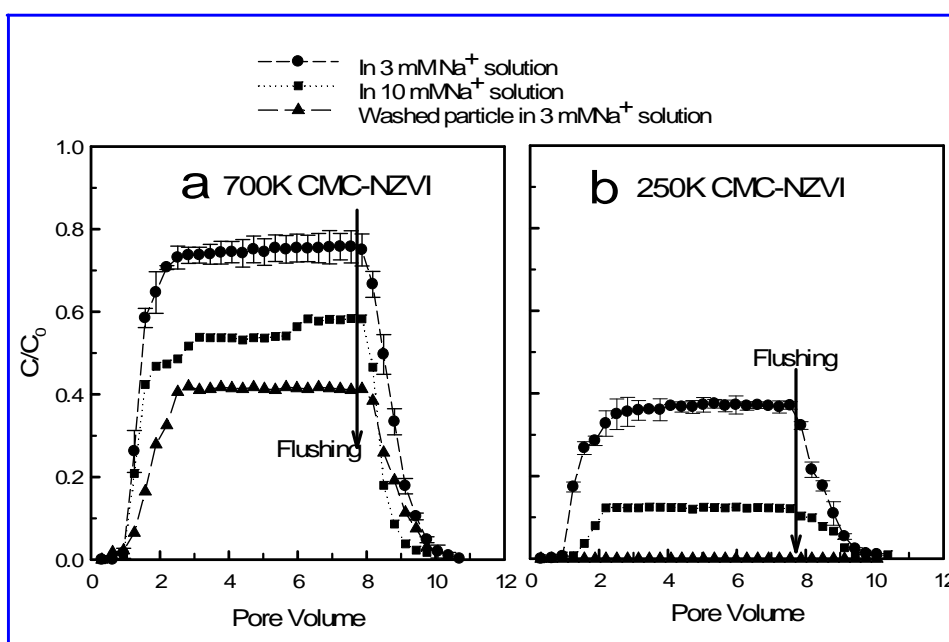


Figure 3.4. The effects of IS and washing on transport of 700K CMC- and 250K CMC-NZVI particles.

Several studies have demonstrated that the ionic strength can substantially affect the stability and transport of NZVI particles [34, 71]. The transport of 250K CMC- and 700K CMC-NZVI particles in 3 mM and 10 mM solutions as well as washed 250K CMC- and 700K CMC-NZVI particles were investigated and compared in this study and shown in Figure 3.4. It can be observed that when Na^+ concentration increased from 3 mM to 10 mM, the steady-state effluent concentration decreased from 0.77 to 0.55 and from 0.38 to 0.12 for 700K CMC- and 250K

CMC-NZVI particles respectively. This result can ascribe to two reasons: Firstly, when IS increased from 3 mM to 10 mM, the mean diameter of NZVI particles increased, which could cause less transport; Secondly, when IS increased, the viscosity of NZVI suspension decreased (from 26.3 cP to 11.3 cP and from 7.3 cP to 3.1 cP for 700K CMC-NZVI and 250 K CMC-NZVI suspension, respectively), resulting in increased single collector contact efficiencies in the high IS. Further, the washed 700K CMC-NZVI particles showed around 0.41 C/C_0 while the washed 250K CMC-NZVI particles did not transport at all. As shown in Table 3.1, the washed 700K CMC-NZVI was relatively less aggregated. Washed 250K CMC-NZVI particles however aggregated very easily. These results indicate that the transport of 250K CMC- and 700K CMC-NZVI particles are significantly sensitive to ionic strength and washing.

The effluent concentrations of washed and unwashed 700K CMC-NZVI samples were compared to reveal the effects of free polyelectrolyte molecules in NZVI suspension on its transport efficiency and the data is shown in Figure 3.3. It can be observed that the transport efficiencies of the washed and unwashed samples were 0.77 and 0.41 respectively under identical experimental conditions. This indicated that the free polyelectrolyte played a significant role in the transport of NZVI particles. The data on adsorbed CMC mass fractions obtained from elemental analysis results present earlier indicates that most of CMC molecules were free in CMC-NZVI suspensions, after losing these free CMC by washing suspension, CMC-NZVI aggregated further. Moreover, free CMC remained in the suspension could coat sand surface, resulting in increased repulsion between sand grains and NZVI particle. The single collector efficiency results listed in Table 3.1 also reveal that the single collector efficiency of washed 700K CMC-NZVI particles is greater than that of the unwashed sample due to the higher viscosity of unwashed sample, as well as because of the smaller size of unwashed particles.

These results are consistent with the finding of Jiemvarangkul et al who observed that the transport of NZVI particles increased with the increase of PAA dosage in the suspension [29].

The attachment efficiencies of various CMC-NZVI particles were calculated based on DLS and optical microscopy measurement results respectively. The results are listed in Table 3.1. The attachment efficiencies determined by DLS characterization results are very high. This result can be attributed to the fact that the very high viscosity values are taken in the single collector contact efficiency calculations, which causes η_0 to be very small, resulting in the attachment efficiency to be high. A recent study [72] also reported very similarly high attachment efficiencies when considering the high viscosity values in the single collector contact efficiency calculations. When IS increased from 3 mM to 10 mM, the attachment efficiency of 700K CMC-NZVI particles increased from 0.69 to 0.79, consistent with the expectation. Nevertheless, even the suspensions' viscosity values were also taken into consideration of the single collector efficiency calculations, the single collector contact efficiencies determined from the optical microscopy characterization results are very big (contributed by the very big particle size results), leading to the attachment efficiency to be very small. The attachment efficiency does not show the expected increase trend with the increase of IS for the same type CMC-NZVI particles. For example, the attachment efficiencies of 700K CMC-NZVI particles are 0.19 and 0.092 in 3 mM and 10 mM IS, respectively. This is due to the complexity of the changes of viscosity and particle diameter with IS.

3.3.3.3 Transport of 700K CMC- and 250K CMC-NZVI at 1 g/L and 3 g/L

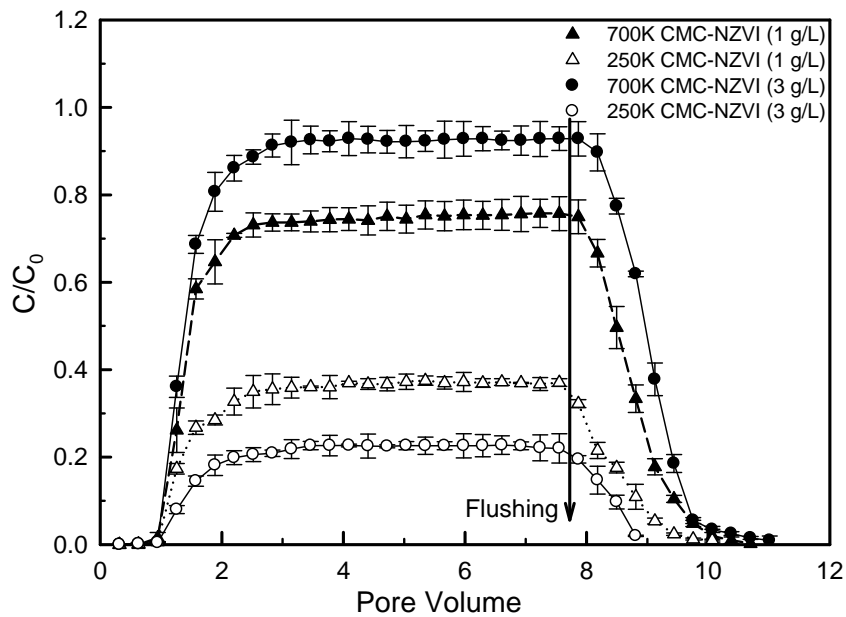


Figure 3.5. The transport of different CMC-NZVI particles at 3 g/L (in 3 mM Na⁺ solution).

The transport of different CMC-NZVI particles at 3 g/L was investigated to examine the transport of CMC-NZVI particles at high concentration required in field application [18]. The results were shown in Figure 3.5. The steady-state effluent concentration of 700K CMC-NZVI at 3 g/L was 0.93, which was higher than the value of 0.77 at 1 g/L. In contrast, the effluent concentration of 250K CMC-NZVI at 3 g/L only remained at 0.23, which was lower than the value of 0.38 at 1 g/L. The mobility of 90K CMC-NZVI particles at 3 g/L was negligible. The higher elution of 700K CMC-NZVI particles 3 g/L than that at 1 g/L is non-intuitive given that several studies observed the decreased elution of NZVI particles with the increase of iron concentration [28, 47]. Furthermore, based on above particle characterization: at 3g/L the CMC-NZVI has a bigger mean aggregate diameter of 3.13 μm than that at 1 g/L (2.12 μm), leading to a slightly higher single collector contact efficiency at 3 g/L (Table 3.1). It could be other external factor enhanced particles to mobile at 3 g/L. When iron concentration increased to 3 g/L, η

values of 250K CMC-NZIV particles increased to 5.20×10^{-3} from 3.33×10^{-3} , due to the increase of aggregate size with particle concentration. This can explain the results that the transport efficiency of 250K CMC-NZVI particles fell to 0.23 at 3 g/L (shown in Figure 3.5).

The interaction energies between different CMC-NZVI particles and collector were presented in Figure 3.1e. 700K CMC-NZVI particles showed the lowest particle-collector interaction energy at the secondary minima, and a value was very close zero. The interaction energy at the secondary minima between 250K CMC- as well as 90 K CMC-NZVI particles and the collector were about 2.5 and 5 times of that between 700K CMC-NZVI particle and the collector. As several studies have shown a positive relationship exists between the depth of the secondary minima and the attachment efficiency α [27, 73, 74], it is reasonable to predict that the attachment of 700K CMC-NZVI particles should be less than that of 250K CMC- and 90K CMC-NZVI particles. However, this expectation is opposite to the empirical calculated results listed in Table 3.1: the calculated attachment efficiencies (based on optical microscopy sizes) of 1 g/L 90K CMC-, 250K CMC- and 700K CMC-NZVI in 3 mM IS are 0.034, 0.045 and 0.19 respectively. Additionally, in terms of the expectation that bigger particle should have stronger magnetic attraction and resultant higher attachment efficiency [74] and 700K CMC-NZVI particle at 3 g/L should have less transport efficiency than that at 1 g/L. The DLVO secondary minimum is insufficient to interpret these two aforementioned results. Other force or energy should be considered to explain the unexpected comparatively high attachment efficiency of 700K CMC-NZVI particles at 1 g/L among 90K CMC, 250K CMC and 700K CMC-NZVI particles and the unreasonable less attachment efficiency at 3 g/L.

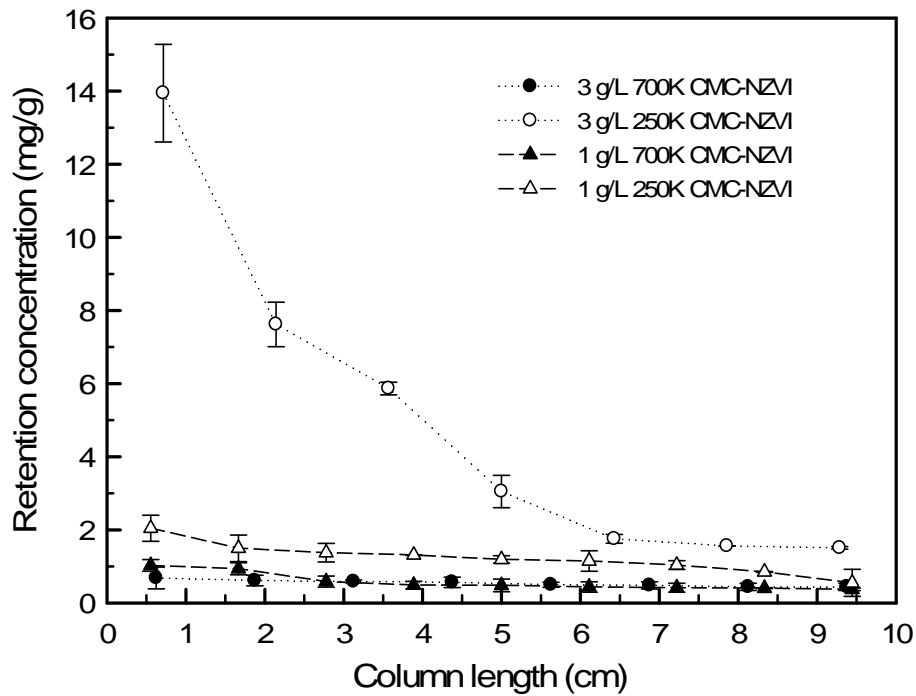


Figure 3.6. Retention profiles along with the column length of 250K CMC- and 700K CMC-NZVI particles.

Figure 3.6 shows that the deposition of CMC-NZVI on the sand particles for the 3 g/L and 1g/L are very similar, and in fact, there is a slightly higher deposition at 1g/L in the first 2 cm of the column. In contrast, for 250K CMC-NZVI particles, the extent of deposition at 3 g/L is much higher than at 1 g/L. The deposition data shown in Figure 3.6 can explain the transport results shown in Figure 3.5. The deposition profiles of 700K CMC-NZVI particles are quite flat. It is likely that the free CMC in the 700K CMC-NZVI samples and the change of particle size are more prominent role in controlling deposition. However, for 250K CMC-NZVI particle, the deposition profile (under 3 g/L NZVI concentration condition) shows the classical colloid deposition model (log-normal distribution), because free 250K CMC in the suspension could not provide a significant repulsion between the particle and the collector.

3.4 Conclusions

The effects of the molecular weight of CMC on the corresponding grafted NZVI particles were systematically investigated in this study to give clear answers to the questions of whether the various products with different molecular weight of the same type of the polyelectrolyte can affect the corresponding grafted NZVI particles' stability and mobility and how. The viscosity results and the corresponding single collector efficiency analysis indicated that 700K CMC processed the highest viscosity and provided the lowest single collector efficiency for 700K CMC-NZVI particles. Ohshima theory fittings and extended DLVO calculations showed that 700K CMC-NZVI particles had the highest surface charge density and the highest electrostatic and electrosteric interparticle energies. These calculation predictions were confirmed by NTA and DLS as well as the sedimentation results: 700K CMC-NZVI particles showed smallest mean size and slowest aggregation rate as well as the highest stability among three CMC-NZVI particles. As expected, 700K CMC-NZVI particles showed the highest mobility. Even at quite high iron concentration (3 g/L), 700K CMC-NZVI particles were still quite mobile. Compared to unwashed particles, washed 700K CMC-NZVI particles showed a considerable decreased transport efficiency. And finally, the conclusion that, among a series of products of the same type of polyelectrolyte, a product with higher molecular weight could give a higher stability and mobility for the corresponding grafted NZVI particles can be drawn. Moreover, a suggestion that both the properties of the grafted NZVI particles and the property of the dispersant should be taken into account to assess the particles' stability and mobility is given based on above results to the researchers in the related fields.

Acknowledgments

The research was funded by the Strategic Project Grant Program of the Natural Sciences and Engineering Research Council of Canada and by Golder Associates Ltd. J. L. was supported in part by a McGill Engineering Doctoral Award. We thank Prof. Nathalie Tufenkji, McGill University for access to the laser Doppler velocimeter.

Supporting information

Section S1. DLS and electrophoretic mobility (Zeta potential) measurements and CHN elemental analysis processes

1) DLS measurement

20 mL 150 mg/L samples were stored in 30 mL vials and fixed on an end-over-end rotator for 24 mins with a slow rotation rate. And then 2 mL of this sample was taken into the cubic vial and sealed for DLS measurement.

2) Electrophoretic Mobility

The electrophoretic mobilities (EMP) of the different CMC-NZVI particles in different concentrations of NaHCO₃ solutions were measured by laser doppler velocimetry (ZetaSizer Nano ZS, Malvern). EMP measurements were quadrupled for each sample at 25.0 °C. The strength of the applied electrical field (E) was 4.8 V.

3) Elemental analysis process

A small amount of dried sample was weighed into a tin capsule. The sample was dropped into the combustion reactor prior to the arrival of oxygen in the combustion reactor. The sample and tin capsule reacted with oxygen and combusted at temperatures of 1700-1800 °C. By sample was broken into its elemental components, N₂, CO₂, H₂O and SO₂. High performance copper wires absorbed the excess oxygen, which was not used to combust the sample. Then, the product gases flowed through the gas chromatographic separation column which was kept at a constant temperature (± 0.1 °C) to be separated and were detected sequentially by a TCD detector. The TCD detector generated a signal, which was proportional to the amount of element in the sample.

The ECS software compared the elemental peak to a known standard material (after calibration) and generated a report for each element on a weight basis.

4) NTA measurement

NTA measurements were conducted as follows. After the original suspension was mixed uniformly, 2 mL of original suspension was taken into specific volume of degassed water (with specific ionic strength) to get 40 mg/L NZVI suspension. Next, 1.5 mL of this 40 mg/L NZVI suspension was injected into NTA machine. The diffusion path of each single particle was tracked and recorded for analyzing particle size.

Section S2. New Ohshima theory and extended DLVO theory calculations

1) Ohshima theory calculation

The characteristics of coated NZVI particles were extracted from Ohshima theory calculations [54]. The calculation procedures involve the following equations:

$$\mu = \frac{\varepsilon_r \varepsilon_0}{v} \frac{\varphi_0 / \kappa_m + \varphi_{DON} / \lambda}{1 / \kappa_m + 1 / \lambda} + \frac{Z_e N}{v \lambda^2} \quad (3.S1)$$

where

$$\phi_{DON} = \frac{K_B T}{ze} \ln \left\{ \frac{ZN}{2zn} + \left[\left(\frac{ZN}{2zn} \right)^2 + 1 \right]^{1/2} \right\} \quad (3.S2)$$

$$\phi_0 = \frac{K_B T}{ze} \left(\ln \left[\frac{ZN}{2zn} + \left\{ \left(\frac{ZN}{2zn} \right)^2 + 1 \right\}^{1/2} \right] + \frac{2zn}{ZN} \left[1 - \left\{ \left(\frac{ZN}{2zn} \right)^2 + 1 \right\}^{1/2} \right] \right) \quad (3.S3)$$

$$\kappa_m = \kappa \left[1 + \left(\frac{ZN}{2zn} \right)^2 \right]^{1/4} \quad (3.S4)$$

and

$$\kappa = \left(\frac{\varepsilon_r \varepsilon_0 K_B T}{2 N e^2 I} \right)^{-1/2} \quad (3.S5)$$

$$I = \frac{1}{2} \sum_{i=1}^M n_i z_i^2 \quad (3.S6)$$

In equation 3.S1, ε_r is the relative permittivity of the solvent, ε_0 is the permittivity of free space, ν is the viscosity of the solution, ϕ_0 is the potential at the boundary between polymer layer and electrolyte, ϕ_{DON} is Donnan potential inside polymer layer, κ_m is the effective Debye-Hückel parameter of the solution, which is given in equation 3.S4, λ is defined as softness with the dimension of the reciprocal of length (which is the unknown parameter and would wait to be fitted), Z is the valence of the ionized groups on the polyelectrolyte, which is -1 for CMC (used in this study), N (m^{-3}) is the density of ionized group (would be obtained from the fitting of the measured μ values at different NaHCO_3 concentrations), and e is the elementary electron charge.

In equation 3.S2, K_B is Boltzmann's constant, T is absolute temperature, n is electrolyte bulk concentration (m^{-3}), z is the valence of a symmetrical electrolyte, which is 1 for a 1:1 electrolyte such as NaHCO_3 used in this study.

In equation 3.S5, κ is Debye-Hückel parameter of the solution, which is dependent on ion strength, determined in equation 3.S6. I is ionic strength of the electrolyte, M is the ionic species in the electrolyte, n_i is the bulk concentration of each species and z_i is the valence of each species.

All parameters obtained from equations 3.S2 to S6 would be employed into equation 3.S1 to fit the measured μ values in each run and to give N and λ values. A Matlab (the Mathworks, Novi, MI) code employing iterative least squares minimization was used for calculations.

After getting the N value, the electrostatic potential between two particles can be calculated by the following equation:

$$U_{electrostatic}(h) = \frac{1}{\epsilon_r \epsilon_0 \kappa^4} \left(\frac{\pi a_1 a_2}{a_1 + a_2} \right) (Z_1 e N_1) (Z_2 e N_2) e^{-\kappa h} \quad (3.S7)$$

In equation 3.S7, a_1 and a_2 are the radiuses of particles, h is the separation distance between two particles. And for CMC-NZVI particles, only one kind of particles exists in each suspension. Thus Z_1 and Z_2 as well as N_1 and N_2 are the same.

2) DLVO calculations

The interaction energy of particle-particle calculated by extended DLVO theory takes into account repulsive electrostatic double layer energy, attractive van der Waals and magnetic energies as well as repulsive steric energy.

The electrostatic repulsion potential between two particles was estimated from equation 3.S7. The contribution of van der Waals force to the interaction between two particles was estimated using the equation described in Israelachvili's book [75]. The attraction interaction caused by magnetic forces between two particles was estimated from the equation in Rosensweig's book [76]. The contribution of repulsive steric force was inferred from the relative studies [59, 64, 77]. These three energies can be calculated by the following equations:

$$U_{sph-sph}^{vdW} = -\frac{A}{6h} \frac{a_1 a_2}{a_1 + a_2} \quad (3.S8)$$

A is Hamaker constant, set to be $1.5 \cdot 10^{-19}$ J for CMC-NZVI particles.

$$U_{mag} = -\frac{8\pi u_0 R^3 M_s^2}{9\left(\frac{h}{a} + 2\right)^3} \quad (3.S9)$$

u_0 , is the permeability of free space, which is $1.26 \times 10^{-6} \text{ m}^2 \cdot \text{kg} / \text{s}^2 \cdot \text{A}^2$ (A is Hamaker constant) for NZVI particle. M_s is the measured saturation magnetization for the iron nanoparticle, which is $1.5 \times 10^5 \text{ A/m}$ for NZVI particle.

$$F_{ES} = 2\pi \left(\frac{a_1 a_2}{a_1 + a_2} \right) \left(\frac{k_B T}{s^3} \right) \left\{ \frac{8l}{5} \left[\left(\frac{2l}{h} \right)^{5/4} - 1 \right] + \frac{8l}{7} \left[\left(\frac{h}{2l} \right)^{7/4} - 1 \right] \right\} \quad (3.S10)$$

$$U_{steric} = - \int_{\infty}^h F_{ST} dh \quad (3.S11)$$

where, s is the distance between polymer chains, which is set to be 2 nm, 5 nm and 6 nm for 700K CMC, 250K CMC and 90K CMC, respectively, l is the film thickness on particle surface, which is determined by TEM in this study.

Section S3. Polydispersed NZVI particles (DLS results) and the analysis of the grafted CMC on CMC-NZVI particles

- 1) Representative polydispersed NZVI particles size by DLS and optical microscopy measurements

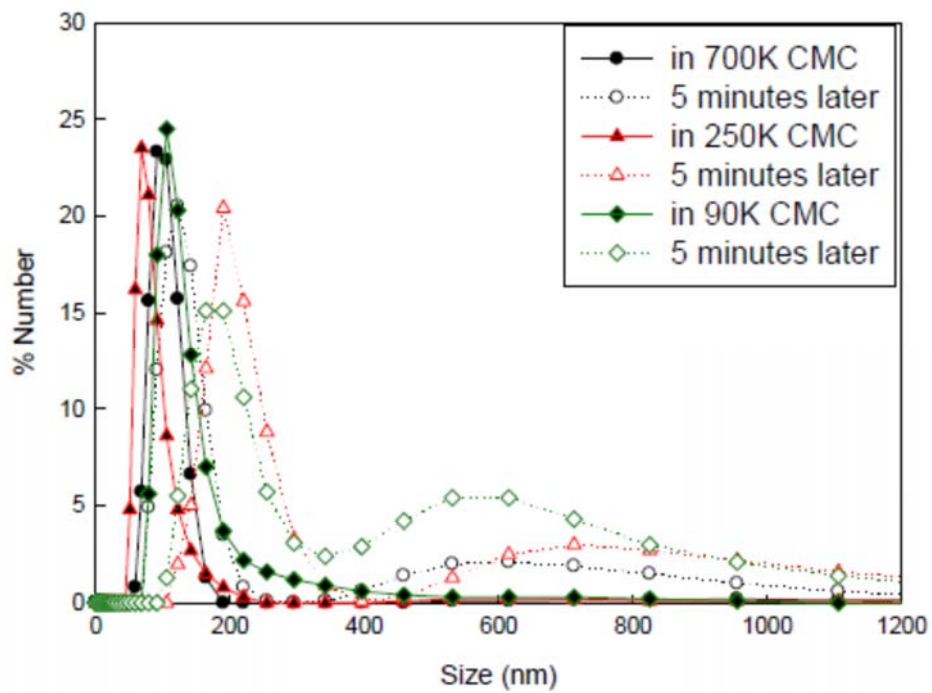


Figure 3.S1. The changes of particle size distribution of different CMC-NZVI particles with time.

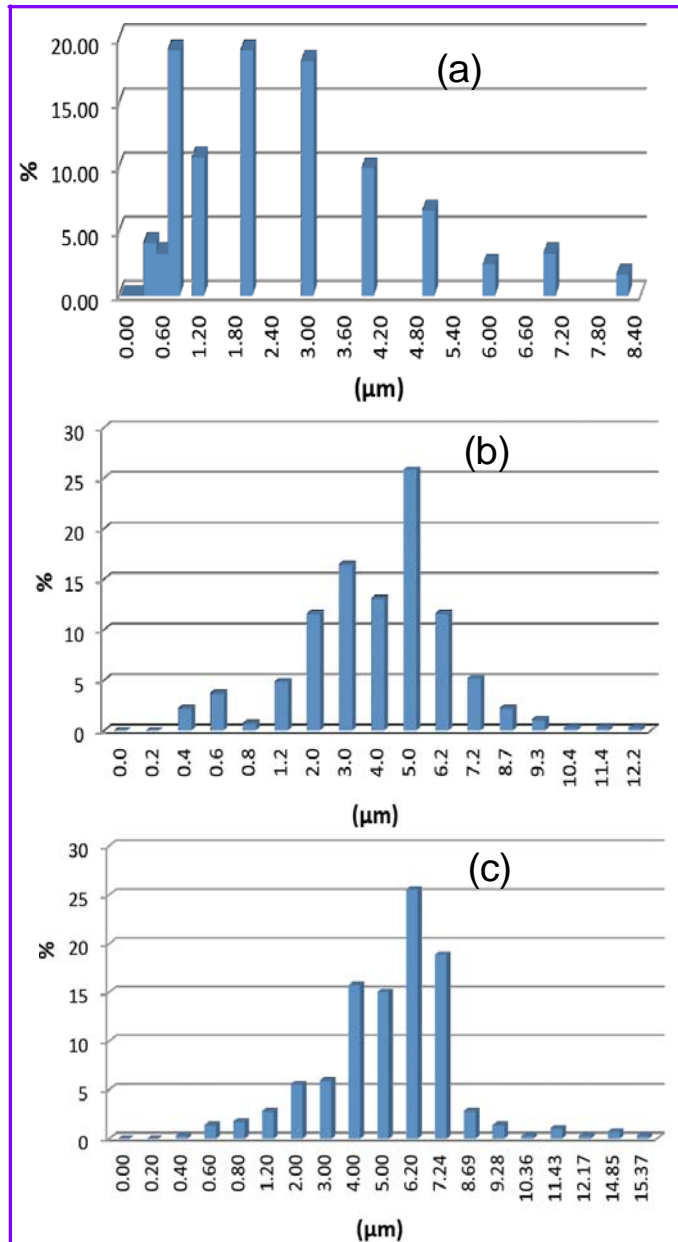


Figure 3.S2. Representatives of size distributions of different NZVI particles determined by optical microscopy, (a) 1 g/L NZVI in 1 g/L 700K CMC (3 mM Na⁺); (b) 1 g/L NZVI in 1 g/L 250K CMC (3 mM Na⁺); (c) 1 g/L NZVI in 1 g/L 90K CMC (3 mM Na⁺).

2) Elemental analysis results

Table 3.S1. CMC mass content of different CMC-NZVI particles.

Samples	C%	CMC content (%)
Pure 90K CMC	34.97	/
Pure 250K CMC	35.20	/
Pure 700K CMC	35.32	/
Bare NZVIr	0	0
1 g/L NZVI in 1 g/L 90K CMC with 0.5 Mm Na ⁺	0.6	1.616
1 g/L NZVI in 1 g/L 250K CMC with 0.5 Mm Na ⁺	0.57	1.719
1 g/L NZVI in 1 g/L 700K CMC with 0.5 Mm Na ⁺	0.63	1.784
1 g/L NZVI in 1 g/L 700K CMC with 7.5 Mm Na ⁺	0.55	1.56
1 g/L NZVI in 1 g/L 700K CMC with 0.5 Mm Na ⁺ (washed)	0.45	1.274

3) Layer thickness measurements by TEM

Table 3.S2. Layer thickness of different CMC-NZVI particles determined by TEM measurement.

Sample	Layer thickness (nm)
90K CMC-NZVI	4.9
250K CMC-NZVI	6.3
700K CMC-NZVI (unwashed)	8.0
700K CMC-NZVI (washed)	5.4

As expected, 700K CMC-NZVI particles had the highest layer thickness (8.0 nm) among these three types of CMC-NZVI particles. And even after removing free CMC, washed 700K CMC-NZVI particles still had quite high layer thickness (5.4 nm). The interaction energy between particle and collector takes into account of electrostatic energy and Van de Waals energy.

- 4) The characterization results of different CMC-NZVI particles by NTA and the corresponding CFT theory calculation results

Section S4. New Ohshima theory calculation results

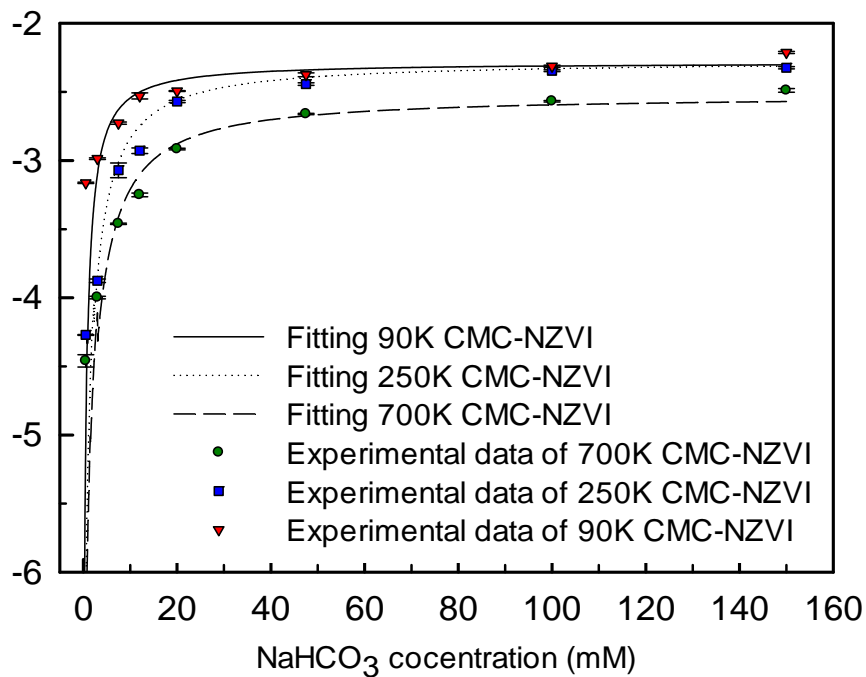


Figure 3.S3. Electrophoretic mobility of different CMC grafted NZVI particles as a function of NaHCO₃ concentration. The surface charge densities (N/m^3) and the softness (λ) of different CMC-NZVI particles were 2.923 and 9.0 (90K CMC-NZVI), 6.538 and 6.0 (250K CMC-NZVI) and 7.769 and 5.8 (700K CMC-NZVI) obtained from the fittings.

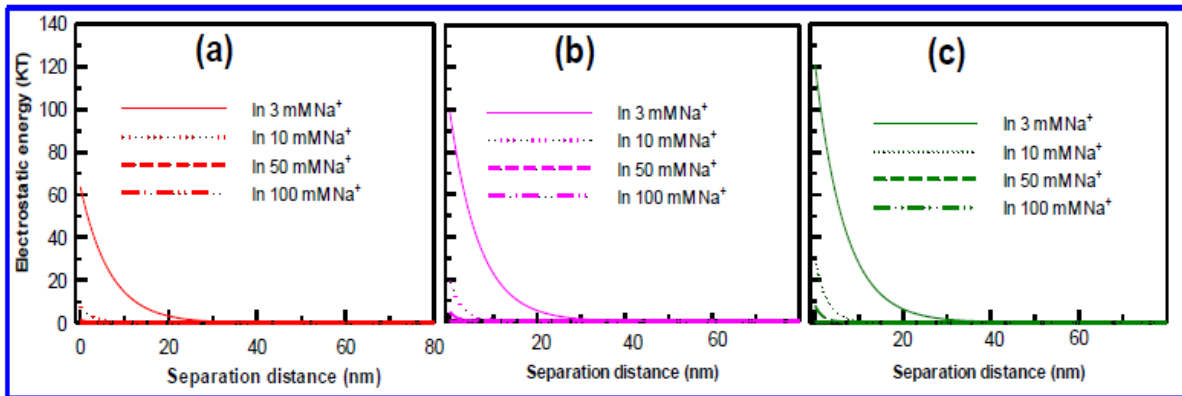


Figure 3.S4. The electrostatic interaction energy of different CMC-NZVI particles in NaHCO₃ solutions (with varied concentrations) calculated from equation (3.S7) and N values obtained in Figure 3.S3. (a) 90K CMC-NZVI; (b) 250K CMC-NZVI; (c) 700K CMC-NZVI.

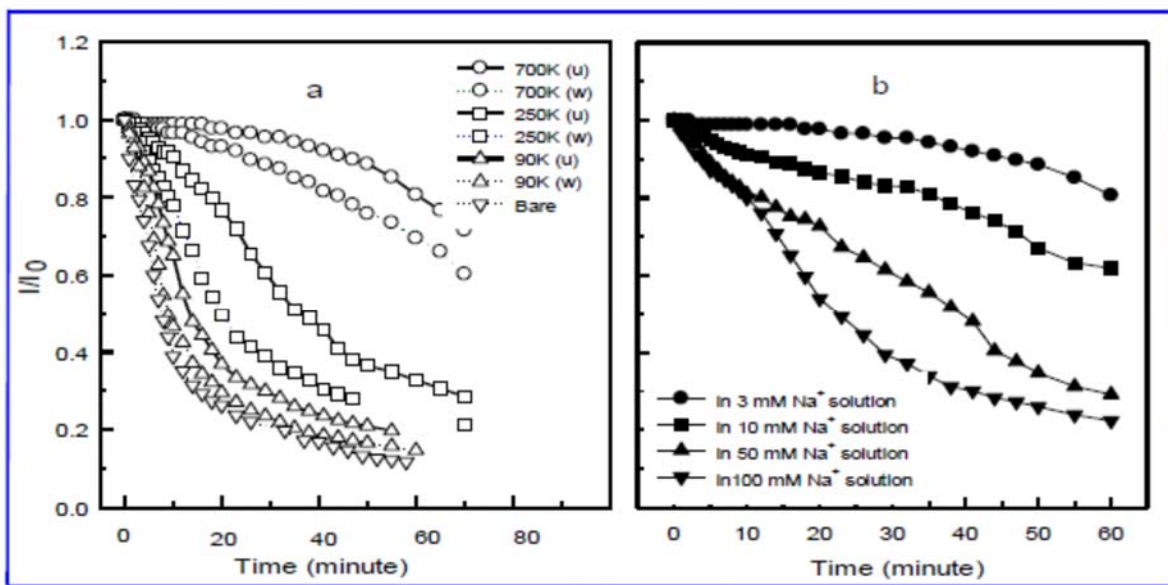


Figure 3.S5. Sedimentation results (a) the effects of different CMC and washing on the sedimentation rate of NZVI particles (all samples were prepared with 3 mM NaHCO₃); (b) the effect of NaHCO₃ concentration on sedimentation rate of 700K CMC-NZVI.

The stabilities of all these three types of CMC-NZVI particles (washed and unwashed) were higher than that of bare particles (results shown in Figure 3.S5a). 700K CMC-NZVI

displayed the highest stability (approximately 80% of particles remained in suspension after 60 min). In comparison 250K CMC-NZVI and 90K CMC-NZVI improved the stability of NZVI particles only slightly with 35% and 25%, respectively, of particles remaining in suspension over the same time period). This result differs from the observations reported in an earlier study [31], in that a smaller difference of stability of 700K CMC- and 90K CMC-NZVI particles was observed. The smaller difference could be explained by the fact that a smaller ratio of CMC mass concentration to NZVI concentration (1:3) was used in that study [31] compared to the 1:1 ratio employed here. A smaller difference of stability between 700K CMC- and 90K CMC-NZVI observed in another study [33], may be due to very low NZVI concentration used (0.1 g/L) for the sedimentation experiment.

Additionally, the stabilities of all three unwashed CMC-NZVI suspensions are higher than the corresponding washed suspension, attributing to the effect of free CMC on preventing particles to contact each other. This is consistent with the observation of Tiraferri et al that the increase of guar gum concentration would be more effective on stabilizing NZVI particles [78]. Also, Kocur et al found that 2.5 g/L NZVI particles in 0.8% wt 250K CMC was much more stable than 0.1 g/L NZVI particles in 0.2% wt 250K CMC [57]. Nevertheless, an opposite result that washed NZVI particles were more stable than unwashed particles was reported by Cirtiu et al. [79]. This was interpreted by flocculation effect of free CMC in the suspension. However in that study, CMC were pre-grafted to the particles.

In Figure 3.S5b, one can observe that the sedimentation rate of 700K CMC-NZVI increased with the rise of the NaHCO_3 concentration. This result can be attributed to the significantly reduction in EDL repulsion between particles with the increase of ionic strength due to charge screen, resulting in higher aggregation of the NZVI particles [78, 80]. This

interpretation is proved by the electrophoretic mobility results shown in Figure 3.S3, in which the negative relationship with the absolute value of electrophoretic mobility value with the IS was displayed.

References

- [1] X.-q. Li, D.W. Elliott, W.-x. Zhang, Zero-valent iron nanoparticles for abatement of environmental pollutants: materials and engineering aspects, *Critical Reviews in Solid State and Materials Sciences*, 31 (2006) 111-122.
- [2] B. Karn, T. Kuiken, M. Otto, Nanotechnology and in situ remediation: a review of the benefits and potential risks, *Environmental health perspectives*, 117 (2009) 1813.
- [3] P. Bennett, F. He, D. Zhao, B. Aiken, L. Feldman, In situ testing of metallic iron nanoparticle mobility and reactivity in a shallow granular aquifer, *Journal of contaminant hydrology*, 116 (2010) 35-46.
- [4] S.R. Kanel, J.-M. Greneche, H. Choi, Arsenic (V) removal from groundwater using nano scale zero-valent iron as a colloidal reactive barrier material, *Environmental Science & Technology*, 40 (2006) 2045-2050.
- [5] W.x. Zhang, D.W. Elliott, Applications of iron nanoparticles for groundwater remediation, *Remediation Journal*, 16 (2006) 7-21.
- [6] J. Quinn, D. Elliott, S. O'Hara, A. Billow, Use of nanoscale iron and bimetallic particles for environmental remediation: A review of field-scale applications, *Environmental applications of nanoscale and microscale reactive metal particles*, Copyright, (2009) 263-285.
- [7] C. Su, R.W. Puls, T.A. Krug, M.T. Watling, S.K. O'Hara, J.W. Quinn, N.E. Ruiz, A two and half year-performance evaluation of a field test on treatment of source zone tetrachloroethene and its chlorinated daughter products using emulsified zero valent iron nanoparticles, *water research*, (2012).
- [8] H.-L. Lien, W.-x. Zhang, Hydrodechlorination of chlorinated ethanes by nanoscale Pd/Fe bimetallic particles, *Journal of environmental engineering*, 131 (2005) 4-10.
- [9] Y. Wang, D. Zhou, Y. Wang, L. Wang, L. Cang, Automatic pH control system enhances the dechlorination of 2, 4, 4'-trichlorobiphenyl and extracted PCBs from contaminated soil by nanoscale Fe⁰ and Pd/Fe⁰, *Environmental Science and Pollution Research*, 19 (2012) 448-457.
- [10] J.-H. Kim, P.G. Tratnyek, Y.-S. Chang, Rapid dechlorination of polychlorinated dibenzo-p-dioxins by bimetallic and nanosized zerovalent iron, *Environmental science & technology*, 42 (2008) 4106-4112.
- [11] Y.M. Kim, K. Murugesan, Y.Y. Chang, E.J. Kim, Y.S. Chang, Degradation of polybrominated diphenyl ethers by a sequential treatment with nanoscale zero valent iron and aerobic biodegradation, *Journal of Chemical Technology and Biotechnology*, 87 (2012) 216-224.
- [12] Y. Zhuang, S. Ahn, R.G. Luthy, Debromination of polybrominated diphenyl ethers by nanoscale zerovalent iron: pathways, kinetics, and reactivity, *Environmental science & technology*, 44 (2010) 8236-8242.
- [13] W. Yan, R. Vasic, A.I. Frenkel, B.E. Koel, Intraparticle reduction of arsenite (As (III)) by nanoscale zerovalent iron (nZVI) investigated with in situ X-ray absorption spectroscopy, *Environmental science & technology*, 46 (2012) 7018-7026.

- [14] D.W. Elliott, H.-L. Lien, W.-x. Zhang, Zerovalent iron nanoparticles for treatment of ground water contaminated by hexachlorocyclohexanes, *Journal of environmental quality*, 37 (2008) 2192-2201.
- [15] T. Raychoudhury, N. Tufenkji, S. Ghoshal, Aggregation and deposition kinetics of carboxymethyl cellulose-modified zero-valent iron nanoparticles in porous media, *Water research*, 46 (2012) 1735-1744.
- [16] T. Phenrat, H.-J. Kim, F. Fagerlund, T. Illangasekare, R.D. Tilton, G.V. Lowry, Particle Size Distribution, Concentration, and Magnetic Attraction Affect Transport of Polymer-Modified Fe₀ Nanoparticles in Sand Columns, *Environmental Science & Technology*, 43 (2009) 5079-5085.
- [17] P.G. Tratnyek, R.L. Johnson, Nanotechnologies for environmental cleanup, *Nano Today*, 1 (2006) 44-48.
- [18] S.O. Hara, T. Krug, J. Quinn, C. Clausen, C. Geiger, Field and laboratory evaluation of the treatment of DNAPL source zones using emulsified zero-valent iron, *Remediation Journal*, 16 (2006) 35-56.
- [19] G.C. Yang, Y.-I. Chang, Integration of emulsified nanoiron injection with the electrokinetic process for remediation of trichloroethylene in saturated soil, *Separation and Purification Technology*, 79 (2011) 278-284.
- [20] J. Quinn, C. Geiger, C. Clausen, K. Brooks, C. Coon, S. O'Hara, T. Krug, D. Major, W.-S. Yoon, A. Gavaskar, T. Holdsworth, Field Demonstration of DNAPL Dehalogenation Using Emulsified Zero-Valent Iron, *Environmental Science & Technology*, 39 (2005) 1309-1318.
- [21] H. Choi, S.R. Al-Abed, S. Agarwal, Effects of aging and oxidation of palladized iron embedded in activated carbon on the dechlorination of 2-chlorobiphenyl, *Environmental science & technology*, 43 (2009) 4137-4142.
- [22] J. Zhan, B. Sunkara, L. Le, V.T. John, J. He, G.L. McPherson, G. Piringer, Y. Lu, Multifunctional Colloidal Particles for in Situ Remediation of Chlorinated Hydrocarbons, *Environmental Science & Technology*, 43 (2009) 8616-8621.
- [23] T. Phenrat, A. Cihan, H.-J. Kim, M. Mital, T. Illangasekare, G.V. Lowry, Transport and Deposition of Polymer-Modified Fe₀ Nanoparticles in 2-D Heterogeneous Porous Media: Effects of Particle Concentration, Fe₀ Content, and Coatings, *Environmental Science & Technology*, 44 (2010) 9086-9093.
- [24] A. Tiraferri, R. Sethi, Enhanced transport of zerovalent iron nanoparticles in saturated porous media by guar gum, *Journal of Nanoparticle Research*, 11 (2009) 635-645.
- [25] F. He, M. Zhang, T. Qian, D. Zhao, Transport of carboxymethyl cellulose stabilized iron nanoparticles in porous media: Column experiments and modeling, *Journal of Colloid and Interface Science*, 334 (2009) 96-102.
- [26] N. Saleh, K. Sirk, Y. Liu, T. Phenrat, B. Dufour, K. Matyjaszewski, R.D. Tilton, G.V. Lowry, Surface modifications enhance nanoiron transport and NAPL targeting in saturated porous media, *Environmental Engineering Science*, 24 (2007) 45-57.
- [27] J. Fatisson, S. Ghoshal, N. Tufenkji, Deposition of Carboxymethylcellulose-Coated Zero-Valent Iron Nanoparticles onto Silica: Roles of Solution Chemistry and Organic Molecules, *Langmuir*, 26 (2010) 12832-12840.
- [28] T. Raychoudhury, G. Naja, S. Ghoshal, Assessment of transport of two polyelectrolyte-stabilized zero-valent iron nanoparticles in porous media, *Journal of contaminant hydrology*, 118 (2010) 143-151.
- [29] P. Jiemvarangkul, W.-x. Zhang, H.-L. Lien, Enhanced transport of polyelectrolyte stabilized nanoscale zero-valent iron (nZVI) in porous media, *Chemical Engineering Journal*, 170 (2011) 482-491.
- [30] N. Sakulchaicharoen, D.M. O'Carroll, J.E. Herrera, Enhanced stability and dechlorination activity of pre-synthesis stabilized nanoscale FePd particles, *Journal of contaminant hydrology*, 118 (2010) 117-127.

- [31] T. Phenrat, N. Saleh, K. Sirk, H.-J. Kim, R. Tilton, G. Lowry, Stabilization of aqueous nanoscale zerovalent iron dispersions by anionic polyelectrolytes: adsorbed anionic polyelectrolyte layer properties and their effect on aggregation and sedimentation, *Journal of Nanoparticle Research*, 10 (2008) 795-814.
- [32] P. Jiemvarangkul, W.-x. Zhang, H.-L. Lien, Enhanced transport of polyelectrolyte stabilized nanoscale zero-valent iron (nZVI) in porous media, *Chemical Engineering Journal*, In Press, Corrected Proof.
- [33] T. Phenrat, Effect of polymeric surface modification on nano-sized zerovalent iron (NZVI) aggregation, transport of concentrated NZVI dispersions in porous media, and reactivity, (2008) 535.
- [34] N. Saleh, K. Sirk, Y. Liu, T. Phenrat, B. Dufour, K. Matyjaszewski, R.D. Tilton, G.V. Lowry, Surface Modifications Enhance Nanoiron Transport and NAPL Targeting in Saturated Porous Media *Environmental Engineering Science*, 24 (2007) 45-57.
- [35] G. Fritz, V. Schädler, N. Willenbacher, N.J. Wagner, Electrosteric Stabilization of Colloidal Dispersions, *Langmuir*, 18 (2002) 6381-6390.
- [36] B.W. Hydutsky, E.J. Mack, B.B. Beckerman, J.M. Skluzacek, T.E. Mallouk, Optimization of Nano- and Microiron Transport through Sand Columns Using Polyelectrolyte Mixtures, *Environmental Science & Technology*, 41 (2007) 6418-6424.
- [37] T. Phenrat, Lowry GV, Physicochemistry of Polyelectrolyte Coatings that Increase Stability, Mobility, and Contaminant Specificity of Reactive Nanoparticles Used for Groundwater, (2008) 15.
- [38] F. He, D. Zhao, Manipulating the Size and Dispersibility of Zerovalent Iron Nanoparticles by Use of Carboxymethyl Cellulose Stabilizers, *Environmental Science & Technology*, 41 (2007) 6216-6221.
- [39] F. He, D. Zhao, J. Liu, C.B. Roberts, Stabilization of Fe–Pd Nanoparticles with Sodium Carboxymethyl Cellulose for Enhanced Transport and Dechlorination of Trichloroethylene in Soil and Groundwater, *Industrial & Engineering Chemistry Research*, 46 (2006) 29-34.
- [40] C.W. Hoogendam, A. de Keizer, M.A. Cohen Stuart, B.H. Bijsterbosch, J.G. Batelaan, P.M. van der Horst, Adsorption Mechanisms of Carboxymethyl Cellulose on Mineral Surfaces, *Langmuir*, 14 (1998) 3825-3839.
- [41] C.M. Cirtiu, T. Raychoudhury, S. Ghoshal, A. Moores, Systematic comparison of the size, surface characteristics and colloidal stability of zero valent iron nanoparticles pre-and post-grafted with common polymers, *Colloids and Surfaces A: Physicochemical and Engineering Aspects*, 390 (2011) 95-104.
- [42] T. Phenrat, H.-J. Kim, F. Fagerlund, T. Illangasekare, G.V. Lowry, Empirical correlations to estimate agglomerate size and deposition during injection of a polyelectrolyte-modified Fe₀ nanoparticle at high particle concentration in saturated sand, *Journal of Contaminant Hydrology*, 118 (2010) 152-164.
- [43] H.-J. Kim, T. Phenrat, R.D. Tilton, G.V. Lowry, Fe₀ nanoparticles remain mobile in porous media after aging due to slow desorption of polymeric surface modifiers, *Environmental science & technology*, 43 (2009) 3824-3830.
- [44] R.L. Johnson, J.T. Nurmi, G.S. O'Brien Johnson, D. Fan, R.L. O'Brien Johnson, Z. Shi, A.J. Salter-Blanc, P.G. Tratnyek, G.V. Lowry, Field-scale transport and transformation of carboxymethylcellulose-stabilized nano zero-valent iron, *Environmental science & technology*, 47 (2013) 1573-1580.
- [45] C.M. Kocur, D.M. O'Carroll, B.E. Sleep, Impact of nZVI stability on mobility in porous media, *Journal of contaminant hydrology*, (2012).
- [46] T. Phenrat, N. Saleh, K. Sirk, H.-J. Kim, R.D. Tilton, G.V. Lowry, Stabilization of aqueous nanoscale zerovalent iron dispersions by anionic polyelectrolytes: adsorbed anionic polyelectrolyte layer properties and their effect on aggregation and sedimentation, *Journal of Nanoparticle Research*, 10 (2008) 795-814.

- [47] T. Phenrat, Y. Liu, R.D. Tilton, G.V. Lowry, Adsorbed Polyelectrolyte Coatings Decrease Fe⁰ Nanoparticle Reactivity with TCE in Water: Conceptual Model and Mechanisms, *Environmental Science & Technology*, 43 (2009) 1507-1514.
- [48] H. Murakami, Y. Kawashima, T. Niwa, T. Hino, H. Takeuchi, M. Kobayashi, Influence of the degrees of hydrolyzation and polymerization of poly(vinylalcohol) on the preparation and properties of poly(-lactide-co-glycolide) nanoparticle, *International Journal of Pharmaceutics*, 149 (1997) 43-49.
- [49] N. Sakulchaicharoen, D.M. O'Carroll, J.E. Herrera, Enhanced stability and dechlorination activity of pre-synthesis stabilized nanoscale FePd particles, *Journal of Contaminant Hydrology*, 118 (2010) 117-127.
- [50] M.J. Truex, V.R. Vermeul, D.P. Mendoza, B.G. Fritz, R.D. Mackley, M. Oostrom, T.W. Wietsma, T.W. Macbeth, Injection of Zero-Valent Iron into an Unconfined Aquifer Using Shear-Thinning Fluids, *Ground Water Monitoring & Remediation*, 31 (2011) 50-58.
- [51] K.J. Cantrell, D.I. Kaplan, T.J. Gilmore, INJECTION OF COLLOIDAL FEO PARTICLES IN SAND WITH SHEAR-THINNING FLUIDS, *Journal of Environmental Engineering*, 123 (1997) 786-791.
- [52] S. Comba, R. Sethi, Stabilization of highly concentrated suspensions of iron nanoparticles using shear-thinning gels of xanthan gum, *Water Research*, 43 (2009) 3717-3726.
- [53] R.L. Johnson, J.T. Nurmi, G.S. O'Brien Johnson, D. Fan, R.L. O'Brien Johnson, Z. Shi, A.J. Salter-Blanc, P.G. Tratnyek, G.V. Lowry, Field-Scale Transport and Transformation of Carboxymethylcellulose-Stabilized Nano Zero-Valent Iron, *Environmental Science & Technology*, (2013).
- [54] O. Hiroyuki, Theory of electrostatics and electrokinetics of soft particles, *Science and Technology of Advanced Materials*, 10 (2009) 063001.
- [55] V. Filipe, A. Hawe, W. Jiskoot, Critical evaluation of Nanoparticle Tracking Analysis (NTA) by NanoSight for the measurement of nanoparticles and protein aggregates, *Pharmaceutical research*, 27 (2010) 796-810.
- [56] D. Dickson, G. Liu, C. Li, G. Tachiev, Y. Cai, Dispersion and stability of bare hematite nanoparticles: Effect of dispersion tools, nanoparticle concentration, humic acid and ionic strength, *Science of The Total Environment*, 419 (2012) 170-177.
- [57] C.M. Kocur, D.M. O'Carroll, B.E. Sleep, Impact of nZVI stability on mobility in porous media, *Journal of Contaminant Hydrology*, 145 (2013) 17-25.
- [58] T. Phenrat, N. Saleh, K. Sirk, R.D. Tilton, G.V. Lowry, Aggregation and Sedimentation of Aqueous Nanoscale Zerovalent Iron Dispersions, *Environmental Science & Technology*, 41 (2006) 284-290.
- [59] A.R. Petosa, D.P. Jaisi, I.R. Quevedo, M. Elimelech, N. Tufenkji, Aggregation and Deposition of Engineered Nanomaterials in Aquatic Environments: Role of Physicochemical Interactions, *Environmental Science & Technology*, 44 (2010) 6532-6549.
- [60] R.F. Domingos, M.A. Baalousha, Y. Ju-Nam, M.M. Reid, N. Tufenkji, J.R. Lead, G.G. Leppard, K.J. Wilkinson, Characterizing manufactured nanoparticles in the environment: multimethod determination of particle sizes, *Environmental science & technology*, 43 (2009) 7277-7284.
- [61] T. Phenrat, H.-J. Kim, F. Fagerlund, T. Illangasekare, G.V. Lowry, Empirical correlations to estimate agglomerate size and deposition during injection of a polyelectrolyte-modified Fe⁰ nanoparticle at high particle concentration in saturated sand, *Journal of contaminant hydrology*, 118 (2010) 152-164.
- [62] S. Comba, D. Dalmazzo, E. Santagata, R. Sethi, Rheological characterization of xanthan suspensions of nanoscale iron for injection in porous media, *Journal of Hazardous Materials*, 185 (2011) 598-605.

- [63] W.F. Reed, S. Ghosh, G. Medjahdi, J. Francois, Dependence of polyelectrolyte apparent persistence lengths, viscosity, and diffusion on ionic strength and linear charge density, *Macromolecules*, 24 (1991) 6189-6198.
- [64] T.L. Byrd, J.Y. Walz, Interaction Force Profiles between *Cryptosporidium parvum* Oocysts and Silica Surfaces, *Environmental Science & Technology*, 39 (2005) 9574-9582.
- [65] E.D. Vecchia, M. Luna, R. Sethi, Transport in Porous Media of Highly Concentrated Iron Micro- and Nanoparticles in the Presence of Xanthan Gum, *Environmental Science & Technology*, 43 (2009) 8942-8947.
- [66] S.M. Hosseini, T. Tosco, Transport and retention of high concentrated nano-Fe/Cu particles through highly flow-rated packed sand column, *Water Research*, 47 (2013) 326-338.
- [67] T. Tosco, J. Bosch, R.U. Meckenstock, R. Sethi, Transport of ferrihydrite nanoparticles in saturated porous media: role of ionic strength and flow rate, *Environmental science & technology*, 46 (2012) 4008-4015.
- [68] B. Schrick, B.W. Hydutsky, J.L. Blough, T.E. Mallouk, Delivery Vehicles for Zerovalent Metal Nanoparticles in Soil and Groundwater, *Chemistry of Materials*, 16 (2004) 2187-2193.
- [69] H.F. Lecoanet, J.-Y. Bottero, M.R. Wiesner, Laboratory Assessment of the Mobility of Nanomaterials in Porous Media, *Environmental Science & Technology*, 38 (2004) 5164-5169.
- [70] N. Tufenkji, M. Elimelech, Correlation Equation for Predicting Single-Collector Efficiency in Physicochemical Filtration in Saturated Porous Media, *Environmental Science & Technology*, 38 (2003) 529-536.
- [71] G.C.C. Yang, H.-C. Tu, C.-H. Hung, Stability of nanoiron slurries and their transport in the subsurface environment, *Separation and Purification Technology*, 58 (2007) 166-172.
- [72] M.M. Krol, A.J. Oleniuk, C.M. Kocur, B.E. Sleep, P. Bennett, Z. Xiong, D.M. O'Carroll, A Field-Validated Model for In Situ Transport of Polymer-Stabilized nZVI and Implications for Subsurface Injection, *Environmental Science & Technology*, 47 (2013) 7332-7340.
- [73] C. Shen, Y. Huang, B. Li, Y. Jin, Predicting attachment efficiency of colloid deposition under unfavorable attachment conditions, *Water Resour. Res.*, 46 (2010) W11526.
- [74] A.J. Pelley, N. Tufenkji, Effect of particle size and natural organic matter on the migration of nano- and microscale latex particles in saturated porous media, *Journal of Colloid and Interface Science*, 321 (2008) 74-83.
- [75] J.N. Israelachvili, *Intermolecular and Surface Forces*, Second Edition: With Applications to Colloidal and Biological Systems. 2nd ed, Academic Press, 1992.
- [76] R.E. Rosensweig, *Ferrohydrodynamics*, Cambridge University Press, New York, 1985.
- [77] d.G. P.G, *Polymers at an interface; a simplified view*, *Advances in Colloid and Interface Science*, 27 (1987) 189-209.
- [78] A. Tiraferri, K.L. Chen, R. Sethi, M. Elimelech, Reduced aggregation and sedimentation of zero-valent iron nanoparticles in the presence of guar gum, *Journal of colloid and interface science*, 324 (2008) 71-79.
- [79] C.M. Cirtiu, T. Raychoudhury, S. Ghoshal, A. Moores, Systematic comparison of the size, surface characteristics and colloidal stability of zero valent iron nanoparticles pre- and post-grafted with common polymers, *Colloids and Surfaces A: Physicochemical and Engineering Aspects*, 390 (2011) 95-104.
- [80] K.M. Sirk, N.B. Saleh, T. Phenrat, H.-J. Kim, B. Dufour, J. Ok, P.L. Golas, K. Matyjaszewski, G.V. Lowry, R.D. Tilton, Effect of Adsorbed Polyelectrolytes on Nanoscale Zero Valent Iron Particle Attachment to Soil Surface Models, *Environmental Science & Technology*, 43 (2009) 3803-3808.

Chapter 4

Comparison of Transport of Nanoscale Zero Valent Iron Nanoparticles under Vertical and Horizontal Flow

by

Jing Li, Subhasis Ghoshal*

Department of Civil Engineering,

McGill University, Montreal, Canada H3A 2K6

Keywords: NZVI particles, colloid transport, viscosity, carboxymethyl cellulose,
DLVO theory calculations, single collector efficiency prediction, ionic strength

*Corresponding author, Department of Civil Engineering, McGill University, 817
Sherbrooke Street West, Montreal, QC, Canada H3A 2K6, e-mail:

subhasis.ghoshal@mcgill.ca,

Tel: (514) 398-6867, Fax: (514) 398-7361

To be published on Water research

4.1 Introduction

Nanoscale zero valent iron (NZVI) particles have been proposed as a promising reactive agent for remediation of sites contaminated by chlorinated organic compounds and heavy metals [1-3]. Several small field-scale site demonstrations have suggested that NZVI can effectively eliminate significant mass of chlorinated solvent compounds following their injection in the subsurface contaminated zones [4, 5].

However, challenges exist in the delivery and transport of NZVI to subsurface contaminated zones. NZVI particles are magnetic and the attractive magnetic forces lead to the formation of aggregates, in sizes up to several microns [6, 7]. When aggregated, NZVI have limited transport in subsurface porous media because of extensive physicochemical filtration. Inadequate remediation may occur due to limited transport and this is recognized as a significant challenge in large-scale field applications of NZVI particles [3, 8-10]. When NZVI are coated with stabilizing polymers or polyelectrolytes, the extent of aggregation is reduced due to the steric and electrostatic forces imparted by the adsorbed polymers on the NZVI surface [11, 12]. However, although polymers and polyelectrolytes can reduce the extent of aggregation and thereby significantly facilitate NZVI transport [13, 14], aggregation cannot be completely prevented, especially at higher concentrations where the frequencies of collisions between NZVI particles are higher [11].

The transport efficiency of the polyelectrolyte modified NZVI particles in field applications has been found to be significantly lower than that obtained in laboratory studies [15, 16]. The overall recoveries of CMC NZVI particles were only 2.6%, 21% and 31% at different sand layers at a 4 m×4 m small scale field and experiment, and the corresponding attachment

efficiencies were 0.01, 0.06 and 0.06 at the flow velocity of 1.5 m/d [17]. However, Vecchia et al observed that 1 to 3 μm ZVI and 70 nm NZVI suspended in xanthan gum had the transport efficiency higher than 88% through a 0.46 m column [18]. Several reasons may account for this declined transport efficiency of NZVI particles in field application [17]: (i) the solution chemistry of the groundwater tends to differ from those of simple electrolyte solution chemistry used in the laboratories; (ii) natural soil grains in field often have uneven surfaces and non-uniform charge distributions, unlike those clean, uniform surface sand grains used in laboratories [19]; (iii) field heterogeneities and preferential pathways could exist in the field, which could undermine the overall transport of NZVI particles to targeted zones [20]; and NZVI particle concentrations required in field application are higher than those used in laboratories [10, 21]. Another reason contributing to the different extents of NZVI transport in laboratory versus field studies is the effects of flow direction on particle deposition: laboratory studies on NZVI transport are typically conducted in packed columns subjected to vertical downward flow [11-13, 22] but in field studies the primary transport from a well head is in the horizontal flow direction [10, 23, 24]. Kanel et al [25] conducted a study where the transport of NZVI injected horizontally from an inlet point into a 2-D tank was investigated. Under horizontal flow, NZVI particles migrated both in the horizontal and vertical directions, and the vertical migration was attributable to the density gradients between the 4 g/L NZVI suspension (1.030 g/cm^3 to 1.036 g/cm^3) and the aqueous medium in which they were transported [26]. It is likely that gravitational settling can influence NZVI transport under the horizontal flow mode, especially for larger (higher mass) particles. Phenrat et al also conducted various polyelectrolytes modified NZVI particles transport in a 2-D tank [27]. Those authors observed that NZVI particles were

more prone to transport through the coarse sand (layered on the bottom of the tank) rather than the fine sand (intermediate layer) and the intermediate sand (top layer).

The objective of this study is to systematically compare the effects of vertical and horizontal flow on the transport and deposition of NZVI particles in model granular subsurface media. An associated objective was to analyze the role of gravity settling on transport of NZVI in the horizontal and vertical directions. The transport of NZVI particles was studied in columns operated either with vertical flow or with horizontal flow. Columns were packed with either coarse sand (average diameter of 1140 μm), intermediate sand (340 μm) or fine sand (180 μm); and the effects of NZVI concentrations (0.3 g/L, 1 g/L and 3 g/L) on the extent of transport in under vertical and horizontal flow were compared. Various grain sizes were examined to assess how shear flow conditions affected transport. Various NZVI concentrations were evaluated because particle concentrations influence the extent of aggregation, and the size of aggregates would directly be influence the extent of gravity settling. NZVI particles were characterized [28] for size by dynamic light scattering (DLS) and microscopy as well as for Zeta potential by laser Doppler velocimetry. Theoretical trajectory analysis of particle transport around a collector under vertical and horizontal flow modes was conducted to estimate the impact of particle size and density on the rate of collision between the particle and the collector.

4.2 Materials and methods

1) Chemicals. Carboxymethyl cellulose (Sigma Aldrich) with a molecular weight of 700000 Da (700K CMC) and a degree of substitution (D.S.) of 0.9 was used as the polyelectrolyte for coating NZVI particles for improved colloidal stability and transport. Sodium bicarbonate (analytical grade, Fisher Scientific) was used for preparing background electrolyte solutions.

2) Silica sands. Silica sands (Unimin corp., WI, USA) with average diameters 1140 μm (coarse sand), 340 μm (intermediate sand) and 180 μm (fine sand) respectively, were used as model porous media. Prior to being used, sands were washed in concentrated hydrochloric acid to remove mineral phases other than silica. After acid-washing, the sand was rinsed with deionized (DI) water and oven dried for 3 h at 550 $^{\circ}\text{C}$.

3) Preparation of Polymer-Coated NZVI. NZVI particles were provided by Golder Associates, Canada and had a typical structure of Fe^0 core and an outer shell composed of iron oxides, as determined with transmission electron microscopy and X-ray photoelectron spectroscopy. The NZVI suspension was stored under nitrogen as concentrated aqueous slurry (240 g/L), at a pH 9.3. A 30 g/L NZVI stock solution was prepared in a 3 mM NaHCO_3 solution and was sonicated for 20 minutes to separate NZVI aggregates formed during storage. NZVI particles in suspensions were post-grafted with CMC by mixing in a 1 g/L 700K CMC solution with 3 mM NaHCO_3 . The mixture of NZVI particles in CMC solution were shaken at 250 rpm for one hour to promote interactions between CMC molecules and NZVI particles. Finally, the coated NZVI (which were referred as 700K CMC-NZVI) particles were sonicated for another 20 minutes prior to use in sedimentation and transport experiments.

4) Physical characterization. The viscosities of 700K CMC solution and 700K CMC-NZVI suspensions with different concentrations were measured by a viscometer (Brookfield, LV DV-I+ with LV1 spindle) at 25 $^{\circ}\text{C}$ and 0.15/s. The diameters of primary NZVI particles were measured by TEM as described elsewhere [29]. The mean diameters of NZVI aggregates at different concentrations were characterized by optical microscopy (Olympus BX51). The measurement processes were as follows: a sample of latex particle with mean diameter of 200 nm (the diameter of 96% of particles ranged from 190 nm to 210 nm) was used as standard particles. The

standard particles were imaged in a microscope with bright field filter under the 100x objective as well as by phase contrast technique. Images were analyzed by ImageJ (totally around 2000 particles were analyzed) to provide the Fetet's diameter of 200 nm particle. Following the same process, NZVI suspensions with original concentrations (0.3 g/L, 1 g/L and 3 g/L) were directly imaged in the microscope to obtain the actual aggregates sizes at these concentrations. Two small drops of original suspensions were placed on glass slides and directly placed under microscope objective for measuring. The diameter of NZVI particles was also characterized by dynamic light scattering (DLS) after dilution to a concentration of 150 mg/L.

5) Sedimentation. The sedimentation rate of the CMC-NZVI particles was qualitatively assessed by measuring the absorbance at 508 nm by UV-Visible spectrophotometry of 0.3, 1 and 3 g Fe/L CMC NZVI suspensions over 210 minutes at 25 °C.

6) Column transport experiments. Transport studies were conducted in sand packed column. Columns were wet-packed and flushed with 15 pore volumes (PV) of 3 mM NaHCO₃ solution to obtain a uniform distribution of charge on the sand surface. The porosities of the coarse, intermediate and fine sands were 0.325, 0.341 and 0.37, respectively. The injection velocity of NZVI suspension was maintained at 0.508 cm/min with a peristaltic pump (Masterflex L/S, model 77200-12). In each run, around 8 PVs of 700K CMC-NZVI suspension was injected downwards into a vertical column during which the suspension was mixed evenly by a shaker at 280 rpm to minimize aggregation and sedimentation. Once the injection was complete, the column was flushed with 10 PV of the background electrolyte. The effluent was collected every 2 minutes by an automatic fraction collector (Spectrum Chromatography Inc). An aliquot of the effluent was digested in acidic mixture (H₂O: HCl: HNO₃=65:30:5, vol ratio) for 24 hrs and the total Fe was measured by flame atomic absorption spectrometry (Perkin Elmer, Flame-AAS

Analyst 100 AAS system). Identical experiments were conducted with the horizontal column with horizontal flow.

The transports of dissolved tracer in both vertical and horizontal columns were performed to inspect whether the flows in both columns were identical as expected from theoretical considerations. In tracer tests, 3 PV of 100 mg/L KNO₃ solution was injected at 0.508 cm/min into the column, followed by flushing DI water. The eluent was collected at the time interval of 3 minutes and the nitrate concentration was measured by UV-vis spectrophotometry (Pharmacia Biotech, Ultrospec 2000) at 220 nm wavelength.

The transport of latex colloids (commonly used model for environmental biocolloids) was evaluated in horizontal and vertical flow columns. Around 2.8 PVs of latex particle (mean diameter of 1 μm, Invitrogen) at the concentration of 1*10⁸/mL (dispersed in 3 mM NaHCO₃ solution) was injected into the column at the approach velocity of 0.508 cm/min (under the identical conditions as above). The elution samples were collected at 2 minutes interval and the concentrations were analyzed by using UV-spectroscope (Ultrospec 2000, Pharmacia Biotech).

The commonly accepted RT and TE models for single collector contact efficiency calculation were created based on simplifying the trajectory (R&T model) and calculating the numerical results of convective-diffusion equation (T&E model) of colloid particles to two dimensions [30, 31]. These simplification strategies are suitable for common colloid particles (such as latex particles, bacterial). The high densities of metal particles (such as NZVI particles) maybe, however, perform differently from common latex particles in transport through porous media. And Chung et al built a model to include the effect of gravity settling of colloid particles in filter theory [32]. The preliminary trajectory analysis of NZVI particles were conducted in two dimensions (for vertical flow model) and three dimensions (for horizontal flow model) to reveal

the effects of the density of NZVI particles on the single collector contact efficiency in vertical and horizontal column transports. The details about the scenarios on trajectory analysis in two dimensions (2-D) and three dimensions (3-D) were given in SI, Section 4.S1.

4.3 Results

4.3.1 NZVI aggregate size characterization

The mean primary particle size of NZVI as characterized by TEM was 75 nm. The mean diameter of the bare NZVI 1 g/L suspension was 15.9 μm . The size of 700K CMC-NZVI aggregates at 0.3, 1 and 3 g/L measured by microscopy are listed in Table 4.1, and the mean diameter of the aggregates in the resulting suspensions in 3 mM Na^+ solution were 3.13 μm , 2.12 μm and 1.76 μm , respectively. Several other studies have also reported that primary nanoparticles tended to aggregate into several microns [33-35], due to the strong magnetic attraction between NZVI particles [36, 37]. The particle size measured by DLS for the 1 g/L was 0.54 μm only. The discrepancy between optical microscopy and DLS measurements is because of disaggregation upon dilution to 150 mg/L, the maximum reliable measurement concentration, and as well due to settling off of large aggregates from the aqueous media during or prior to measurement.

Table 4.1. The diameter of NZVI aggregates as measured by conventional optical microscopy under different conditions.

Sample/Characterization method	NZVI concentration (mg/L)	700K CMC-NZVI	Bare NZVI	Number (or conc.) of particles measured
Average diameter of particles based on microscopy [38]	300	1760 \pm 176	/	2327
	1000	2220 \pm 384	15940 \pm 1247	1956
	3000	3130 \pm 611	/	2048
Average diameter of	300	352 \pm 82		150 mg/L

particles based on DLS	1000	540±118	/	150 mg/L
measurement (nm)	3000	1283±266	/	150 mg/L

The extent of aggregation as measured from particle size analysis was reflected in the sedimentation tests, shown in Figure 4.S3. The CMC-NZVI sedimentation rate was the slowest at the concentration of 0.3 g/L with approximately 63% of CMC-NZVI particles remaining in the suspension after 200 minutes), and was faster at higher concentrations with approximately 30% of particles remaining in solution for the 1 g/L suspension and only 20% of particles remaining in solution for the 3 g/L suspension over the same time period. The data is provided in Figure 4.S1. These results confirm the trends observed from the particle size assays that CMC-NZVI aggregation was more rapid at a higher NZVI concentrations and the trends are similar to that reported in a previous study [8].

4.3.2 Tracer tests

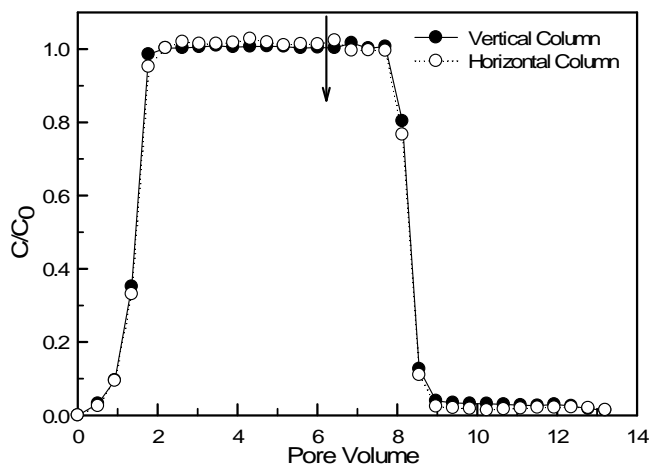


Figure 4.1. Breakthrough curves of nitrate through vertical and horizontal columns packed with coarse sand (average diameter 1140 μm).

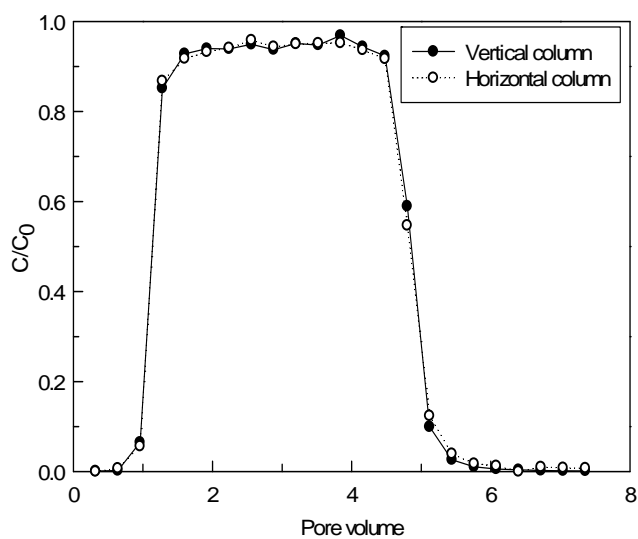


Figure 4.2. Breakthrough curves of latex particles (average diameter 1 μm) through vertical and horizontal columns packed with intermediate sand (average diameter 340 μm).

Prior to studying the transport of CMC-NZVI particles, the transport of the nitrate tracer was analyzed in both the vertical and horizontal columns (the results are shown in 4.Fig. 1). This was used as a control to examine whether moving from the vertical to the horizontal flow mode had any influence on dissolved ions or colloids with a density similar to that of background

electrolyte. The comparison between the breakthrough curves obtained from the horizontal and vertical columns showed that changing the orientation of the column did not affect the flow of the nitrate tracer or the latex beads, as expected from theoretical solute transport knowledge. This also confirms that there were no artefacts in the packing and the operation of the columns during the experiment. The transports of latex particles in the vertical and horizontal columns were also compared, as shown in **Figure 4.2**. The breakthrough curves of latex particles in the vertical and horizontal columns were also very identical, indicating that there was no inherent difference between the transport performance of latex particles in the vertical and horizontal column.

4.3.3 Breakthrough curves of CMC-NZVI from horizontal and vertical columns

Results of the transport of CMC-NZVI particles at 0.3 g/L under both vertical and horizontal flow modes in coarse, intermediate and fine sands are shown in Figures 4.3a, 3b and 3c, respectively. It can be observed (from **Fig. 3a**) that under the identical conditions, the steady-state relative effluent concentration of CMC-NZVI particles in the horizontal column (0.68) was significantly lower than that obtained in the vertical column (0.92).

The steady-state CMC-NZVI relative effluent concentration of CMC-NZVI particles in intermediate sand under the vertical and the horizontal flow mode were 0.85 and 0.77, respectively as shown in **Fig. 3b**. The difference of the transport efficiency of CMC-NZVI particles between the horizontal and the vertical flow mode was even smaller in the fine sand as shown in **Fig. 3c**. The CMC-NZVI relative effluent concentration was 0.52 at 7 PV. Breakthrough curves for both the vertical and horizontal columns showed a gradual increasing trend between 3 and 7 PV and did not reach a strict steady-state, and this can be attributed to detachment of deposited CMC NZVI particles under the high shear conditions in the fine sand [11].

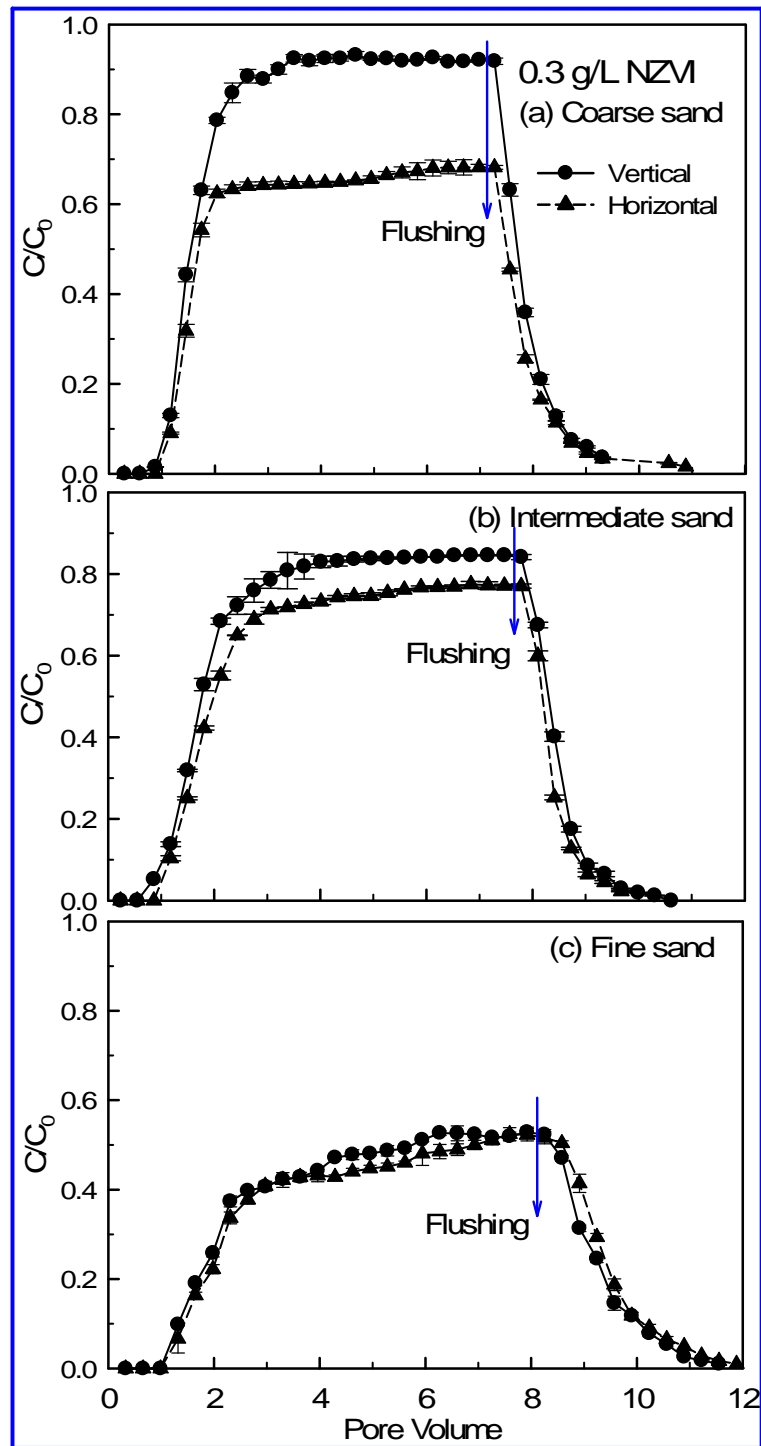


Figure 4.3. Comparison of transport in vertical and horizontal columns at 0.3 g/ L CMC-NZVI.

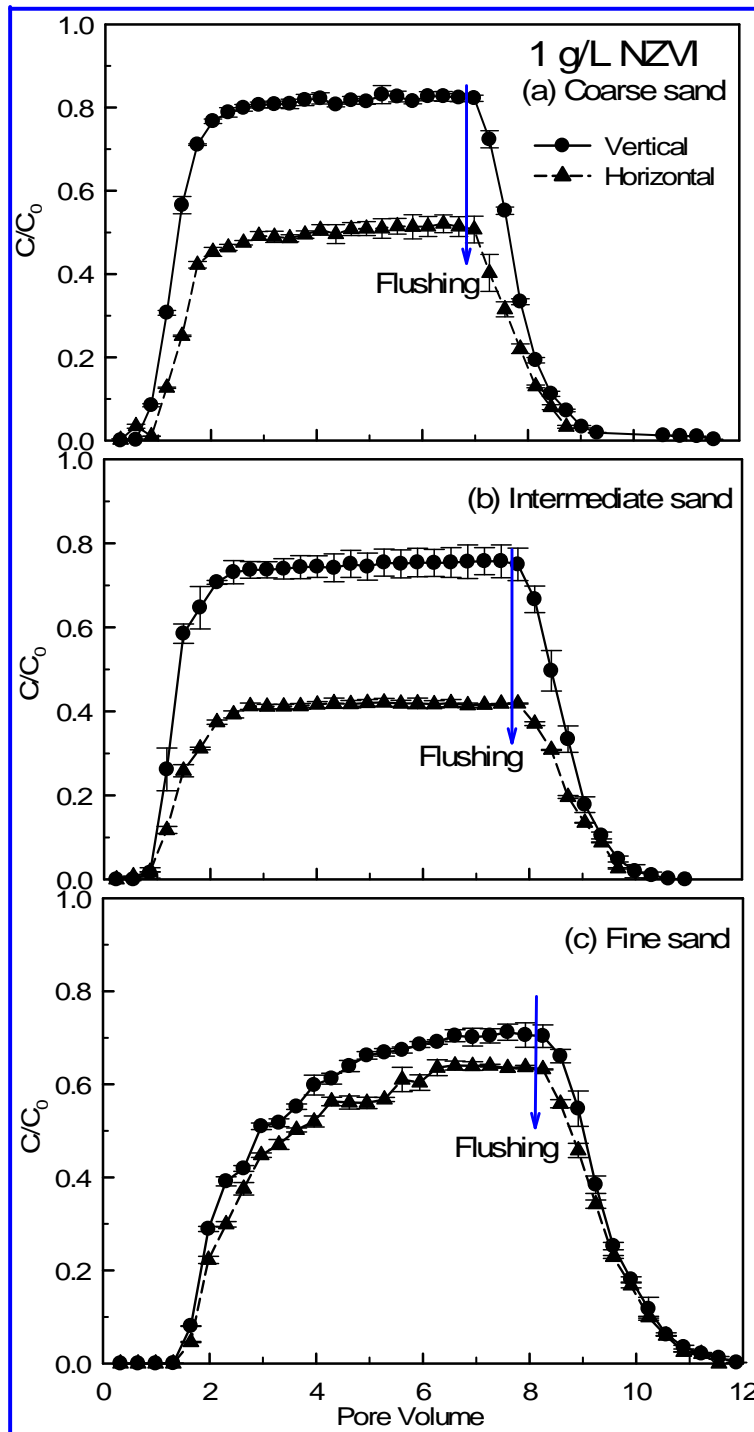


Figure 4.4. Comparison of transport in vertical and horizontal columns at 1 g/ L CMC-NZVI.

Qualitatively, similar trends in CMC-NZVI elution patterns were observed at higher influent concentrations of 1 and 3 g/L CMC NZVI as shown in Figures 4.4 and 4.5. However, one noteworthy difference is that there was a greater difference in the steady-state elution concentration of horizontal and vertical columns with the intermediate and fine sand at 1 g/L and 3 g/L influent concentrations. Furthermore, the relative elution concentrations in the fine sand columns operated either with vertical or horizontal flow, increased with the increase of influent concentration. The total deposited masses in the fine sand for 0.3, 1 and 3 g/L NZVI suspensions are 3.54 mg and 3.84 mg, 7.6 mg, respectively, for the vertical column and 8.99, 14.80 mg and 23.34 mg in the horizontal column calculated by integrating of BTCs, respectively. These results are counter intuitive, as the classical colloid filtration theory states that elution concentrations should not change with influent concentration [39]. However, given that particle sizes increased with CMC-NZVI concentration, it is likely that there were higher drag forces on larger deposited particles[40].

Overall, Figures 4.3, 4.4 and 4.5 indicate that CMC-NZVI transport is higher in the vertical and horizontal columns, particularly for the coarser sand grains.

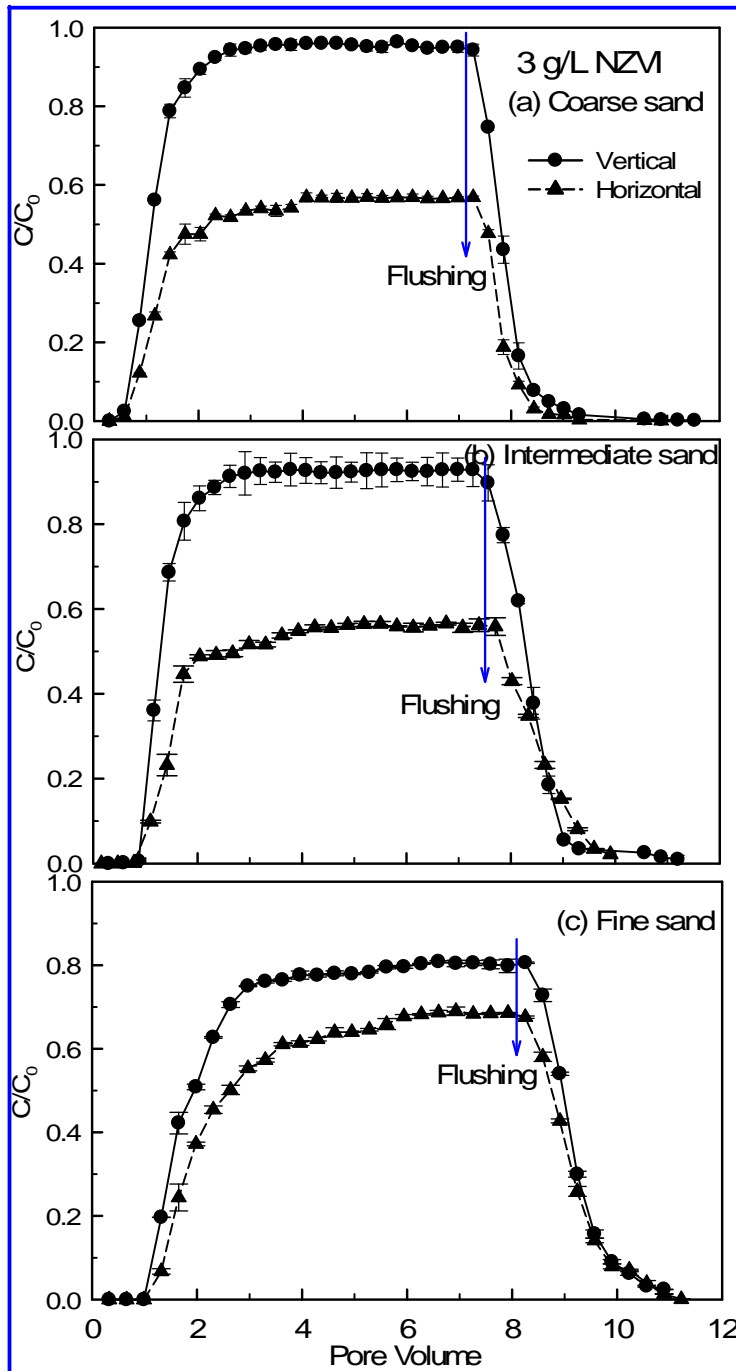


Figure 4.5. Comparison of transport in vertical and horizontal columns at 3 g/ L CMC-NZVI.

4.3.4 Retention of CMC-NZVI in vertical and horizontal columns



Figure 4.6. The picture of the peculiar column with six sample ports in the both top and bottom sides.

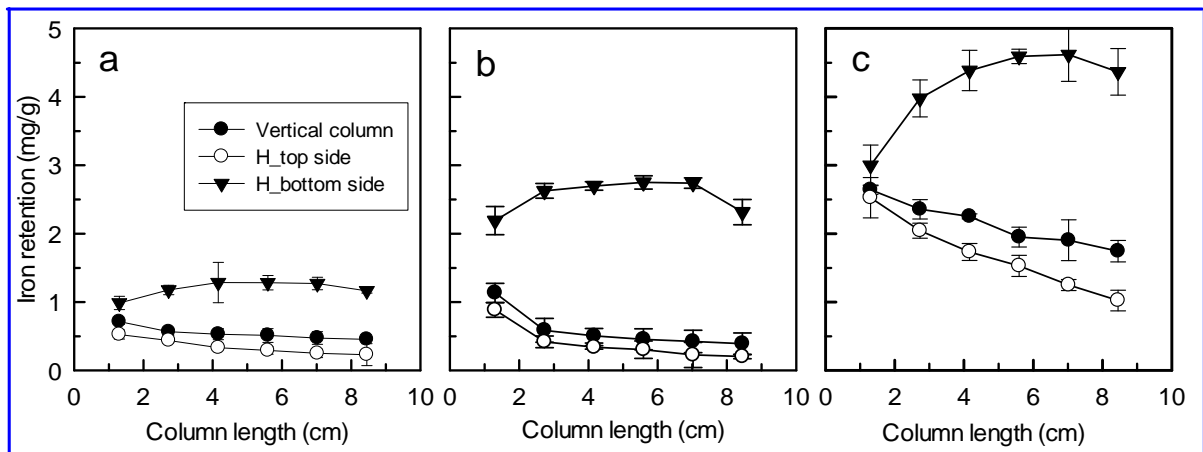


Figure 4.7. The retention of NZVI particles in the vertical and horizontal columns packed with intermediate sand at the end of the NZVI injection and electrolyte flushing periods: (a) 0.3 g/L NZVI; (b) 1 g/L NZVI; (c) 3 g/L NZVI.

At the end of the column experiments for vertical flow, i.e., after the NZVI injection phase and subsequent electrolyte flushing phase, the flow was terminated and sand from the vertical columns were carefully extruded and sectioned at 1 cm intervals. The sand was digested with 2 normal chloride acid solution and analyzed for total Fe by ICP-OES. For the horizontal flow experiment, sectioning of the sand was done differently, as extrusion of the sand with minimal disturbance to the deposited particles could not be achieved in the horizontal orientation. Thus, separate from the experiments used to obtain the BTCs, identical column experiments were conducted with specially made columns with 6 sampling ports along the length of the column to extract sand from top side and bottom side the horizontal column as shown in Figure

4.7. The top and bottom of the column was sampled because it was visibly evident that greater NZVI deposition was occurring in the bottom side of the column during horizontal flow. The sands were analyzed for total Fe as mentioned above.

The retention of NZVI particles in the intermediate sand at different NZVI particle concentrations are shown in Figure 4.7. Comparing Figures 4.7a, b and c, it is obvious that with the increase of NZVI injection concentration, the retention concentration increased in both the vertical and horizontal columns. Additionally, with the increase of NZVI concentration, the difference of mass retained between the top side and bottom side increased, indicating that the settling of NZVI particles in the horizontal column increased particle concentration. The retention concentrations in the top side of the horizontal columns were lower than those in the vertical columns under the identical conditions. This result is attributable to the fact that during transport in the horizontal column, particles settled to the bottom side, leaving fewer particles in the top side and the resultant lower retention concentration. This is an anomalous deposition behavior, where deposition is non-uniform along the column cross section, and is attributable to the gravitational settling of the NZVI aggregates, and is discussed in more detail in the following section.

The mass retained in the bottom of the column increased in the sections of the column closer to the injection end, and then approached a constant value. This is contrary to predictions from the CFT [41] where deposition is predicted to be the greatest near the inlet end, as observed for the vertical column and with the NZVI deposition at the top of the column. This anomalous deposition pattern indicates that as the NZVI migrates through the horizontal column, the settled mass of NZVI increases due to the coupled effects of horizontal transport and vertical settling.

4.4 Analyses of deposition mechanisms in vertical and horizontal columns

The results from the BTC experiments are summarized in **Table 4.2**. The classical colloid filtration theory (CFT) calculations are conducted for the vertical column experiments. According to this CFT, the first order particle deposition rate constant, k , is represented as function of the single collector contact efficiency (η_0) and the attachment efficiency (α) as shown in equations 4.1 and 4.2 [22, 42].

$$k = \left[\frac{3(1-f)u}{2d_s f} \alpha \right] \eta_0 \quad (4.1)$$

where f is porosity of media and d_s is the average diameter of the collector. The parameter η_0 is the probability of collision of a particle with the collector surface during transport through porous media and can be theoretically determined by the Tufenkji and Elimelech equation correlation equation [31].

The attachment efficiency, α , represents the probability of sticking of a particle on the collector after collision. The attachment efficiency is usually determined from experimental breakthrough curves by solving for equation 4.2.

$$\alpha = -\frac{2d_s \ln(C/C_0)}{3(1-f)L\eta_0} \quad (4.2)$$

where C/C_0 is the steady-state effluent concentration, and is taken as C/C_0 at 7 PV.

However, for the horizontal columns, as the flow direction differs from the commonly used vertical direction, the TE equation is no longer valid as the force and torque balance on which is equation is derived fundamentally changes. Therefore, the η_0 and α calculations have not been conducted for the horizontal column results based on equations 4.1 and 4.2. Instead, the single collector contact efficiencies of NZVI particles in horizontal columns were calculated by

the trajectory analysis of colloids around a collector based on the analyses of Rajagopalan and Tien [43] but modified for particle flow around a three dimension collector, as described in detail in the SI. The results from the analyses are listed in Table 4.3. In addition, the profiles of the analyzed trajectories of NZVI particles and common colloid particles (usually latex particles with the density of 1.05 g/cm^3) in 3-D are also listed in Table 4.3 to highlight the effects of gravity of particles on their transport through the porous media.

Table 4.2. Deposition parameters for CMC NZVI transport in vertical and horizontal columns.

Sample	Mean diameter (nm)	Sand	C/C_0	η_0 predicted from TE equation	(η_0) calculated from 3-D trajectory simulation	Attachment efficiency (α)	Deposition rate (k, s^{-1})	
0.3 g/L NZVI in 1 g/L 700K CMC	1760	Coarse	Vertical	0.92	$2.81 \cdot 10^{-3}$	/	0.3592	$1.91 \cdot 10^{-4}$
			Horizontal	0.68	/	$5.71 \cdot 10^{-3}$	0.8148	$8.80 \cdot 10^{-4}$
		Intermediate	Vertical	0.85	$3.52 \cdot 10^{-3}$	/	0.1613	$5.58 \cdot 10^{-4}$
			Horizontal	0.77	/	$8.18 \cdot 10^{-3}$	0.1099	$8.84 \cdot 10^{-4}$
		Fine	Vertical	0.52	$5.70 \cdot 10^{-3}$	/	0.2039	$1.73 \cdot 10^{-3}$
			Horizontal	0.52	/	$1.65 \cdot 10^{-2}$	0.0705	$1.73 \cdot 10^{-3}$
1 g/L NZVI in 1 g/L 700K CMC	2220	Coarse	Vertical	0.82	$4.43 \cdot 10^{-3}$	/	0.5441	$4.54 \cdot 10^{-4}$
			Horizontal	0.51	/	$1.62 \cdot 10^{-2}$	0.5014	$1.53 \cdot 10^{-3}$
		Intermediate	Vertical	0.77	$5.02 \cdot 10^{-3}$	/	0.1908	$9.54 \cdot 10^{-4}$
			Horizontal	0.42	/	$1.78 \cdot 10^{-2}$	0.1676	$2.97 \cdot 10^{-3}$
		Fine	Vertical	0.72	$8.04 \cdot 10^{-3}$	/	0.073	$8.56 \cdot 10^{-4}$
			Horizontal	0.64	/	$2.85 \cdot 10^{-2}$	0.0278	$1.16 \cdot 10^{-3}$
3 g/L NZVI in 1 g/L 700K CMC	3130	Coarse	Vertical	0.96	$8.41 \cdot 10^{-3}$	/	0.0586	$9.34 \cdot 10^{-5}$
			Horizontal	0.57	/	$3.47 \cdot 10^{-2}$	0.1954	$1.28 \cdot 10^{-3}$
		Intermediate	Vertical	0.93	$8.89 \cdot 10^{-3}$	/	0.0278	$2.49 \cdot 10^{-4}$
			Horizontal	0.55	/	$3.43 \cdot 10^{-2}$	0.0600	$2.07 \cdot 10^{-3}$
		Fine	Vertical	0.81	$1.36 \cdot 10^{-2}$	/	0.0275	$5.48 \cdot 10^{-4}$
			Horizontal	0.69	/	$5.08 \cdot 10^{-2}$	0.0130	$9.68 \cdot 10^{-4}$

From **Table 4.2** it is evident that vertical columns packed with coarse sand or intermediate sand, C/C_0 and k values of CMC-NZVI at 1 g/L are lower than those at 0.3 g/L and

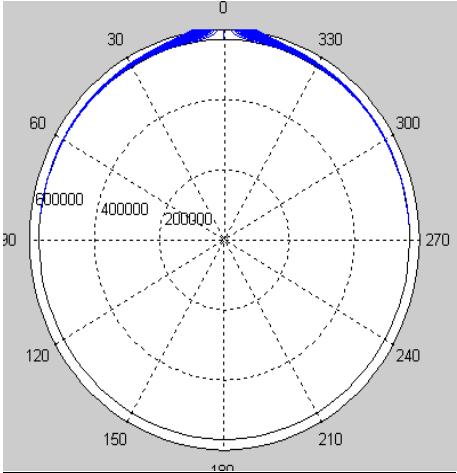
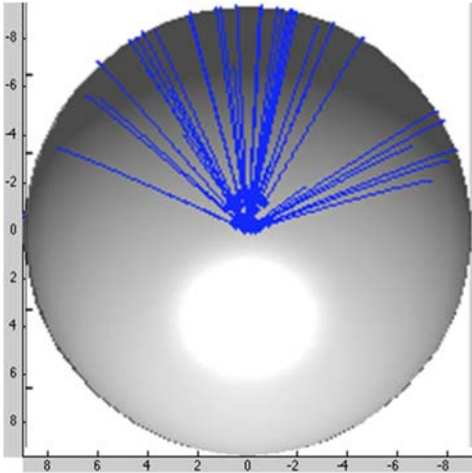
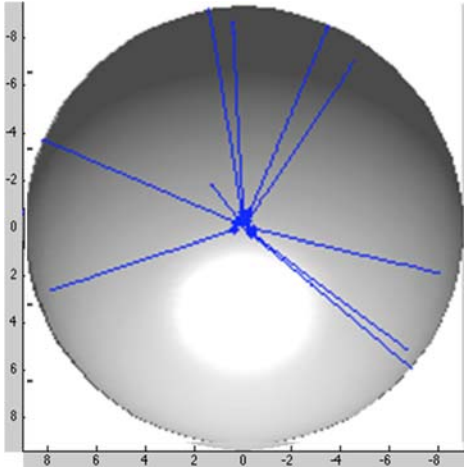
3 g/L. The increase in deposition between 0.3 g/L and 1 g/L CMC-NZVI injection concentrations can be attributed in part to the increase in η_0 . At 3 g/L injection concentration the deposition of CMC-NZVI in the coarse and intermediate sands are significantly higher than with lower injection concentrations.

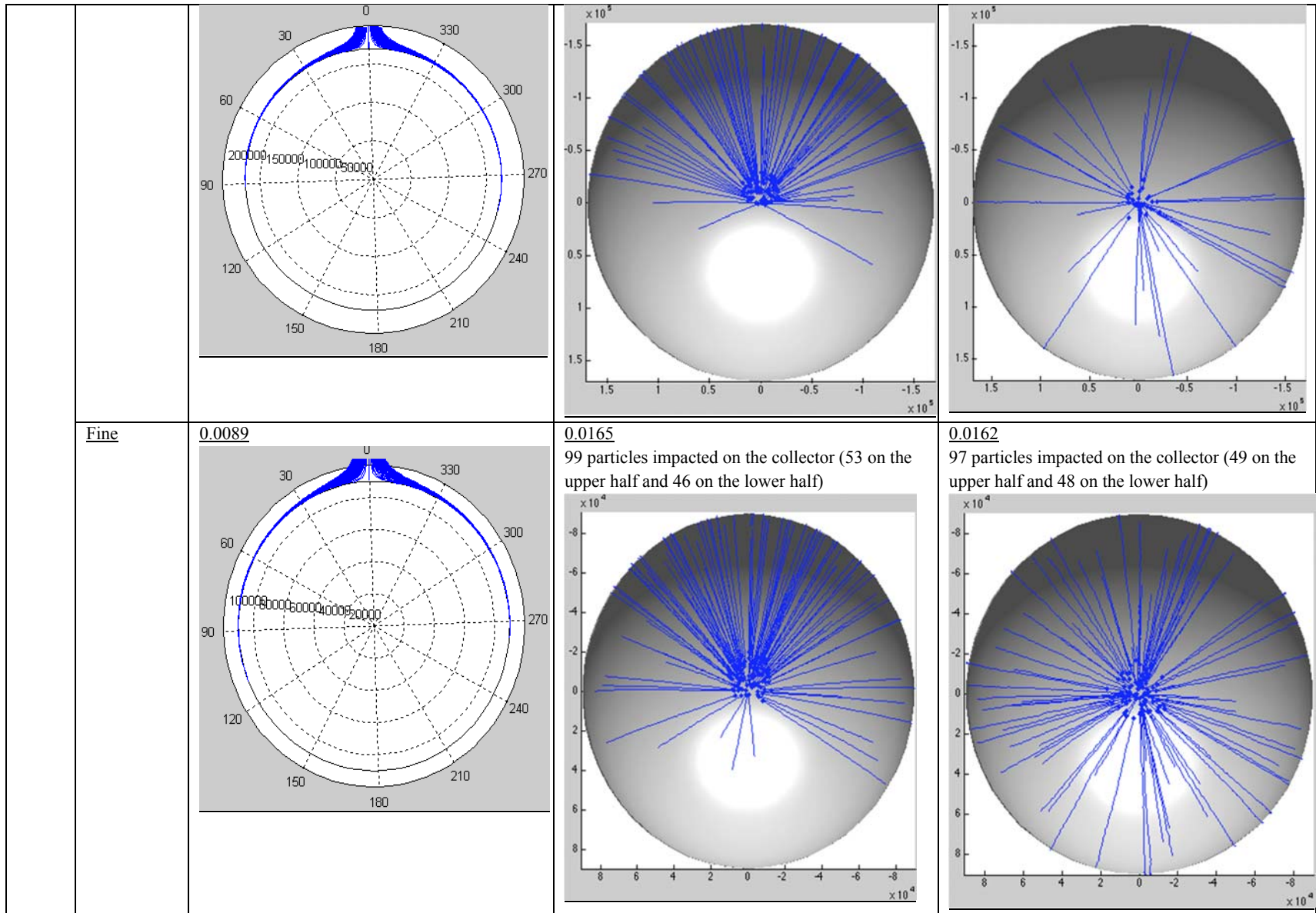
Changes in the fluid flow from vertical to horizontal direction changes the influence of gravitational force on particle trajectories around the collector. The effects of gravitational forces on CMC-NZVI deposition are evident from the results in Tables 4.3 and 4.4. The single collector contact efficiencies in the horizontal flow model are always higher than those in the vertical flow model under the identical conditions, as shown in Table 4.3. This can partly explain the results that C/C_0 values in the vertical columns were higher than those in the horizontal columns under the identical conditions. Further, the comparisons of the profiles of trajectories of NZVI particles and the latex particles in 3-D calculations reveal that CMC-NZVI particles are mainly impacted on the upper half collector, particularly in the coarse and intermediate sands, indicating the significant settling of NZVI particles during transport in the horizontal columns. The profiles of 3-D trajectories of NZVI particles in the fine sand, however, show that particles impact almost equally in the upper half collector and the lower half collector in the fine sand case, unlike those in the coarse and intermediate sands. The more uniform deposition of NZVI particles on the fine sand was caused by the combined influence of the gravity of NZVI particle and hydraulic forces of flow around the sand. This can contribute to the smaller difference of C/C_0 values in the fine sand between the vertical and horizontal columns than these in the coarse and intermediate sands. The impacts of NZVI particles on the fine sand tend to locate on the upper half collector with the increase of NZVI concentration, indicating the increased gravitational settling with the increase of NZVI concentration during transport in the fine sand. This finding can contribute to the results

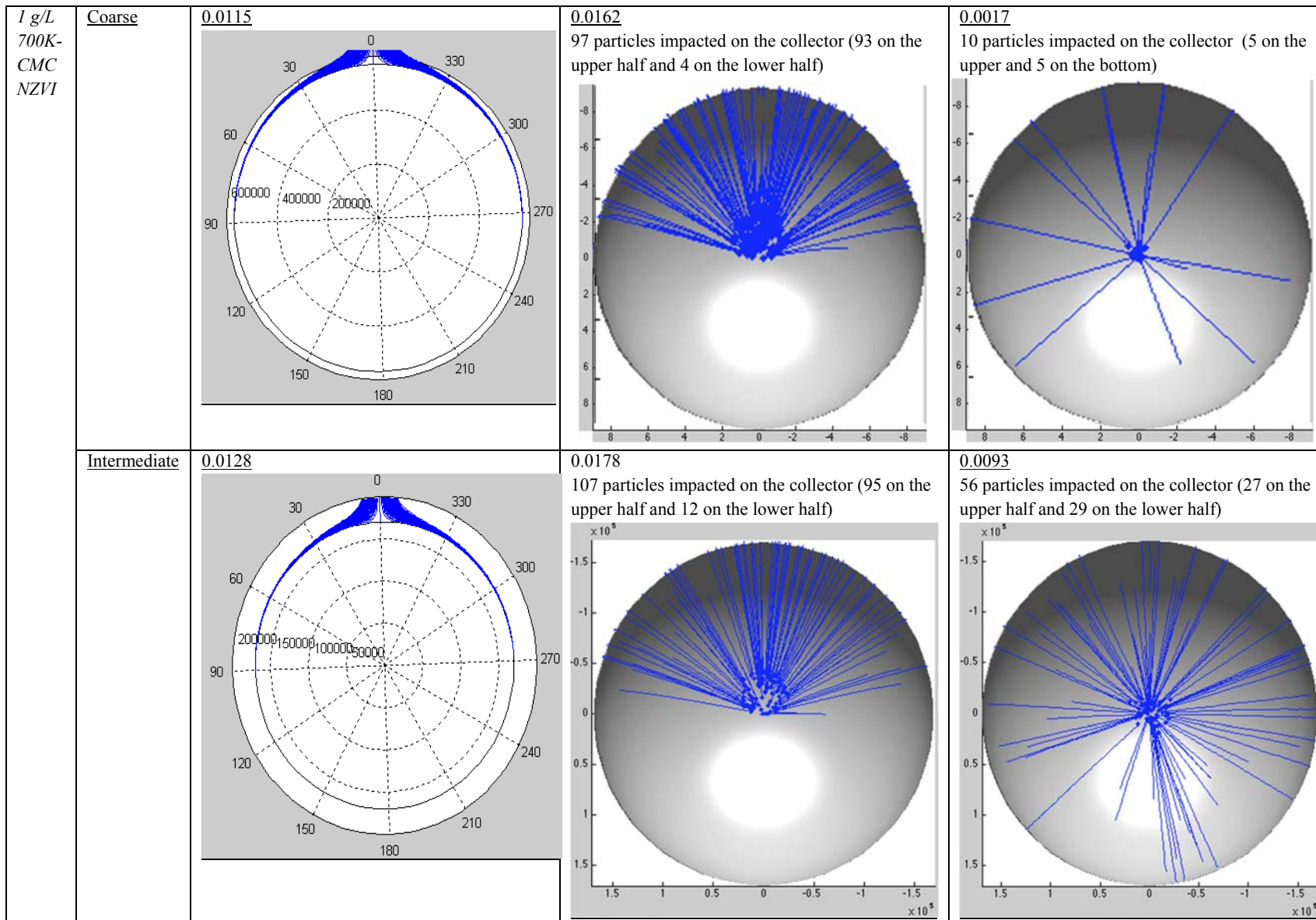
that C/C_0 values in the fine sand with the increase of NZVI concentration between the vertical and horizontal columns.

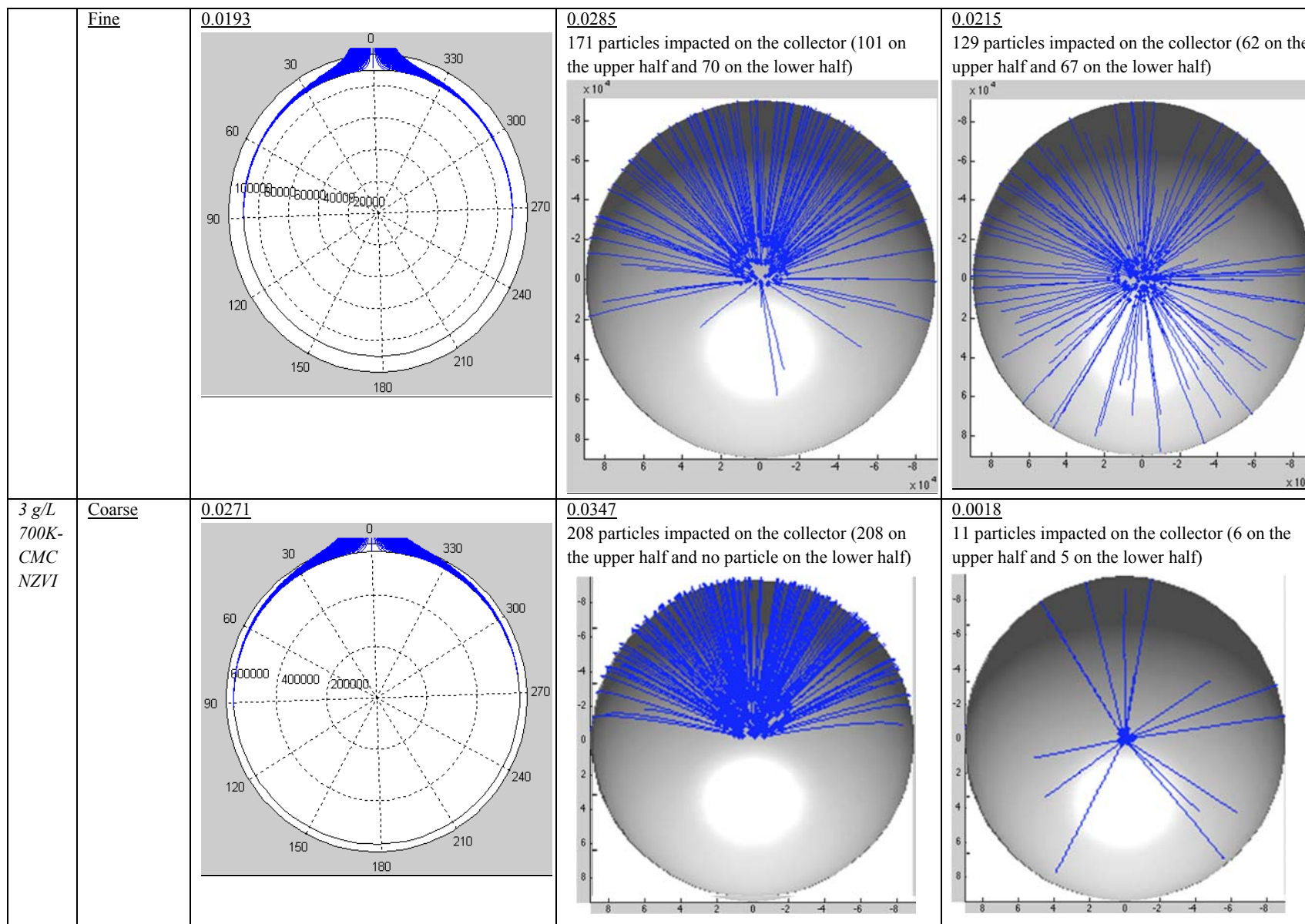
The calculations of the mean of the closest distances encountered by each CMC-NZVI or latex particle and the collector surface, during their trajectory, under different conditions are listed in Table 4.4. The mean values of the distances of NZVI particles at 1 g/L are 25.21 μm and 26.43 μm , 7.28 μm and 7.80 μm as well as 3.48 μm and 3.71 μm in the upper half and lower half of the coarse sand, intermediate sand and fine sand, respectively. When NZVI concentration increased to 3 g/L, the mean values of the distances are 21.00 μm and 22.36 μm , 6.12 μm and 6.75 μm as well as 3.27 μm and 3.51 μm in the upper half and lower half of the coarse sand, intermediate sand and fine sand, respectively. Overall, in all cases, the mean of the closest distance between NZVI particle and the upper half collector surface is less than that between the particle and the lower half collector surface under the identical conditions. However, for the latex particles, the means of the closest distances from the collector in the upper half and the lower half collector are very similar under the identical collector and particle sizes, indicating no gravitational settling during latex particle transport in horizontal columns. This result verifies that NZVI particles experience very significant gravitational setting in the horizontal columns, which led to deviations in deposition behavior between the vertical and horizontal columns. Further, examining the mean distance values, one can find that, for NZVI particles, the difference of the mean of the minimum distances between the upper half and lower half collector increased with the increase of collector diameter for a given mean NZVI particle size (corresponding to the mean diameter for a specific suspension concentration). This explains the results of greater divergence in the C/C_0 values in vertical and horizontal columns in the coarse and intermediate sand are higher than that in the fine sand at the same NZVI concentration.

Table 4.3. The calculations of the single collector contact efficiency (η_0) of the current modified trajectory analysis as well as the profiles of particles' trajectories under different conditions.

Sample	Sand	η_0 of NZVI calculated from current modified trajectory analysis in 2-D (vertical column)	η_0 of NZVI calculated from current modified trajectory analysis in 3-D (horizontal column)	η_0 of latex particle calculated from current modified trajectory analysis in 3-D
0.3 g/L 700K-CMC NZVI	Coarse	<u>0.0049</u> 	<u>0.0057</u> 34 particles impacted on the collector (30 on the upper half and 4 on the lower half). 	<u>0.0012</u> 7 particles impacted on the collector (3 on the upper half and 4 on the lower half) 
	Intermediate	<u>0.0060</u>	<u>0.0082</u> 49 particles impacted on the collector (40 on the upper half and 9 on the lower half)	<u>0.0037</u> <u>22 particles impacted on the collector (10 on the upper half and 12 on the lower half)</u>







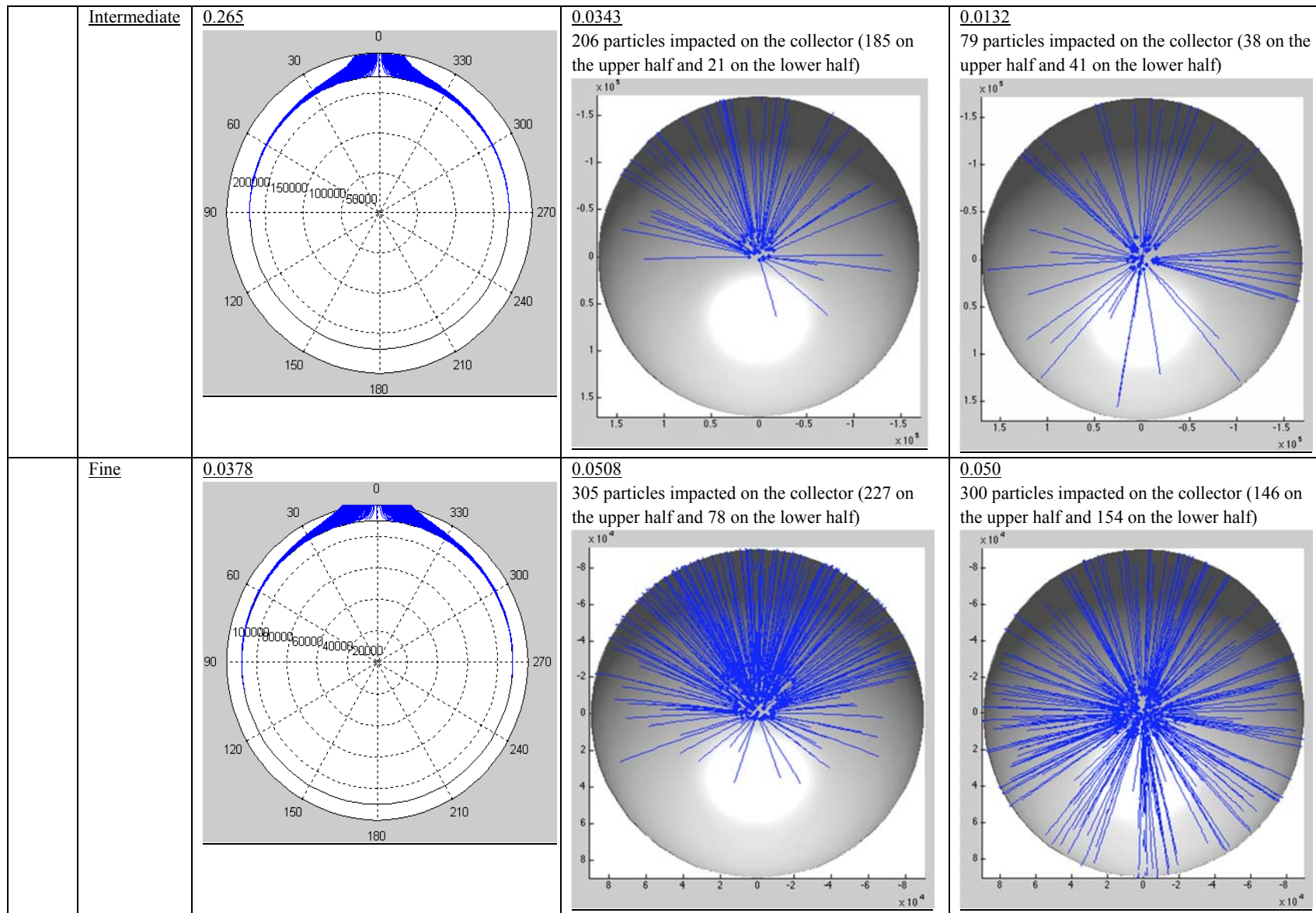
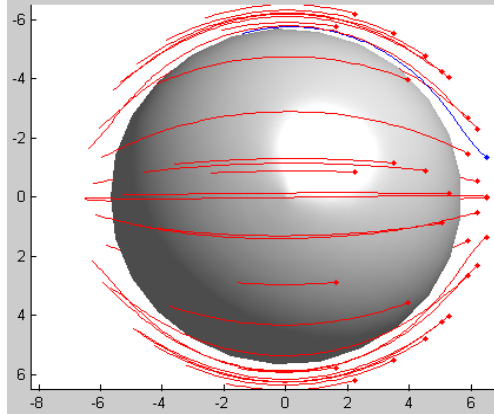
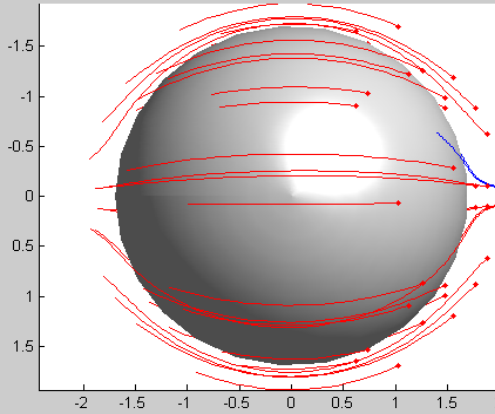
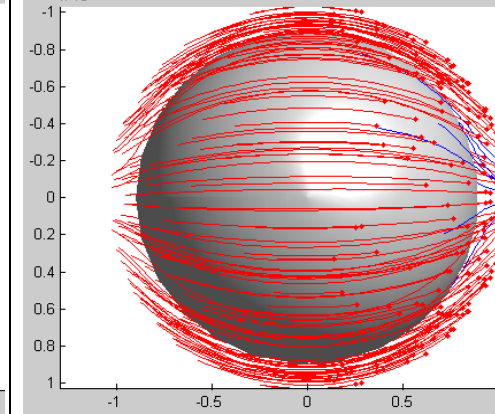
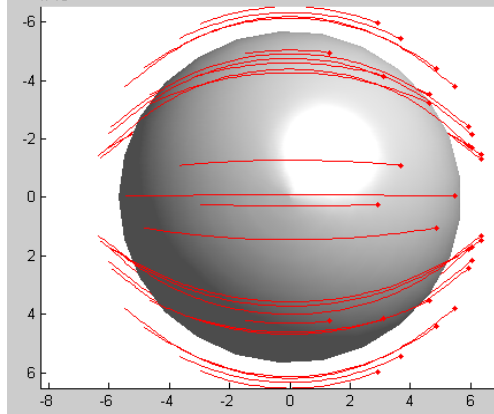
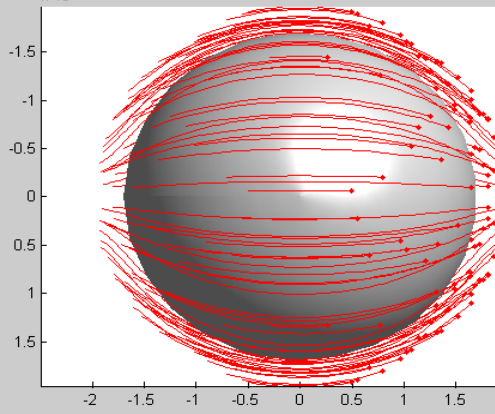
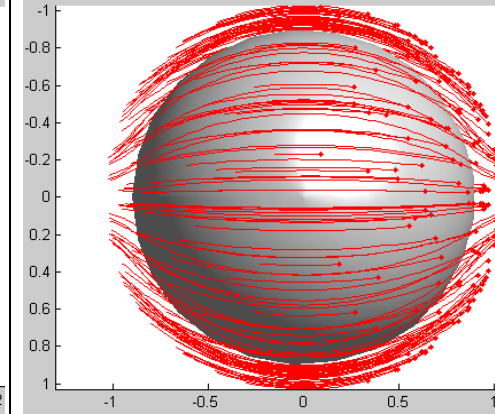
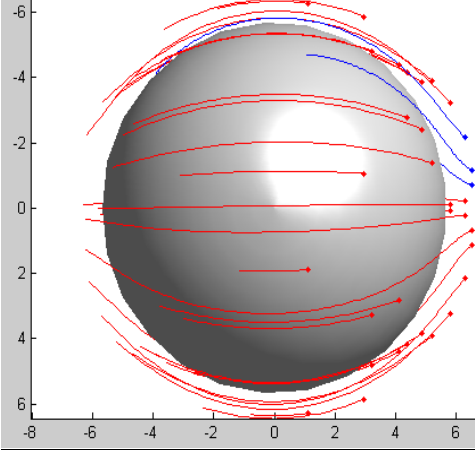
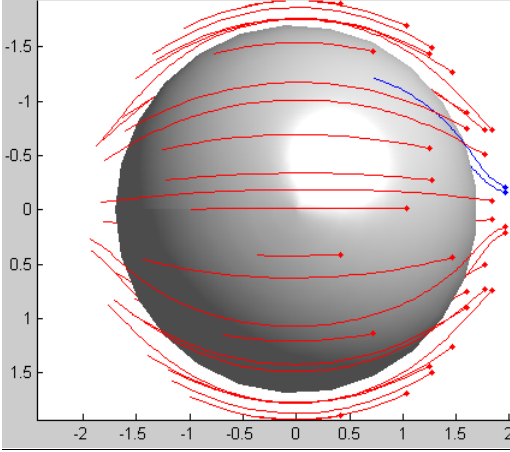
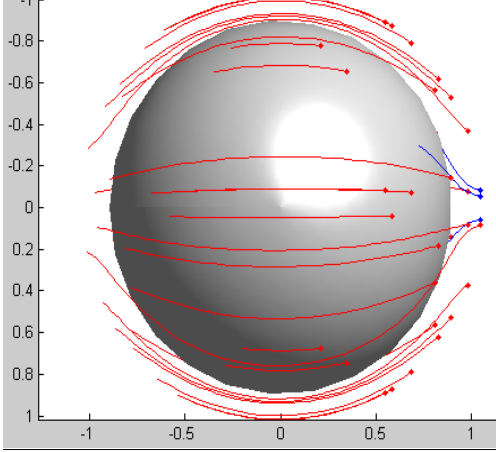
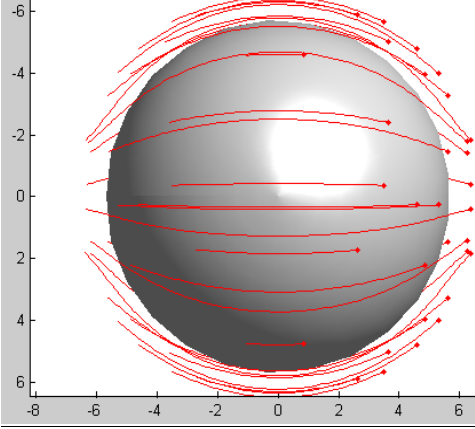
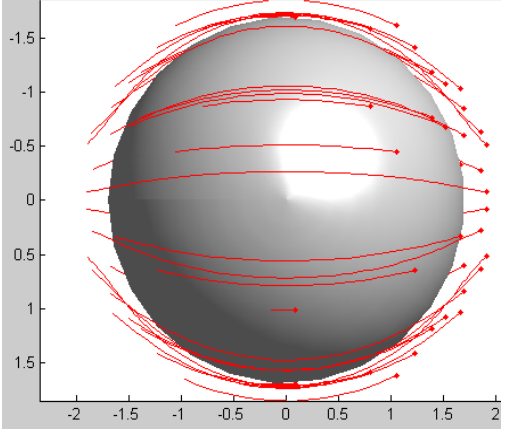
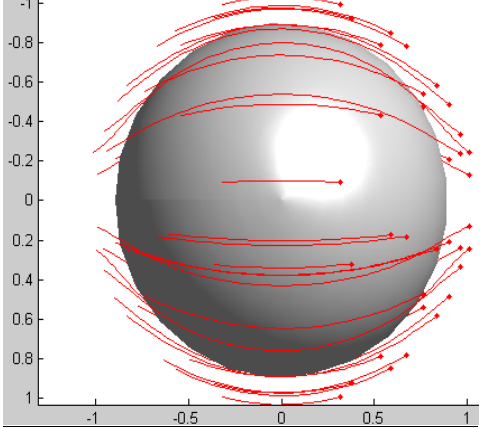


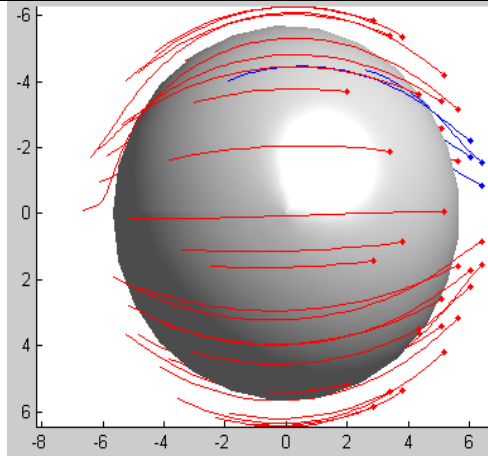
Table 4.4. The comparisons of the mean of minimum distances between NZVI and latex particles' trajectories and the upper/lower half collector surface under different conditions.

Particle diameter [38]	Particle	The mean of minimum distances between particles' trajectory and the coarse sand surface (um)	The mean of minimum distances between particles' trajectory and the intermediate sand surface (um)	The mean of minimum distances between particles' trajectory and the fine sand surface (um)
1760	NZVI	 <p>25.03 (upper half collector) 26.51 (lower half collector)</p>	 <p>7.25 (upper half collector) 7.80 (lower half collector)</p>	 <p>3.79 (upper half collector) 3.89 (lower half collector)</p>
	Latex	 <p>30.02 (upper half collector) 30.03 (lower half collector)</p>	 <p>8.71 (upper half collector) 8.72 (lower half collector)</p>	 <p>4.40 (upper half collector) 4.41 (lower half collector)</p>

2220	NZVI	 <p>25.21 (upper half collector) 26.43 (lower half collector)</p>	 <p>7.28 (upper half collector) 7.80 (lower half collector)</p>	 <p>3.48 (upper half collector) 3.71 (lower half collector)</p>
	Latex	 <p>30.72 (upper half collector) 30.78 (lower half collector)</p>	 <p>8.88 (upper half collector) 8.89 (lower half collector)</p>	 <p>4.37 (upper half collector) 4.41 (lower half collector)</p>

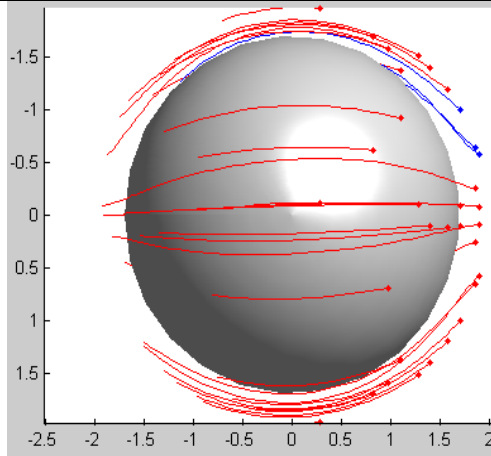
3130

NZVI



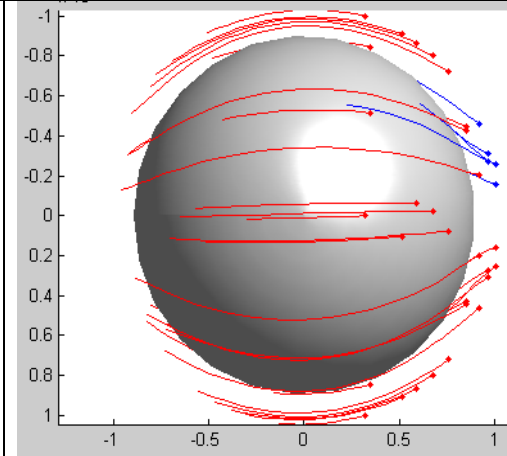
21.00 (upper half collector)

22.36 (lower half collector)



6.12 (upper half collector)

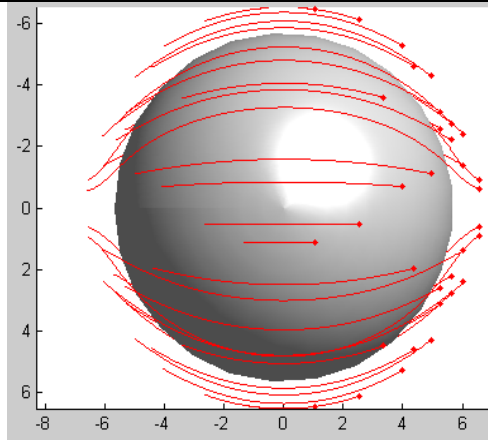
6.75 (lower half collector)



3.27 (upper half collector)

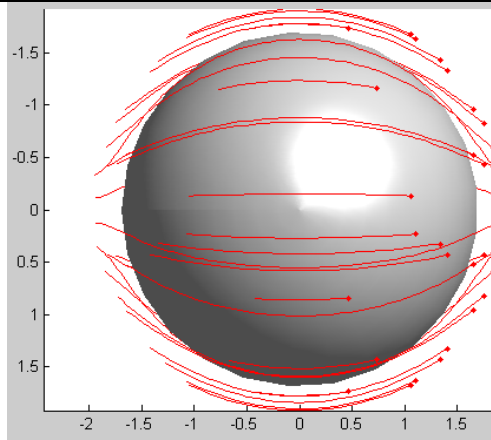
3.51 (lower half collector)

Latex



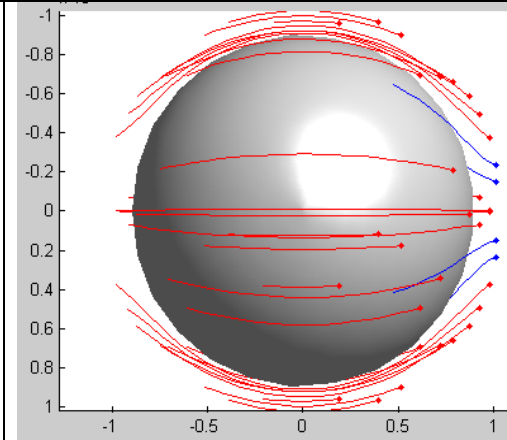
24.63 (upper half collector)

24.65 (lower half collector)



6.78 (upper half collector)

6.79 (lower half collector)



3.33 (upper half collector)

3.33 (lower half collector)

4.5 Conclusions

In this study, the transport of CMC-NZVI aggregates in vertical and the horizontal flow columns were compared. In the latter, gravitational settling of CMC-NZVI aggregate (due to its high density 6.58 g/cm³) exhibited deposition patterns very different from the vertical column. The effects of different sand mean grain sizes and NZVI concentrations on the transport efficiency of CMC-NZVI aggregate transport efficiency were also studied in both the vertical and the horizontal column. It was found that in the horizontal columns CMC-NZVI aggregate were prone to sediment in coarse sand caused by strong gravitational force, which resulted in them having very low transport efficiency in the horizontal column. In fine sand, on the other hand, CMC-NZVI particles were less prone to sediment in the horizontal column, especially at low CMC-NZVI concentrations. This is attributed to the different deposition patterns of NZVI particles on coarse and fine sands: only depositing on the top side of the coarse sand and more uniform deposition on the fine sand. The findings can help explain the possible challenges with efficient transport of NZVI which could arise during field applications of CMC-NZVI particles where the particles are injected horizontally from well screens. The findings in this study can be used to accurately assess the transport of NZVI particles in field applications.

Acknowledgments

The research was funded by the Strategic Project Grant Program of the Natural Sciences and Engineering Research Council of Canada and by Golder Associates Ltd. J. L. was supported in part by a McGill Engineering Doctoral Award. We thank Prof. Nathalie Tufenkji, McGill University for access to the laser Doppler velocimeter.

Supporting information

Section 4.S1. Equations for trajectories of NZVI particles in 2-D and 3-D

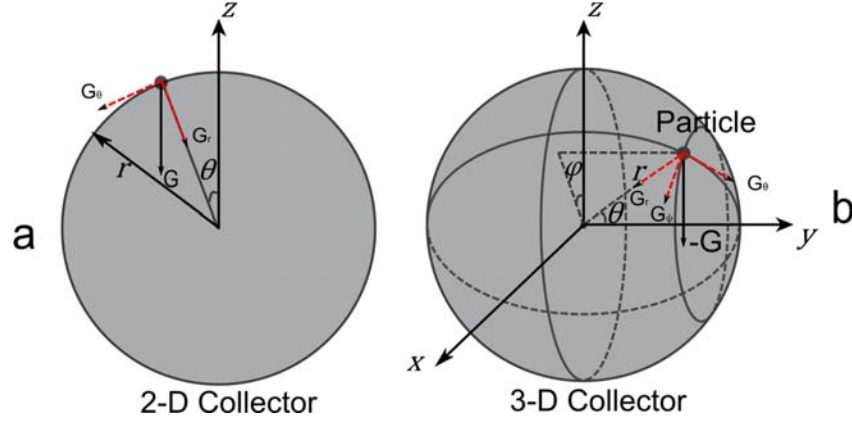


Figure 4.S1. The gravity decomposition on the collector: a) 2-D collector; b) 3-D collector.

This figure shows how to calculate the decomposition of gravity in the 2-D and 3-D collectors.

1) Scenarios for forces calculations

The basic forces balance as well as torque balance equations were similar as those used in developing RT model [30]. The main forces included gravity, London force and drag force. In the 2-D trajectory analysis, the forces are listed as following:

$$\begin{aligned}
 \varphi &= (U/2) \sin^2 \theta * a_s^2 [(K_1/r^*) - K_2 r^* + K_3 r^{*2} + K_4 r^{*4}] \\
 r^* &= r/a_s \\
 K_1 &= 1/w \\
 K_2 &= (2+3p^5)/w \\
 K_3 &= p(3+2p^5)/w \\
 K_4 &= -p^5/w
 \end{aligned}
 \quad \left. \vphantom{\begin{aligned} \varphi &= (U/2) \sin^2 \theta * a_s^2 [(K_1/r^*) - K_2 r^* + K_3 r^{*2} + K_4 r^{*4}] \\ r^* &= r/a_s \\ K_1 &= 1/w \\ K_2 &= (2+3p^5)/w \\ K_3 &= p(3+2p^5)/w \\ K_4 &= -p^5/w \end{aligned}} \right\} \quad (4.S1)$$

$$w = 2 - 3p + 3p^5 - 2p^6$$

$$\text{And } p = (1 - \varepsilon)^{1/3} = a_s / b \quad (4.S2)$$

These equations are used to describe and simulate the flow stream around the collector.

And based on the above flow stream function, the velocity of the flow around the collector can be described as:

$$V = -\left(\frac{1}{r \sin \theta} \frac{\partial \psi}{r \partial \theta}\right) e_r + \left(\frac{1}{r \sin \theta} \frac{\partial \psi}{\partial r}\right) e_\theta \quad (4.S3)$$

Equation 4.S3 can be simplified as:

$$V = -A_C y^2 e_r + (B_C y + D_C y^2) e_\theta \quad (4.S4)$$

In terms of the equations 4.S2, 4.S3 and 4.S4, A, B and D can be expressed as:

$$A_C = U a_s^2 * \cos \theta * (K_1 / r^* - K_2 * r^* + K_3 * r^{*2} + K_4 * r^{*4}) / r^2 / (r - a_s)^2 \quad (4.S5)$$

$$B_C = U \sin \theta \left[-\frac{K_1 a_s^4}{r^2} - K_2 a_s^2 + (2K_3 - 4K_4) r a_s + 8K_4 r^2 \right] / [2r a_s (r - a_s)] \quad (4.S6)$$

$$D_C = \frac{2U K_4 \sin \theta}{a_s^2} \quad (4.S7)$$

Forces accounted into the calculations of the trajectory of particles:

I) Inertial force and torque

$$f^I = m \frac{Du}{Dt} \quad (4.S8)$$

$$\text{Where, } \frac{D}{Dt} = \left(\frac{\partial}{\partial t} + u \bullet \nabla \right)$$

$$t^I = 0$$

Because the colloidal particle sizes are commonly very small, thus the inertial force is usually ignorable.

II) Gravitational force and torque

$$f^G = (4/3)\pi a_p^3 (\rho_p - \rho_f) g = (4/3)\pi a_p^3 (\rho_p - \rho_f) g [-\cos\theta \times e_r + \sin\theta \times e_\theta] \quad (4.S9)$$

$$f^G = (4/3)\pi a_p^3 (\rho_p - \rho_f) g = (4/3)\pi a_p^3 (\rho_p - \rho_f) g [-\sin\theta \times \cos\phi \times e_r - \cos\theta \times \cos\phi \times e_\theta - \sin\phi \times e_\phi] \quad (4.S10)$$

$$t^G = 0$$

$$g = |g|$$

Equations 4.S9 and 4.S10 were the description of gravities for 2-D and 3-D trajectories calculations, respectively. In 2-D collector mode, the gravity is only decomposed in radial (r) and one angular (θ) directions, while, in 3-D collector model, the gravity is decomposed in radial (r) and two angular (θ and ϕ) directions

III) Surface force and torque

a) Molecular dispersion force and torque (London force and torque)

$$f_2^{Lo} = [-2Aa(\delta, a_p, \lambda_e) a_p^3 / 3\delta^2 (2a_p + \delta)^2] e_r \quad (4.S11)$$

where, $a(\delta, a_p, \lambda_e)$ is the retardation correction factor.

$$t^{Lo} = 0$$

This London force is representative of van der Waals force.

b) Double-layer interaction force and torque

$$f^{DL} = \{[\nu a_p \kappa (\xi_c^2 + \xi_p^2) / 2] \times [(2\xi_c \xi_p / (\xi_c^2 + \xi_p^2)) - e^{-\kappa\delta}] [e^{-\kappa\delta} / (1 - e^{-2\kappa\delta})]\} e_r \quad (4.S12)$$

$$t^{DL} = 0$$

This double-layer interaction force is ignored in the calculations of this study.

IV) Drag forces and torques

a) Due to the translation of the particles

$$(f^D)^t = -6\pi\mu\alpha_p[u_r f_r^t(\delta^+)e_r + u_\theta f_\theta^t(\delta^+)e_\theta] \quad (4.S13)$$

$$(t^D)^t = 8\pi\mu\alpha_p^2 u_\theta g_\phi^t(\delta^+)e_\phi \quad (4.S14)$$

b) Due to the rotation of the particle

$$(f^D)^r = 6\pi\mu\alpha_p w_1 f_\theta^r(\delta^+)e_\theta \quad (4.S15)$$

$$(t^D)^r = -8\pi\mu\alpha_p^3 w_1 g_\phi^r(\delta^+)e_\phi \quad (4.S16)$$

c) Due to the fluid velocity in the presence of the stationary particle:

$$(f^D)^m = 6\pi\mu\alpha_p \{-Ay^2 f_r^m(\delta^+)e_r + [Byf_{1\theta}^m(\delta^+) + Dy^2 f_{2\theta}^m(\delta^+)]e_\theta\} \quad (4.S17)$$

$$(t^D)^m = -8\pi\mu\alpha_p^3 \{[Bg_{1\varphi}^m(\delta^+) + Dyg_{2\varphi}^m(\delta^+)]e_\phi\} \quad (4.S18)$$

The impacts of drag force on the trajectory mainly included three parts, as described in equations 4.S16, 4.S17 and 4.S18.

Based on these force and torque balances analysis, the dependences of velocities on forces were derived as followings:

$$\frac{du_r}{dt} = \frac{U}{f_r^t} \left(\frac{1}{N_R} + 1 + \delta^+ \right) \{-A^+(1 + \delta^+)^2 f_r^m - N_G \cos \theta + N_{E1} [N_{E2} - e^{-N_{DL}\delta^+}] \times [e^{-N_{DL}\delta^+} / (1 - e^{-2N_{DL}\delta^+})] - [N_{Lo}\alpha / (\delta^{+2})(2 + \delta^+)^2]\} \quad (4.S19)$$

$$\frac{du_r}{dt} = \frac{U}{f_r^t} \left(\frac{1}{N_R} + 1 + \delta^+ \right) \{-A^+(1 + \delta^+)^2 f_r^m - N_G \sin \theta \cos \varphi + N_{E1} [N_{E2} - e^{-N_{DL}\delta^+}] \times [e^{-N_{DL}\delta^+} / (1 - e^{-2N_{DL}\delta^+})] - [N_{Lo}\alpha / (\delta^{+2})(2 + \delta^+)^2]\} \quad (4.S20)$$

Equations 4.S14 and 4.S15 were the dependences of velocities in radial directions on forces in 2-D and 3-D calculations.

$$\frac{\partial u_\theta}{\partial t} = \frac{U}{rs_1} \{B^+ s_2 + D^+ (1 + \delta^+) s_3 + N_G \sin \theta\} \quad (4.S21)$$

$$\frac{\partial u_\theta}{\partial t} = \frac{U}{rs_1} [B^+ s_2 + D^+ (1 + \delta^+) s_3 + N_G \cos \theta \cos \varphi] \quad (4.S22)$$

Equations 4.S16 and 4.S17 were the dependences of velocities in radial directions on forces in 2-D and 3-D calculations.

$$\frac{\partial u_\varphi}{\partial t} = \frac{U}{rs_1} N_G \sin \varphi \quad (4.S23)$$

Equation 4.S18 was only for 3-D calculation.

$$s_1 = (f_\theta^t g_\phi^r - f_\theta^r g_\phi^t) / g_\phi^r \quad (4.S24)$$

$$s_2 = (f_\theta^t g_{1\phi}^m + y^+ f_{1\theta}^m g_\phi^r) / g_\phi^r \quad (4.S25)$$

$$s_3 = (f_\theta^r g_{2\phi}^m + y^+ f_{2\theta}^m g_\phi^r) / g_\phi^r \quad (4.S26)$$

Via the forth-order Runge-Kutta method, equations 4.S19, 4.S21 or equations 4.S20, 4.S22 and 4.S23 were solved separately for 2-D and 3-D trajectory results, respectively.

2) Scenarios for Brownian motion simulation

The Brownian motion effects were considered by directly adding a term referred from an early study [44]. In the simulations, the fourth order Runge-Kutta method was used to compute the trajectory of a particle. p_n was denoted the position of the particle at time t_n , and Δt was denoted the step size of time used in the RK process. We have the following iteration

$$\bar{p}_{n+1} = p_n + \sum_{i=1}^4 b_i k_i \quad (4.S27)$$

$$t_{n+1} = t_n + \Delta t \quad (4.S28)$$

Brownian motion was not taken into the consideration in the above. After \bar{p}_{n+1} is computed, a small displacement (considered as the Brownian motion traces) was added to it to

simulate the traces of particles under all effects (Brownian motion, gravity, London force, and hydraulic forces).

$$p_{n+1} = \bar{p}_{n+1} + \Delta p \quad (4.S29)$$

$$\Delta p = [\Delta x, \Delta y, \Delta z]^T \quad (4.S30)$$

where, p_{n+1} is the ultimate displacement of the particle at time t_{n+1} , Δp is the three dimensional displacement vector generated by Brownian motion, which can be expressed in Cartesian coordinates :

$$\Delta y = n_y \sqrt{2D_\infty \Delta t} \quad (4.S31)$$

$$\Delta y = n_y \sqrt{2D_\infty \Delta t} \quad (4.S32)$$

$$\Delta z = n_z \sqrt{2D_\infty \Delta t} \quad (4.S33)$$

where n_x , n_y and n_z are random variables of normal (0,1). D_∞ is the diffusion coefficient of the particle and the same as above bulk diffusion. It should be noted that the equation used to calculate the displacement of Brownian particles differs from those used in previous studies. This is due to the fact that the displacement of Brownian particles is dependent on the dimension number of Brownian motion. And the model developed in this study is expanded to 3-D, which varies from those models developed in the previous studies. Further, the time step Δt is adaptively controlled in the Runge-Kutta fourth order method (it ranges from 10-16 to 10-18 s).

3) Scenarios for calculating the single collector contact efficiency

6000 particles were distributed in the across area of the collector by using the following method: the across area of the collector was symmetrically divided into 20 regions with equal area, and then 300 particles were assigned into each region (shown in **Figure 4.S2**). The 300 particles in each region were randomly distributed. The trajectories of particles were simulated from the central regions moving towards the circumferential regions (the number of hits are simultaneously recorded). If there was no any impact of the trajectory on the collector surface in any one region, the calculation of the trajectory of particles was skipped in the outer layer of the region. The total times of the impact between the trajectory and the collector divided the total particle number (6000) to obtain the single collector contact efficiency.

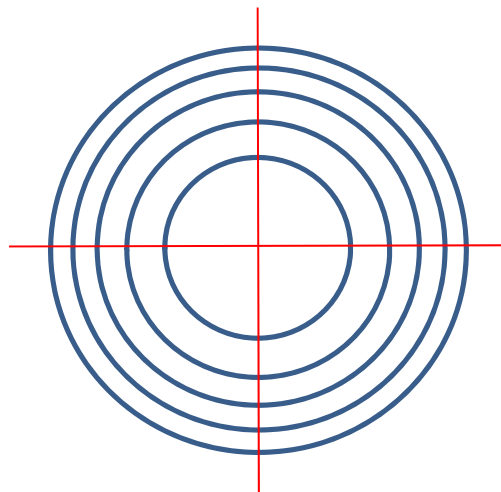


Figure 4.S2. The uniform partition of the cross-section area into 20 regions (equal area method).

4) **Scenarios for calculating the mean minimum distances between NZVI particles' trajectories and collector surface**

Setting the lateral side of the collector sphere as the symmetrical plane, 100 particles were assumed symmetrically distributed on the collector surface. The trajectories of these 100 particles were calculated. Then the minimum distances between trajectories and collector surface

were recorded. The means of these distances (50 values on the upper half collector and 50 values on the lower half collector) were calculated and compared in 3-D simulations to reveal the effect of gravity on particle transport in upper and lower half collector.

Section 4.S2. The sedimentation experimental results

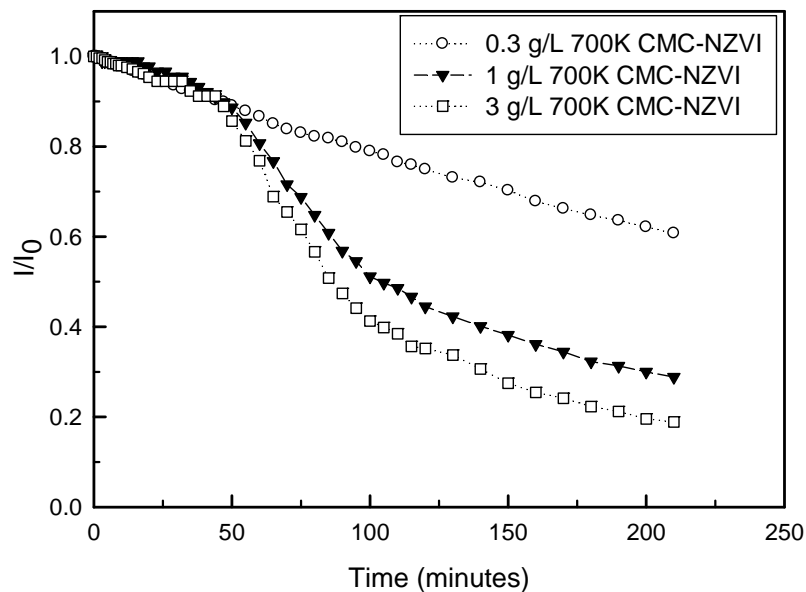


Figure 4.S3. Sedimentation experimental results of CMC-NZVI at different concentrations.

The sedimentation experiments were done at three different NZVI concentrations (0.3 g/L, 1 g/L and 3 g/L) to examine the effect of NZVI concentration on particle aggregation (shown in Fig. 1). It could be observed that NZVI sedimentation was the slowest at the concentration of 0.3 g/L (more than 63% of NZVI particles remained in suspension at the end of the experiment), considerably faster at 1 g/L NZVI (only around 30% of particles remained in the suspension at the end of the experiment), and the highest at 3 g/L (only around 20% of particles remained in the suspension after the experiment). These results indicated that NZVI aggregation proceeded much more rapidly at higher NZVI concentrations and much more slowly at lower NZVI

concentrations. Similar relationship between NZVI sedimentation and concentration was also obtained in previous studies [8]. And this was consistent with the theory mentioned in [45], which entailed that the aggregation rate had a second-order dependence on particle concentration.

Section 4.S3. The section results of the retained NZVI particles on sand in columns

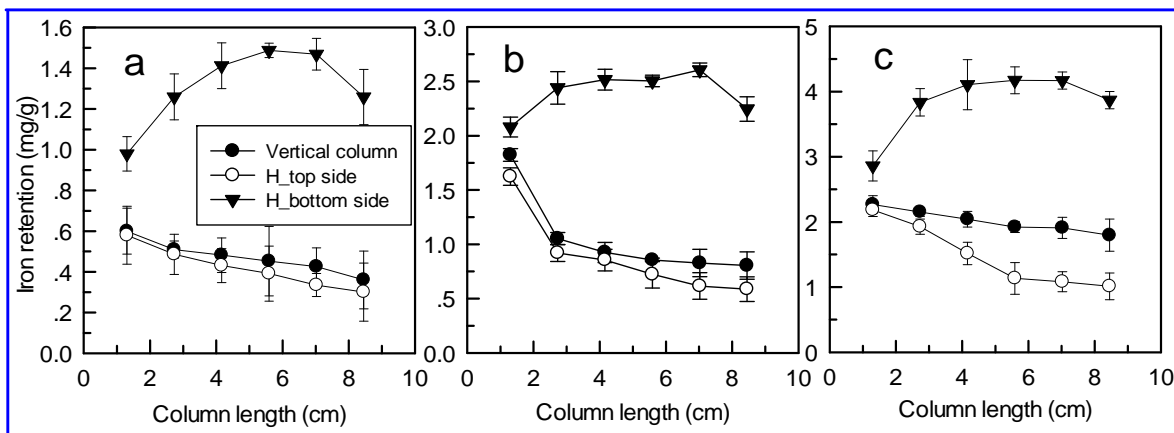


Figure 4.S4. Iron retention in the coarse sand: a) 0.3 g/L 700K CMC-NZVI; b) 1 g/L 700K CMC-NZVI; c) 3 g/L 700K CMC-NZVI.

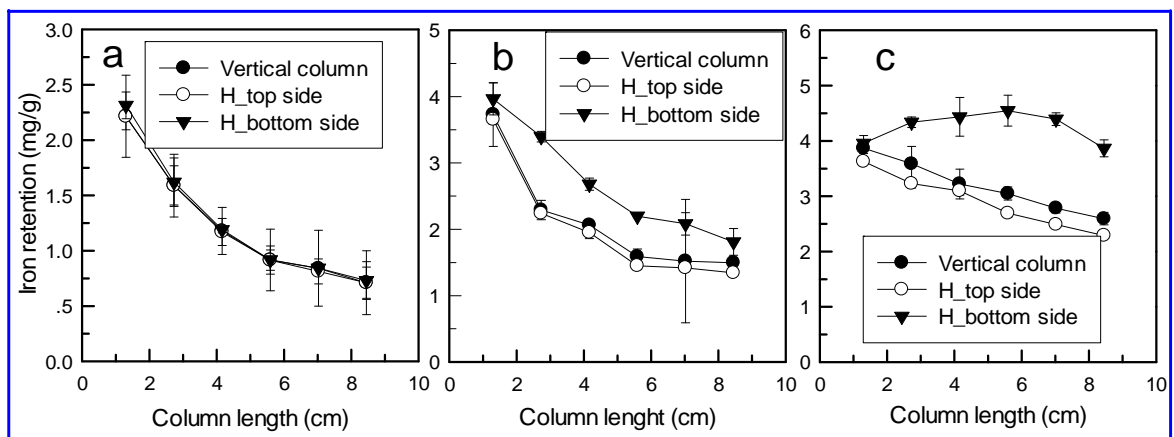


Figure4. S5. Iron retention in the fine sand: a) 0.3 g/L 700K CMC-NZVI; b) 1 g/L 700K CMC-NZVI; c) 3 g/L 700K CMC-NZVI.

Section 4.S4. The abbreviation of parameters for the mathematical calculations

A	Hamaker constant
A_C	the coefficient in equation 4.S4
A_C^+	the dimensionless A_C defined by $A_C a_p^2 / U$
A_s	porosity-dependent parameter of Happel's model; $A_s = 2(1 - p^5) / (2 - 3p + 3p^5 - 2p^6)$
a_p	radius of particle
a_s	radius of the spherical collector
b	radius of the Happel cell
B_C	the coefficient in equation S4
B_C^+	the dimensionless B_C defined by $B_C a_p / U$
C_0	the number concentration of particles in the suspension
D_C	the coefficient in equation 4.S4
D_C^+	the dimensionless D_C defined by $D_C a_p^2 / U$
D_∞	diffusion coefficient in an infinite medium, $D_\infty = k_B T / (6\pi\eta a_p)$
d_s	diameter of spherical collector, $d_s = 2a_s$
d_p	diameter of particle, $d_p = 2a_p$
e_r, e_θ, e_φ	unit vectors in r, θ and φ directions
$f_r^l, f_\theta^l, f_r^m, f_{1\theta}^m, f_{2\theta}^m$ and f_θ^r	Drag correction factors, functions of δ
f_i^j	force vector on the particle, superscript specifies the source of the force
g	magnitude of the gravity vector, $g=9.81 \text{ g/s}^2$
$g_\varphi^r, g_\varphi^l, g_{1\varphi}^m$ and $g_{2\varphi}^m$	torque correction factors, functions of δ

k	particle deposition rate constant
k_B	Boltzmann constant, 1.3805×10^{-23} J/K
K_1, K_2, K_3 and K_4	coefficients that appear in equations S1
N_G	gravity group, $N_G = 2a_p^2(\rho_p - \rho_f)g/9\nu U$
N_{Lo}	London group, $N_{Lo} = A/9\pi\alpha_p^2 U$
N_{PE}	Peclet number, $N_{PE} = Ud_s/D_\infty$
N_R	relative size group, $N_R = a_p/a_s$
p	Defined in equation S2, $p = a_s/b$
r	radial coordinate
r^*	dimensionless radial coordinate, $r^* = r/a_s$
s_1	$s_1 = (f_\theta^t g_\phi^r - f_\theta^r g_\phi^t)/g_\phi^r$
s_2	$s_2 = (f_\theta^r g_{1\phi}^m - y^+ f_{1\theta}^m g_\phi^r)/g_\phi^r$
s_3	$s_3 = (f_\theta^r g_{2\phi}^m - y^+ f_{2\theta}^m g_\phi^r)/g_\phi^r$
t	time variable
T	absolute temperature
U	approach velocity
V	liquid flow field
y	$y = (r - a_s)$
$a(\delta, a_p, \lambda_e)$	retardation correction, a function of δ , a_p and λ_e
δ	surface-to-surface separation between the collector and the particle
δ^+	dimensionless parameter, $\delta^+ = \delta/a_p$
f	porosity of the porous media
η_0	the single collector contact efficiency
η_D, η_I and η_G	collection efficiencies due to diffusion, sedimentation and interception, respectively
θ	angular coordinate

φ	angular coordinate
κ	Debye-Huckel reciprocal length
λ_e	wavelength of electron oscillation, $\lambda_e = 100nm$
ν	viscosity of suspension
π	circular constant, $\pi = 3.14$
ρ_f	the density of the liquid
ρ_p	the density of the particle
ψ	stream function
u	Darcy velocity
u_r, u_θ, u_ϕ	the velocity vectors in different directions

References

- [1] P.G. Tratnyek, R.L. Johnson, Nanotechnologies for environmental cleanup, *Nano Today*, 1 (2006) 44-48.
- [2] K.D. Grieger, A. Fjordbøge, N.B. Hartmann, E. Eriksson, P.L. Bjerg, A. Baun, Environmental benefits and risks of zero-valent iron nanoparticles (nZVI) for in situ remediation: Risk mitigation or trade-off?, *Journal of Contaminant Hydrology*, 118 (2010) 165-183.
- [3] W.-x. Zhang, Nanoscale Iron Particles for Environmental Remediation: An Overview, *Journal of Nanoparticle Research*, 5 (2003) 323-332.
- [4] S.O. Hara, T. Krug, J. Quinn, C. Clausen, C. Geiger, Field and laboratory evaluation of the treatment of DNAPL source zones using emulsified zero-valent iron, *Remediation Journal*, 16 (2006) 35-56.
- [5] J. Quinn, C. Geiger, C. Clausen, K. Brooks, C. Coon, S. O'Hara, T. Krug, D. Major, W.-S. Yoon, A. Gavaskar, T. Holdsworth, Field Demonstration of DNAPL Dehalogenation Using Emulsified Zero-Valent Iron, *Environmental Science & Technology*, 39 (2005) 1309-1318.
- [6] T. Phenrat, H.-J. Kim, F. Fagerlund, T. Illangasekare, G.V. Lowry, Empirical correlations to estimate agglomerate size and deposition during injection of a polyelectrolyte-modified Fe⁰ nanoparticle at high particle concentration in saturated sand, *Journal of contaminant hydrology*, 118 (2010) 152-164.
- [7] T. Phenrat, N. Saleh, K. Sirk, R.D. Tilton, G.V. Lowry, Aggregation and sedimentation of aqueous nanoscale zerovalent iron dispersions, *Environmental science & technology*, 41 (2007) 284-290.
- [8] T. Phenrat, N. Saleh, K. Sirk, R.D. Tilton, G.V. Lowry, Aggregation and Sedimentation of Aqueous Nanoscale Zerovalent Iron Dispersions, *Environmental Science & Technology*, 41 (2006) 284-290.
- [9] D.W.E. Xiao-qin Li, and Wei-xian Zhang, Zero-Valent Iron Nanoparticles for Abatement of Environmental Pollutants: Materials and Engineering Aspects, *Critical Reviews in Solid State and Materials Sciences*, 31 (2006) 12.

- [10] D.W. Elliott, W.-x. Zhang, Field Assessment of Nanoscale Bimetallic Particles for Groundwater Treatment, *Environmental Science & Technology*, 35 (2001) 4922-4926.
- [11] T. Raychoudhury, N. Tufenkji, S. Ghoshal, Aggregation and deposition kinetics of carboxymethyl cellulose-modified zero-valent iron nanoparticles in porous media, *Water research*, 46 (2012) 1735-1744.
- [12] T. Phenrat, H.-J. Kim, F. Fagerlund, T. Illangasekare, R.D. Tilton, G.V. Lowry, Particle size distribution, concentration, and magnetic attraction affect transport of polymer-modified Fe⁰ nanoparticles in sand columns, *Environmental science & technology*, 43 (2009) 5079-5085.
- [13] P. Jiemvarangkul, W.-x. Zhang, H.-L. Lien, Enhanced transport of polyelectrolyte stabilized nanoscale zero-valent iron (nZVI) in porous media, *Chemical Engineering Journal*, 170 (2011) 482-491.
- [14] N. Saleh, K. Sirk, Y. Liu, T. Phenrat, B. Dufour, K. Matyjaszewski, R.D. Tilton, G.V. Lowry, Surface modifications enhance nanoiron transport and NAPL targeting in saturated porous media, *Environmental Engineering Science*, 24 (2007) 45-57.
- [15] J.T.N. Richard L. Johnson, Reid O'Brien Johnson, , Injection of Nano Zero-Valent Iron for Subsurface Remediation: A Controlled Field-Scale Test of Transport, *Proceedings of the 7th International Conference on Remediation of Chlorinated and Recalcitrant Compounds*, 6.
- [16] P. Jiemvarangkul, W.-x. Zhang, H.-L. Lien, Enhanced transport of polyelectrolyte stabilized nanoscale zero-valent iron (nZVI) in porous media, *Chemical Engineering Journal*, In Press, Corrected Proof.
- [17] M.M. Krol, A.J. Oleniuk, C.M. Kocur, B.E. Sleep, P. Bennett, X. Zhong, D.M. O'Carroll, A Field-Validated Model for In Situ Transport of Polymer-Stabilized nZVI and Implications for Subsurface Injection, *Environmental science & technology*, (2013).
- [18] E.D. Vecchia, M. Luna, R. Sethi, Transport in porous media of highly concentrated iron micro-and nanoparticles in the presence of xanthan gum, *Environmental science & technology*, 43 (2009) 8942-8947.
- [19] P.R. Johnson, N. Sun, M. Elimelech, Colloid transport in geochemically heterogeneous porous media: Modeling and measurements, *Environmental science & technology*, 30 (1996) 3284-3293.
- [20] M.J. Truex, V.R. Vermeul, D.P. Mendoza, B.G. Fritz, R.D. Mackley, M. Oostrom, T.W. Wietsma, T.W. Macbeth, Injection of Zero-Valent Iron into an Unconfined Aquifer Using Shear-Thinning Fluids, *Ground Water Monitoring & Remediation*, 31 (2011) 50-58.
- [21] Y.-T. Wei, S.-C. Wu, C.-M. Chou, C.-H. Che, S.-M. Tsai, H.-L. Lien, Influence of nanoscale zero-valent iron on geochemical properties of groundwater and vinyl chloride degradation: A field case study, *Water Research*, 44 (2010) 131-140.
- [22] F. He, M. Zhang, T. Qian, D. Zhao, Transport of carboxymethyl cellulose stabilized iron nanoparticles in porous media: Column experiments and modeling, *Journal of Colloid and Interface Science*, 334 (2009) 96-102.
- [23] P. Bennett, F. He, D. Zhao, B. Aiken, L. Feldman, In situ testing of metallic iron nanoparticle mobility and reactivity in a shallow granular aquifer, *Journal of contaminant hydrology*, 116 (2010) 35-46.
- [24] R.L. Johnson, J.T. Nurmi, G.S. O'Brien Johnson, D. Fan, R.L. O'Brien Johnson, Z. Shi, A.J. Salter-Blanc, P.G. Tratnyek, G.V. Lowry, Field-scale transport and transformation of carboxymethylcellulose-stabilized nano zero-valent iron, *Environmental science & technology*, 47 (2013) 1573-1580.
- [25] S. Kanel, R. Goswami, T. Clement, M. Barnett, D. Zhao, Two dimensional transport characteristics of surface stabilized zero-valent iron nanoparticles in porous media, *Environmental science & technology*, 42 (2007) 896-900.

- [26] S.R. Kanel, R.R. Goswami, T.P. Clement, M.O. Barnett, D. Zhao, Two Dimensional Transport Characteristics of Surface Stabilized Zero-valent Iron Nanoparticles in Porous Media, *Environmental Science & Technology*, 42 (2007) 896-900.
- [27] T. Phenrat, A. Cihan, H.-J. Kim, M. Mital, T. Illangasekare, G.V. Lowry, Transport and Deposition of Polymer-Modified Fe⁰ Nanoparticles in 2-D Heterogeneous Porous Media: Effects of Particle Concentration, Fe⁰ Content, and Coatings, *Environmental Science & Technology*, 44 (2010) 9086-9093.
- [28] N.R.C. Committee on Source Removal of Contaminants in the Subsurface, *Contaminants in the subsurface: Source zone Assessment and remediation*, in, Washington, D.C., 2005.
- [29] C.M. Cirtiu, T. Raychoudhury, S. Ghoshal, A. Moores, Systematic comparison of the size, surface characteristics and colloidal stability of zero valent iron nanoparticles pre-and post-grafted with common polymers, *Colloids and Surfaces A: Physicochemical and Engineering Aspects*, 390 (2011) 95-104.
- [30] R. Rajagopalan, C. Tien, Trajectory analysis of deep-bed filtration with the sphere-in-cell porous media model, *AIChE Journal*, 22 (1976) 523-533.
- [31] N. Tufenkji, M. Elimelech, Correlation Equation for Predicting Single-Collector Efficiency in Physicochemical Filtration in Saturated Porous Media, *Environmental Science & Technology*, 38 (2003) 529-536.
- [32] J.Y. Chung, K.J. Lee, Analysis of colloid transport and colloidal size effect using filtration theory, *Annals of Nuclear Energy*, 19 (1992) 145-153.
- [33] J.A. Brant, J. Labille, C.O. Robichaud, M. Wiesner, Fullerol cluster formation in aqueous solutions: Implications for environmental release, *Journal of Colloid and Interface Science*, 314 (2007) 281-288.
- [34] J. Jiang, G. Oberdörster, P. Biswas, Characterization of size, surface charge, and agglomeration state of nanoparticle dispersions for toxicological studies, *Journal of Nanoparticle Research*, 11 (2009) 77-89.
- [35] K.L. Chen, M. Elimelech, Influence of humic acid on the aggregation kinetics of fullerene (C₆₀) nanoparticles in monovalent and divalent electrolyte solutions, *Journal of Colloid and Interface Science*, 309 (2007) 126-134.
- [36] T. Phenrat, N. Saleh, K. Sirk, H.-J. Kim, R. Tilton, G. Lowry, Stabilization of aqueous nanoscale zerovalent iron dispersions by anionic polyelectrolytes: adsorbed anionic polyelectrolyte layer properties and their effect on aggregation and sedimentation, *Journal of Nanoparticle Research*, 10 (2008) 795-814.
- [37] D. Lin, X. Tian, F. Wu, B. Xing, Fate and Transport of Engineered Nanomaterials in the Environment All rights reserved. No part of this periodical may be reproduced or transmitted in any form or by any means, electronic or mechanical, including photocopying, recording, or any information storage and retrieval system, without permission in writing from the publisher, *J. Environ. Qual.*, 39 (2010) 1896-1908.
- [38] C. Su, R.W. Puls, T.A. Krug, M.T. Watling, S.K. O'Hara, J.W. Quinn, N.E. Ruiz, A two and half year-performance evaluation of a field test on treatment of source zone tetrachloroethene and its chlorinated daughter products using emulsified zero valent iron nanoparticles, *water research*, (2012).
- [39] M. Elimelech, X. Jia, J. Gregory, R. Williams, *Particle deposition & aggregation: measurement, modelling and simulation*, Butterworth-Heinemann, 1998.
- [40] J. Bergendahl, D. Grasso, Prediction of colloid detachment in a model porous media: hydrodynamics, *Chemical Engineering Science*, 55 (2000) 1523-1532.
- [41] N. Tufenkji, M. Elimelech, Spatial distributions of *Cryptosporidium* oocysts in porous media: Evidence for dual mode deposition, *Environmental science & technology*, 39 (2005) 3620-3629.

- [42] N. Tufenkji, M. Elimelech, Correlation equation for predicting single-collector efficiency in physicochemical filtration in saturated porous media, *Environmental science & technology*, 38 (2004) 529-536.
- [43] R. Rajagopalan, C. Tien, Trajectory analysis of deep - bed filtration with the sphere - in - cell porous media model, *AIChE Journal*, 22 (1976) 523-533.
- [44] K.E. Nelson, T.R. Ginn, Colloid Filtration Theory and the Happel Sphere-in-Cell Model Revisited with Direct Numerical Simulation of Colloids, *Langmuir*, 21 (2005) 2173-2184.
- [45] B.D. editor, *Coagulation and Flocculation: Theory and Applications*, Book, (1993) 720.

Chapter 5

Transport of polyelectrolyte-coated zero valent iron nanoparticles in a sand tank: Effects of nanoparticle concentration and injection velocity

by

Jing Li, Subhasis Ghoshal*

Department of Civil Engineering,

McGill University, Montreal, Canada H3A 2K6

Keywords: NZVI particles, colloid transport, viscosity, carboxymethyl cellulose, DLVO theory calculations, single collector efficiency prediction, ionic strength

*Corresponding author, Department of Civil Engineering, McGill University, 817 Sherbrooke Street West, Montreal, QC, Canada H3A 2K6, e-mail: subhasis.ghoshal@mcgill.ca,

Tel: (514) 398-6867, Fax: (514) 398-7361

To be published on Environmental Science & Technology

5.1 Introduction

Direct injection of nanoscale zero-valent iron (NZVI) particles into the subsurface to restore groundwater contamination is a promising *in situ* remediation technology. Zero-valent iron has a high redox potential, and combined with the high specific surface area for nanoparticles can yield very high rates of reduction reactions for many chlorinated solvents, nitrates, heavy metals, pesticides etc. [1-7]. The delivery and distribution of NZVI into the contaminated zone is challenging because these particles tend to exhibit a very high degree of deposition and filtration in subsurface porous media. Several field demonstrations have indicated that NZVI particles cannot be effectively or readily transport to DNAPLs zones [8-11]. NZVI particles are magnetic and thus tend to aggregate extensively, particularly at the g/L concentrations required for remediation [12]. These aggregates are retained extensively in the porous media due to physico-chemical deposition as well as by physical straining [13-18].

Coating NZVI with polymers, polyelectrolytes or surfactants, for a higher degree of colloidal stabilization through repulsive steric or electrosteric contributions of the coating materials reduces the extent of aggregation as well as the extent of retention in porous media due to transport. Several different non-toxic polymers and macromolecules have been shown to colloidally stabilize NZVI to a significant extent, and these include carboxymethyl cellulose (CMC) [19], polyacrylic acid (PAA) [20], poly-styrene sulfonate (PSS) [13], guar gum [21] and polyaspartate (PAP) [14, 22]. Although polymers improve the colloidal stabilization of NZVI, there is still some aggregation of NZVI, particularly at g/L levels, which can contribute to its high retention in porous media [15, 18, 23, 24].

The deposition of NZVI in subsurface porous media is also influenced by groundwater composition, the fluid velocity, porous media grain size, and the Fe(0) content of NZVI which is

related to its magnetic activity [13, 16]. Polymer-coated NZVI is retained to a lesser extent at higher pore water velocities and this is caused by the significant drag forces on deposited particles at higher velocities that can result in detachment of deposited particles [25-27]. At high ionic strengths and particularly in the presence of multivalent cations the colloidal stability and transport of coated-NZVI is diminished due to the charge-screening effect of the cations.

Recently, Tosco et al have extensively studied the effects of the shear-thinning fluids (such as guar gum and xanthan gum) used to stabilize NZVI particles on the transport of NZVI [28]. They found that the fluid viscosity, flow velocity, and the changes in porous media permeability as important factors are influencing particle transport with shear-thinning fluids. It was reported that at high xanthan gum concentration (3 g/L) required for NZVI stabilization, very high pressure drops or flow velocities were required to achieve significant extent of NZVI transport [29].

The above studies on transport of NZVI have been conducted in 1-D column studies. Additional factors which might impact the fate and transport of polyelectrolyte stabilized particles are likely to be related to up-scaling. To address the challenges of interpreting the scaling-up effects in NZVI transport, several studies have used 2-dimensional tanks systems packed with homogenous or heterogeneous media to investigate the transport of NZVI particles. Kanel et al. used a tank of dimensions of 0.5 m (length) \times 0.29 m (height) \times 0.02 m (width) to visually observe the transport of a pulse of injected bare NZVI and PAA-stabilized NZVI [30]. The results showed that bare NZVI particles were not transported in the porous media, while, PAA-stabilized NZVI were transported in the tank, although the particles migrated downward within the process of moving forward, due to gravity effects. Phenrat et al employed a 2-D tank (0.30 m (length) \times 0.18 m (height) \times 0.025 m (width)) which was heterogeneously layered with sands of various grain diameters (coarse to fine) was used to assess the effects on transport caused by injection of various concentrations

(0.3 g/L, 3 g/L and 6 g/L) of polyelectrolyte-stabilized NZVI, as well as the effects of particle Fe^0 content (24% and 10% reflecting particles at various states of oxidation) and the coating layer thickness (30 nm and 70 nm) on transport [23]. The results show that at low concentration (0.3 g/L), NZVI particles transported more extensively than those at high concentrations (3 g/L and 6 g/L). The high content of Fe^0 was unfavorable for NZVI transport as it promoted more aggregation during transport, and polystyrene sulfonate (PSS) coating of 70 nm improved the transport of NZVI compared to particles coated with 30 nm of PSS. The total eluted NZVI mass at the end of the water flushing period that followed the injection period for 0.3 g/L, 3 g/L and 6 g/L NZVI suspensions injected were 80%, 70% and 40%, respectively. Further, the excess polymer in a concentrated MRNIP2 dispersion decreased its transport. For the oxidized NZVI particles the total mass fraction eluted was 65% of elution (at 6 g/L), while fresh NZVI particles showed 50% of elution at the identical concentration. For all of these cases much of the transport was attained by channeling through the coarse grained sand (higher conductivity) and by-passing of the lower conductivity (lower porosity sand) was evident. Darko-Kagya and Reddy [31] investigated the transport of bare and lactate modified NZVI particles in homogenous and heterogeneous (bilayered) porous media under typical pressurized groundwater flow conditions. Different injection pressure gradients (0.5, 0.8, 1 and 2 psi) were employed to injection NZVI particles. The 2-D tank had internal dimensions of 20 cm×20 cm×5 cm with 9 ports on the back side of the tank for sampling sand. During the experiment, 2-3 PV of 4 g/L NZVI suspension was injected. The results showed that higher pressure gradients enhanced the transport. Lactate modified NZVI could transport more uniformly than bare NZVI particles. In addition, the solid phase iron concentrations deposited in sand decreased with distance from the inlet to the outlet and increased from the top to the bottom of the test cell, indicating that the particles underwent aggregation and gravity sedimentation during transport. For heterogeneous (layered) porous media, NZVI particles transported through the high-porosity and high permeability soil layer. Overall, the study showed that the non-uniform distribution of NZVI particles and lactate modified NZVI particles occurred under two-dimensional transport conditions.

In this study, the spatial and temporal distribution of carboxymethyl cellulose (CMC) (which is demonstrated to be very efficient on stabilizing NZVI particles, see SI section 5.S1 Table 5.S1 for the review of 22 pioneered papers on CMC stabilized NZVI) -stabilized NZVI suspensions injected into a Plexiglas 2D sand tank 2-D tank (0.70 m (length) \times 0.35 m (height) \times 0.02 m (width)) was assessed. The concentrations of CMC-NZVI in the aqueous phase at various locations in the tank were assessed, along with changes in CMC-NZVI aggregate size during the transport. The spatial distribution of deposited CMC-NZVI, conductivity changes caused by injecting CMC-NZVI suspension and the changes in pressure drop during NZVI suspension injection at two-different polyelectrolyte and NZVI were assessed. The first set experiments were conducted by packing three sizes of sand (coarse sand, intermediate sand and fine sand) into the tank in each trial, respectively, to study the effects of sand size on particle transport and aggregation during injection of 1 g/L NZVI in 1 g/L CMC solution. The second set experiments were conducted with two different NZVI concentrations (1 g/L and 3 g/L) in 1 g/L or 2 g/L 700K CMC solution with the intermediate sand to determine the relationship between aggregation and CMC-NZVI concentrations in the suspension injected, as well as to investigate the effect of the suspension viscosity on transport. Additionally, two different injection velocities were also tested to display the effect of flow velocity on viscous 700K CMC medium of the suspension and its effect on NZVI transport performance. The extent of NZVI transport was characterized by sampling aqueous samples from 9 sample ports at 20 minutes interval and from 3 effluents ports at 10 minutes interval.

The transient NZVI concentrations in porous media during injection and subsequent aqueous flushing evaluated in this study has not been reported to date and provides unique insight on NZVI transport. Furthermore, this is the first tank study to report on the effectiveness

as of CMC as a stabilizing polymer. The high effectiveness of 700K CMC as a stabilizing polymer has been established in the previous chapters of this thesis.

5.2 Materials and Methods

CMC-coated NZVI Particles. The sodium salt of carboxymethyl cellulose with 700,000 Da (referred as 700K CMC) was obtained from Sigma Aldrich. NZVI particles were supplied by Golder Associates Ltd. A stock solution of bare NZVI at 190 g/L (as Fe) was stored under an inert N₂ atmosphere in a glove box. CMC was dissolved in a 0.5 mM NaHCO₃ electrolyte solution to obtain 1 g/L CMC solution or dissolved in DI water to obtain 2 g/L CMC solution. The ionic strength of these two solutions were identical given that Na is dissolved from the sodium salt of CMC. Thirty mL or 90 mL of the original stock NZVI slurry were dispersed into 5.6 L above CMC solutions respectively to make 1 g/L and 3 g/L CMC-NZVI suspensions, respectively.

Particle Characterization. The diameters of individual NZVI particles in different CMC solutions were characterized by nanoparticle tracking analysis (NTA) (Nanosight NTA2.2 LM14C) at NZVI concentration of 40 mg/L. The electrophoretic mobility of NZVI particles was measured by laser doppler velocimetry (ZetaSizer Nano ZS, Malvern). The mean aggregate diameters of CMC-NZVI particles at different concentrations as well as of different samples from different sample ports during transport were determined by a microscopy (Olympus, BX51). Additional details are provided in SI, Section 5.S2.

Homogenous Two Dimensional (2-D) Tank. A pilot scale 2-D tank (Plexiglass, length=0.7 m, height=0.35 m, width=0.02 m, as shown in **Figure 5.1a**), equipped with nine sampling ports in the front side of the tank (1/8 in. M-NPT Mininert valves), was used in this study to investigate the transport of CMC-NZVI particles. There were three inlet ports, connected to a narrow

percolated diffuser (ID, ¼ inch), installed in one end the tank for electrolyte flow with a rate of 12 mL/min in each port. Three outlet ports were also fabricated on the other end of the tank. Another narrow diffusor made of PTFE (OD=3/16 inch, ID= 1/8 inch, length=30 cm, with 100 holes of 0.3 mm diameter each along a line on one side of the diffuser) was installed. A filter (Spectrum labs, Spectra/mesh macroporous filters, open area=100 µm), was positioned 3 cm from the inlet side of the tank. The hole line of the narrow diffuser was fixed pointing towards the flow direction and in the centre of the tank. This diffuser was connected to 3 injection ports in the inlet end of the tank, from which CMC-NZVI was injected into the diffuser by peristaltic pumps (Masterflex L/S, Compact pump) at 19.2 mL/min or 8.4 mL/min, resulting in the desired flow velocity of 0.96 and 0.40 cm/min. The ends of the tubes connected to the outlets were positioned higher than the top of the tank to ensure uniform injection along the height of the tank.

Three types of sand with average diameters of 1140 µm (coarse sand), 340 µm (intermediate sand) and 180 µm (fine sand) (as described in Chapter 4) were used to yield different uniform sand tanks.

A deoxygenated water supply system provides distilled water with constant flow rate from a water head, to the tank (shown in **Figure 5.1b**). 3 mM NaHCO₃ (which is of equivalent IS of 1 g/L CMC-NZVI suspension with 0.5 mM NaHCO₃, (because 1 g/L CMC solution contributed to 2.5 mM Na⁺ into the suspension), resulting in a total IS of 3 mM of the suspension, as described in Chapter 3 was pumped into a big water reservoir, followed by constantly flowing into the column from the top side (0.5 L/min). The concentration of dissolved oxygen in the water at the bottom of the column was measured to be in the range of 0.5-1.5 mg/L by an oxygen meter (YSI, 5000, YSI 5010BOD probe). This constant water level provided a constant flow rate (12 mL/min in each port) for the 3 inputs.

Tracer Test. After packing the tank with sand, the tank was saturated by flushing with the electrolyte for 5 hrs (around 6.3 pore volume). Then, 1 pore volume (around 1.72 L) of red dye (disodium 6-hydroxy-5-((2-methoxy-5-methyl-4-sulfophenyl)azo)-2-naphthalenesulfonate, food grade, The ADI group, USA) (degassed) at the concentration of 10 mg/L was injected into the tank through the 3 injection ports at the flow rate of 12 mL/min in each port. The electrolyte flow was switched off during dye injection process, which would be switched on after dye injection to flush the tank for 5 hours at the rate of 12 mL/min in each outlet to complete uniform the surface charge of the packed sand. A series of images were taken during dye injection and electrolyte flushing process to verify the flow pattern in the tank. Then, the electrolyte flow was switched off again to proceed to inject NZVI suspension.

CMC-NZVI Particle Transport. In all cases, 3 pore volumes (~5.3 L) of CMC-NZVI particles in 1 g/L CMC or in 3 mM NaHCO₃ solution were injected into the tank through the 3 injection ports, followed by flushing of 3 PVs of degassed 3 mM NaHCO₃ electrolyte. During the injection process, NZVI suspension was shaken on a shaker (InFors HT, Labotron, Switzerland) at 300 rpm/min). A time series of images was taken to illustrate the transport of NZVI particles. Additionally, aqueous phase samples (1 mL) were spatially taken out from the 9 sampling ports at intervals of 20 minutes and effluent at each of 3 outlets was collected at the time intervals of 10 minutes. The total effluent was also collected from the beginning of the injection process to analyze the total mass of NZVI particles, which could transport out the tank. Prior to injecting NZVI suspension, the water head was fixed in the tank system to provide constant flow and to determine to the conductivity of the tank. After NZVI suspension injection process, the effluent of the electrolyte was also collected to determine the conductivity of the tank. All these solution samples were digested in acid solution and then measured by AAS to determine the Fe

concentrations. At the end of experiment, 18 sand samples were collected at 18 different locations (see Supporting Information for the locations of these 18 points), followed by acid digestion and AAS measurement to determine the total Fe concentration. From the dry weight of the sand, solid phase concentrations were determined to describe the spatial distribution of deposited NZVI particles.

Measurement of Pressure Drop in the Tank. The pressure drop measurement was conducted separately from the transport experiments. Eleven narrow piezometers were fixed vertically in the sample ports to measure water levels caused by injecting different solutions (see Figure 5.S1 in SI). These eleven ports were located at four distances from the injection ports and these four distances were assigned as ports (I), ports (II), ports (III) and ports [32]. In ports (I), the water levels of the two tubes should be the same, due to the same distance to the injection ports, whose mean value represented the pressure drop in ports (I). Similarly, the mean of the three water levels of the three tubes in ports (II) represents the pressure drop there, and so on so forth for ports (III) and ports [32]. Six experiments were conducted with different solutions and injection flow velocity (pure water at 0.96 cm/min, 1 g/L 700K CMC solution at 0.96 cm/min, 1 g/L 700K CMC with 1 g/L NZVI at 0.96 cm/min, 2 g/L 700K CMC solution at 0.96 cm/min and 2 g/L 700K CMC solution at 0.40 cm/min). All these 5 experiments were conducted in the tank packed with intermediate sand ($D_{50}=340$ μm).

Colloid filtration theory (CFT) calculations. The classical clean-bed colloid filtration theory and T&E equation [25, 33, 34] were employed to predict the transport distance of NZVI particles under different conditions (see section 5.S4 in SI for the details). The scenarios for the calculations were as follows: The mean diameter of NZVI aggregates in T1, M1 and B1 at the time, when the mean maximum C/C_0 value obtained, was determined by optical microscope.

Then, the mean diameter value was taken into T&E equation to predict the single collector contact efficiency followed by the attachment efficiency calculation (by using the classical colloid filtration theory). The determined attachment efficiency was combined with the mean maximum C/C_0 values at T2, M2 and B2 at T3, M3 and B3 as well as at T4, M4 and B4 to predict the distance at which NZVI particles could transport. The predicted distances were compared with the experimental distances to reveal the deposition mechanics of NZVI particles under different conditions.

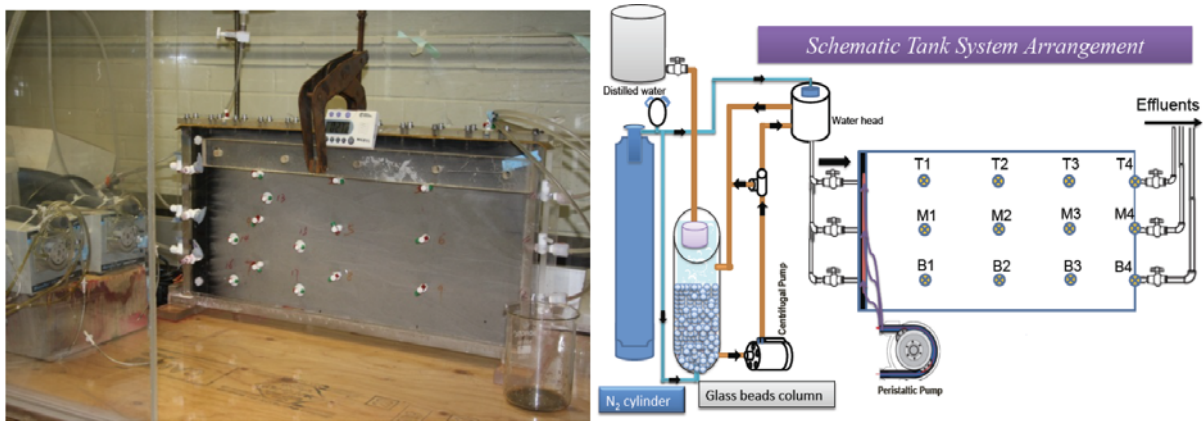


Figure 5.1. (a) The image of the tank; (b) Schematic of 2-D tank system.

5.3 Results and Discussion

5.3.1 Particle Characterization

The corresponding mean hydrodynamic diameters of CMC-NZVI particles (15 mg/L Fe in 1 g/L and 2 g/L CMC solutions) were 61 and 75 nm measured by NTA, respectively. The average electrophoretic mobility (EPM) of CMC-NZVI particles at 1 g/l was $-5.65 \text{ } \mu\text{m s}^{-1} \text{ V}^{-1} \text{ cm}$, corresponding to -48.6 mV of Zeta potential. The mean diameters of NZVI particles measured by microscopy were 1000 nm and 568 nm for 1 g/L NZVI in 1 g/L and 2 g/L CMC solutions, respectively. The smaller mean diameter of NZVI in 2 g/L CMC solution was attributable to the

much better stabilization effect of CMC solution with higher concentration. The mean diameters of NZVI particles measured by DLS were 334 nm and 218 nm for 50 mg/L NZVI in 1 g/L and 2 g/L CMC solutions, respectively.

5.3.2 Flow test by Dye Tracer

The flow of tracer injected from the three injection ports shows in **Figure 5.S2**, which displays the uniform flow of tracer in the tank. This result shows that the flow path is horizontally uniform in the tank. Further, the transport of NZVI particles can also be roughly judged by the color change along the flow distance, as shown in Figure 5.S3.

5.3.3 The Effect of Sand Size on NZVI Transport

Previous studies have shown that the porous media size is one of factors controlling the transport of NZVI particles [25, 35] as discussed in the previous Chapter. The values showed in Figures 5.2, 5.3 and 5.4 displays the effect of sand size on the transport of NZVI particles in 1 g/L 700K CMC solution. The results of aqueous NZVI concentrations in these figures were obtained under identical conditions of particles suspension composition (1 g/L NZVI particles in 1 g/L 700K CMC solution), and injection velocity of 0.96 cm/min. The mean of C/C_0 values at 15 cm, 32.5 cm and 50 cm from the injection point (as determined from the three sampling ports) and at the effluent ports were 0.90, 0.61 and 0.51 and 0.37, respectively, with the coarse sand (Figure 2.). The maximum of C/C_0 values at the sampling points for the intermediate experiment were 0.82, 0.51, 0.38 and 0.29, and 0.73, 0.49, 0.32 and 0.11 with the the fine sand (shown in Figures 5.3 and 5.4, respectively). These results indicate that NZVI particles are more easily transported in coarser sands. This result is reasonable and consistent with previous studies [25,

35] and Chapter 3. Moreover, C/C_0 values in the tank decrease more rapidly with distance from the injection point in the fine sand, than in the coarsest sand.

Several mechanisms can contribute to the difference of C/C_0 values with distance between these three sands—first, more attachment of NZVI particles occurred in the fine sand due to the larger surface area available for depositions; and secondly, there was likely more significant straining of NZVI in the fine sand. In order to clarify the effects of aggregation on NZVI deposition, the advection-dispersion equation is employed to calculate the deposition rate changes caused by NZVI aggregation. Additionally, C/C_0 values at three ports at a fixed distance from the injection port do not show a very big difference in all three sands, indicating a very uniform transport of CMC-NZVI particles along the height of the tank.

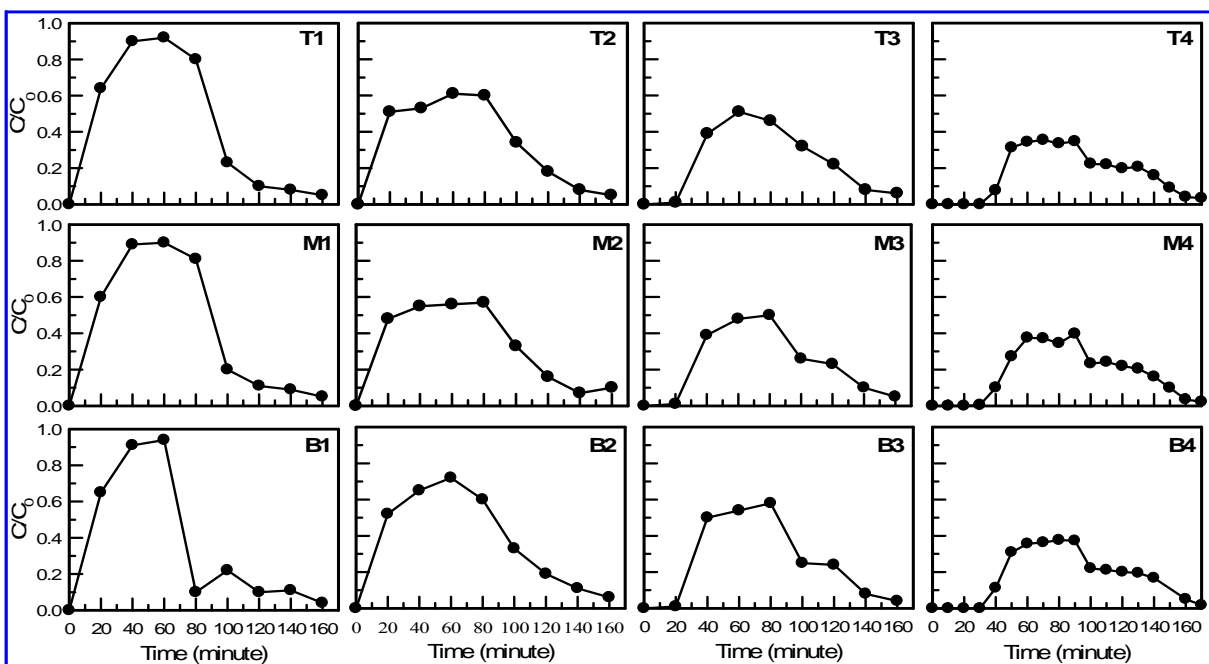


Figure 5.2. The iron concentration distribution in the aqueous phase (1 g/L NZVI in 1 g/L CMC solution), packed with coarse sand ($d_{50}=1140 \mu\text{m}$), at injection velocity of 0.96 cm/min.

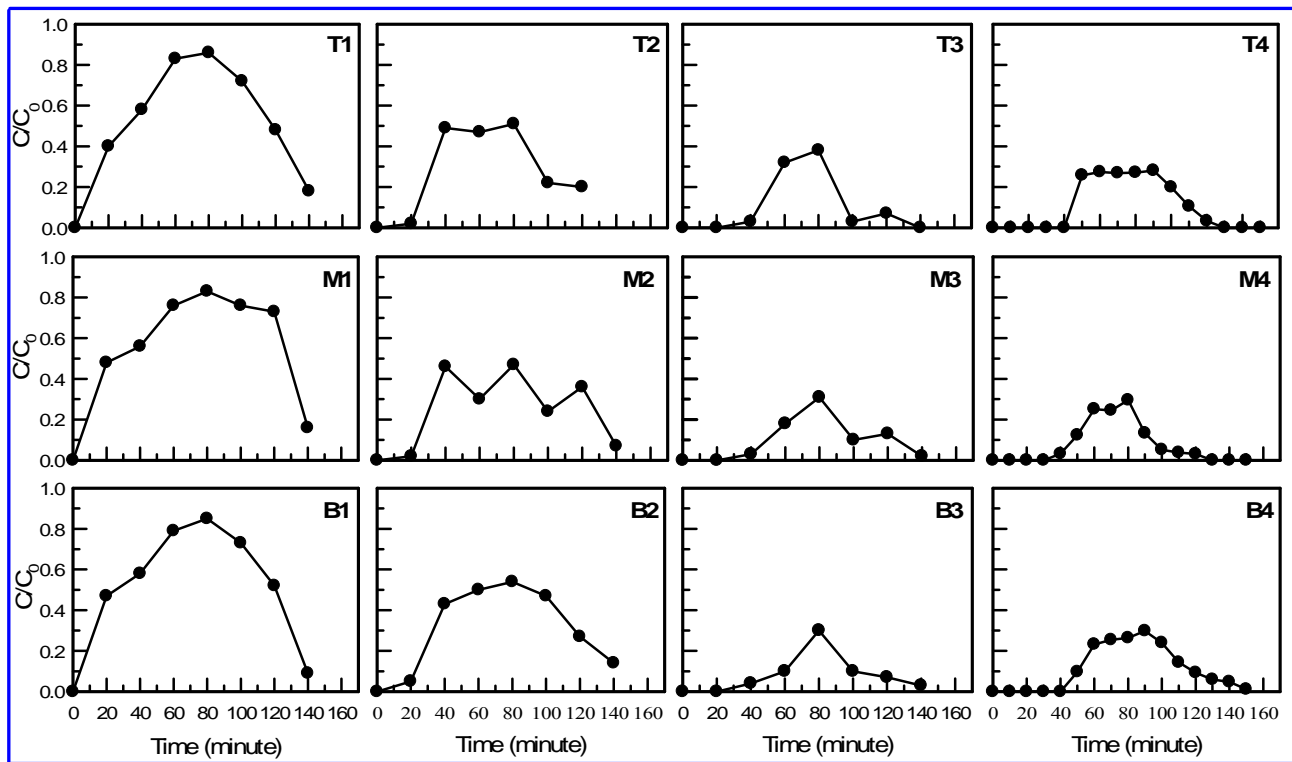


Figure 5.3. The iron concentration distribution in the aqueous phase (1 g/L NZVI in 1 g/L CMC solution); packed with intermediate sand ($d_{50}=340 \mu\text{m}$), at injection velocity of 0.96 cm/min.

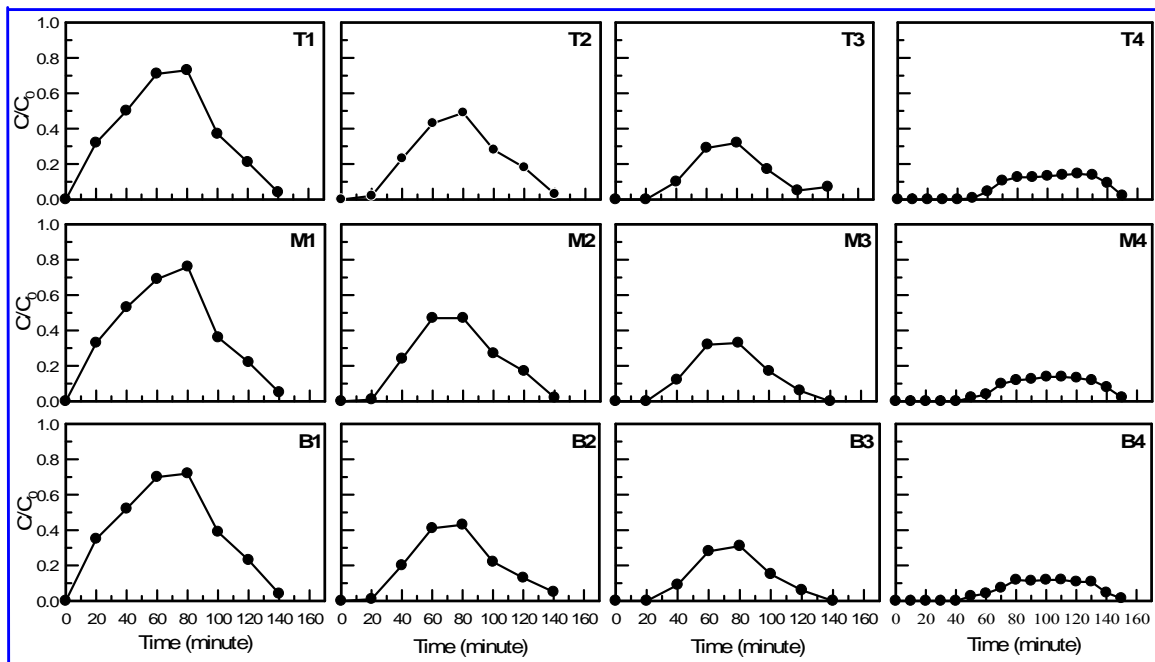


Figure 5.4. The iron concentration distribution in the aqueous phase (1 g/L NZVI in 1 g/L CMC solution), packed with fine sand ($d_{50}=180 \mu\text{m}$), at injection velocity of 0.96 cm/min.

5.3.4 The Effect of CMC concentration on NZVI Particle Transport

Several studies reported that NZVI particles in relative high polymer or polyelectrolyte solutions showed very high transport [21, 36, 37]. This is partly due to the reduction of single collector contact efficiency of NZVI particles with the increase of the viscosity of suspension (as demonstrated in Chapter 3), which in turn results in the reduction of deposition rate and an increase in transport. Additionally, a large amount of free polymer/polyelectrolyte molecules existed in the suspension can remain on the collector surface and then reduce the attachment of NZVI particles [10]. On the other hand, several studies pointed out that the high viscosity of NZVI suspension caused by adding polymer/polyelectrolyte would induce resistance for flow to move forward, due to the viscosity of the fluid [28, 29]. To assess how higher polymer concentrations impact transport of CMC-NZVI in the sand-tank, the transport experiment of

NZVI particles in 2 g/L CMC solution was also conducted and the results obtained in 2 g/L CMC solution were compared with those obtained in 1 g/L CMC solution under identical NZVI suspension injection conditions represented by 3 g/L NZVI at 0.96 cm/min injection velocity. The results are shown in Figures 5.5 and 5.6. C/C_0 values shown in Figure 5.5 at all 12 ports are much higher than those in Figure 5.6. This indicates that the higher CMC concentration in NZVI suspension is favourable to the transport of NZVI particles. The result demonstrates that at the injection velocity of 0.96 cm/min, higher viscosity at a CMC dose of 2 g/L did not impede transport likely due to shear-thinning effects and increased stabilization of NZVI.

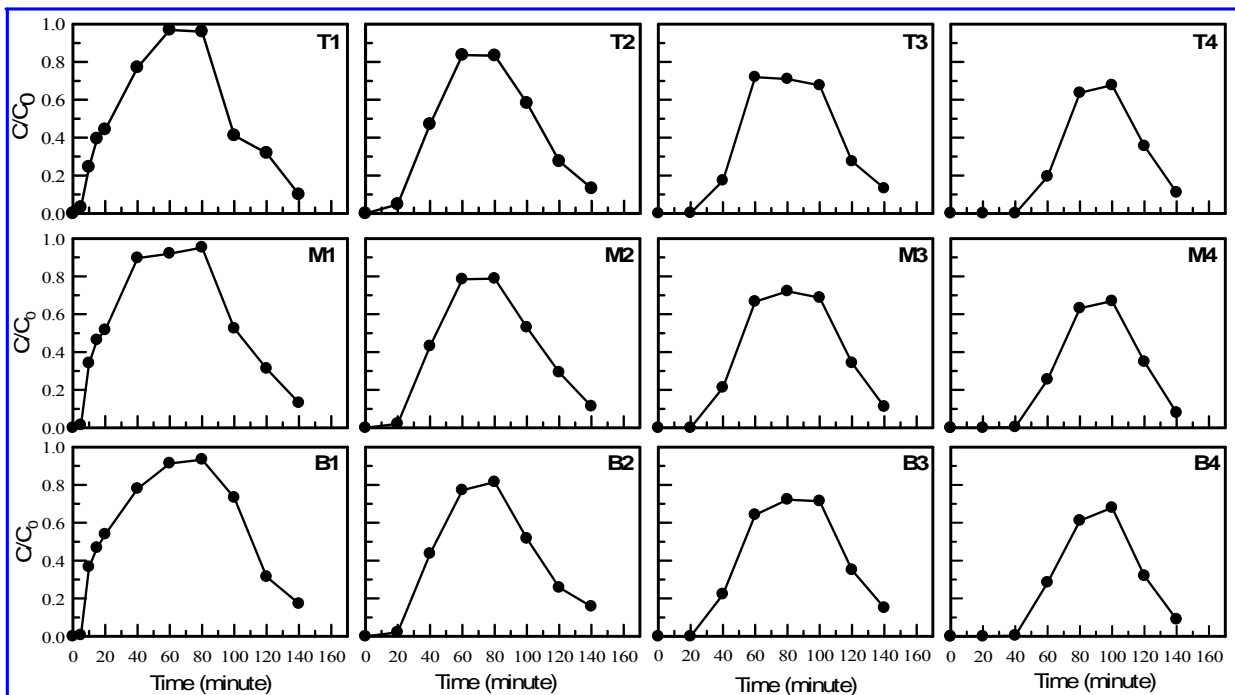


Figure 5.5. The iron concentration distribution in the aqueous phase (3 g/L NZVI suspension in 2 g/L CMC solution), packed with intermediate sand ($d_{50}=340 \mu\text{m}$), at injection velocity of 0.96 cm/min.

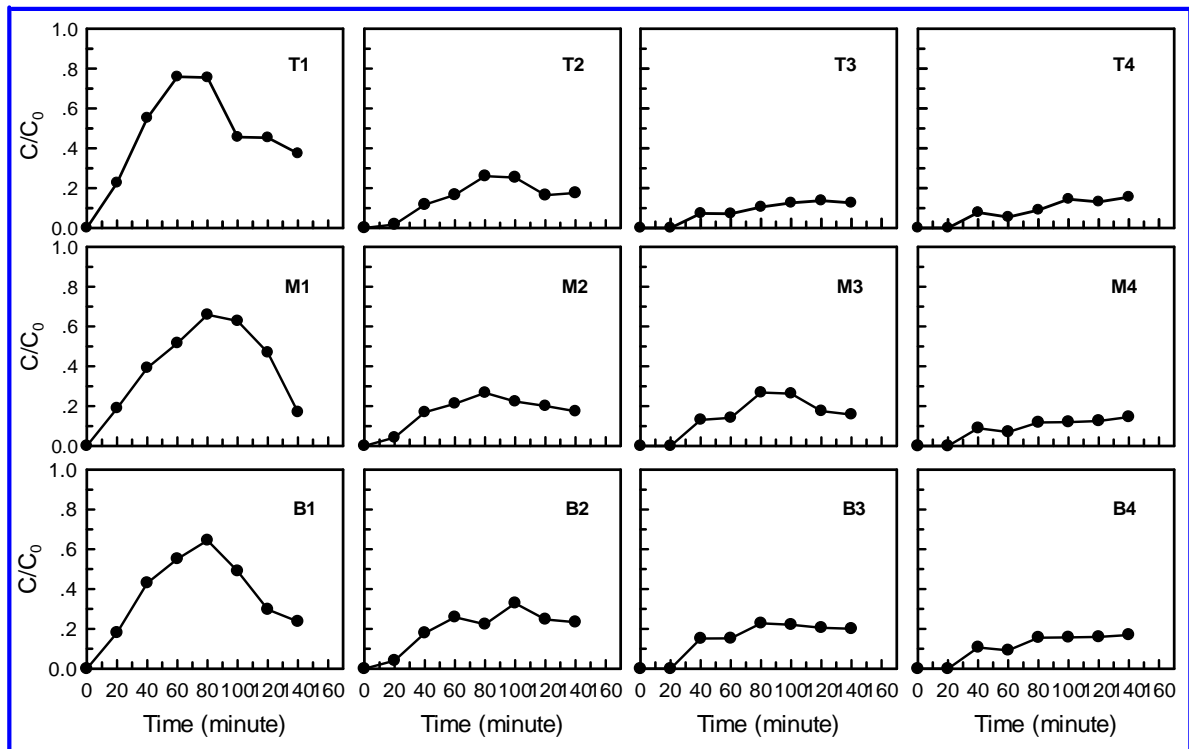


Figure 5.6. The iron concentration distribution in the aqueous phase (3 g/L NZVI suspension in 1 g/L CMC solution), packed with intermediate sand ($d_{50}=340 \mu\text{m}$), at injection velocity of 0.96 cm/min.

5.3.5 The Effect of Injection Velocity on NZVI Transport

Although early studies have made considerable efforts in investigating the effect of flow velocity on NZVI particles [25, 33, 36], most of these studies were conducted under Newtonian fluid condition. Tosco et al. reported that the flow velocity influenced NZVI particles transport in a complex manner for non-Newtonian fluids [28]. The effects of flow velocity of suspension on NZVI particles transport are studied by comparing the transport results at two flow velocities (0.96 cm/min and 0.40 cm/min) in intermediate sand. The results are shown in Figure 5.3 and Figure 5.7, respectively. The maximum C/C_0 values for 0.40 cm/min in Figure 5.7 are 0.81, 0.41, 0.21 and 0.11 at flow distance of 15 cm, 32.5 cm and 55 cm from the injection port and at the

effluent ports, respectively. These values are lower than the corresponding values (0.96, 0.51, 0.38 and 0.29) shown in Figure 5.3. This result indicates that the slow velocity is unfavourable to NZVI particles transport. It should be noted that after injecting NZVI suspension at low flow velocity, the electrolyte solution provided by water head cannot flow through the tank (thus no reported C/C_0 value in flush process). This is because the resistance caused by CMC solution (remained in the pores of the sand) at high concentration is very high, resulting in significant reduction of the conductivity (which will be discussed in the following section).

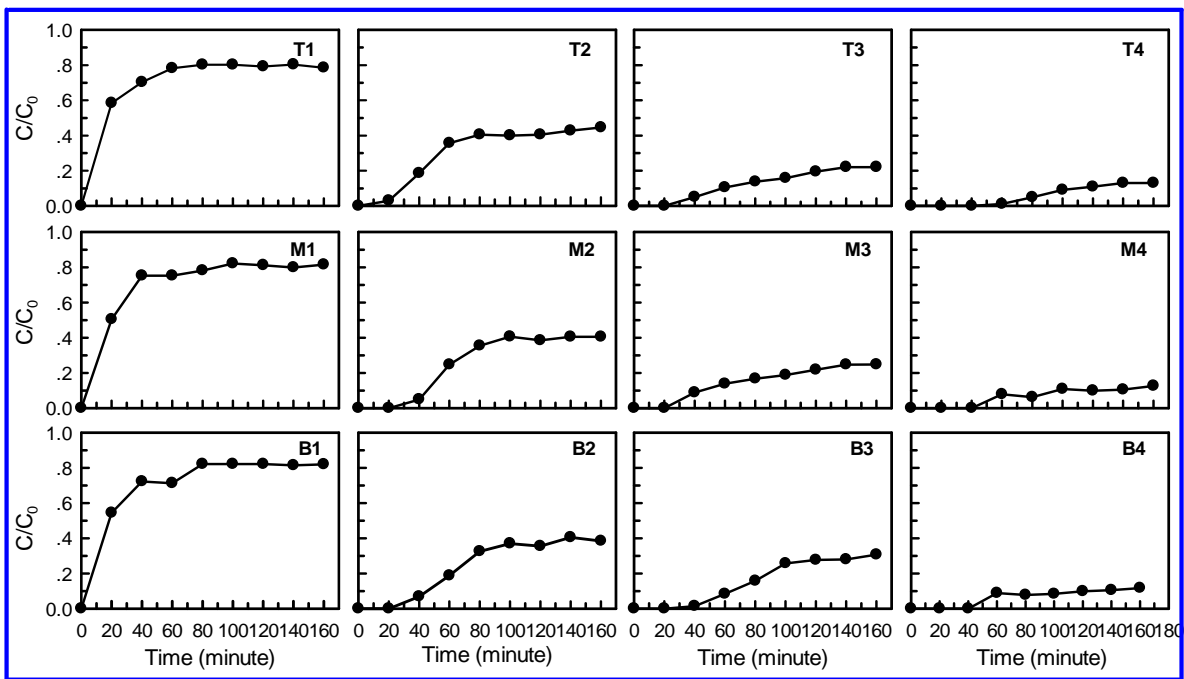


Figure 5.7. The iron concentration distribution in the aqueous phase (1 g/L NZVI suspension in 1 g/L CMC solution), packed with intermediate sand ($d_{50}=340 \mu\text{m}$), at injection velocity of 0.40 cm/min.

5.3.6 Deposition of NZVI Particles

Figures 5.S8-5.S13 shows the spatial retention concentration of Fe concentration. The values show that the retention concentrations of NZVI in the coarse sand are very low, compared with the results in the intermediate and in the fine sand under identical conditions (1 g/L NZVI in 1 g/L CMC solution, injection velocity of 0.96 cm/min). These retention concentration results are consistent with the results shown in Figures 5.2, 5.3 and 5.4. Higher retention is observed for decreasing sand diameter, and corresponds to the lower C/C_0 values observed as discussed above. Moreover, the retention concentration of NZVI reduces with the farther the distance from the injecting ports, which is consistent with the clean-bed colloid filtration theory.

Using the mean deposition rate (obtained from the η_0 and α estimated on the basis of C/C_0 obtained at the first sampling ports (T1, M1, B1) at 15 cm calculations shown in Table 5.S2), the distance should be 73.3 cm, 95.5 cm, and 131.6 cm for the C/C_0 values to be 0.61, 0.51 and 0.40. In the experiment these values C/C_0 were obtained at 32.5 cm, 55 cm and 67.5 cm distant from the injection ports in the tank in the coarse sand. These much farther distances from the calculations indicate that more deposition occurred in the experiment than expected.

Figure 5.S4 also shows that the retention concentrations of NZVI particles in the coarse sand are practically higher than the calculation values, except for the value at the effluent ports. Particularly, the closer distance from the injection ports, much bigger difference between the experimental retention value and the calculated value is obtained in the coarse sand. Finally, the retention concentrations of NZVI particles at three layers with the same distance from the injection diffusor are more or less the same, confirming that the flow of NZVI suspension is uniform in the homogeneous sand.

5.3.7 The Aggregation of NZVI Particles during Transport

Table 5.S3 shows the aggregation trend of NZVI particles during transport at various conditions. The results of aggregates sizes show that NZVI particles do not significantly aggregate during transport in this study. However, some aggregation was observed in two cases: the experiment in the intermediate sand with 1 g/L NZVI particles in 1 g/L CMC solution and the experiment in the fine sand with 1 g/L NZVI particles in 1 g/L CMC solution. Comparing the aggregate sizes in the transport experiments with coarse sand, intermediate sand and fine sand under identical conditions, one can observe that the initial aggregates sizes at all sampling ports in the coarse sand (ranging from 600 nm to 820 nm) are higher than those obtained at the corresponding ports in the intermediate sand and fine sand (ranging from 400 to 762 nm in the former case, from 415 nm to 631 nm in the latter case). This can be interpreted by the C/C_0 values rapidly reach to very high values in the coarse sand tank, representing that the concentrations of NZVI particles remained in the aqueous phase are pretty high. And the aggregation degree of NZVI particle depends on its concentration [12, 15] as discussed in Chapter 3. Taken together, the initial aggregate sizes of NZVI particles in the coarse sand reach to bigger sizes. With the continuous injection, the concentrations of NZVI particles in the intermediate and fine sands increase, leading to increases in the size of aggregate sizes. When CMC concentration increases from 1 g/L to 2 g/L, the mean aggregates sizes reduced significantly: in the latter case, the mean aggregates approximately remain at 400 nm (1 g/L NZVI) and at 520 nm (3 g/L NZVI).

5.3.8 The Conductivity and Pressure Drop Measurements

Table 5.S4 displays the conductivity results in various cases. The results show that after injecting NZVI suspension, the conductivity values of the tank system reduce significantly in all cases: in the coarse, intermediate and fine sands (1 g/L NZVI particles in 1 g/L CMC solution, at 0.96 cm/min), the conductivity values reduce from 21.44 cm/min, 3.47 cm/min and 1.54 cm/min (prior to conducting injection) to 4.06 cm/min, 0.56 cm/min and 0.32 cm/min (after injecting NZVI suspension), respectively. When the flow velocity reduces from 0.96 cm/min (3 g/L NZVI particles in 2 g/L CMC solution, intermediate sand tank) to 0.40 cm/min (1 g/L NZVI particles in 2 g/L CMC solution, intermediate sand tank), the conductivity values (after injecting NZVI suspension) reduce from 0.148 cm/min to 0.104 cm/min. As CMC concentrations in NZVI suspension increase from 1 g/L (1 g NZVI in 1 g/L CMC solution, intermediate sand tank) to 2 g/L (3 g/L NZVI in 2 g/L CMC, intermediate sand tank), the conductivity values (after the injection conducted) reduce from 0.56 cm/min to 0.148 cm/min.

The result of conductivity reduction caused by injecting NZVI suspension proves the previous assumption that the injection of NZVI suspension with the high viscosity 700K CMC fluid would tend to create a significant resistance for flow to move forward [28, 29]. Given the small amount of retained NZVI particles on sand in the whole tank (ranging from 4.5 g to 11.34 g), the contribution of deposited NZVI particles in the tank to the reduction of conductivity of the tank system is small. Thus, we believe that the significant reduction of conductivities of the tank system is mainly caused by the retained suspension (containing abundant CMC) in the tank after the transport experiments are completed. This viewpoint can also be proved by the much more significant reduction of conductivity in the case with higher CMC solution. Additionally, the conductivity of the tank system reduces with the decrease of the injection velocity, which is also

can be elucidated by the fact the suspension remained in the tank after injecting NZVI suspension shows higher dynamic viscosity at low velocity (0.40 cm/min) than that at rapid velocity (0.96 cm/min), yielding more resistance to flow at the former case. These conductivity results shed some light on understanding the conductivity changes associated with the injecting shear-thinning fluid of NZVI particles into the subsurface under different conditions.

Tables 5.S5 and 5.S6 showed the pressure drop in the tank under various conditions. The data demonstrated that free CMC in NZVI suspension caused very higher pressure drop during injecting the suspension than those for pure water (data shown in Figure 5.S1). Further, as the increase of CMC concentration, the pressure drop increased. Particularly, after injecting 1 PV of suspension, the pressure drop significantly increased. The injecting velocity also influenced the pressure drop. Briefly, lower injecting velocity caused higher pressure drop, which can be attributed by the higher dynamic viscosity of the suspension at lower injecting velocity. These pressure drop results revealed the reasons for the observations that hydraulic conductivity decreased significantly after injecting CMC-NZVI suspension and in particular at lower injection velocity (very little water could pass through the tank in the case of 2 g/L CMC and 0.40 cm/min injection velocity).

5.4 Implications for Assessment of NZVI Injections

The measurements of temporal and spatial distributions of NZVI concentrations through the tank system presented above reflect a complex transport performance of CMC coated NZVI particles (in particular, with a large amount of free CMC in the suspension). The retained NZVI particles on sand were more than the calculated results based the classical colloid filtration theory. Injecting 3 PV NZVI suspension, the maximum transport efficiency was only

around 36% and the minimum efficiency was merely around 3%. The aggregation of the particle was not apparently observed, thus, cannot be used to explain the very limited transport of NZVI particles. The quite high viscosity of the suspension should take into account for the above transport results, in particular, for the cases of the low injection velocity and high CMC concentrations. The significant pressure drop was observed in the tank system when injecting CMC solution, which was consistent with the decrease of hydraulic conductivity of the tank system after injecting CMC-NZVI suspension.

As this study was conducted in 2-D tank, unlike those small laboratory scale 1-D column, we found that when realizing the stabilization of NZVI particles by using polyelectrolyte, another the viscosity of the polyelectrolyte would cause other transport issues, such as, the resistance of the flow, the pressure drop, the decrease of the hydraulic conductivity of the porous media. Given the observations of this study, how to stabilize NZVI particles without a lot of free CMC in the suspension would need to be solved. The implication of this is that the thorough investigations on NZVI transport in large scale reactor rather than laboratory scale 1-D column are critical for extensive assessing the effectiveness of NZVI delivery and for exploring the other effects of other physical parameters (about flow) on NZVI transport.

Supporting information

Section 5.S1. The summary of previous studies on CMC-NZVI

Table 5.S1. Review of the studies on the synthesis, stability and transport of CMC-NZVI particles

Type of CMC	Nanoparticle	Characterization	Grafting method	Stability assessment	Transport in lab-scale columns	Transport in field demonstration	Reactivity	Conclusion	References
90K CMC and 250K CMC	NZVI	NZVI particle diameter	Pre-grafting	n/a	n/a	n/a	n/a	CMC with a greater <i>Mr</i> is more effective in stabilizing ZVI nanoparticles.	He and Zhao, 2007
90K CMC	Fe-Pd nanoparticle	Particle size (TEM and DLS) and the intensity of COO- on the particle (FTIR)	Pre-grafting	n/a	Around 98% of Fe-Pd nanoparticle passed through the column	n/a	CMC stabilized Fe-Pd nanoparticle showed a very high reactivity rate	n/a	He et al, 2007
90K CMC and 250K CMC	Fe-Pd nanoparticle	TEM	Pre-grafting	n/a	n/a	n/a	CMC coated Fe-Pd nanoparticle showed a very improved reactivity	CMC at high concentration would inhibit the reactivity of nanoparticle	He and Zhao, 2008
90K CMC	NZVI	TEM, DLS, Zeta potential,	Pre-grafting	n/a	CMC-Fe nanoparticle can be readily delivered through porous media.	n/a	n/a	The attachment efficiency for CMC-Fe was found to be 1–2 orders of magnitude lower than reported for ZVI nanoparticles stabilized	He et al, 2009
90K CMC	Fe-Pd nanoparticle	n/a	Pre-grafting	n/a	n/a	In some area, Fe-Pd nanoparticle can significantly transport through porous media.	Fe-Pd nanoparticle is reactive to TCE, PCE. The reactivity reduced with time.	CMC coated Fe-Pd nanoparticle can transport effectively to down gradient to deduce chlorinated contaminants.	He et al, 2010
90K CMC	Fe-Pd nanoparticle	n/a	Pre-grafting	n/a	n/a	n/a	After injecting the particles, the chlorinated contaminants significantly reduced	The mobility of CMC Fe-Pd nanoparticle reduced with time	Bennett, 2010
90K CMC and 700K CMC	NZVI	TEM, DLS, Zeta potential	Post-grafting	CMC stabilized NZVI particles is more stable than bare NZVI particle	n/a	n/a	n/a	The layer thicknesses of 90K CMC- and 700K CMC-NZVI particles are 7 nm and 40 nm, respectively	Phenrat et al, 2008
90K CMC and 700K CMC	NZVI	TEM, DLS, Zeta potential	Post-grafting	CMC stabilized NZVI particles	About 80% of injected NZVI	n/a	n/a	After aging, CMC stabilized NZVI	Kim et al, 2009

				are slightly more stable than bare NZVI particles	particles can transport through the column			particles remain mobile in porous media	
90K CMC and 700K CMC	NZVI	n/a	Post-grafting	n/a	n/a	n/a	Reactivity was reduced due to the adsorbed CMC	n/a	Phenrat et al, 2009
90K CMC	NZVI	TEM, NTA, Zeta potential	Pre-grafting	CMC stabilized NZVI particles are very stable	CMC stabilized NZVI particles are very mobile, even at very slow flow velocity	n/a	n/a	The transport of CMC-NZVI particles are increased with time, due to the aggregation	Raychoudhury et al, 2010
90K CMC	NZVI	TEM, NTA, DLS, Zeta potential, QCM-D, DLVO prediction	Pre-grafting	n/a	n/a	n/a	n/a	n/a	Fatissou
90K CMC, 250K CMC and 700 K CMC	Fe-Pd nanoparticle	TEM,	Pre-grafting	The stability of NZVI particles increases with the increase of the molecular weight of CMC	n/a	n/a	The reactivity of NZVI particle decreases with the increase of the molecular weight of CMC	CMC yielded very stable NZVI suspensions.	Sakulchaicharoen et al, 2010
90K CMC	NZVI	TEM, SEM, XRD, FTIR, high-resolution ESCA	Pre-grafting	n/a	CMC stabilized NZVI particles are very mobile	n/a	n/a	n/a	Lin et al, 2010
90K CMC	TiO ₂ nanoparticle	TEM, XRD, EDX	Post-grafting	n/a	CMC stabilized TiO ₂ particles are very mobile	n/a	n/a	n/a	Joo et al, 2009
90K CMC	NZVI	TEM, NTA	Pre-grafting	n/a	The transport of CMC-NZVI particles decreases with the increase of NZVI concentration	n/a	n/a	The aggregation of the NZVI particles during transport influences the transport of NZVI particles	Raychoudhury et al, 2012
90K CMC	NZVI	TEM, NTA, XPS	Pre-grafting and Post-grafting	The stability of pre-grafted CMC-NZVI particles is slightly higher than that of post-grafted CMC-NZVI particles	n/a	n/a	n/a	n/a	Cirtiu et al, 2011
250K CMC	NZVI	TEM, DLS, Zeta potential	Post-grafting	CMC stabilized NZVI particles	More than 90% of CMC-	n/a	n/a	n/a	Kocur et al, 2013

				can be stable for several hours	NZVI particles can transport through the column				
N	Micron ZVI particle	n/a	Post-grafting	n/a	CMC formed shear thinning fluid significantly improved the mobility of micron ZVI particles	n/a	n/a	Shear thinning fluid inhibited the settling of ZVI particles	Cantrell, et al, 1997
90K CMC	NZVI	TEM,	Post-grafting	n/a	n/a	In very high CMC solution, NZVI particles cannot transport easily to a very far distance	The reactivity of CMC stabilized NZVI particles reduced during transport	The shear thinning property of CMC-NZVI suspension would bring resistance for NZVI particles to transport forward	Johnson et al, 2013
90K CMC	NZVI impregnated on hard hydrophobic carb particle	SEM, TEM	Pre-grafting	CMC stabilized NZVI/C particles are very stable in the suspension	97-99% of particles transported through the column	n/a	CMC stabilized particles showed an improved reactivity rate for TCE	n/a	Zhan et al, 2009

Section 5.S2. The details on DLS and microscopy measurements

5) DLS measurement

20 mL 50 mg/L samples were stored in 30 mL vials and fixed on an end-over-end rotator for 24 minutes with a slow rotation rate. And then 2 mL of this sample was taken into the cubic vial and sealed for DLS measurement.

6) Microscopy measurement

Optical microscopy measurements were conducted as follows: A latex particle sample with mean diameter of 200 nm (the diameter of 96% of particles ranged from 190 nm to 210 nm) was used as standard particles for method validation. The standard particles were imaged in a microscope (Olympus BX51) with bright field filter under the 100x objective as well as by phase contrast technique. Images were analyzed by ImageJ (totally around 2000 particles were analyzed) to provide the Fetet's diameter of 200 nm particle. Following the same process, NZVI suspensions with original concentrations (1 g/L in 1 g/L and 2 g/L CMC solutions, respectively, in this study) were directly imaged in the microscope to obtain the actual aggregates sizes at these concentrations.

Section 5.S3. The design for pressure drop measurement

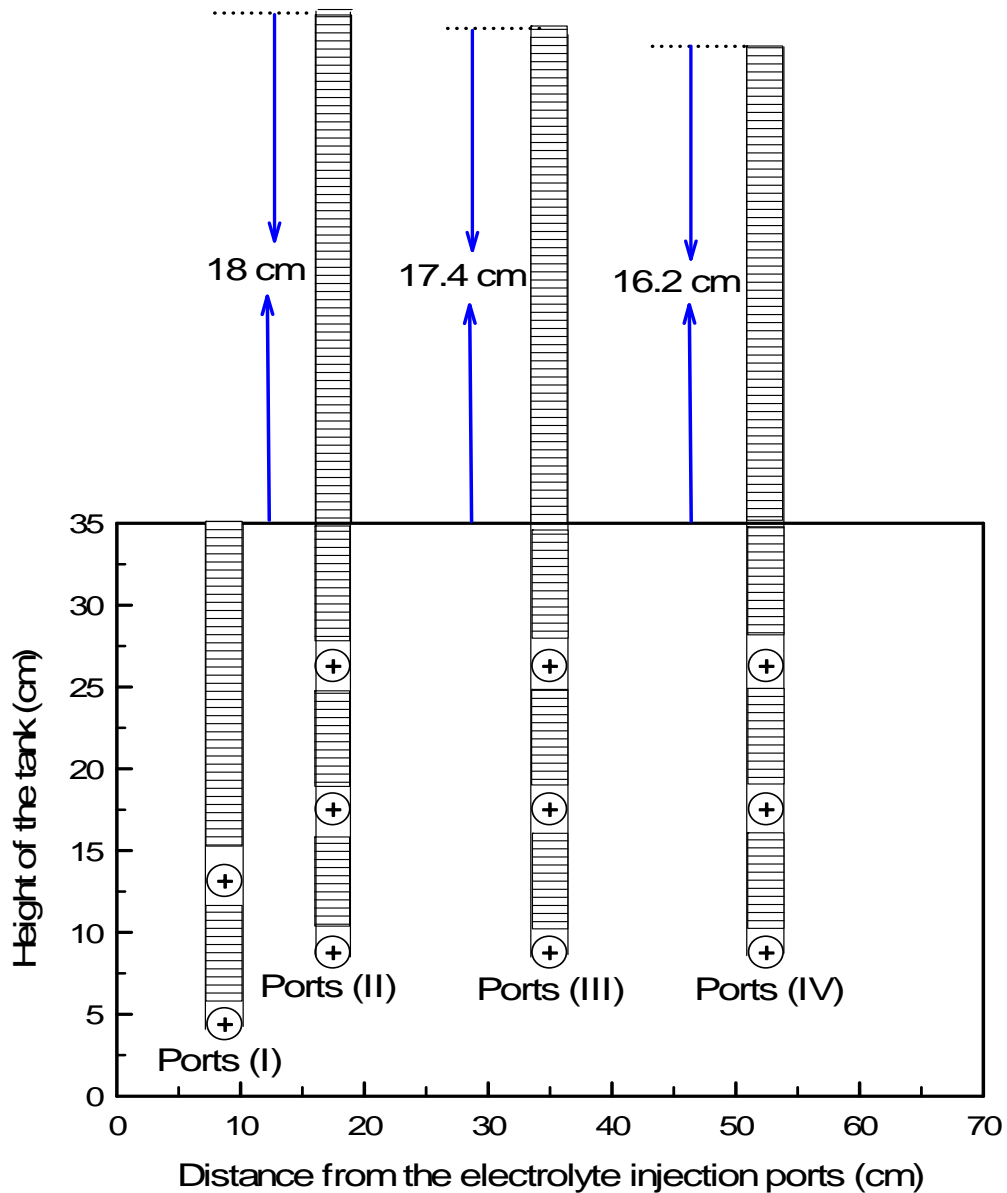


Figure 5.S1. The pressure drop at different places in the tank (electrolyte flow)

Section 5.S4. The CFT theory calculations

Nanoparticle deposition in porous media has been described by the colloid filtration theory in several studies [20, 38]. According to this theory, the particle deposition rate coefficient is represented as function of the single collector contact efficiency (η_0) and the attachment efficiency (α) as shown in equations 5.S1 and 5.S2.

$$k = \left[\frac{3(1-f)U}{2d_s f} \alpha \right] \eta_0 \quad (5.S1)$$

In the above equation ε is porosity of media and d_c is the average diameter of collector. The parameter η_0 is the probability of collision of a particle flowing through the porous media and can be theoretically determined by the Tufenkji and Elimelech equation [39]:

$$\eta_0 = 2.4 A_S^{1/3} N_R^{-0.081} N_{Pe}^{-0.715} N_{vdW}^{0.052} + 0.55 A_S N_R^{1.675} N_A^{0.125} + 0.22 N_R^{-0.24} N_G^{1.11} N_{vdW}^{0.053} \quad (5.S2)$$

The parameter α represents the probability of sticking of a particle on the collector after collision, or in other words the probability of a collision that leads to deposition. The attachment efficiency is usually determined from experimental data of C versus t (or breakthrough curves) by solving for equations 5.S1 and 5.S2 with the assumption of steady state transport (or $\partial C/\partial t=0$) and negligible dispersion [25, 40].

$$\alpha = -\frac{2d_s \ln(C/C_0)}{3(1-f)L\eta_0} \quad (5.S3)$$

The single collector contact efficiency (η_0) is extensively determined by T&E equation (equation 5.S2).

Section 5.S5. Dye test of the tank system and NZVI transport in the tank system

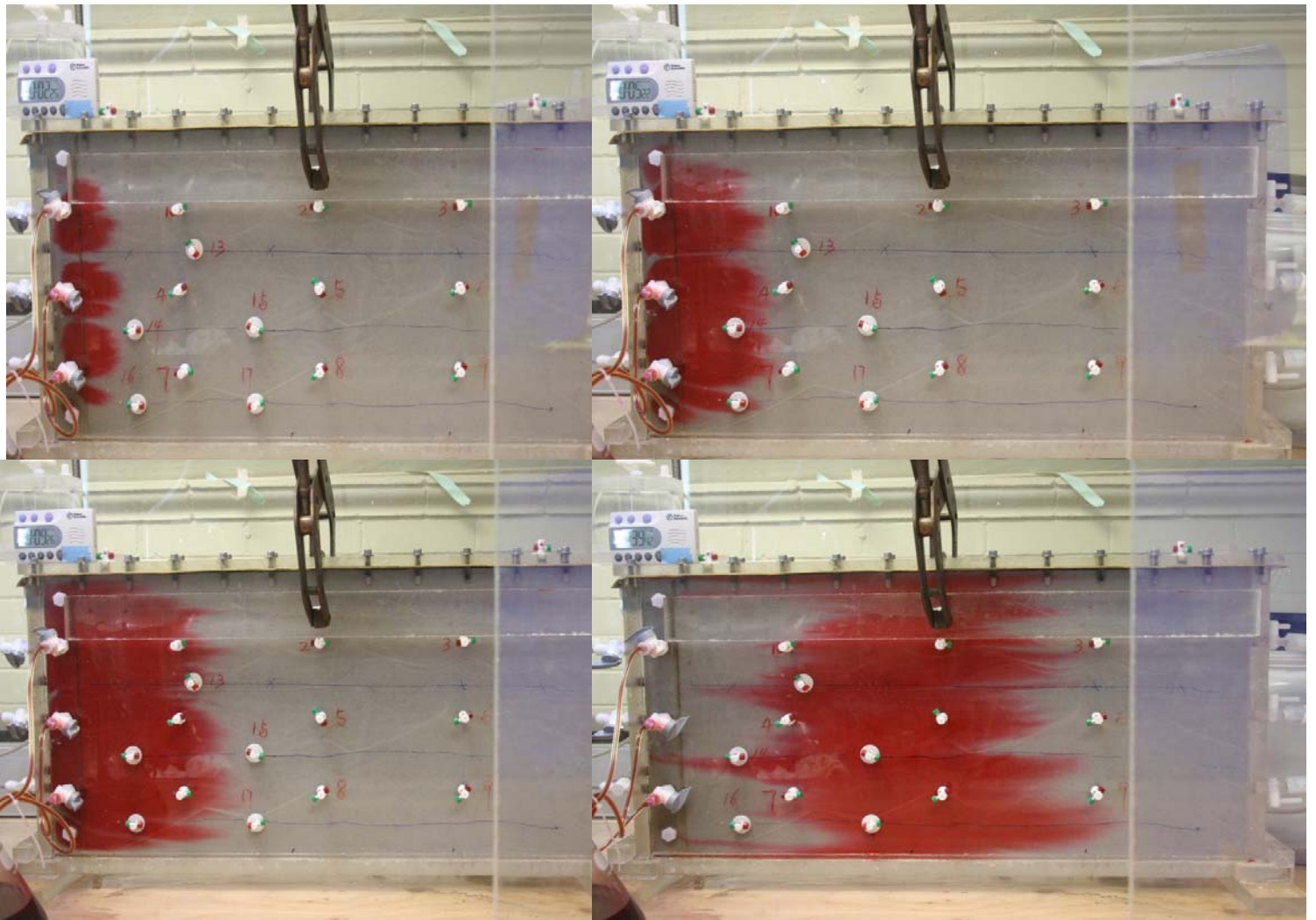


Figure 5.S2. Representative images illustrating the transport of the red tracer.

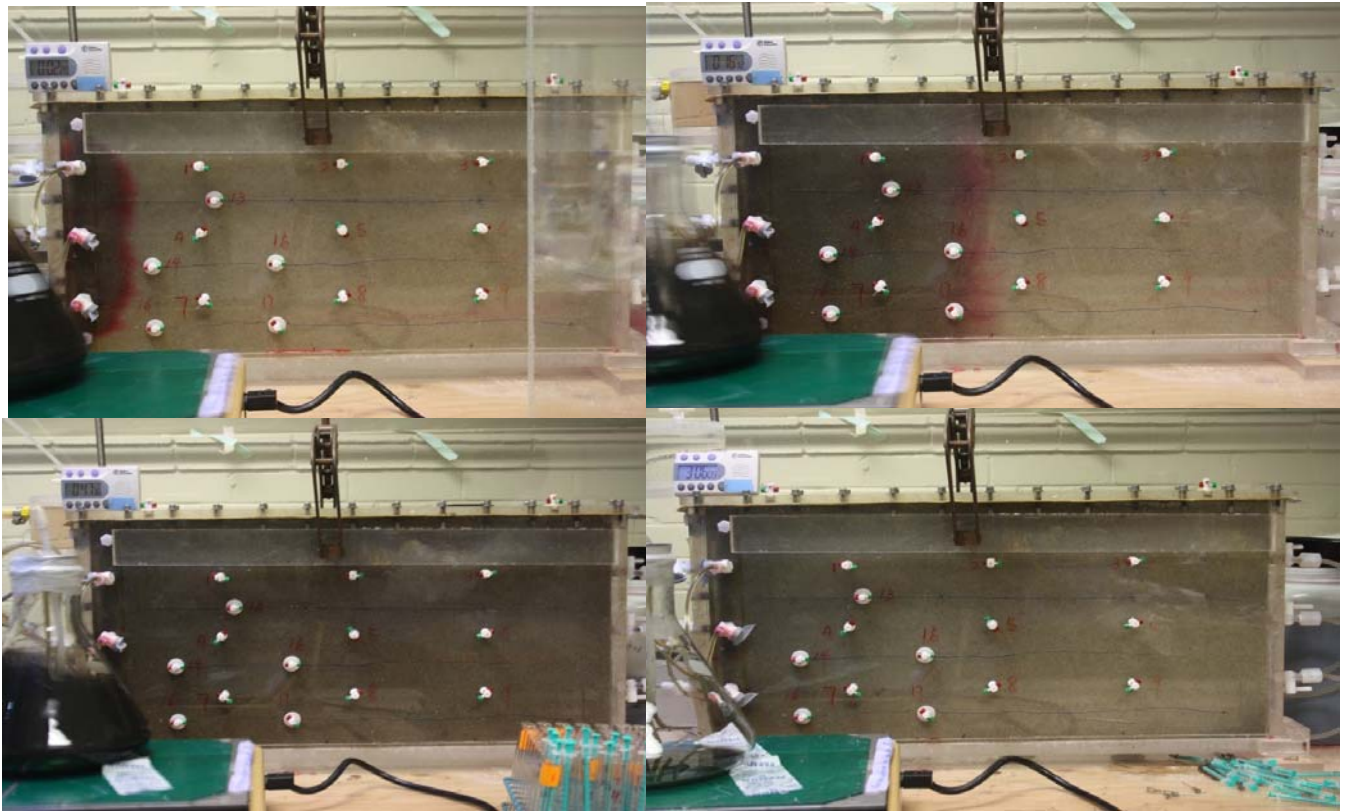


Figure 5.S3. Representative images illustrating the transport of NZVI particles.

Section 5.S6. The summary of the parameters for the tank experiments and CFT calculation results

Table 5.S2. The parameters for the tank experiments and the CFT calculation results.

Sample	Sand	Injection velocity (cm/minute)	Viscosity (c.P)	Mean C/C ₀ value of T1, M1 and B1 ports	Mean diameter of iron NPs at T1, M1 and B1 ports (nm)	The single collector contact efficiency (η_0) at T1, M1 and B1 ports	The attachment efficiency (α) at T1, M1 and B1 ports	Mean C/C ₀	Actual distance from injection ports along the flow direction (cm)	Predicted distance based on η_0 and α values obtained at T1, M1 and B1 ports (cm)
1 g/L NZVI in 1 g/L 700K CMC with 0.5 mM NaHCO ₃	Coarse	0.96	26.3 ±1.2	0.90±0.02	880±123	6.13±*10 ⁻⁴	1.38	0.61±0.03	32.5	73.3
								0.51±0.02	50	95.9
								0.37±0.02	67.5	131.6
1 g/L NZVI in 1 g/L 700K CMC with 0.5 mM NaHCO ₃	Intermediate	0.96	26.3 ±1.2	0.86±0.02	962±143	1.20*10 ⁻³	0.31	0.51±0.04	32.5	64.0
								0.33±0.04	50	94.3
								0.29±0.01	67.5	111.1
1 g/L NZVI in 1 g/L 700K CMC with 0.5 mM NaHCO ₃	Fine	0.96	26.3 ±1.2	0.74±0.02	1000±158	3.02*10 ⁻³	0.13	0.46±0.03	32.5	33.5
								0.32±0.01	50	53.5
								0.13±0.01	67.5	75.8
3 g/L NZVI in 2 g/L 700K CMC with 0.5 mM NaHCO ₃	Intermediate	0.96	36.2±2.3	0.95±0.02	620±104	8.44*10 ⁻⁴	8.42*10 ⁻²	0.82±0.03	32.5	91.8
								0.72±0.01	50	135.2
								0.67±0.01	67.5	219.8

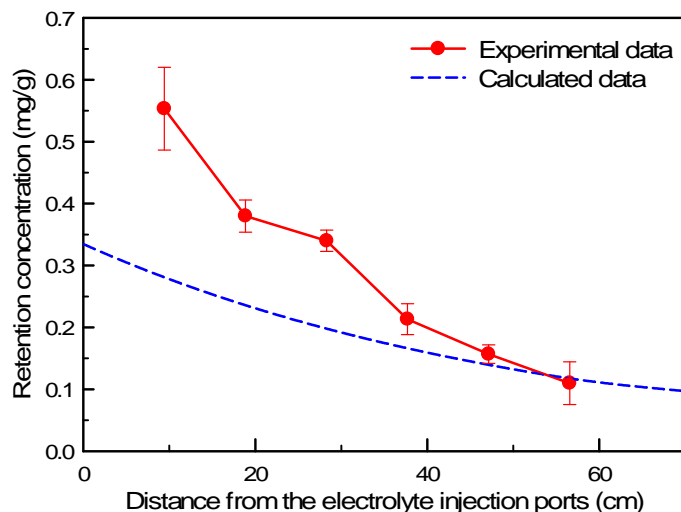


Figure 5.S4. The comparison of the experimental retention of iron NPs (with flow distance) and the calculated retention of iron NPs (with flow distance) in the coarse sand tank (under the conditions: 1 g/L NZVI in 1 g/L 700K CMC with 0.5 mM NaHCO₃ at 0.96 cm/minute).

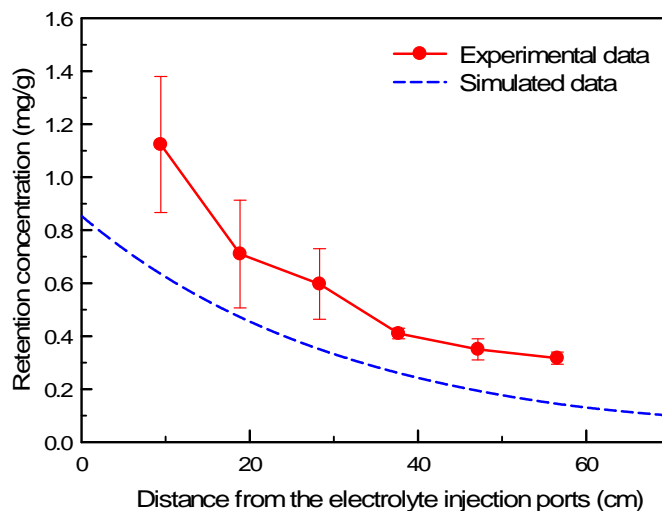


Figure 5.S5. The comparison of the experimental retention of iron NPs (with flow distance) and the calculated retention of iron NPs (with flow distance) in the intermediate sand tank (under the conditions: 1 g/L NZVI in 1 g/L 700K CMC with 0.5 mM NaHCO₃ at 0.96 cm/minute).

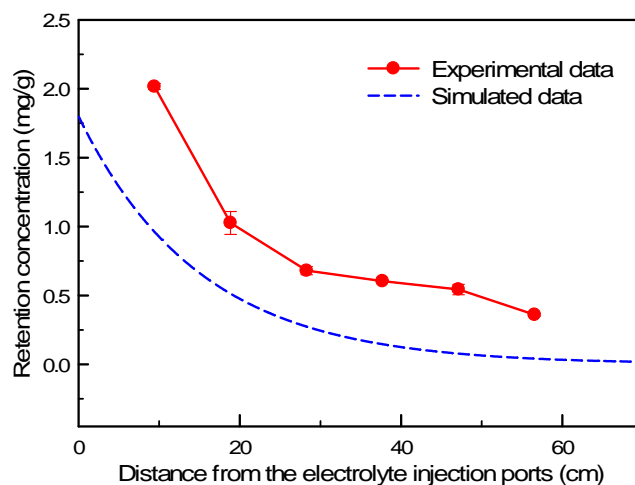


Figure 5.S6. The comparison of the experimental retention of iron NPs (with flow distance) and the calculated retention of iron NPs (with flow distance) in the fine sand tank (under the conditions: 1 g/L NZVI in 1 g/L 700K CMC with 0.5 mM NaHCO₃ at 0.96 cm/minute).

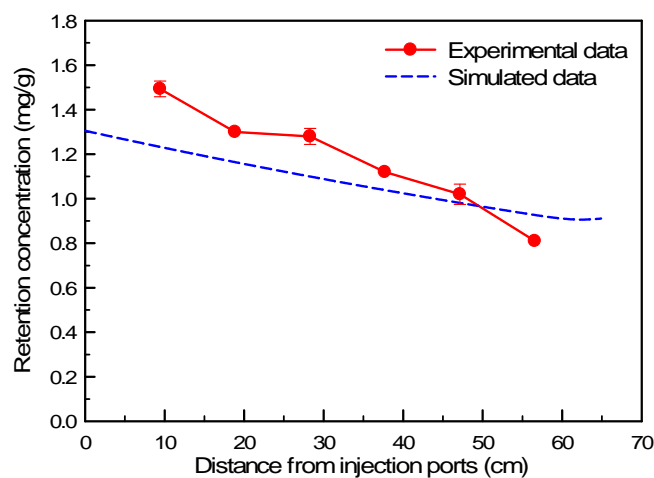


Figure 5.S7. The comparison of the experimental retention of iron NPs (with flow distance) and the calculated retention of iron NPs (with flow distance) in the intermediate sand tank (under the conditions: 3 g/L NZVI in 2 g/L 700K CMC at 0.96 cm/min).

Section 5.S7. The spatial retention concentrations of NZVI particles

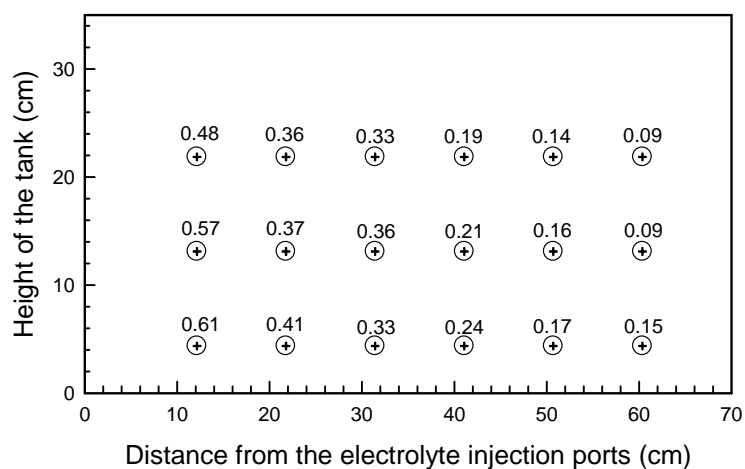


Figure 5.S8. The retention of iron NPs on sand (coarse sand packed tank) under the conditions: 1 g/L NZVI in 1 g/L 700K CMC (with 0.5 mM NaHCO₃) and 0.96 cm/minute of injection velocity.

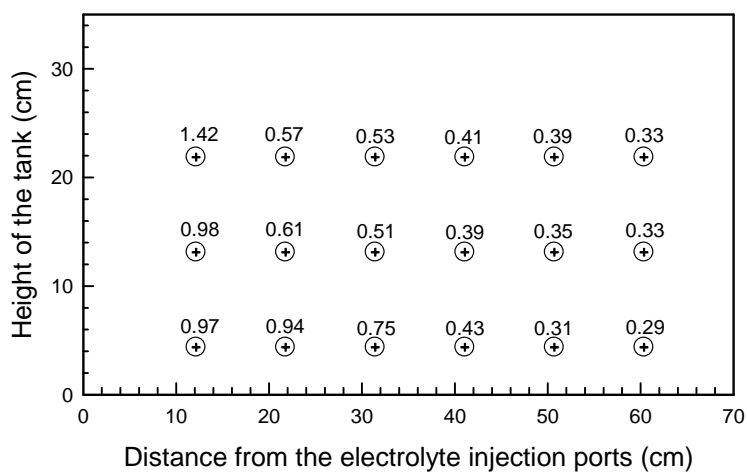


Figure 5.S9. The retention of iron NPs on sand (intermediate sand packed tank) under the conditions: 1 g/L NZVI in 1 g/L 700K CMC (with 0.5 mM NaHCO₃) and 0.96 cm/minute of injection velocity.

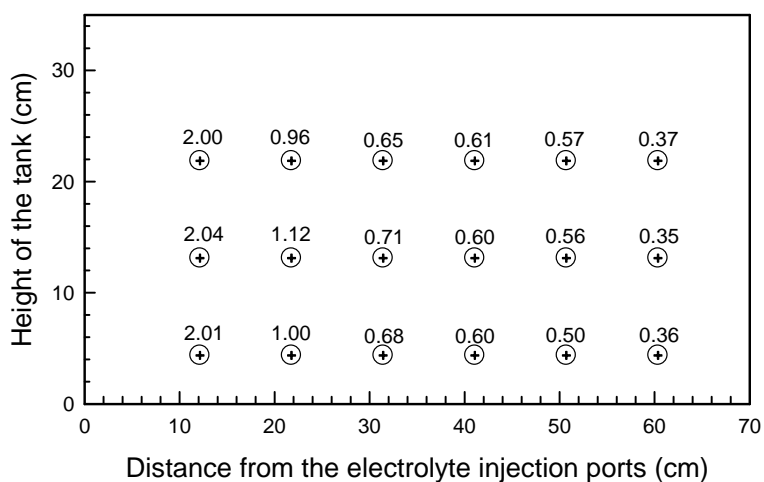


Figure 5.S10. The retention of iron NPs on sand (fine sand packed tank) under the conditions: 1 g/L NZVI in 1 g/L 700K CMC (with 0.5 mM NaHCO₃) and 0.96 cm/minute of injection velocity.

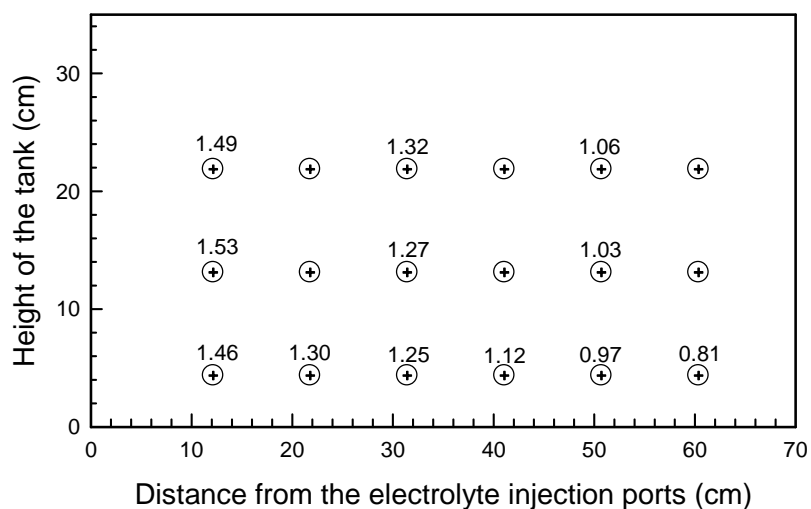


Figure 5.S11. The retention of iron NPs on sand (intermediate sand packed tank) under the conditions: 3 g/L NZVI in 2 g/L 700K CMC (with 0.5 mM NaHCO₃) and 0.96 cm/minute of injection velocity.

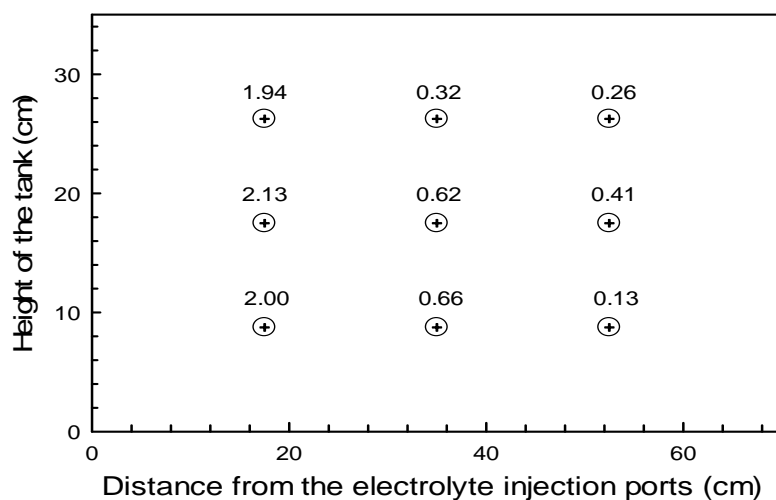


Figure 5.S12. The retention of iron NPs on sand (intermediate sand packed tank) under the conditions: 1 g/L NZVI in 1 g/L 700K CMC (with 0.5 mM NaHCO₃) and 0.40 cm/minute of injection velocity.

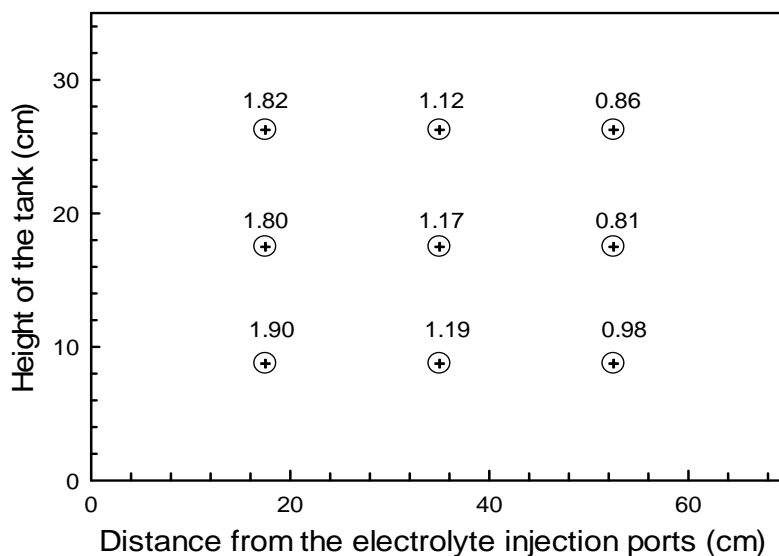


Figure 5.S13. The retention of iron NPs on sand (intermediate sand packed tank) under the conditions: 3 g/L NZVI in 1 g/L 700K CMC (with 0.5 mM NaHCO₃) and 0.96 cm/minute of injection velocity.

Section S8. The mean diameters of CMC-NZVI particles results

Table 5.S3. Mean diameters of iron NPs measured by microscopy.

Time (minute)	Coarse sand tank (1 g/L NZVI, 1 g/L CMC, 0.96 cm/minute)						Intermediate sand tank (1 g/L NZVI, 1 g/L CMC, 0.96 cm/minute)						Fine sand tank (1 g/L NZVI, 1 g/L CMC, 0.96 cm/minute)						Intermediate sand tank (3 g/L NZVI, 2 g/L CMC, 0.96 cm/minute)					
	T1	T2	T3	B1	B2	B3	T1	T2	T3	B1	B2	B3	T1	T2	T3	B1	B2	B3	T1	T2	T3	B1	B2	B3
20	868	786	621	908	799	645	729	529	468	766	538	409	689	559	509	703	584	501	529	—	—	529	—	—
40	898	804	639	956	812	651	862	711	539	883	735	512	831	710	633	854	738	651	554	409	302	561	413	301
60	875	843	651	944	834	649	932	784	635	945	792	683	1038	899	605	1056	906	644	602	418	318	593	439	329
80	856	838	705	923	896	745	1130	908	811	1109	901	797	1269	987	765	1287	956	759	623	436	333	618	470	345
100	1160	842	709	1193	1022	857	1289	901	837	1255	869	712	1235	1068	798	1238	1011	756	633	462	354	643	487	386
120	— ^a	—	—	—	—	—	—	—	—	—	—	—	—	—	—	—	—	—	666	494	380	669	501	400

Section 5.S9. The conductivity results of different tank experiments

Table 5.S4. Conductivity changes of different tank experiments

Sample	Sand	Injection velocity (cm/minute)	Total transport efficiency (%)	Conductivity (before injection) (cm/min)	Conductivity (after injection) (cm/min)
1 g/L NZVI in 1 g/L 700K CMC (with 0.5 mM NaHCO ₃)	Coarse	0.96	36.21	21.44	4.06
1 g/L NZVI in 1 g/L 700K CMC (with 0.5 mM NaHCO ₃)	Intermediate	0.96	25.16	3.47	0.56
1 g/L NZVI in 1 g/L 700K CMC (with 0.5 mM NaHCO ₃)	Fine	0.96	15.75	1.54	0.32
3 g/L NZVI in 2 g/L 700K CMC (no NaHCO ₃)	Intermediate	0.96	37.89	3.45	0.148
3 g/L NZVI in 1 g/L 700K CMC (no NaHCO ₃)	Intermediate	0.96	11.21	3.45	0.355
1 g/L NZVI in 1 g/L 700K CMC (no NaHCO ₃)	Intermediate	0.40	2.33	3.46	0.201

Section 5.S10. Pressure drop measurements

Table 5.S5. The pressure drop of 1 g/L CMC in 0.5 mM NaHCO₃ in the tank

Time (minute)	Height at ports (I) (cm)	Height at ports (II) (cm)			Height at ports (III) (cm)			Height at ports (IV) (cm)		
		0.96 cm/min	0.40 cm/min	With 1 g/L NZVI (0.40 cm/min)	0.96 cm/min	0.40 cm/min	With 1 g/L NZVI (0.40 cm/min)	0.96 cm/min	0.40 cm/min	With 1 g/L NZVI (0.40 cm/min)
10	44.5	43.9	19.9	21.4	25.9	16.4	17.1	16.1	10.9	8
15	52.4	49.8			31.9			18.9		
20	59.9	56.9	20.4	34.1	35.9	16.9	28.9	21.7	11.2	12.5
25	64.4	61.3			39.5			23		
30	68.9	65.1	29.1		42.9	20.9	42.4	24.1	12.1	26.1
35	72.9	69			46.9			26		
40	76	72.8	41.4	56.9	51.3	31.9	52.2	30.9	14.2	29.7
45	79.1	76.2			57.4			34.7		
50	82	79.4	53.5		61.7	42.9	63.9	38.7	19.9	32
60			69	69.7		55.2	71.2		26.9	34.1
70			72.8	77.7		65.5	75.2		35.9	36.9
80				80.2						39.6

Table 5.S6. The pressure drop of 2 g/L CMC in the tank

Time (minute)	Height at ports (II) (cm)		Height at ports (III) (cm)		Height at ports (IV) (cm)	
	0.96 cm/min	0.40 cm/min	0.96 cm/min	0.40 cm/min	0.96 cm/min	0.40 cm/min
10	42.4	7	33.9	5.7	15.9	4.4
20	62.7	7	50.7	5.7	32.9	4.4
30	82.9	15.4	68.9	5.7	Over 41.9	4.4
40	Over 102.7	26.5	88.8	5.7		4.4
50		40.1		14.4		4.4
60		52.9		37.8		12.3
70		77.2		47.5		27.2
80		93.9		57.8		38.3

References

- [1] P. Bennett, F. He, D. Zhao, B. Aiken, L. Feldman, In situ testing of metallic iron nanoparticle mobility and reactivity in a shallow granular aquifer, *Journal of contaminant hydrology*, 116 (2010) 35-46.
- [2] W.x. Zhang, D.W. Elliott, Applications of iron nanoparticles for groundwater remediation, *Remediation Journal*, 16 (2006) 7-21.
- [3] S.R. Kanel, J.-M. Greneche, H. Choi, Arsenic (V) removal from groundwater using nano scale zero-valent iron as a colloidal reactive barrier material, *Environmental Science & Technology*, 40 (2006) 2045-2050.
- [4] Y.-S. Keum, Q.X. Li, Reduction of nitroaromatic pesticides with zero-valent iron, *Chemosphere*, 54 (2004) 255-263.
- [5] Z. Jiang, L. Lv, W. Zhang, Q. Du, B. Pan, L. Yang, Q. Zhang, Nitrate reduction using nanosized zero-valent iron supported by polystyrene resins: role of surface functional groups, *water research*, 45 (2011) 2191-2198.
- [6] K.-H. Shin, D.K. Cha, Microbial reduction of nitrate in the presence of nanoscale zero-valent iron, *Chemosphere*, 72 (2008) 257-262.
- [7] S.-S. Chen, H.-D. Hsu, C.-W. Li, A new method to produce nanoscale iron for nitrate removal, *Journal of Nanoparticle Research*, 6 (2004) 639-647.
- [8] R.L. Johnson, J. Nurmi, R. Johnson, Z. Shi, P. Tratnyek, T. Phenrat, G. Lowry, Injection of nano zero-valent iron for subsurface remediation: A controlled field-scale test of transport, in: *Proceedings of the 7th International Conference on Remediation of Chlorinated and Recalcitrant Compounds*. Battelle, Monterey, CA, 2010.
- [9] J. Quinn, D. Elliott, S. O'Hara, A. Billow, Use of nanoscale iron and bimetallic particles for environmental remediation: A review of field-scale applications, *Environmental applications of nanoscale and microscale reactive metal particles*, Copyright, (2009) 263-285.

- [10] R.L. Johnson, G.O.B. Johnson, J.T. Nurmi, P.G. Tratnyek, Natural Organic Matter Enhanced Mobility of Nano Zerovalent Iron, *Environmental Science & Technology*, 43 (2009) 5455-5460.
- [11] K.W. Henn, D.W. Waddill, Utilization of nanoscale zero-valent iron for source remediation—A case study, *Remediation Journal*, 16 (2006) 57-77.
- [12] T. Phenrat, N. Saleh, K. Sirk, R.D. Tilton, G.V. Lowry, Aggregation and sedimentation of aqueous nanoscale zerovalent iron dispersions, *Environmental science & technology*, 41 (2007) 284-290.
- [13] T. Phenrat, H.-J. Kim, F. Fagerlund, T. Illangasekare, R.D. Tilton, G.V. Lowry, Particle Size Distribution, Concentration, and Magnetic Attraction Affect Transport of Polymer-Modified Fe⁰ Nanoparticles in Sand Columns, *Environmental Science & Technology*, 43 (2009) 5079-5085.
- [14] T. Phenrat, N. Saleh, K. Sirk, H.-J. Kim, R.D. Tilton, G.V. Lowry, Stabilization of aqueous nanoscale zerovalent iron dispersions by anionic polyelectrolytes: adsorbed anionic polyelectrolyte layer properties and their effect on aggregation and sedimentation, *Journal of Nanoparticle Research*, 10 (2008) 795-814.
- [15] T. Raychoudhury, N. Tufenkji, S. Ghoshal, Aggregation and deposition kinetics of carboxymethyl cellulose-modified zero-valent iron nanoparticles in porous media, *Water research*, 46 (2012) 1735-1744.
- [16] A.R. Petosa, D.P. Jaisi, I.R. Quevedo, M. Elimelech, N. Tufenkji, Aggregation and deposition of engineered nanomaterials in aquatic environments: Role of physicochemical interactions, *Environmental science & technology*, 44 (2010) 6532-6549.
- [17] E.M. Hotze, T. Phenrat, G.V. Lowry, Nanoparticle aggregation: Challenges to understanding transport and reactivity in the environment, *Journal of environmental quality*, 39 (2010) 1909-1924.
- [18] T. Raychoudhury, N. Tufenkji, S. Ghoshal, Straining of Polyelectrolyte-Stabilized Nanoscale Zero Valent Iron Particles during Transport through Granular Porous Media, *Water Research*, (2013).
- [19] F. He, D. Zhao, Manipulating the Size and Dispersibility of Zerovalent Iron Nanoparticles by Use of Carboxymethyl Cellulose Stabilizers, *Environmental Science & Technology*, 41 (2007) 6216-6221.
- [20] B. Schrick, B.W. Hydutsky, J.L. Blough, T.E. Mallouk, Delivery Vehicles for Zerovalent Metal Nanoparticles in Soil and Groundwater, *Chemistry of Materials*, 16 (2004) 2187-2193.
- [21] A. Tiraferri, K.L. Chen, R. Sethi, M. Elimelech, Reduced aggregation and sedimentation of zero-valent iron nanoparticles in the presence of guar gum, *Journal of colloid and interface science*, 324 (2008) 71-79.
- [22] N. Saleh, K. Sirk, Y. Liu, T. Phenrat, B. Dufour, K. Matyjaszewski, R.D. Tilton, G.V. Lowry, Surface modifications enhance nanoiron transport and NAPL targeting in saturated porous media, *Environmental Engineering Science*, 24 (2007) 45-57.
- [23] T. Phenrat, A. Cihan, H.-J. Kim, M. Mital, T. Illangasekare, G.V. Lowry, Transport and Deposition of Polymer-Modified Fe⁰ Nanoparticles in 2-D Heterogeneous Porous Media: Effects of Particle Concentration, Fe⁰ Content, and Coatings, *Environmental Science & Technology*, 44 (2010) 9086-9093.
- [24] T. Phenrat, H.-J. Kim, F. Fagerlund, T. Illangasekare, G.V. Lowry, Empirical correlations to estimate agglomerate size and deposition during injection of a polyelectrolyte-modified Fe⁰ nanoparticle at high particle concentration in saturated sand, *Journal of contaminant hydrology*, 118 (2010) 152-164.
- [25] F. He, M. Zhang, T. Qian, D. Zhao, Transport of carboxymethyl cellulose stabilized iron nanoparticles in porous media: Column experiments and modeling, *Journal of Colloid and Interface Science*, 334 (2009) 96-102.

- [26] T. Phenrat, H.-J. Kim, F. Fagerlund, T. Illangasekare, G.V. Lowry, Empirical correlations to estimate agglomerate size and deposition during injection of a polyelectrolyte-modified Fe₀ nanoparticle at high particle concentration in saturated sand, *Journal of Contaminant Hydrology*, 118 (2010) 152-164.
- [27] T. Raychoudhury, G. Naja, S. Ghoshal, Assessment of transport of two polyelectrolyte-stabilized zero-valent iron nanoparticles in porous media, *Journal of Contaminant Hydrology*, 118 (2010) 143-151.
- [28] T. Tosco, R. Sethi, Transport of Non-Newtonian Suspensions of Highly Concentrated Micro- And Nanoscale Iron Particles in Porous Media: A Modeling Approach, *Environmental Science & Technology*, 44 (2010) 9062-9068.
- [29] M.J. Truex, V.R. Vermeul, D.P. Mendoza, B.G. Fritz, R.D. Mackley, M. Oostrom, T.W. Wietsma, T. Macbeth, Injection of Zero - Valent Iron into an Unconfined Aquifer Using Shear - Thinning Fluids, *Ground Water Monitoring & Remediation*, 31 (2011) 50-58.
- [30] S. Kanel, R. Goswami, T. Clement, M. Barnett, D. Zhao, Two dimensional transport characteristics of surface stabilized zero-valent iron nanoparticles in porous media, *Environmental science & technology*, 42 (2007) 896-900.
- [31] K. Darko - Kanya, K.R. Reddy, Two - dimensional transport of lactate - modified nanoscale iron particles in porous media, *Remediation Journal*, 21 (2011) 45-72.
- [32] M.O. Rivett, S.W. Chapman, R.M. Allen-King, S. Feenstra, J.A. Cherry, Pump-and-Treat Remediation of Chlorinated Solvent Contamination at a Controlled Field-Experiment Site, *Environmental Science & Technology*, 40 (2006) 6770-6781.
- [33] T. Raychoudhury, G. Naja, S. Ghoshal, Assessment of transport of two polyelectrolyte-stabilized zero-valent iron nanoparticles in porous media, *Journal of contaminant hydrology*, 118 (2010) 143-151.
- [34] N. Tufenkji, M. Elimelech, Correlation equation for predicting single-collector efficiency in physicochemical filtration in saturated porous media, *Environmental science & technology*, 38 (2004) 529-536.
- [35] G.C.C. Yang, H.-C. Tu, C.-H. Hung, Stability of nanoiron slurries and their transport in the subsurface environment, *Separation and Purification Technology*, 58 (2007) 166-172.
- [36] C.M. Kocur, D.M. O'Carroll, B.E. Sleep, Impact of nZVI stability on mobility in porous media, *Journal of Contaminant Hydrology*, 145 (2013) 17-25.
- [37] E.D. Vecchia, M. Luna, R. Sethi, Transport in Porous Media of Highly Concentrated Iron Micro- and Nanoparticles in the Presence of Xanthan Gum, *Environmental Science & Technology*, 43 (2009) 8942-8947.
- [38] H.F. Lecoanet, J.-Y. Bottero, M.R. Wiesner, Laboratory Assessment of the Mobility of Nanomaterials in Porous Media, *Environmental Science & Technology*, 38 (2004) 5164-5169.
- [39] N. Tufenkji, M. Elimelech, Correlation Equation for Predicting Single-Collector Efficiency in Physicochemical Filtration in Saturated Porous Media, *Environmental Science & Technology*, 38 (2003) 529-536.
- [40] A. Tiraferri, R. Sethi, Enhanced transport of zerovalent iron nanoparticles in saturated porous media by guar gum, *Journal of Nanoparticle Research*, 11 (2009) 635-645.

Chapter 6

Correlation equation for predicting single-collector efficiency using trajectory analysis method in three dimensions

Jing Li¹, Xiaohu Xie², Subhasis Ghoshal^{1*}

1 Department of Civil Engineering, McGill University, Montreal, Canada H3A 2K6

2 Department of Computer Science, McGill University, Montreal, Canada H3A 2K6

Keywords: NZVI particles, colloid transport, viscosity, carboxymethyl cellulose, DLVO theory calculations, single collector contact efficiency prediction, ionic strength

*Corresponding author, Department of Civil Engineering, McGill University, 817 Sherbrooke Street West, Montreal, QC, Canada H3A 2K6, e-mail: subhasis.ghoshal@mcgill.ca,

Tel: (514) 398-6867, Fax: (514) 398-7361

To be published on Environmental Science & Technology

6.1 Introduction

Advancing the understanding of the transport and deposition of engineered nanoparticles in saturated porous media is essential for the assessment of their fate and transport in subsurface media, their removal in sand filters, and their mobility from injection wells during remediation operations.[1-5] The colloid filtration theory (CFT) is widely used in modeling the fate and transport of nano as well as submicron particles and biocolloids.[6-11]

In the CFT, the probability of contact of colloids to a collector is quantified by the single collector contact efficiency (η_0), and the probability of successful attachment of the colloids that contacted the collector is quantified by the attachment efficiency or sticking efficiency (α). The value of η_0 is calculated from correlation equations.[12-16] The value of α is usually obtained from the experimental transport data and the known η_0 value. With the CFT equation the rate of deposition for transport of colloids in saturated porous media is given by:

$$k = \left[\frac{3(1-f)u}{2d_{sf}} \alpha \right] \eta_0 \quad (6.1)$$

Considerable efforts have been made in analyzing the impact of various forces acting on colloids during its transport around collectors, including hydraulic and gravity forces, Brownian diffusion, van der Waals and electrostatics double-layer interaction forces for calculation of the single collector contact efficiency (η_0), as an estimate of the rate of colloid deposition.[12-26] Brownian motion is considered as the main cause for contact with the collector for particles with diameter less than 1000 nm[15, 22] and the contribution of Brownian motion to the single collector contact efficiency is dominant. There are two common approaches used for the estimation of η_0 : (1) Lagrangian trajectory analysis of the colloid that predicts the path of colloid

around model collectors such as the Happel's sphere-in-cell,[12, 13, 16, 22, 26] Happel's-hemisphere-in-cell,[23, 25] spheres in series, unit bed porous media geometries or a constricted tube;[17, 18, 20, 26] (2) The numerical solution of the convective-diffusion equation describing the concentration of colloids around similar collectors (Eulerian approach).[14, 15, 21, 27]

Several studies have provided correlation equations to facilitate calculation of η_0 . [12, 13, 15, 16, 23] Two popular correlation equations for η_0 prediction are the equations developed by Rajagopalan and Tien[13] (referred henceforth as RT equation) and the equation developed by Tufenkji and Elimelech (referred henceforth as TE equation).[14] The RT equation was developed based on the trajectory analysis of colloids around a Happel's sphere-in-cell collector model for downward flow, and force and torque balance equations for gravity, surface force as well as hydraulic drag on the colloid were solved. The RT equation does not account for Brownian diffusion in their colloid trajectory simulation, but rather a Brownian diffusion term was directly superimposed with terms describing interception and sedimentation. A recent study done by Nelson and Ginn [22] suggested that the simple superimposition of the Brownian diffusion term to the η_0 correlation equation could lead to overestimation. Several subsequent studies have incorporated Brownian diffusion directly into equations for colloid transport around the collector for calculation of η_0 , [15, 20, 22, 23, 28] generally by considering Brownian diffusion as a Brownian force. This approach, however, ignored the sensitivity of Brownian diffusion to time step and to particle size.[22] The TE equation, was also developed based on Happel's sphere-in-cell but the deposition rate was calculated based on the numerical simulation of the convective-diffusion equation (Eulerian approach). This equation is improved on the RT equation by considering the effects of van der Waals forces and hydrodynamic interactions on

particles as well as including the diffusion effect into the simulation. However, the TE equation may overestimate the Brownian diffusion for calculating η_0 . [15, 16]

The RT and TE correlation equations have been derived for two dimensional analyses of colloid transport around collectors in two dimensions for vertical flow. In this study, we show that the equations need to be modified for horizontal flow conditions, particularly when the colloids have high density. These conditions are relevant for the transport of nanoscale zero valent iron (NZVI) particles in subsurface porous media. The direct injection of NZVI for remediation of sites contaminated by chlorinated organic compounds and heavy metals has been suggested. [29-32] In such scenarios, NZVI particles with densities in the range of 6-7 g/cm³ would travel horizontally following injection from wells.

We demonstrate that a modified correlation equation based on the flow of colloids around a three-dimensional collector provides better estimates of the single collector contact efficiency. Unlike the case of the vertical flow, in the horizontal flow, the trajectory of particle needs to be extended to three-dimensions, due to the changes of the actions of the gravity force: in the vertical flow, the gravity force is concordant with the flow direction, while, in the horizontal flow, the gravity force is perpendicular with the flow direction. In the former case, the trajectory of particle is commonly simulated in two dimensions and the gravity is decomposed in radius and tangent directions (as shown in Figure 6.1a). In the later case, the directions of various forces are more complicated. Thus, the trajectory of particle determined by complicated actions of forces needs to be simulated in three dimensions and the gravity needs to be decomposed in three directions (as shown in Figure 6.1b).

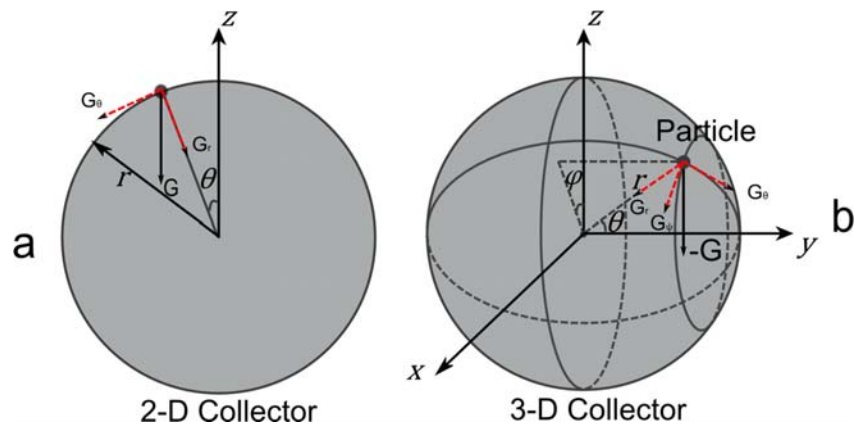


Figure 6.1. The gravity decomposition on the collector: a) 2-D collector; b) 3-D collector.

In addition to accounting for horizontal flow and the effects of density for metal nanoparticles, we also consider the effects of solution viscosity. The presence of polymers or polyelectrolytes, commonly used to coat engineered nanoparticles or added to achieve shear thinning of the aqueous medium to promote the colloidal stability and transport of particles, in the electrolyte solution as excess dissolved polymers leads to high viscosity. [33-36] The changes in viscosity can directly influence the rate of deposition of colloids.

Herein, we develop a modified equations based on the RT model for predicting η_0 for particle transport in 3-D around a collector. The correlation equations developed here are based on the RT model, except that Brownian diffusion was explicitly incorporated in trajectory simulations in this study. The RT model was used as it was easier to implement for 3-D particle transport around the collectors and account for changes in force and torque in 3-D versus 2-D. The model was used to assess the changes in η_0 for a wide range of parameter values for the particle density (1 to 7 g/cm³), viscosity of the suspension (1 to 26.3 cP), flow velocity ($4 \cdot 10^{-7}$ - $2 \cdot 10^{-3}$ m/s) and collector diameter (0.05-1.2 mm).

6.2 Numerical simulation for η_0

A. Geometry of the collector and forces acting on the particle. η_0 is calculated in the RT model[13] as :

$$\eta_0 = \frac{I}{\pi b^2 U C_0} \quad (6.2)$$

where I is the rate at which particle collides onto the collector, b is the summation of the collector radius and the thickness of the liquid shell, which is dependent on the radius and porosity of the collector (as described in the equation 6.S1 in SI), U is the approach velocity of fluid, and C_0 is the number concentration of colloid particles in fluid. In the RT model, the trajectories of the suspended particles across the collector were accordant with the direction of the fluid flow and symmetrical. Thus, the trajectory can be expressed in polar coordinates (r, θ) . [13] The trajectory path $(r(t), \theta(t))$ of the suspended particle in the RT model was derived by solving the force and torque balances on the particle using the fourth-order Runge-Kutta numerical integration method. Finally, the calculation was simplified to search the critical value of θ_s , below which all trajectories can contact the collector. The value of η_0 can be determined from θ_s as:

$$\eta_0 = \sin^2 \theta_s \quad (6.3)$$

In contrast, for the 3-D collector, in addition to r and θ coordinates used in the 2-D collector, a third polar coordinate φ is employed. Because randomized Brownian motion was included in the trajectory simulations which can result in deviations from the trajectory path calculated on the basis of flow, gravity, surface forces and hydrodynamic drag, we did not

compute the limiting φ (similar to the aforementioned θ_s) to determine the initial area in which all trajectories would contact the collector. Instead, in our analyses, a sufficiently large number of particles are considered to be uniformly distributed in the flow cross-section (shown in Figure 6.2). This is systematically performed by dividing the cross-section into 20 equal and concentric areas as well as the trajectories are calculated starting from the central section moving towards the circumferential regions, and the number of particle contacts with the collector is simultaneously recorded. Once a concentric area with no trajectory contacting on the collector is encountered, the calculations were skipped for the regions in the outer layers. The trajectories were calculated for 6000 particles, as several conditions showed that there was minimal change in the number of contacts of particle and collector by increasing the particle number to 10,000. The total calculated contact events divided by the total particles number (6000) yielded η_0 .

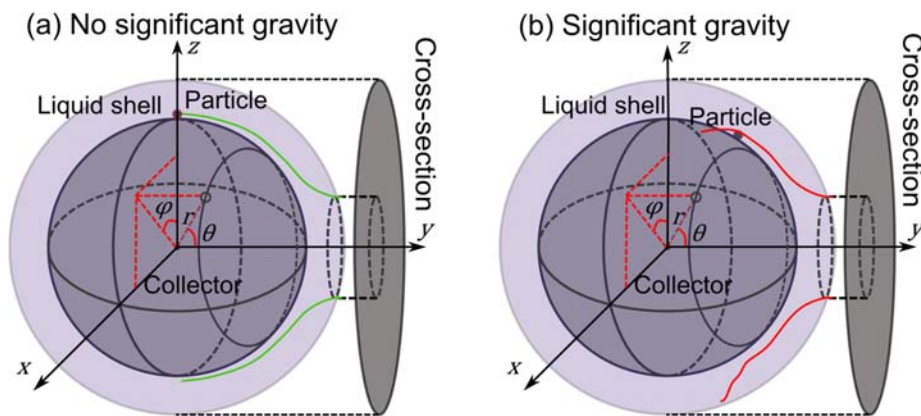


Figure 6.2. Happel's sphere-in-cell porous media model in horizontal flow origination. (a) The symmetrical deposition of colloids on top and bottom of the collector under small gravity forces (small particle size and/or particle density); (b) The unsymmetrical trajectory of colloids around the collector under significant gravity forces.

Table 6.1. Summary of the dimensionless parameters

$N_R = \frac{d_p}{d_s}$	aspect ratio
$N_{PE} = \frac{Ud_s}{D_\infty}$	Peclet number
$N_{Lo} = \frac{A}{9\pi\nu a_p^2 U}$	London attraction
$N_G = \frac{2 a_p^2 (\rho_p - \rho_f) g}{9 \nu U}$	gravity number, ratio of Stokes particle settling velocity to approach velocity of the fluid
<p>d_p is the diameter of the collector (nm), d_s is the diameter of the collector (nm), a_p is the radius of the particle (nm), U is the approach flow velocity (nm/s), A is Hamaker constant (J), g is gravity constant, T is fluid absolute temperature (here it was set to be 298 K), D_∞ is bulk diffusion coefficient, ν is viscosity of the suspension (kg/m/s), ρ_p is the density of the particle (kg/m³), ρ_f is the density of the dispersant.</p>	

Particle Velocity. Even though the particle trajectory is considered in three dimensions in this study, the fluid velocity was considered in two dimensions, as described by the RT model. This is because the stream function is not altered due to the volume flux through the surface bounded by a constant value ψ of the Stokes stream function.[37] Thus, the stream function can still be depicted in plane coordinate system (r, θ) .

The stream function in the liquid shell is referred from Rajagopalan and Tien's study[13] and depicted in SI section II in detail. As a result, the velocity field of the flow in the liquid shell is:

$$V = -\left(\frac{1}{r \sin \theta} \frac{\partial \psi}{r \partial \theta}\right) e_r + \left(\frac{1}{r \sin \theta} \frac{\partial \psi}{\partial r}\right) e_\theta \quad (6.4)$$

where ψ is the stream function (additional details are presented in SI).

The force and torque, corresponding to gravity, surface, and hydraulic drag are described and listed in detail in Table 6.2.

Table 6.2. Forces and torques acting on the suspended particles through 2-D and 3-D collectors.

1) Gravitational force and torque

I: In 2-D collector

$$f_2^G = (4/3)\pi a_p^3 (\rho_p - \rho_f) g = (4/3)\pi a_p^3 (\rho_p - \rho_f) g [-\cos\theta \times e_r + \sin\theta \times e_\theta]$$

$$t_2^G = 0$$

II: In 3-D collector

$$f_3^G = (4/3)\pi a_p^3 (\rho_p - \rho_f) g = (4/3)\pi a_p^3 (\rho_p - \rho_f) g [-\sin\theta \times \cos\phi \times e_r - \cos\theta \times \cos\phi \times e_\theta - \sin\phi \times e_\phi]$$

$$t_3^G = 0$$

$$g = |g|$$

2) Surface force and torque

a) Landon force and torque

I: In 2-D collector

$$f_2^{Lo} = [-2Aa(\delta, a_p, \lambda_e) a_p^3 / 3\delta^2 (2a_p + \delta)^2] e_r$$

where, $a(\delta, a_p, \lambda_e)$ is the retardation correction factor, whose values can be referred from Rajagopalan' thesis. [38]

$$t_2^{Lo} = 0$$

b) Double-layer interaction force and torque

$$f^{DL} = \{[\varepsilon a_p \kappa (\xi_c^2 + \xi_p^2) / 2] \times [(2\xi_c \xi_p / (\xi_c^2 + \xi_p^2)) - e^{-\kappa\delta}] [e^{-\kappa\delta} / (1 - e^{-2\kappa\delta})]\} e_r$$

$$t^{DL} = 0$$

II: In 3-D collector

In 3-D collector, all surface force and torque worked on particle are the same as those in 2-D collector.

3) Drag forces and torques

I: In 2-D collector

a) Due to the translation of the particles

$$(f^D)^t = -6\pi\nu a_p [u_r f_r^t(\delta^+) e_r + u_\theta f_\theta^t(\delta^+) e_\theta]$$

$$(t^D)^t = 8\pi\nu a_p^2 u_\theta g_\phi^t(\delta^+) e_\phi$$

b) Due to the rotation of the particle

$$(f^D)^r = 6\pi\nu a_p w_1 f_\theta^r(\delta^+) e_\theta$$

$$(t^D)^r = -8\pi\nu a_p^3 w_1 g_\phi^r(\delta^+) e_\phi$$

c) Due to the fluid velocity in the presence of the stationary particle:

$$(f^D)^m = 6\pi\nu a_p \{-A_C y^2 f_r^m(\delta^+) e_r + [B_C y f_{1\theta}^m(\delta^+) + D_C y^2 f_{2\theta}^m(\delta^+)] e_\theta\}$$

$$(t^D)^m = -8\pi\nu a_p^3 \{[B_C g_{1\phi}^m(\delta^+) + D_C y g_{2\phi}^m(\delta^+)] e_\phi\}$$

II: In 3-D collector

Each drag force and each torque in 3-D collector are the same as the corresponding force and torque in 2-D collector.

From the balances of forces and torques, we obtain the velocity of particles in the liquid shell around the 3-D collector in r , θ , ϕ directions:

$$m\left(\frac{\partial u}{\partial t}\right)_r = -6\pi\nu a_p u_r f_r^t - 6\pi\nu a_p A_C y^2 f_r^m - \frac{4}{3}\pi a_p^3 (\rho_p - \rho_f) g \cos\phi \sin\theta - \{2Aa_p^3 \alpha / [3\delta^2(2a_p + \delta)^2]\} + \{[\varepsilon a_p \kappa (\xi_c^2 + \xi_p^2) / 2] \times [(2\xi_c \xi_p / (\xi_c^2 + \xi_p^2)) - e^{-\kappa\delta}] [e^{-\kappa\delta} / (1 - e^{-2\kappa\delta})]\} \quad (6.5)$$

$$m\left(\frac{\partial u}{\partial t}\right)_\theta = -6\pi\nu a_p u_\theta f_\theta^t + 6\pi\nu a_p^2 w_1 f_\theta^r + 6\pi\nu a_p [B_C y f_{1\theta}^m + D_C y^2 f_{2\theta}^m] - \frac{4}{3}\pi\nu a_p^3 (\rho_p - \rho_f) g \cos\theta \cos\phi \quad (6.6)$$

$$m\left(\frac{\partial u}{\partial t}\right)_\phi = 6\pi\nu a_p u_\phi f_\phi^t + \frac{4}{3}\pi\nu a_p^3 (\rho_p - \rho_f) g \sin\phi \quad (6.7)$$

Equations 6.5, 6.6 and 6.7, which present the determinations of particle's velocities in three coordinates on the forces in the corresponding coordinate, can be simplified as:

$$\frac{\partial u_r}{\partial t} = \frac{U}{f_r^t} \left(\frac{1}{N_R} + 1 + \delta^+ \right) \left[-A_C^+ (1 + \delta^+)^2 f_r^m + N_G \sin \theta \cos \varphi - \frac{N_{Lo} a_s (\delta^+)^2}{4(a_s + a_p)} \right] \quad (6.8)$$

$$\frac{\partial u_\theta}{\partial t} = \frac{U}{rs_1} [B_C^+ s_2 + D_C^+ (1 + \delta^+) s_3 + N_G \cos \theta \cos \varphi] \quad (6.9)$$

$$\frac{\partial u_\varphi}{\partial t} = \frac{U}{rs_1} N_G \sin \varphi \quad (6.10)$$

In the above equations, N_R , N_G and N_{Lo} are dimensionless numbers that characterize the various forces acting on the particle. The wall-effect correction factors (s_1 , s_2 and s_3) are incorporated in the calculations.

Brownian Diffusion. In the simulations, we use the fourth order Runge-Kutta method to compute the trajectory of a particle. Brownian motion is simulated by the method used in Nelson and Ginn's study.[22] Briefly, the method can be described as followings.

p_n is the three dimensional displacement vector at time t_n , and Δt is the time step. The displacement with time is calculated by [22]:

$$\bar{p}_{n+1} = p_n + \sum_{i=1}^4 b_i k_i \quad (6.11)$$

$$t_{n+1} = t_n + \Delta t \quad (6.12)$$

where, \bar{p}_{n+1} is the provisional three dimensional displacement vector, which is derived from the forces (London van der Waals force, gravity, hydrodynamic forces) at time t_{n+1} . Brownian motion is not taken into the calculations in the above steps. After \bar{p}_{n+1} is computed, the displacement rendered by Brownian motion is added to the above calculations:

$$p_{n+1} = \bar{p}_{n+1} + \Delta p \quad (6.13)$$

$$\Delta p = [\Delta x, \Delta y, \Delta z]^T \quad (6.14)$$

where, p_{n+1} is the ultimate displacement of the particle at time t_{n+1} , Δp is the three dimensional displacement vector generated by Brownian motion, which can be expressed in Cartesian coordinates :

$$\Delta x = n_x \sqrt{2D_\infty \Delta t} \quad (6.15)$$

$$\Delta y = n_y \sqrt{2D_\infty \Delta t} \quad (6.16)$$

$$\Delta z = n_z \sqrt{2D_\infty \Delta t} \quad (6.17)$$

where n_x , n_y and n_z are random variables of normal (0,1). D_∞ is the diffusion coefficient of the particle, whose value is the same as the bulk diffusion coefficient referred in Table 6.1. It should be noted that the equation used to calculate the displacement of Brownian particles differs from those used in previous studies.[22] This is due to the fact that the displacement of Brownian particles is dependent on the number of dimensions of Brownian motion. And the model developed in this study is expanded to 3-D, which varies from those models developed in the previous studies. Further, the time step Δt is adaptively controlled in the Runge-Kutta fourth order method with values ranging from 10^{-16} to 10^{-18} s.

C. Regression Analysis to Obtain the Correlation Equation. The superposition of the three deposition mechanisms of diffusion, interception and sedimentation to yield the correlation equation of η_0 , as in the RT equation and TE equations, is assumed in this study:

$$\eta_0 = \eta_D + \eta_I + \eta_G \quad (18)$$

where η_D is the contribution of Brownian motion to the impact, η_I is the contribution of interception to the impact and η_G is the contribution of gravitational sedimentation to the impact. Although previous studies [13, 14, 39] have suggested that all of these three terms were power function of multiple dimensionless parameters, Nelson and Ginn have suggested that the gravitational sedimentation term is not a power function of N_G . [16] Each correlation of these three terms is determined by using the methodology developed by Tufenkji and Elimelech. [14] Briefly, η_D is assigned firstly by “turning off” the other two mechanics by the setting particle density to be the same as dispersant density (no gravitational sedimentation) and assuming particle size to be infinite small (no interception effect). The single collector contact efficiencies, numerically calculated for 1500 times by randomly selecting 300 integers of each of the five parameters, d_p , d_s , ν , A and U (particle density which was kept fixed) over the entire range of parameter values listed in Table 6.3, are taken into account for the regression calculation of the diffusion term. Then the dimensionless parameters (N_R , N_{PE} and N_{Lo}) are calculated based on the above 1500 times calculation, followed by forming the correlation equation of η_D with these three dimensionless parameters. Subsequently, using the same scenario to conduct another 1500 times of numerical calculations of the single collector contact efficiency with the same five parameters (ρ_p is still set to be equal to ρ_f) used in η_D term establishment, but the particle size are not treated as an infinite small point. Then the dimensionless parameters (N_R , N_{Lo}) are calculated based on the above 1500 times calculations. The numerical results of the single collector contact efficiency would be subtracted by the impact contributed by diffusion motion (subtracting η_D

formula obtained above) and the consequent results of single collector contact efficiencies, which would be correlated with two dimensionless parameters (N_R , N_{Lo}) to render η_I formula. Finally, the single collector contact efficiency would be numerically calculated 1200 times over the six parameters (d_p , d_s , ν , A, U and ρ_p) over the entire ranges listed in Table 6.3—each parameter is run 200 times. The dimensionless parameters (N_R , N_G) are calculated based on the above six parameters, whose values are randomly assigned from the corresponding range. The single collector contact efficiency values would be subtracted by the values of η_D and η_I , and the yielded values of the single collector contact efficiency would be correlated with N_R and N_G to form η_G formula.

Table 6.3. Summary of Parameter Values Used in Numerical Calculations

Parameters	Range
Particle diameter, d_p	0.01-10 μm
Collector (grain) diameter, d_s	0.05-1.2 mm
Particle density, ρ_p	1.00-7.00 g/cm ³
Dispersant viscosity, ν	1.0-26.3 cP
Approach velocity, U	4*10 ⁻⁷ -2*10 ⁻³ m/s
Hamaker constant, A	1*10 ⁻²⁰ -4*10 ⁻²⁰ J
Temperature, T	298 K
Porosity, f	0.37

6.3 Results

6.3.1 Comparison of the Numerical Results with the RT Equation and TE Equation

The validation of our model is conducted by comparing several simulations for various parameter values with those predicted by RT and TE equations. The results from the RT and TE equations here, use the reported correlation equations derived based on conditions of vertical flow in 2-D for a Happel's sphere collector.[13, 40] The results are shown in the seventeen figures (listed as Figures 6.S1-6.S2, and Figures 6.S4-6.S8 in SI). The changes of the predictions of η_0 for the RT, TE and our model for various parameters are presented in a series of figures: particle diameter (Figures 6.S1-6.S2), particle density (Figures 6.S4-6.S6), viscosity of the suspension (Figures 6.S7-6.S10), approach velocity (Figures 6.S11-6.S13) and collector diameter (Figures 6.S14-6.S18).

In Figure 6.S1, there is a significant difference displayed between our 3-D model simulation or the TE equation and the RT results as the particle diameter increased, the 3-D model and the TE equation predict higher values of η_0 than those predicted by the RT equation, for a particle density of 1.05 g/cm³ (similar to density of latex particles, commonly used as a model environmental biocolloid). This can be interpreted by the difference of η_G expressions in the RT equation and TE equation. The coefficient value of η_G expression in RT equation is 2.4×10^{-3} , while in TE equation it is 0.22, indicating underestimation of η_G in the RT equation. No apparent difference (except in the 0.01-0.1 μm particle diameter range) of size values exists between the TE prediction and our 3-D simulation, suggesting that our 3-D model methodologies are reliable for the range of parameter values used for developing the of the RT and TE correlation equations. However, when particle density is increased to 6.58 g/cm³, a significant

difference is observed between the TE equation and our 3-D simulations, as shown in Figure 6.S2. The predicted η_0 values from the 3-D simulation matches closely with the RT and TE equations upto a particle diameter of 3000 nm, but the η_0 values remain constant at around 0.3 for larger particles in the 3-D simulation, whereas the η_0 values increase with the increase of particle diameter for the TE and RT equations.

The 3-D model simulates a very different particle contact pattern for particles with density of 6.58 g/cm³ compared to those for density with of 1.05 g/cm³. As shown in Figure 6.S3a: the particle with density of 1.05 g/cm³ and diameter of 4000 nm is deposited uniformly on the top and bottom of the collector, however, when the density increased to 6.58 g/cm³, the particle is deposited only on the top part of the collector as shown in Figure 6.S3b. No particle can contact with the collector from the bottom side, as a result of the significant settling of particles out of the liquid shell trajectory space around the collector caused by their considerable gravity (as drawing in Figure 6.2b), verifying the result shown in Figure 6.S2 that the η_0 values obtained from 3-D simulation is lower than those predicted by the TE and RT equations. Further, the result that η_0 values remain constant in 4000-10000 nm particle (with density of 6.58 g/cm³) diameter range can ascribe to the likelihood that with the increase of particle size in this range, the population of particles which can be transported onto the top side of the collector would decrease. On the other hand, with the increase of particle size (with density of 6.58 g/cm³), the contact possibility of particles onto the top side of collector would increased. These two effects finally maybe balance to yield a constant η_0 .

The influence of particle density and diameter on η_0 as predicted by the RT, TE and 3-D simulation are discussed in the SI (Figures 6.S4-6.S6). Overall there was a good agreement

between the 3-D numerical simulations with the RT model, except at big particle diameters of 4000 nm and highdensitites than 4000 kg/m³ as highlighted in Figure 6.S3.

Metal colloids such as NZVI used in remediation are often dispersed in polymers or polyelectrolytes to improve their colloidal stability. The polymers and polyelectrolyte solutions are generally more viscous than water. Thus the effect of viscosity of the suspension on the single collector contact efficiency was extensively investigated in this study and the results are shown in Figures 6.S7-6.S10. It can be observed from Figures 6.S7 and 6.S8 that for large particle diameter (such as 2000 nm), the dependence of the single collector contact efficiency on the suspension viscosity differs under different particle densities in our current 3-D simulations from the TE equation. For a particle density of 6.58 g/cm³, the single collector contact efficiency values of our numerical simulation are less than those predicted from TE and RT equations in the range of 1-26.3 cP viscosity values as shown in Figure 6.S7. On the contrary, with a particle density of 1.05 g/cm³, the single collector contact efficiency values obtained from our 3-D simulations are larger than those predicted from TE and RT equations in the same viscosity range as shown in Figure 6.S8). These results can be interpreted by the influence of gravity. For the range of viscosity values, the gravity force on a high density particle settles it away from the liquid shell on the bottom of the collector, yeiding a small value of the single collector contact efficiency with the 3-D simulations, while, with the increase of the suspension viscosity, the resistance to settling from the visous solution counteracts the gravity settling, leading to little difference in the single collector contact efficiency between the 3-D simulation and TE and RT equations. When particle density is only 1.05 g/cm³, the gravity force would not be sufficient to drag the particle away from the bottom part of collector. For a smaller particle diameter such as 400 nm, no noticable difference in η_0 between the 3-D simulation and the RT and TE equations

is observed for the range of viscosity of 1 cP to 26.3 cP, at particle densities of either 1.05 g/cm³ or 6.58 g/cm³ as shown in Figures 6.S9 and 6.S10. For a smaller particle, the gravity force would not influence the trajectory of particles even at a density such as 6.58 g/cm³.

The effect of the approach velocity on the single collector contact efficiency are presented in Figures 6.S11-6.S13. The simulated η_0 values in the current 3-D model do not display any difference from those predicted from the RT and TE equations at particle diameter of 400 nm (shown in Figure 6.S11). When the particle diameter increases to 4000 nm, the single collector contact efficiency simulated from our 3-D model shows a distinct difference from those predicted in TE and RT equations in low approach velocity range (shown in Figure 6.S12): the 3-D model yield is lower than those predicted in the TE and RT equations. This is attributable to the significant settling of particles in our 3-D model at this low flow velocity range, yielding less particle contact possibility. An earlier study[16] has already illustrated that the single collector contact efficiency values predicted from the TE and RE equations commonly exceed unity in very low approach velocity range. But our 3-D numerical simulations do not ever show the excess of unity under the identical conditions, indicating that the prediction of our 3-D model would be more rational than the previous correlations. The reasonable single collector contact efficiency values obtained from our 3-D numerical simulations can be attributed to the 3-D analysis of the gravity force during horizontal flow used in this study to simulate the particle motion with fluid. It should be noted that at very low velocity range, η_0 values increased then decreased with the increase of the approach velocity from our numerical calculations (shown in Figure 6.S12). It can be ascribed to the possibility that particles could not be transported onto the top side of the collector at very low velocity, but with the increase of velocity, the proportion of particles transported on the top side increased, leading to the increase of the contact efficiency.

The single collector contact efficiency, however, reduces to less than unity in all three methods (our 3-D numerical simulation, TE equation and RT equation) at the particle density of 1.05 g/cm^3 (shown in Figure 6.S13) under the identical conditions as in Figure 6.S12

The effect of collector diameter on the single collector contact efficiency is extensively explored and the results are shown in Figures 6.S14-6.S18. The dependence of the single collector contact efficiency of smaller particles (with diameter of 200 nm and density of 6.58 g/cm^3) from our 3-D numerical simulations differs slightly from those predicted from TE and RT equations, as shown in Figure 6.S14. In the range of small collector diameter (50-260 μm), the 3-D simulations data are higher than those from the existing correlations; while, the results are reversed, in the range of big collector diameter (260-1200 μm). This result could be caused by the different methodologies used in this 3-D simulations and in TE and RT equations to consider Brownian diffusion effect on the single collector contact efficiency. As particle diameter is increased to 2000 nm, the dependence of the single collector contact efficiency on the collector diameter overall remains constant in our 3-D simulation, unlike the trends of the increase of single collector contact efficiency with the increase of the single collector contact efficiency in the predictions from TE and RT equations as shown in Figure 6.S15. When the particle density reduces from 6.58 g/cm^3 to 1.05 g/cm^3 , the single collector contact efficiency decreases with the increase of the collector diameter in our 3-D simulation and in the RT and TE equations (shown in Figure 6.S16), all other conditions being identical to the conditions shown for the case shown in Figure 6.S15. The interception and gravity sedimentation mainly determine the single collector contact efficiency (due to the high particle density). Further, as discussed above, the particles would mainly remain in the top part of the collector at this big particle size and density ($d_p=2000 \text{ nm}$, $\rho_p=6.58 \text{ g/cm}^3$) in our 3-D simulation, leading to an overall constant of single

collector contact efficiency with the increase of the collector diameter. Nevertheless, more particles would deposit on the collector with the increase of the collector diameter in the RT and TE models, leading to the trends of the increase of the single collector contact efficiency with the increase of the collector diameter in these two models. Similar trends are also obtained when particle diameter rises to 4000 nm under identical conditions (shown in Figures 6.S17 and 6.S18).

6.3.2 New Correlation Equation for Colloid Transport

From the regression analysis, the final correlation equation for predicting single collector contact efficiency in 3-D model can be expressed as:

$$\eta_0 = 14.16 A_S^{1/3} N_R^{-0.04434} N_{PE}^{-0.8538} + 0.621 A_S N_R^{1.6548} N_{Lo}^{0.105} + 0.0399 N_R^{-0.75} / [1 + \exp(2.6683 - 6.796 N_G)] [N_G^{0.81} / (2.38 + 0.78 N_G^{1.2})] \quad (22)$$

Scrutinizing the correlation equation (eq 6.22), we can observe the major difference between our 3-D correlation to the other two commonly used RT and TE equations: (1) The gravitational sedimentation term (η_G) derived on the basis of the 3-D particle transport for horizontal flow is not a simple power function of the dimensionless parameters: $\eta_G = 0.0399 N_R^{-0.75} / [1 + \exp(2.6683 - 6.796 N_G)] [N_G^{0.81} / (2.38 + 0.78 N_G^{1.2})]$ as in the η_G expressed in TE and RT equations. A similar expression for η_G was also derived by Nelson and Ginn[16] based on RT equation development method with the modification of Brownian motion impact. (2) The diffusion term in this current new equation differs from the η_D expressions in the RT and TE equations: $\eta_D \sim N_R^{-0.04434}$ in this study as compared to $\eta_D \sim N_R^{-0.081}$ in TE equation and N_R is not contained in η_D expression for the RT equation. This difference indicates the dependence of the single collector contact efficiency on the ratio of particle radius to collector radius is more significant in the TE equation (might due to the hydrodynamic retardation effect considered in

the model). (3) The expression of η_I ($=0.621A_s N_R^{1.6548} N_{Lo}^{0.105}$) in the current correlation equation also differs from those in the TE equation ($\eta_I = 0.55A_s N_R^{1.675} N_A^{0.125}$) and RT equation ($\eta_I = 0.72A_s N_R^{15/8} N_{Lo}^{1/8}$). Due to $N_{Lo} = \frac{3}{4}N_A$, η_I expressions in TE and RE equations are very close to each other. Overall, the key distinction of our new correlation equation is the η_G expression, which can be used to more precisely predict the single collector contact efficiency of particles with big gravity in horizontal flow mode.

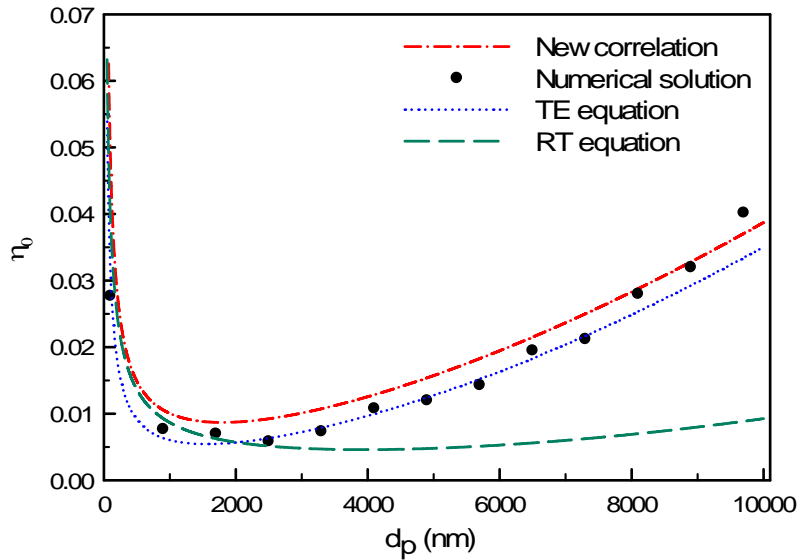


Figure 6.3. The comparison of predictions of single collector contact efficiency (η_0) based on rigorous numerical simulations of trajectories of particles (closed circle), the new correlation (red line), the predictions from TE equation (blue line) and the predictions from the RT equation under the conditions: $\rho_p = 1.05 \text{ g/cm}^3$, $\nu = 1 \text{ cP}$, $U = 0.508 \text{ cm/min}$, $d_s = 340 \text{ }\mu\text{m}$.

The comparison of the numerical data, the correlation equation, TE equation and RT equation data of single collector contact efficiency with the particle diameter under the low particle density condition ($\rho_p = 1.05 \text{ g/cm}^3$) is shown in Figure 6.3. It can be observed that our correlation equation fits the numerical data very closely. Even though there is a slight difference

between the correlation equation proposed here and the TE equation, the overall trends of the single collector contact efficiency with the particle diameter are very similar. The differences of the prediction of η_0 between the current new correlation equation and the TE as well as RT equations can be interpreted by the explanation, which was used to expound the difference of the numerical simulated η_0 and the TE as well as RT equations shown in Figures 6.S1-6.S2.

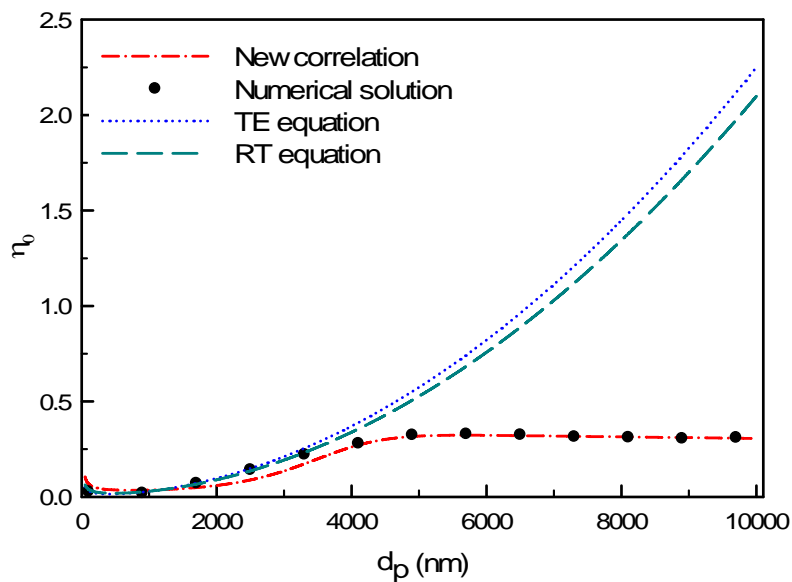


Figure 6.4. The comparison of predictions of single collector contact efficiency (η_0) based on rigorous numerical simulations of trajectories of particles (closed circle), the new correlation (red line), the predictions from TE equation (blue line) and the predictions from the RT equation under the conditions: $\rho_p=6.58 \text{ g/cm}^3$, $\nu=1 \text{ cP}$, $U=0.508 \text{ cm/min}$, $d_s=340 \text{ }\mu\text{m}$.

Unlike the results shown in Figure 6.3, the dependence of single collector contact efficiency on particle diameter (at high particle density, $\rho_p=6.58 \text{ g/cm}^3$) in the current new equation significantly diverged from those obtained from TE and RE equations. Similarly, the reason for this divergence is discussed in the above section (the explanation to the results shown

in Figure 6.S2). The gravity settling term in our correlation ($\eta_G = 0.0399N_R^{-0.75} / [1 + \exp(2.6683 - 6.796N_G)] [N_G^{0.81} / (2.38 + 0.78N_G^{1.2})]$) does not remain power law dependence on N_G . The discrepancy of η_0 predictions between the TE or RT equation and the current correlation equation, shown in Figure 6.4, is mainly caused by the different dependence of the single collector contact efficiency on N_G in the new correlation equation.

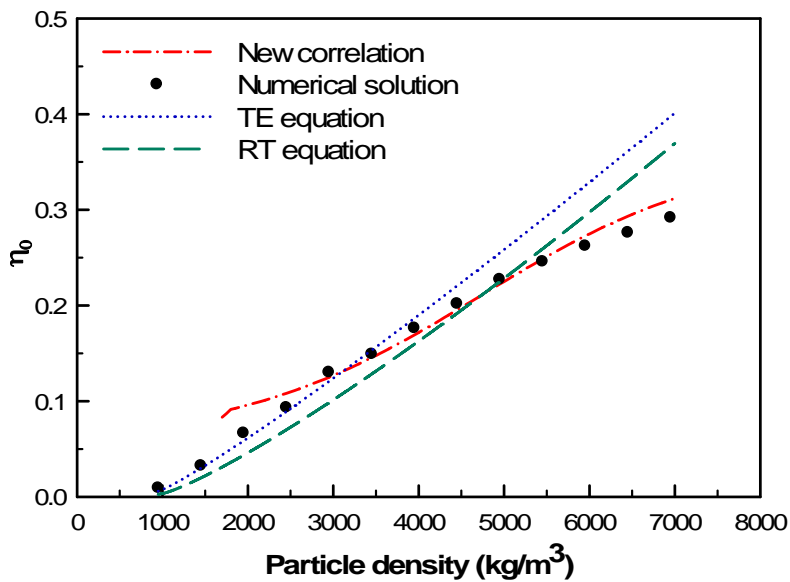


Figure 6.5. The comparison of predictions of single collector contact efficiency (η_0) based on rigorous numerical simulations of trajectories of particles (closed circle), the new correlation (red line), the predictions from TE equation (blue line) and the predictions from the RT equation under the conditions: $d_p = 4000$ nm, $\nu = 1$ cP, $U = 0.508$ cm/min, $d_s = 340$ μ m.

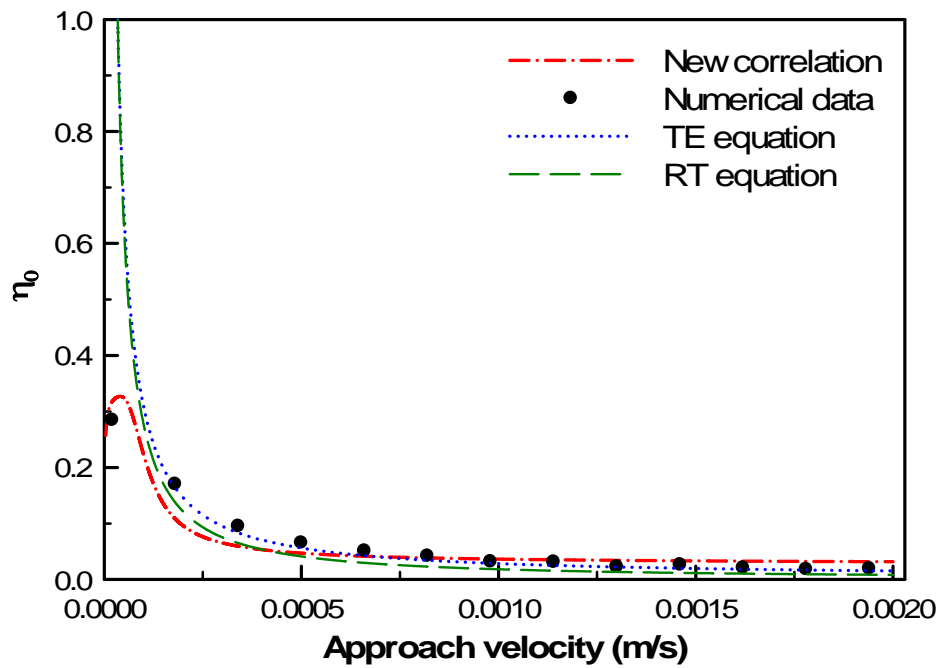


Figure 6.6. The comparison of predictions of single collector contact efficiency (η_0) based on rigorous numerical simulations of trajectories of particles (closed circle) , the new correlation (red line), the predictions from TE equation (blue line) and the predictions from the RT equation under the conditions: $d_p=4000$ nm, $\nu=1$ cP, $\rho_p=6.58$ g/cm³, $d_s=340$ μ m.

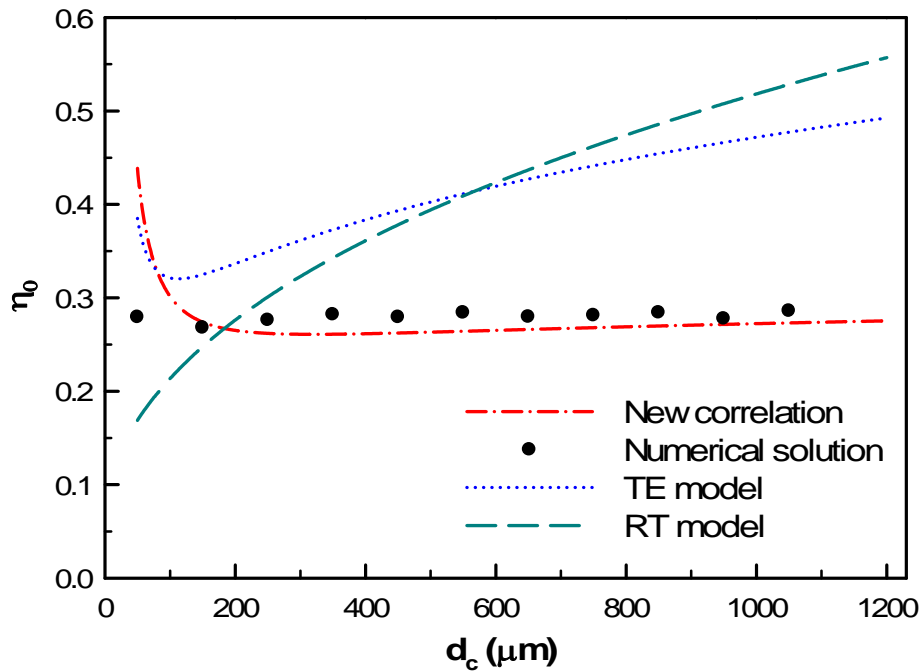


Figure 6.7. The comparison of predictions of single collector contact efficiency based on rigorous numerical simulations of trajectories of particles (closed circle) , the new correlation (red line), the predictions from TE equation (blue line) and the predictions from the RT equation under the conditions: $d_p=4000$ nm, $\nu=1$ cP, $U=0.508$ cm/min, $\rho_p=6.58$ g/cm³.

The comparison of η_0 values with the particle density, approach velocity and the collector diameter predicted by current correlation equation, numerical calculations, the TE and RT equations are shown in Figures 6.5, 6.6 and 6.7, respectively. The results predicted by the current correlation equation match well with the numerical simulation results in these three figures. The reasons for the difference between the numerical simulation results and the TE and RT equations are given in Section 6.3.1.

6.4 Conclusions

The correlation equation and the framework for trajectory analyses suggested here is application for high density particles, such as metal nanoparticles, such as NZVI. Flow of metal

colloids in the subsurface may often be in the horizontal direction, and this study shows that accounting for the effects of gravity force becomes very important. The effects of gravity forces are not captured effectively by commonly used single collector contact efficiency correlation equations such as the RT and TE equations, and this can cause erroneous predictions of η_0 during horizontal flow as demonstrated in this study.

Acknowledgements

The research was funded by the Strategic Project Grant Program of the Natural Sciences and Engineering Research Council of Canada and by Golder Associates Ltd. J. L. was supported in part by a McGill Engineering Doctoral Award.

Nomenclature

Symbols

A	Hamaker constant
A_C	the coefficient in equation 6.S4
A_C^+	the dimensionless A_C defined by $A_C a_p^2 / U$
A_S	porosity-dependent parameter of Happel's model; $A_S = 2(1 - p^5) / (2 - 3p + 3p^5 - 2p^6)$
a_p	radius of particle
a_s	radius of the spherical collector
b	radius of the Happel cell
B_C	the coefficient in equation 6.S4
B_C^+	the dimensionless B_C defined by $B_C a_p / U$
C_0	the number concentration of particles in the suspension

D_C	the coefficient in equation 6.S4
D_C^+	the dimensionless D_C defined by $D_C a_p^2 / U$
D_∞	diffusion coefficient in an infinite medium, $D_\infty = k_B T / (6\pi\eta a_p)$
d_S	diameter of spherical collector, $d_c = 2a_c$
d_p	diameter of particle, $d_p = 2a_p$
e_r, e_θ, e_φ	unit vectors in r, θ and φ directions
$f_r^t, f_\theta^t, f_r^m, f_{1\theta}^m, f_{2\theta}^m$ and f_θ^r	Drag correction factors in Table 6.2, functions of δ
f_i^j	force vector on the particle, superscript specifies the source of the force
g	magnitude of the gravity vector, $g=9.81 \text{ g/s}^2$
$g_\varphi^r, g_\varphi^t, g_{1\varphi}^m$ and $g_{2\varphi}^m$	torque correction factors in Table 6.2, functions of δ
k	particle deposition rate constant
k_B	Boltzmann constant, $1.3805 \times 10^{-23} \text{ J/K}$
K_1, K_2, K_3 and K_4	coefficients that appear in equations 6.S1
N_G	gravity group, $N_G = 2a_p^2(\rho_p - \rho_f)g / 9\nu U$
N_{Lo}	London group, $N_{Lo} = A / 9\pi\eta a_p^2 U$
N_{PE}	Peclet number, $N_{PE} = U d_s / D_\infty$
N_R	relative size group, $N_R = a_p / a_s$
p	Defined in equation 6.S2, $p = a_s / b$
r	radial coordinate
r^*	dimensionless radial coordinate, $r^* = r / a_s$
s_1	$s_1 = (f_\theta^t g_\varphi^r - f_\theta^r g_\varphi^t) / g_\varphi^r$
s_2	$s_2 = (f_\theta^r g_{1\varphi}^m - y^+ f_{1\theta}^m g_\varphi^r) / g_\varphi^r$
s_3	$s_3 = (f_\theta^r g_{2\varphi}^m - y^+ f_{2\theta}^m g_\varphi^r) / g_\varphi^r$
t	time variable

T	absolute temperature
U	approach velocity
V	liquid flow field
y	$y = (r - a_s)$

Greek letters

$a(\delta, a_p, \lambda_e)$	retardation correction, a function of δ , a_p and λ_e
δ	surface-to-surface separation between the collector and the particle
δ^+	dimensionless parameter, $\delta^+ = \delta / a_p$
f	porosity of the porous media
η_0	the single collector contact efficiency
η_D , η_I and η_G	collection efficiencies due to diffusion, sedimentation and interception, respectively
θ	angular coordinate
φ	angular coordinate
κ	Debye-Huckel reciprocal length
λ_e	wavelength of electron oscillation, $\lambda_e = 100nm$
ν	viscosity of suspension
π	circular constant, $\pi = 3.14$
ρ_f	the density of the liquid
ρ_p	the density of the particle
ψ	stream function
u	Darcy velocity
u_r, u_θ, u_ϕ	the velocity vectors in different directions

Supporting information

Section S1. Review of the existing papers on peer-reviewed journals about the single collector contact efficiency simulations and modeling

Table 6.S1. Summary of the studies on the simulation and modeling of single collector contact efficiency^a

Modelling approach	Model collector	Dimensions of the model	Method on dealing with Brownian motion	Correlation equation	Particle density (g/cm ³)	Particle diameter range (nm)	References
Lagrangian trajectory analysis	Happel' sphere-in-cell	Two dimensional model and downward flow	No Brownian motion in trajectory analysis. Brownian motion term was super	$\eta \approx 0.72 A_S N_{Lo}^{1/8} N_R^{15/8} + 2.4 \times 10^{-3} A_S N_G^{1.2} N_R^{-0.4} + 4 A_S^{1/3} N_{pe}^{-2/3}$	n/a	n/a	Rajagopalan and Tien, 1976
Lagrangian trajectory analysis	Constricted tube	Three dimensional model	Brownian motion was not considered (particle size bigger than 0.3 μm)	n/a	1.5	3000-5000	Paraskeva and Burganos, 1991
Trajectory analysis	Dense/loose cubic packing method	Three dimensional model	Brownian motion was not considered	$\eta_s = 0.029 N_{Lo}^{0.012} N_R^{0.023} + 0.48 N_G^{1.8} N_R^{-0.38}$	2.45	Several micron	Cushing, 1998
Eulerian simulation results of convective-diffusion equation of colloid transport	Happel's sphere	Two dimensional model	Brownian motion was included in solving the convective-diffusion equation	$\eta_0 = 2.4 A_S^{1/3} N_R^{-0.081} N_{Pe}^{-0.715} N_{vdW}^{0.052} + 0.55 A_S N_R^{1.675} N_A^{0.125} + 0.22 N_R^{-0.24} N_G^{1.11} N_{vdW}^{0.053}$	1.0-1.8	10-10000	Tufenkji and Elimelech, 2004
Lagrangian trajectory analysis	Happel' sphere-in-cell	Two dimensional model	Brownian motion was included in the trajectory calculations	n/a	n/a	Bacterial colloids	Nelson and Ginn, 2005
Trajectory analysis	Dense/loose packing structure	Three dimensional model	Brownian motion was considered as Brownian force	n/a	n/a	n/a	Johnson et al, 2007
Trajectory analysis	Happel' hemisphere-in-cell	Two dimensional model	Brownian motion was considered as Brownian force	$\eta = \gamma^2 [2.3 A_S^{1/3} N_R^{-0.08} N_{PE}^{-0.65} N_A^{0.052} + 0.55 A_S N_R^{1.8} N_A^{0.15} + 0.2 N_R^{-0.1} N_G^{1.1} N_A^{0.053} N_{PE}^{0.053}]$	1.055	10-10000	Ma et al, 2009
Lattice-Boltzmann Method	n/a	Three dimensional model	Brownian motion was considered in the simulation process	$\eta_0 = (15.56 \pm 0.21) \frac{(1-\epsilon)^3}{\epsilon^2} N_R^{-0.65 \pm 0.023} N_{Pe}^{-0.19 \pm 0.03} + 0.55 A_S N_R^{1.675} N_A^{0.125} + 0.22 N_R^{-0.24} N_G^{1.11} N_{vdW}^{0.053}$	1.05	100-1000	Long and Hilpert, 2009
Trajectory analysis	constricted-tube model	Two dimensional model	Brownian motion was considered as Brownian force	n/a	1.07	10-10000	Wei and Wu, 2010
Lattice-Boltzmann Method	n/a	Three dimensional model	Brownian motion was considered in the simulation process	n/a		500-12000	Li et al, 2010

Lagrangian trajectory analysis	Happel' sphere-in-cell	Two dimensional model	Brownian motion was included in the trajectory calculations	$\eta_0 \approx \gamma^2 [2.4 A_s^{1/3} (\frac{N_{PE}}{N_{PE} + 16})^{0.75} N_{PE}^{-0.68} N_{LO}^{0.015} + A_s N_{LO}^{1/8} N_R^{15/8} + 0.7 (\frac{N_{Gi}}{N_{Gi} + 0.9}) N_G N_R^{-0.05}]$	0.995-1.00	5-5000	Nelson and Ginn, 2011
--------------------------------	------------------------	-----------------------	---	---	------------	--------	-----------------------

^a n/a indicates that the parameters (or the correlation equation) were not reported in the original reference.

Section S2. The stream function

The stream function in the liquid shell (see Figure 6.1) is referred from Rajagopalan and Tien's study [13], and is depicted as:

The stream function for the region $a_s \leq r \leq b$ is given by

$$\left. \begin{aligned} \psi &= (U/2) \sin^2 \theta^* a_s^2 [(K_1/r^*) - K_2 r^* + K_3 r^{*2} + K_4 r^{*4}] \\ r^* &= r/a_s \\ K_1 &= 1/w \\ K_2 &= (2 + 3p^5)/w \\ K_3 &= p(3 + 2p^5)/w \\ K_4 &= -p^5/w \\ w &= 2 - 3p + 3p^5 - 2p^6 \end{aligned} \right\} \quad (6.S1)$$

$$\text{And } p = (1 - \varepsilon)^{1/3} = a_s/b \quad (6.S2)$$

$$A_s = 2(1 - p^5)/w \quad (6.S3)$$

The stream function described in equation (6.S1) can be specified in the following form to describe the following hydrodynamic forces and torques calculations:

$$V = -A_C y^2 e_r + (B_C y + D_C y^2) e_\theta \quad (6.S4)$$

where y is the distance from the collector surface to the centre of the particle. Combining the stream function and equation S3, the coefficients of A_C , B_C , and D_C can be obtained and expressed as:

$$A_C = Ua_s^2 * \cos \theta * (K_1 / r^* - K_2 * r^* + K_3 * r^{*2} + K_4 * r^{*4}) / r^2 / (r - a_s)^2 \quad (6.S5)$$

$$B_C = U \sin \theta \left[-\frac{K_1 a_s^4}{r^2} - K_2 a_s^2 + (2K_3 - 4K_4) r a_s + 8K_4 r^2 \right] / [2r a_s (r - a_s)] \quad (6.S6)$$

$$D_C = \frac{2UK_4 \sin \theta}{a_s^2} \quad (6.S7)$$

where, a_s is the radius of the collector, ε is the porosity of the porous media, r is the position vector, r^* is the dimensionless position vector, b is the radius of the Happel cell, w is the function of a_s / b , K_1 , K_2 , K_3 and K_4 are coefficients, $(r - a_s)$ equals the above y .

Section S3. The comparisons of the numerical data of the single collector contact efficiency with the RT and TE equations data under various conditions

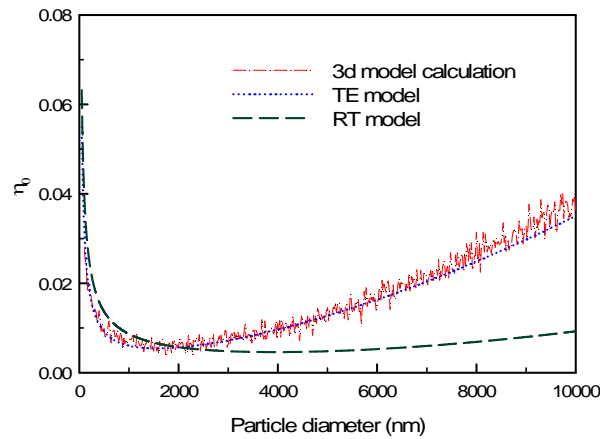


Figure 6.S1. The predictions of η_0 from the TE and RT equations as well as the 3-D numerical simulated η_0 with particle diameter under the conditions: $\rho_p = 1.05 \text{ g/cm}^3$, $d_s = 340 \text{ }\mu\text{m}$, $f = 0.37$, $U = 0.508 \text{ cm/min}$, $\mu = 1 \text{ cP}$.

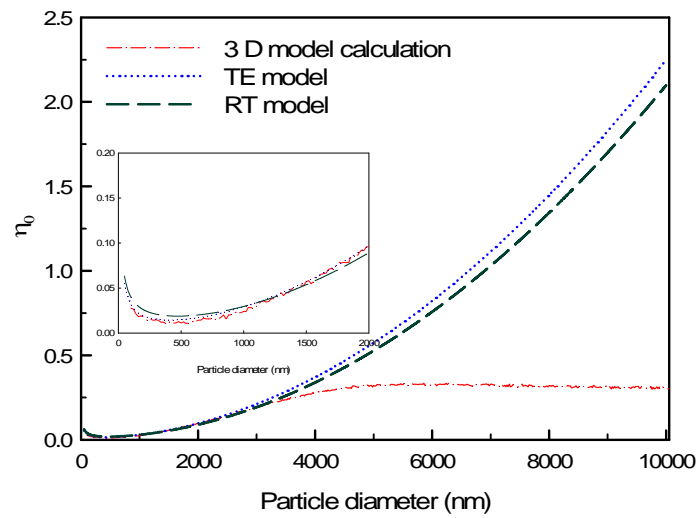


Figure 6.S2. The predictions of η_0 from the TE and RT equations as well as the 3-D numerical simulated η_0 with particle diameter under the conditions: $\rho_p=6.58 \text{ g/cm}^3$, $d_s=340 \text{ }\mu\text{m}$, $f=0.37$, $U=0.508 \text{ cm/min}$, $\mu=1 \text{ cP}$.

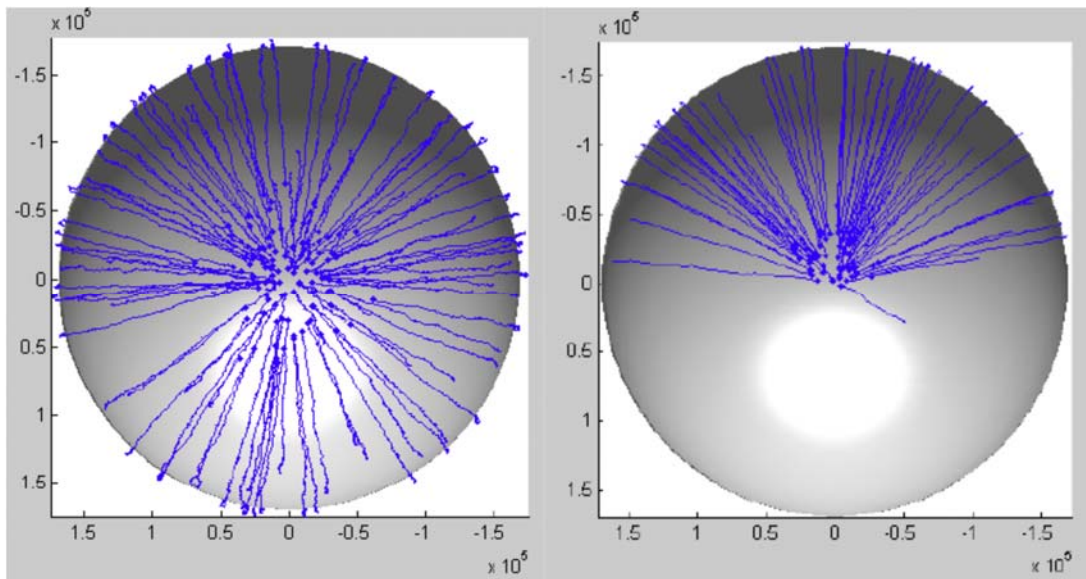


Figure 6.S3. The demonstrations of the deposition locations of particles. a) the particles with the density of 1.05 g/cm^3 and 4000 nm diameter; b) the particles with the density of 6.58 g/cm^3 and 4000 nm , (other conditions: $U=0.508 \text{ cm/min}$, $d_s=340 \text{ }\mu\text{m}$, $\mu=1 \text{ cP}$).

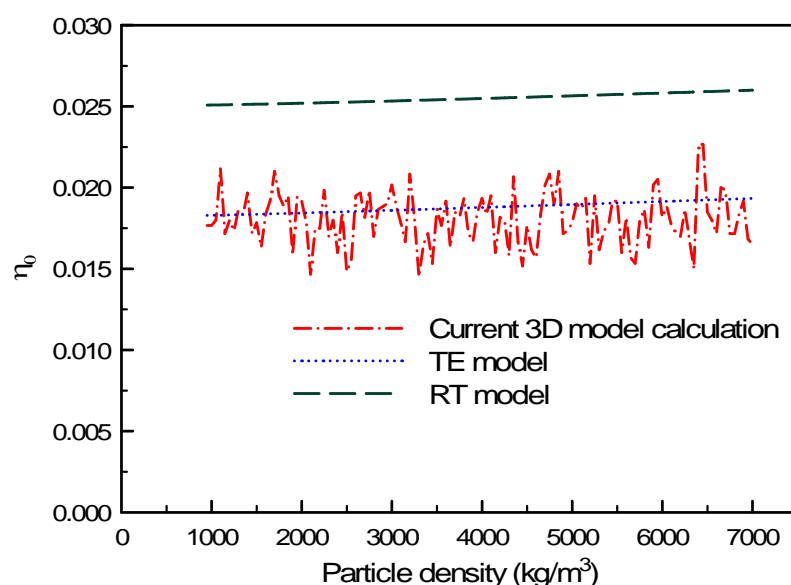


Figure 6.S4. The predictions of η_0 from the TE and RT equations as well as the 3-D numerical simulated η_0 with particle density under the conditions: $d_p=200$ nm, $d_s=340$ μm , $f=0.37$, $U=0.508$ cm/min, $\mu=26.3$ cP.

For the particle with the diameter of 200 nm, no obvious difference of the dependence of η_0 values on particle density between our current 3-D numerical calculations and TE equation predictions (Figure S4): η_0 values approximately remain at a constant value (0.018) with particle density in both our current 3-D numerical calculations and the predictions from TE equation. The single collector contact efficiency of a colloidal particle is mainly contributed by the Brownian diffusion mechanic, when the particle diameter is less than 1000 nm. Thus, the very approximate η_0 values of our 3-D numerical simulation to those predicted by TE equation under the identical conditions indicate that the methodology used in this study to simulate the effect of Brownian diffusion on η_0 is appropriate. Additionally, as pointed out by Nelson and Ginn [22] the RT equation overestimated the impact of Brownian diffusion on η_0 prediction, can account for the bigger η_0 values predicted from RT equation than those predicted from TE equation in the whole range of particle density (Figure S4). When particle diameter increases to 2000 nm, the increase trend of the simulated η_0 values with particle density in 3-D is very similar with that obtained in TE equation (shown in Figure S5). As particle diameter rises to 4000 nm (shown in Figure S6),

the increasing trend of η_0 with particle density is retarded in our 3-D simulations, compared to the TE equation, beyond 4000 kg/m³. This result proves our hypothesis that when the particle's density grows to a certain value, gravity forces would result in a very significant gravitational settling of particles in the horizontal flow mode.

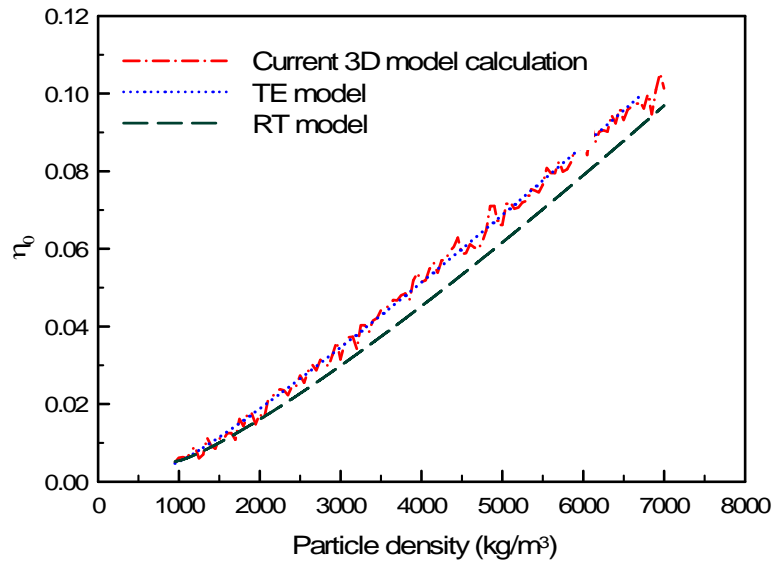


Figure 6.S5. The predictions of η_0 from the TE and RT equations as well as the 3-D numerical simulated η_0 with particle density under the conditions: $d_p=2000\text{nm}$, $d_s=340\ \mu\text{m}$, $f=0.37$, $U=0.508\ \text{cm/min}$, $\mu=1\ \text{cP}$.

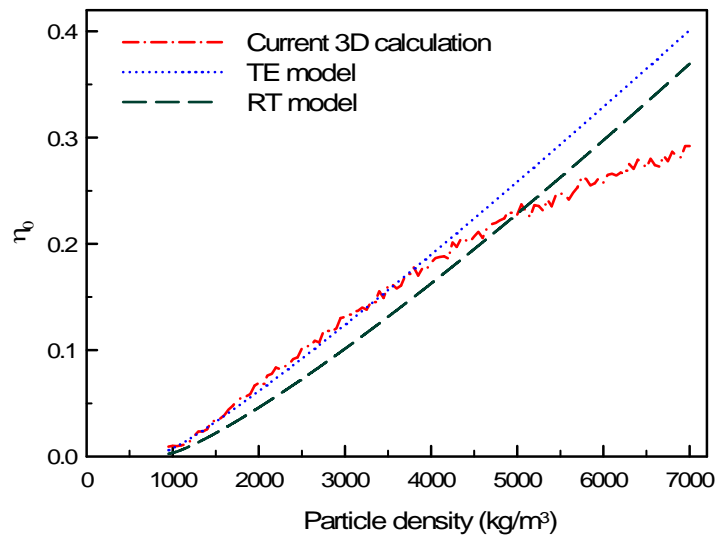


Figure 6.S6. The predictions of η_0 from the TE and RT equations as well as the 3-D numerical simulated η_0 with particle density under the conditions: $d_p=4000$ nm, $d_s=340$ μm , $f=0.37$, $U=0.508$ cm/min, $\mu=1$ cP.

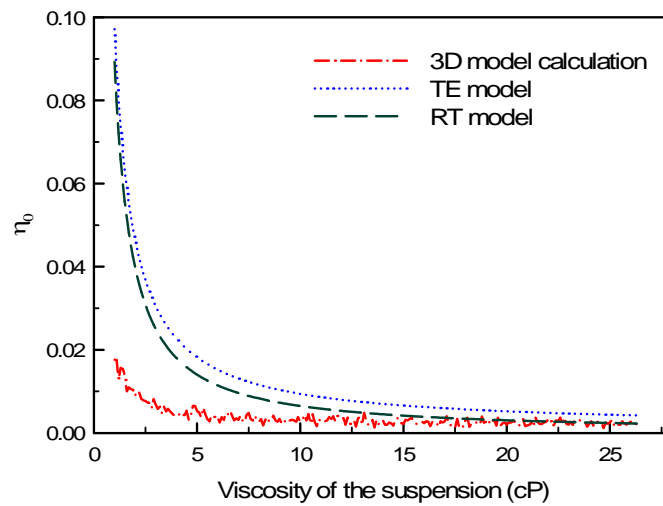


Figure 6.S7. The predictions of η_0 from the TE and RT equations as well as the 3-D numerical simulated η_0 with the viscosity of the suspension under the conditions: $d_p=2000$ nm, $d_s=340$ μm , $f=0.37$, $U=0.508$ cm/min, $\rho_p=6.58$ g/cm³.

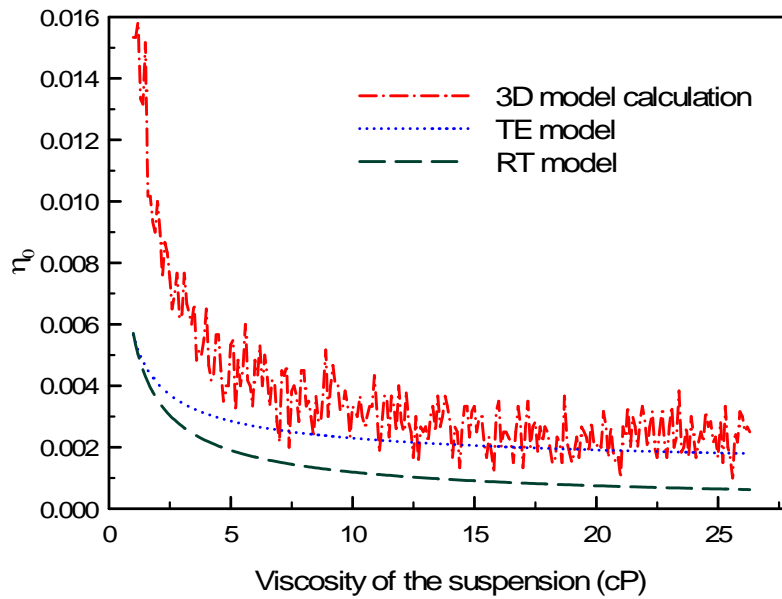


Figure 6.S8. The predictions of η_0 from the TE and RT equations as well as the 3-D numerical simulated η_0 with the viscosity of the suspension under the conditions: $d_p=2000$ nm, $d_s=340$ μm , $f=0.37$, $U=0.508$ cm/min, $\rho_p=1.05$ g/cm³.

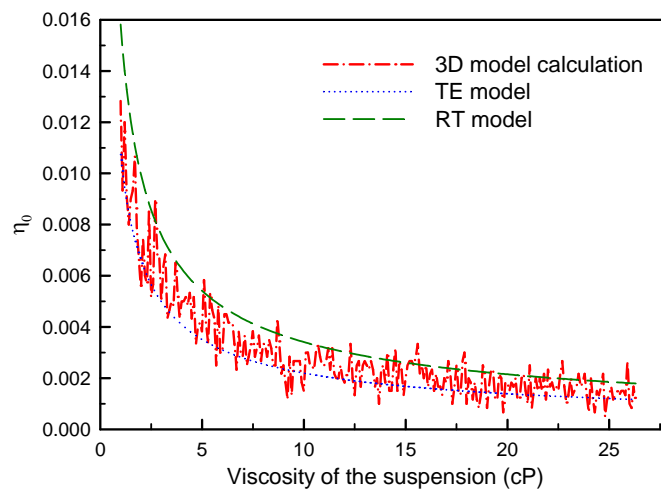


Figure 6.S9. The predictions of η_0 from the TE and RT equations as well as the 3-D numerical simulated η_0 with the viscosity of the suspension under the conditions: $d_p=400$ nm, $d_s=340$ μm , $f=0.37$, $U=0.508$ cm/min, $\rho_p=1.05$ g/cm³.

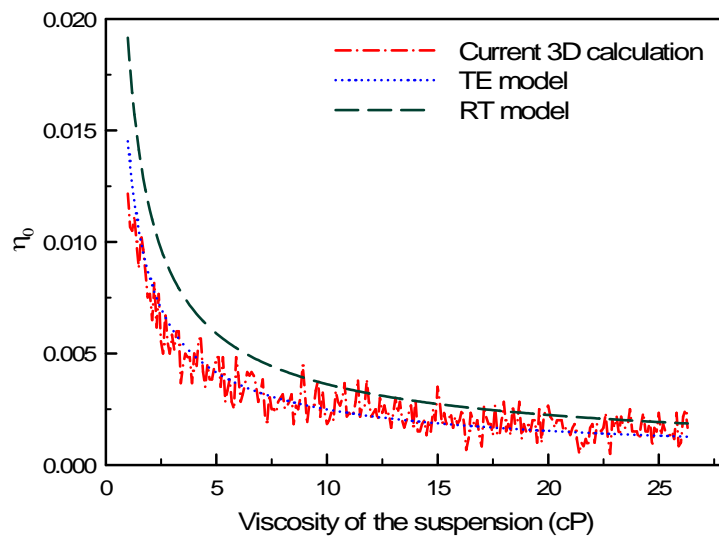


Figure 6.S10. The predictions of η_0 from the TE and RT equations as well as the 3-D numerical simulated η_0 with the viscosity of the suspension under the conditions: $d_p=400$ nm, $d_s=340$ μm , $f=0.37$, $U=0.508$ cm/min, $\rho_p=6.58$ g/cm³.

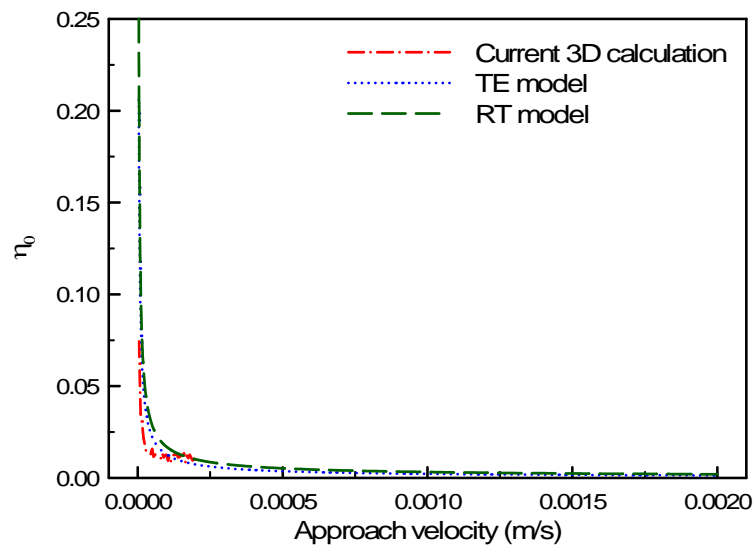


Figure 6.S11. The predictions of η_0 from the TE and RT equations as well as the 3-D numerical simulated η_0 with approach velocity under the conditions: $d_p=400$ nm, $d_s=340$ μm , $f=0.37$, $\mu=1$ cP, $\rho_p=6.58$ g/cm³.

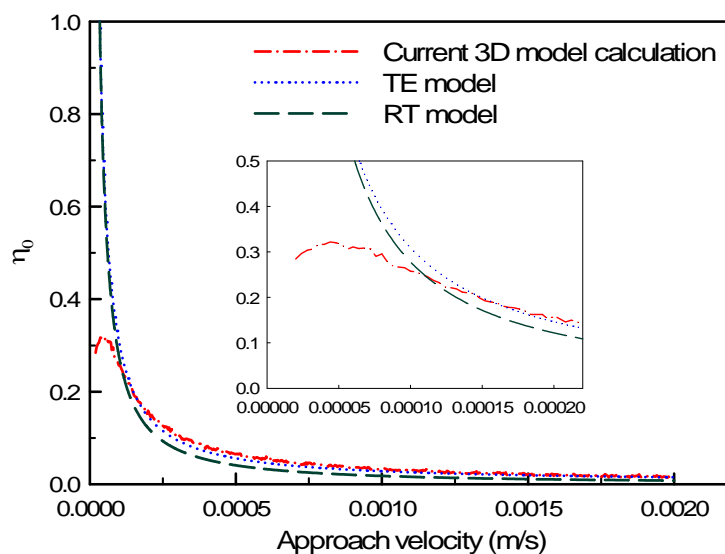


Figure 6.S12. The predictions of η_0 from the TE and RT equations as well as the 3-D numerical simulated η_0 with approach velocity under the conditions: $d_p=4000$ nm, $d_s=340$ μm , $f=0.37$, $\mu=1$ cP, $\rho_p=6.58$ g/cm³.

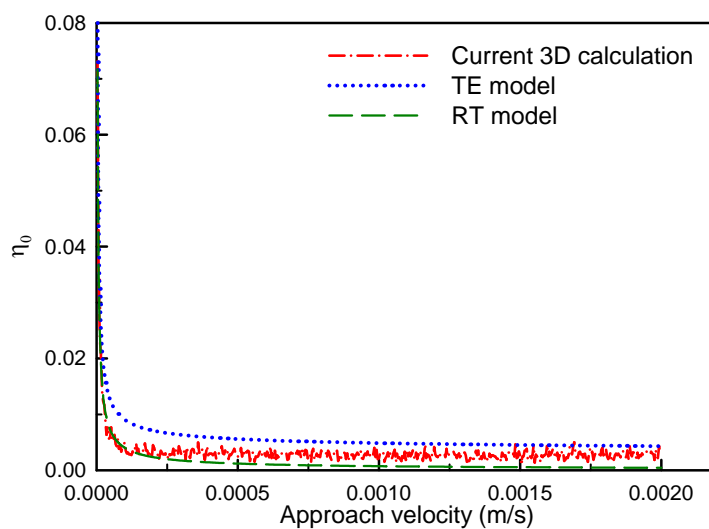


Figure 6.S13. The predictions of η_0 from the TE and RT equations as well as the 3-D numerical simulated η_0 with approach velocity under the conditions: $d_p=4000$ nm, $d_s=340$ μm , $f=0.37$, $\mu=1$ cP, $\rho_p=1.05$ g/cm³.

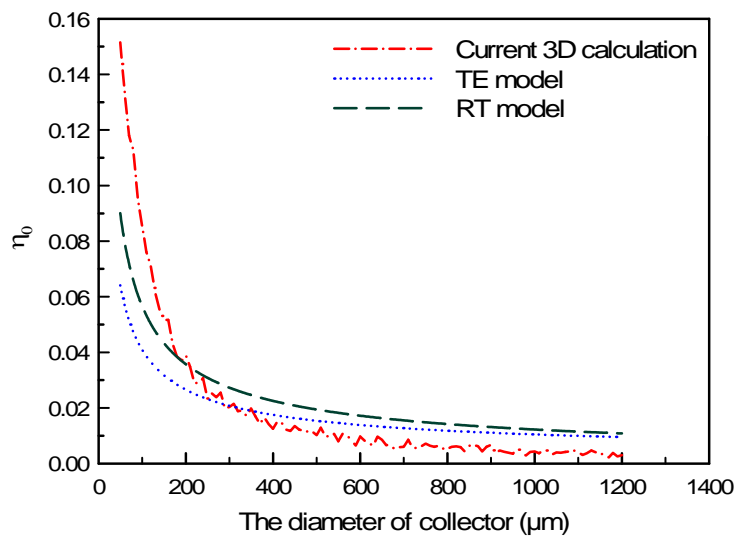


Figure 6.S14. The predictions of η_0 from the TE and RT equations as well as the 3-D numerical simulated η_0 with the diameter of collector under the conditions: $d_p=200$ nm, $U=0.508$ cm/min, $f=0.37$, $\mu=1$ cP, $\rho_p=6.58$ g/cm³.

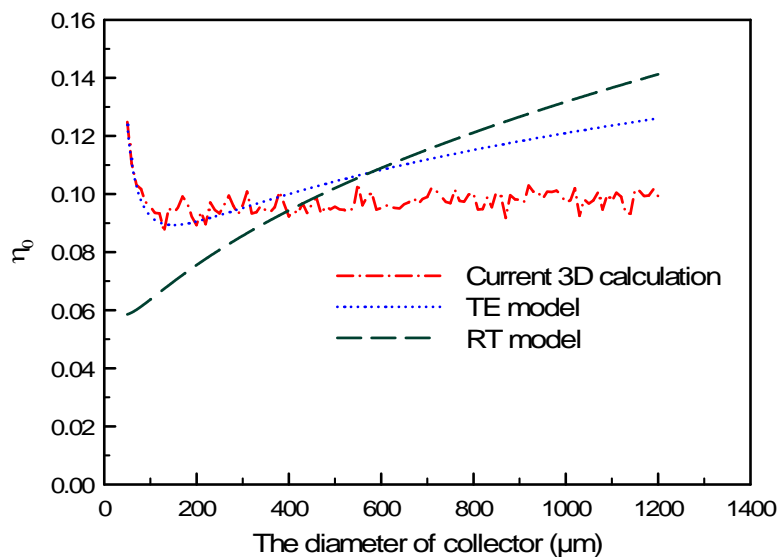


Figure 6.S15. The predictions of η_0 from the TE and RT equations as well as the 3-D numerical simulated η_0 with the diameter of collector under the conditions: $d_p=2000$ nm, $U=0.508$ cm/min, $f=0.37$, $\mu=1$ cP, $\rho_p=6.58$ g/cm³.

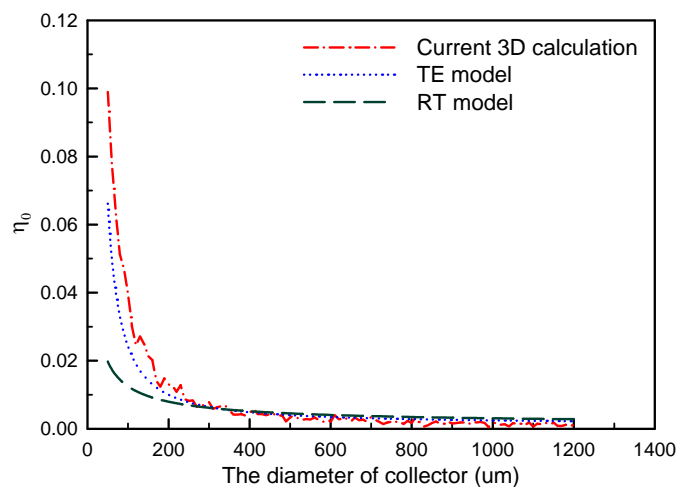


Figure 6.S16. The predictions of η_0 from the TE and RT equations as well as the 3-D numerical simulated η_0 with the diameter of collector under the conditions: $d_p=2000$ nm, $U=0.508$ cm/min, $f=0.37$, $\mu=1$ cP, $\rho_p=1.05$ g/cm³.

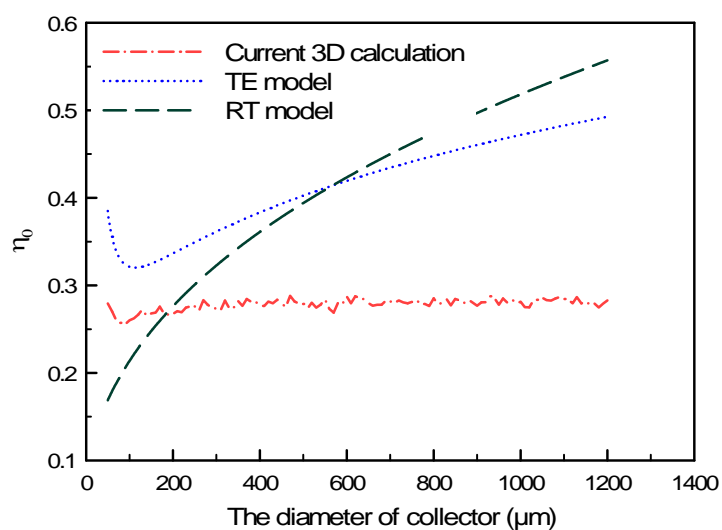


Figure 6.S17. The predictions of η_0 from the TE and RT equations as well as the 3-D numerical simulated η_0 with the diameter of collector under the conditions: $d_p=4000$ nm, $U=0.508$ cm/min, $f=0.37$, $\mu=1$ cP, $\rho_p=6.58$ g/cm³.

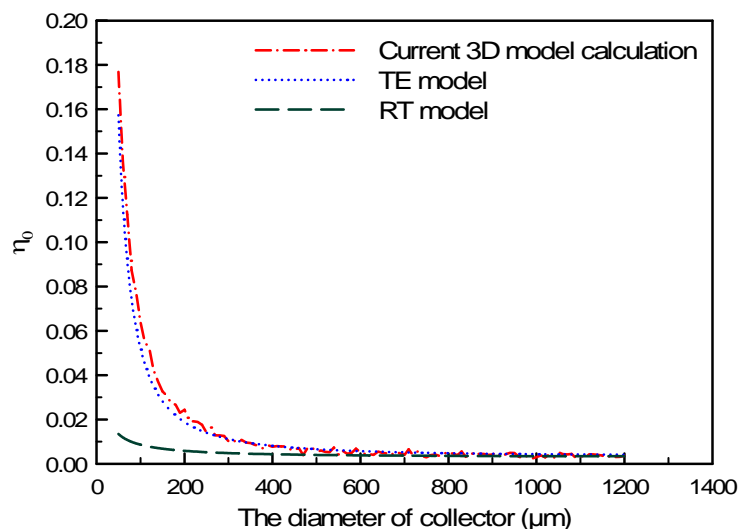


Figure 6.S18. The predictions of η_0 from the TE and RT equations as well as the 3-D numerical simulated η_0 with the diameter of collector under the conditions: $d_p=4000$ nm, $U=0.508$ cm/min, $f=0.37$, $\mu=1$ cP, $\rho_p=1.05$ g/cm³.

References

- [1] N. Tufenkji, J.N. Ryan, M. Elimelech, Peer Reviewed: The Promise of Bank Filtration, *Environmental Science & Technology*, 36 (2002) 422A-428A.
- [2] I.R. Quevedo, A.L.J. Olsson, N. Tufenkji, Deposition Kinetics of Quantum Dots and Polystyrene Latex Nanoparticles onto Alumina: Role of Water Chemistry and Particle Coating, *Environmental Science & Technology*, 47 (2013) 2212-2220.
- [3] I. Heidmann, Metal oxide nanoparticle transport in porous media—an analysis about (un) certainties in environmental research, in: *Journal of Physics: Conference Series*, IOP Publishing, 2013, pp. 012042.
- [4] T. Raychoudhury, N. Tufenkji, S. Ghoshal, Aggregation and deposition kinetics of carboxymethyl cellulose-modified zero-valent iron nanoparticles in porous media, *Water research*, 46 (2012) 1735-1744.
- [5] Y. Ouyang, D. Shinde, R. Mansell, W. Harris, Colloid - enhanced transport of chemicals in subsurface environments: A review, *Critical reviews in environmental Science and Technology*, 26 (1996) 189-204.
- [6] N. Tufenkji, Application of a dual deposition mode model to evaluate transport of *Escherichia coli* D21 in porous media, *Water resources research*, 42 (2006).

- [7] F. He, M. Zhang, T. Qian, D. Zhao, Transport of carboxymethyl cellulose stabilized iron nanoparticles in porous media: Column experiments and modeling, *Journal of Colloid and Interface Science*, 334 (2009) 96-102.
- [8] N. Saleh, H.-J. Kim, T. Phenrat, K. Matyjaszewski, R.D. Tilton, G.V. Lowry, Ionic Strength and Composition Affect the Mobility of Surface-Modified Fe₀ Nanoparticles in Water-Saturated Sand Columns, *Environmental Science & Technology*, 42 (2008) 3349-3355.
- [9] J.N. Ryan, M. Elimelech, J.L. Baeseman, R.D. Magelky, Silica-coated titania and zirconia colloids for subsurface transport field experiments, *Environmental science & technology*, 34 (2000) 2000-2005.
- [10] S.A. Bradford, S.R. Yates, M. Bettahar, J. Simunek, Physical factors affecting the transport and fate of colloids in saturated porous media, *Water Resources Research*, 38 (2002) 1327.
- [11] C.H. Bolster, S.L. Walker, K.L. Cook, Comparison of and Transport in Saturated Porous Media, *Journal of environmental quality*, 35 (2006) 1018-1025.
- [12] K.-M. Yao, M.T. Habibian, C.R. O'Melia, Water and waste water filtration. Concepts and applications, *Environmental Science & Technology*, 5 (1971) 1105-1112.
- [13] R. Rajagopalan, C. Tien, Trajectory analysis of deep - bed filtration with the sphere - in - cell porous media model, *AIChE Journal*, 22 (1976) 523-533.
- [14] N. Tufenkji, M. Elimelech, Correlation equation for predicting single-collector efficiency in physicochemical filtration in saturated porous media, *Environmental science & technology*, 38 (2004) 529-536.
- [15] W. Long, M. Hilpert, A Correlation for the Collector Efficiency of Brownian Particles in Clean-Bed Filtration in Sphere Packings by a Lattice-Boltzmann Method, *Environmental Science & Technology*, 43 (2009) 4419-4424.
- [16] K.E. Nelson, T.R. Ginn, New collector efficiency equation for colloid filtration in both natural and engineered flow conditions, *Water Resources Research*, 47 (2011) W05543.
- [17] C. Paraskeva, V. Burganos, A. Payatakes, Three-dimensional trajectory analysis of particle deposition in constricted tubes, *Chemical engineering communications*, 108 (1991) 23-48.
- [18] R.S. Cushing, D.F. Lawler, Depth filtration: Fundamental investigation through three-dimensional trajectory analysis, *Environmental science & technology*, 32 (1998) 3793-3801.
- [19] J.E. Tobiason, C.R. O'melia, Physicochemical aspects of particle removal in depth filtration, *Journal (American Water Works Association)*, (1988) 54-64.
- [20] W. Johnson, X. Li, G. Yal, Colloid retention in porous media: Mechanistic confirmation of wedging and retention in zones of flow stagnation, *Environmental science & technology*, 41 (2007) 1279-1287.
- [21] J.N. Ryan, M. Elimelech, Colloid mobilization and transport in groundwater, *Colloids and Surfaces A: Physicochemical and Engineering Aspects*, 107 (1996) 1-56.
- [22] K.E. Nelson, T.R. Ginn, Colloid filtration theory and the Happel sphere-in-cell model revisited with direct numerical simulation of colloids, *Langmuir*, 21 (2005) 2173-2184.
- [23] H. Ma, J. Pedel, P. Fife, W.P. Johnson, Hemispheres-in-cell geometry to predict colloid deposition in porous media, *Environmental Science & Technology*, 43 (2009) 8573-8579.

- [24] A.R. Petosa, D.P. Jaisi, I.R. Quevedo, M. Elimelech, N. Tufenkji, Aggregation and deposition of engineered nanomaterials in aquatic environments: Role of physicochemical interactions, *Environmental science & technology*, 44 (2010) 6532-6549.
- [25] H. Ma, E.F. Pazmino, W.P. Johnson, Gravitational Settling Effects on Unit Cell Predictions of Colloidal Retention in Porous Media in the Absence of Energy Barriers, *Environmental Science & Technology*, 45 (2011) 8306-8312.
- [26] Y.-T. Wei, S.-c. Wu, Development of a trajectory model for predicting attachment of submicrometer particles in porous media: Stabilized NZVI as a case study, *Environmental science & technology*, 44 (2010) 8996-9002.
- [27] Z. Li, D. Zhang, X. Li, Tracking colloid transport in porous media using discrete flow fields and sensitivity of simulated colloid deposition to space discretization, *Environmental science & technology*, 44 (2010) 1274-1280.
- [28] Z. Li, D. Zhang, X. Li, Tracking colloid transport in real pore structures: Comparisons with correlation equations and experimental observations, *Water Resources Research*, 48 (2012).
- [29] S.R. Kanel, J.-M. Greneche, H. Choi, Arsenic (V) removal from groundwater using nano scale zero-valent iron as a colloidal reactive barrier material, *Environmental Science & Technology*, 40 (2006) 2045-2050.
- [30] P. Bennett, F. He, D. Zhao, B. Aiken, L. Feldman, In situ testing of metallic iron nanoparticle mobility and reactivity in a shallow granular aquifer, *Journal of contaminant hydrology*, 116 (2010) 35-46.
- [31] W.x. Zhang, D.W. Elliott, Applications of iron nanoparticles for groundwater remediation, *Remediation Journal*, 16 (2006) 7-21.
- [32] P.G. Tratnyek, R.L. Johnson, Nanotechnologies for environmental cleanup, *Nano today*, 1 (2006) 44-48.
- [33] E.D. Vecchia, M. Luna, R. Sethi, Transport in porous media of highly concentrated iron micro-and nanoparticles in the presence of xanthan gum, *Environmental science & technology*, 43 (2009) 8942-8947.
- [34] R.L. Johnson, J.T. Nurmi, G.S. O'Brien Johnson, D. Fan, R.L. O'Brien Johnson, Z. Shi, A.J. Salter-Blanc, P.G. Tratnyek, G.V. Lowry, Field-Scale Transport and Transformation of Carboxymethylcellulose-Stabilized Nano Zero-Valent Iron, *Environmental Science & Technology*, 47 (2013) 1573-1580.
- [35] M.J. Truex, V.R. Vermeul, D.P. Mendoza, B.G. Fritz, R.D. Mackley, M. Oostrom, T.W. Wietsma, T. Macbeth, Injection of Zero - Valent Iron into an Unconfined Aquifer Using Shear - Thinning Fluids, *Ground Water Monitoring & Remediation*, 31 (2011) 50-58.
- [36] Y. Liu, T. Phenrat, G.V. Lowry, Effect of TCE concentration and dissolved groundwater solutes on NZVI-promoted TCE dechlorination and H₂ evolution, *Environmental science & technology*, 41 (2007) 7881-7887.
- [37] G.K. Batchelor, *An introduction to fluid dynamics*, Cambridge university press, 2000.
- [38] R. Rajagopalan, *Stochastic modeling and experimental analysis of particle transport in water filtration*, (1974).

[39] D.C. Prieve, E. Ruckenstein, Effect of London forces upon the rate of deposition of Brownian particles, *AIChE Journal*, 20 (1974) 1178-1187.

[40] N. Tufenkji, M. Elimelech, Correlation Equation for Predicting Single-Collector Efficiency in Physicochemical Filtration in Saturated Porous Media, *Environmental Science & Technology*, 38 (2003) 529-536.

Chapter 7

Intellectual contributions

Direct injection of NZVI particles into contaminated aquifers to restore chlorinated solvent-contaminated groundwater is considered to be a promising cleanup approach as NZVI can reductively degrade such chemicals rapidly. The success in applying this method in field will mainly depend on the feasibility of transport of NZVI from injection wells to chlorinated organics DNAPLs contaminated zones. The transport of NZVI in aquifers is limited due to the significant aggregation of particles at g/L concentration levels, which is required for field remediation applications.

Coating NZVI particles with polymer or polyelectrolyte is considered to be an effective method to stabilize NZVI particles and thereby promote their transport in porous media. CMC was found to be very effective in stabilizing NZVI particles. Homologous CMCs with various molecular weights were evaluated in this research to investigate the effects of molecular weights of CMCs on stabilizing NZVI particles and on enhancing their transport.

The research demonstrated that groundwater flow directions can significantly influence NZVI particle transport through porous media. The transport experiments were conducted in vertically-placed column and in horizontally-placed column under different porous media sizes and NZVI concentrations. The simulations of the trajectories of NZVI particles in these two flow modes were also performed to explain the mechanics on particles transport in these flow modes.

The transport of CMC-coated NZVI particles was also investigated in scaled up 2-D tank to systemically study the transport and depositions of NZVI particles under different concentrations and injection velocities. The effects of properties of NZVI suspensions on particle transport were also examined. The particles sizes were also measured in the transport process to verify the aggregation extent.

The mathematical simulation of NZVI particle transport around a collector were performed by using Lagrangian trajectory analysis method to thoroughly estimate the effects of

flow modes, the density of particle, the flow velocity, the size of the collector, the viscosity of particle suspension on the transport of particles the single collector contact efficiency and thus on the subsequent deposition and transport of particles.

The specific intellectual contributions of this research are:

7.1 Determining the role of stabilizing polymer molecular weights on enhancing colloidal stabilization and transport of NZVI.

Overall, the stability and transport of CMC-stabilized NZVI increased with the molecular weight of CMC. To date no other studies have systematically investigated the effects of a set of homologous polymer or polyelectrolyte on stabilizing and on enhancing NZVI transport as well as no any other studies has thoroughly seek the reasons for the above results.

700K CMC stabilized NZVI particles are more stable and mobile than those of 90K CMC and 250K CMC stabilized NZVI particles. The viscosities of these CMC-NZVI suspensions (prepared in 1 g/L CMC solutions) increase with the increase of CMC molecular weight, which is partly attributable to the above stability and transport results. Further, the mass of adsorbed NZVI particle surface does not differ significantly for different CMCs, but the new Ohshima theory as well as DLVO theory calculations revealed that 700K CMC coatings on NZVI surface provided more surface charge on particle and yielded much stronger particle-particle repulsion than 250K- or 90K-CMC. The contributions of polymer viscosity to NZVI stabilization and transport and are original contributions of this research.

7.2 Demonstrating the role of horizontal and vertical flow direction on CMC-NZVI transport behavior.

The transport of NZVI particles was investigated in horizontal flow mode, which is more likely to occur for natural groundwater. The comparison of transport results obtained in horizontal and vertical flow modes demonstrated that NZVI transport efficiencies in horizontal

flow mode were lower than those in the vertical mode, in particular, in coarse sand and high NZVI concentrations.

The retention profiles of NZVI particles in top and bottom sides of the horizontally-placed column showed a very big difference, because a significant mass of particles collected at the bottom side of the horizontally-placed columns packed with coarser sands. This result indicates that particles settled under gravity to the bottom side during transport, but only in the coarser sands. In the fine sand, the retention profiles of NZVI particles in the top and bottom sides of the horizontally-placed column did not differ significantly at 0.3 and 1 g/L. The obvious difference occurred at 3 g/L.

The mathematical simulations of the trajectory of NZVI particles around sand collectors verified the considerable setting of NZVI particles in the coarse and intermediate sands in the horizontal flow mode. The effects of flow direction on NZVI transport in porous media have not been clearly demonstrated to date.

7.3 The changes in temporal and spatial distribution of NZVI particles during NZVI injection and transport in a scaled-up 2-D tank was demonstrated for a range of porous media size and particle suspension characteristics.

The transport of 700K CMC-NZVI NZVI particles was systematically studied under different NZVI concentrations and injection velocity in a pilot scale 2-D tank. High injection velocity were very favorable for NZVI particle transport, while high NZVI concentration showed less transport, being consistent with the results obtained in 1-D columns.

The hydraulic conductivity of the tank system reduced significantly after injecting 700K CMC-NZVI particles, in particular, for the NZVI particles at 2 g/L in 700K CMC solutions. Further, the hydraulic conductivity of the tank system also reduced when the injection velocity reduced. At high CMC concentration (2 g/L), the pressure drop during injection was much higher than those at low CMC solution (1 g/L). These hydraulic conductivity and pressure drop results are attributed to the higher viscosity of with higher CMC concentrations.

The research presents new data how NZVI concentrations in aqueous solutions change with time and distance from the injection source, and improves our understanding of NZVI transport under injection conditions.

7.4 This study is the first to mathematically simulate the trajectory of colloidal particles around a collector under horizontal flow mode by using Lagrangian trajectory analysis combined with Brownian motion. A new correlation equation for horizontal flow of colloids around a collector was presented. The study demonstrates that the density of engineered metal nanoparticles result in different trajectories in horizontal flow mode from those in vertical flow mode.

A new methodology is developed in three dimensions (3-D) to more precisely predict the single collector efficiency of NZVI particles in wider ranges of particle density, viscosity of the suspension and flow velocity. The trajectory analysis of particles in 3-D simulations revealed that particles with high density and large size showed different collision pattern on collector surface from those predicted from 2-D simulations.

A new correlation equation overcomes the limitations of the current approaches in predicting η_0 of colloids with high density in horizontal flow modes and shows exceptional agreement with numerical simulations of η_0 over a wide range of conditions. Furthermore, the new equation presented in this study shows reasonable predictions of η_0 of emerging engineered metal nanoparticles transported in saturated porous media. The experimental transport data of nanoscale zero valent iron particles in horizontal column (shown in Chapter 4) can be satisfactorily explained by the findings of different deposition pattern of NZVI particles on collector in horizontal flow mode.

